Techno-economics of the anodic peroxide evolution reaction

M.S. van Leeuwen

Delft University of Technology

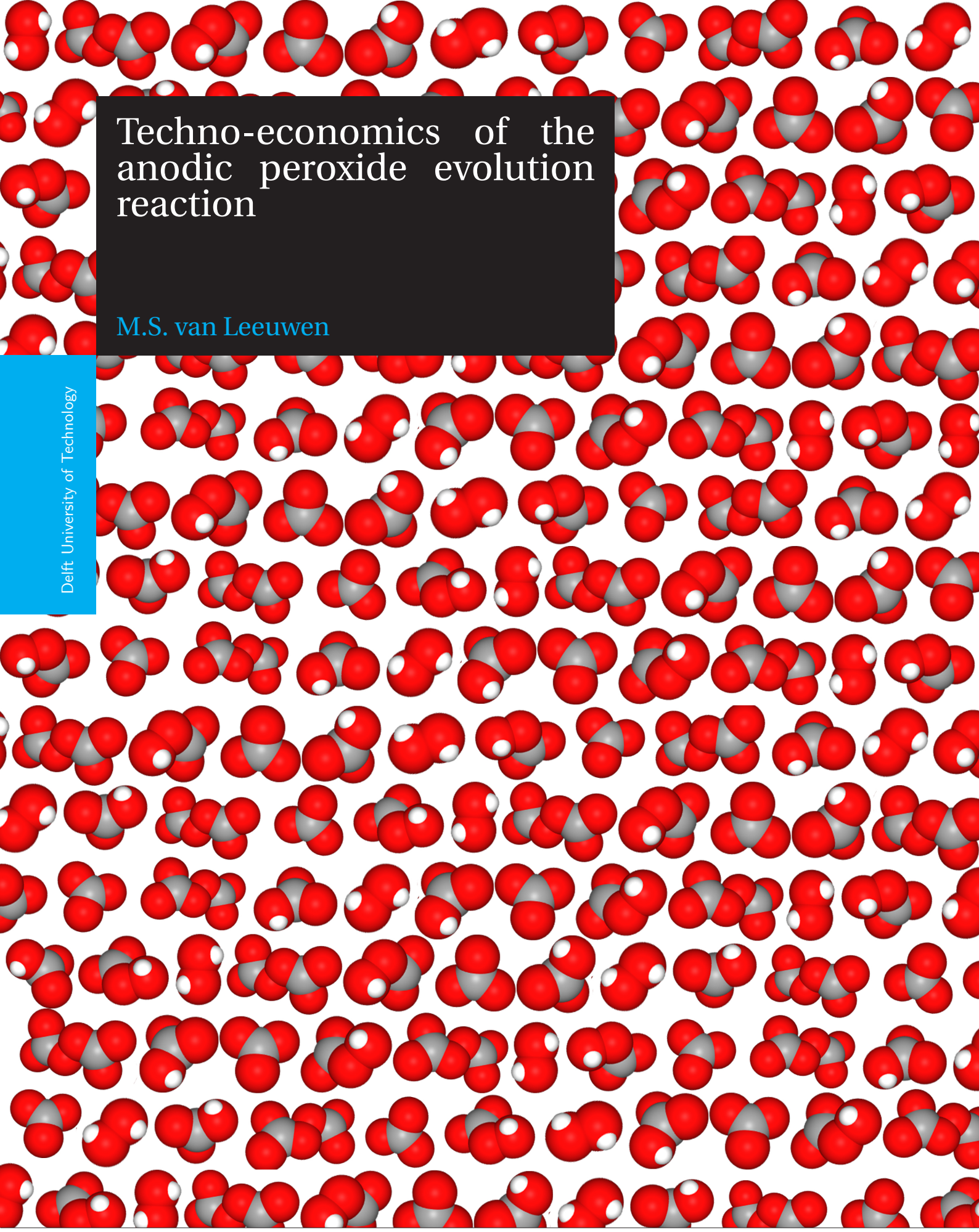

TU Delft Delft University of Technology

Challenge the future

TECHNO-ECONOMICS OF THE ANODIC PEROXIDE EVOLUTION REACTION

M.S. van Leeuwen

To obtain the degree of

Master of Science
in Chemical Engineering

at the Delft University of Technology,

To be defended publicly on Thursday, June 18th 2020 at 9:00.

Student number:	4429672	
Supervising professor:	Prof. dr. B. Dam	MECS, TU Delft
Daily supervisor:	Ir. A. Venugopal	MECS, TU Delft
Thesis committee:	Dr. E.M. Kelder	SEE, TU Delft
	Prof. dr. ir. C.A. Ramirez Ramirez	TPM, TU Delft

TU Delft Delft University of Technology

ABSTRACT

The Oxygen Evolution Reaction (OER) is the anodic reaction usually considered in electrochemical processes. Next to having sluggish kinetics, a drawback of this reaction is the lack of value of its product stream. In order to boost the feasibility of electrochemical processes, research is being conducted on alternative anodic reactions. Even though thermodynamically less favorable, the hydrogen peroxide evolution yields an added-value product which the OER does not. In this study, the industrial relevance of the anodic peroxide evolution reaction was investigated. The aim was to assess the potential for industrial application of this reaction. To do so, the electrochemical parameters of influence were to be investigated and the mechanisms behind them were to be understood.

In order to evaluate both economic and technical feasibility of the process, three main threads were followed. Firstly, a gross margin model was introduced. This model allowed to define performance targets of the electrolytic process based on viability requirements. Secondly, electrochemical experiments were carried out. Materials fit for large scale implementation were to be identified. Tin oxide- based materials (SnO_2, Sn_3O_4, ITO and FTO) were investigated due to the stability of tin oxide in a large pH window. Carbon-based materials (CFP, PTFE-coated CFP and GDE) were investigated for their high current density responses and high peroxide yield. Once these materials were identified, systematic studies on electrolyte effects were to be carried out. Finally, product characterization methods were investigated in order to understand the role of ions such as HCO_3^- and CO_3^{2-} in the enhanced production of electrochemical peroxide.

Thanks to the gross margin model, the added-value of the anodic peroxide evolution reaction over the OER was confirmed. The viability of coupling the two-electron WOR with four cathodic reactions (HER, CO_2 reduction to CO and C_2H_4 and two-electron ORR) was explored. Experimental performance targets were defined, thus providing a road-map from lab-scale work to industrial implementation. Electrochemical experiments explored the achievement of these techno-economic targets. Tin oxide-based materials only yielded very low current densities and peroxide evolution. Methods such as doping, thickness, crystallinity, surface morphology and substrate variations did not significantly improve performances for these materials. Carbon-based materials on the other hand presented very promising features regarding current density and yield. The mechanisms behind these improved performances were however not yet fully understood thus highlighting the importance of product characterization methods. Calibration experiments were performed for permanganate titration and NMR spectroscopy. Titration was investigated to quantify the peroxide yield during electrolysis. The potential of NMR spectroscopy for a qualitative study of the peroxide components produced was investigated. All peroxide compounds thought to be involved in the enhanced peroxide evolution (H_2O_2, HCO_3^-, HCO_4^-, CO_3^{2-}, $C_2O_6^{2-}$) could be differentiated. Calibration was achieved for all compounds apart from HCO_4^-, for which further research is needed. Even though the implementation of NMR studies for the understanding of mechanisms behind the peroxide evolution reactions seem promising, some concerns regarding detection limits arose.

ACKNOWLEDGEMENTS

A special word deserves to be said for all those who contributed directly or indirectly to the completion of this thesis.

First, I would like to thank Pr.dr. Bernard Dam for his supervision. From our first meeting, he took the time for me whenever was needed. Even his nomination as *ad interim* head of department Chemical Engineering position did not prevent him from making sure he was keeping track of my progress. His sharp comments and critical feedback helped me to get the best out of my work. A special word should also be said for Dr. Erik Kelder. I would not only like to thank him for accepting my invitation to join my thesis committee, but also for triggering my interest for electrochemistry during my bachelor thesis. Next, I would also like to thank Pr.dr.ir. A. Ramirez Ramirez for joining my thesis committee.

I could not have wished for a better daily supervisor than Anirudh Venugopal. Not only is he a great researcher, he always made time to discuss any issues I was facing. His involvement but also the room he gave me to make it my own project motivated me and shaped this project. He triggered my interest for the anodic peroxide evolution and motivated me throughout the project. The course of the project may not have been what we expected due to restricted time for lab-work, but thanks to him I look back proudly at the work I have delivered. I wish him all the best in the final years of his PhD as well as in all his other undertakings.

Next, I would like to thank everyone at the MECS group for their contribution to this project. The group meetings are always a good way of getting new insights from other fields. I would like to thank especially Herman and Joost for their humour and for their help with any technical issue in the lab. Also, I would like thank Giorgio and Diana for their help with sputtering-related issues. Same goes for Kailun who always took the time to answer my questions. Her interest in people and joyful mood made me feel welcome at the MECS group. I am also very grateful to Stephen Eustache for is valuable insights and help with NMR measurements.

I would like to express my gratitude to all my friends who were part of my journey in Delft. I would not be who I am now without them. They were there through the best and worst times, and I can not thank them enough for that. Last but not least, I would like to thank my family for their invaluable support. Even miles away, I know I can always fall back on them. Not only do they inspire me every day, they always know how to bring the little rays of sunshine in my life.

Marieke van Leeuwen
03-06-2020

CONTENTS

1

INTRODUCTION

Over the course of the twentieth century, the world population has increased from 1.65 to 6 billion [1]. In order to meet and improve living standards, the overall energy consumption has increased by a factor 9 over the same period of time [2]. Different sources are being exploited in order to face this substantial demand. Coal, natural gas and oil together represent already 65 % of the energy supply [3]. The sources are of limited availability which implies that their exploitation will become increasingly difficult and expensive. Moreover, with an outlook for future generations, a solution needs to be found in order not to deplete the Earth of its resources.

Other problems are paired to our current fossil-based energy supply system. Emissions of greenhouse gasses such as carbon dioxide and methane are induced by the combustion of these sources. Their accumulation over the past years due to anthropogenic activity has triggered climate change. Lately, international awareness has been rising regarding the emissions of the current infrastructure. This has led for example to the "Green Deal" proposed by the European Union in March 2020, which aims at making Europe the first continent with "*no net emissions of greenhouse gases in 2050 and where economic growth is decoupled from resource use*" [4]. The successful achievement of these energy transition goals heavily depends on technical developments in the renewable energy field. One of the main challenges of this transition is the important dependence of these sources on natural conditions. This dependence implies an intermittent availability and unpredictability of supply. Different solutions are being implemented to diminish these effects, including models and smart grids that allows efficient control and dispatch of energy depending on the offer and demand. However, most of these control mechanisms depend on efficient energy storage to provide energy during times of low production (*e.g.* night hours for solar energy production).

1.1. MOTIVATION

Batteries offer a broad range of solutions for storage of electrical energy into chemical energy [5]. The numerous options already available allow implementation on both small and large scales as well as for short and medium term storage. The broad offer allow flexibility in size, price, speed and discharge rate. Lead acid batteries for example have a relatively low energy density, but as the most mature battery technology can be implemented for a low price. These batteries are therefore usually implemented for solar energy storage, which requires competitive prices and does usually not have particular size constraints [6]. Lithium ion batteries on the other hand are often preferred for light-weight storage such as for mobile phones or for electric vehicles. However, batteries also present some drawbacks. They are among others characterized by a discharge rate, which makes them for example non-suitable for seasonal storage of renewable energy.

Electrolysis provides an alternative to batteries for electrical to chemical energy conversion. The generation of a fuel circumvents the discharge problems related to batteries, which in turn could allow for seasonal storage of energy. Other advantages include elemental abundance and possibilities for renewable energy transfer into other sectors including the heat, transport and chemical sector [7].

Several cathodic reactions have received particular attention for electrolytic application. Production of hydrogen from water reduction using sustainably generated electricity could allow to decarbonize our energy

system. This is a popular concept, often referred to as the *hydrogen economy*. Hydrogen can fairly easily be implemented in major sectors including transportation, heating, and chemicals [8–10]. Cathodic ammonia production is a second promising pathway for renewable energy storage into chemicals [11]. Ammonia is the second largest produced chemical world-wide, usually obtained via the Haber-Bosch process. Next to its main use as fertilizer, it has promising characteristics to be used as fuel for vehicles [12]. Another interesting reaction is the reduction of carbon dioxide to value-added products such as carbon monoxide and formic acid [13, 14]. This reaction not only allows the storage of energy through chemical bonds, but also allows the use of captured CO_2.

Even thought these concepts are extremely promising, they are still not competitive yet compared to industrial processes for the production of the above mentioned fuels. This is mainly due to high capital costs and to the lack of maturity of the technology [7, 15].

Most of these reduction reactions are coupled to the Oxygen Evolution Reaction (OER) [16] as shown in Figure 1.1 . The formation of oxygen indeed provides protons needed for the reaction at the other electrode. However, this reaction is a four electron process which implies that the development of appropriate catalysts

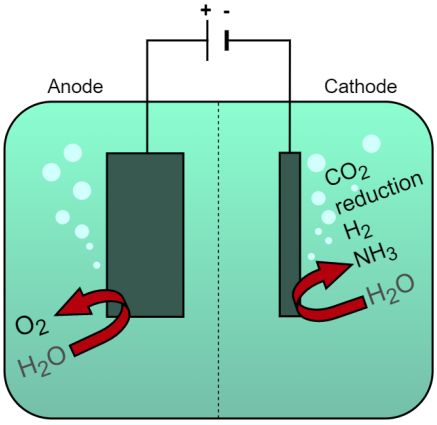

Figure 1.1: Overview of promising reduction reactions coupled to the OER

is a challenge [17]. The number of steps entails that a rather high practical overpotential is required for the formation of oxygen thus making the OER kinetically rather sluggish [18, 19]. Recently, attention has therefore been drawn to alternative anodic reactions that can be a proton donor - or hydroxyl sink - and at the same time produce a high value product [18, 20]. A promising alternative to the OER seems to be the hydrogen peroxide evolution reaction [21, 22].

1.2. CONCEPTS

1.2.1. THE HYDROGEN PEROXIDE PRODUCT

Hydrogen peroxide is a fundamental chemical with an annual demand growing by 4 % per year and expected to reach 5.2 million tons per year by the end of 2020 [23]. This green oxidizing agent is involved in various sectors. It is vastly used in the bleaching industry, notably for paper and textile production [24]. It is also commonly used for wastewater treatment as its decomposition products are simply water and oxygen. This makes it a promising alternative to chlorine-based oxidizing agents. The demand for hydrogen peroxide in the chemical sector is also consequent and has been growing in the past years. This is in particular due to the increasing demand for polyurethane plastics, made from polypropylene oxide whose synthesis requires H_2O_2.

The anthraquinone route accounts for 95 % of the hydrogen peroxide production [25]. This process is predominantly implemented because it is a reliable one, operated at rather mild conditions. The main steps of this process are subsequent hydrogenation and oxidation of an alkylanthraquinone precursor, followed by liquid-liquid extraction of the product [26]. However, this process has some important drawbacks. Some organic contaminations in the water phase tend to occur during the extraction. The presence of unwanted components in the product stream is tackled by the implementation of an extra energy intensive separation

step: distillation. The hydrogen peroxide obtained from this process is in concentrated form, which poses major safety concerns regarding storage and transport. The usual approach to circumvent this problem is dilution to lower concentrations. Most applications indeed only require concentrations below the safety limit. The transport of diluted solutions from a centralized production facility highlights some major flaws in the current hydrogen peroxide production. This can be improved by finding solutions for decentralized production with a product at low concentration.

Different alternatives have been investigated to mitigate the losses linked to the previously mentioned problems. Examples are the direct synthesis from hydrogen and oxygen [23], promising due to its atom efficiency, or obtaining H_2O_2 and CO_2 via CO/ O_2/ H_2O mixtures [26]. This reaction is thermodynamically favorable, however, low turnover values and rapid deactivation characterize this process. Electochemical solutions seem a third promising alternative to these processes.

1.2.2. ELECTROCHEMICAL SYNTHESIS OF HYDROGEN PEROXIDE

Electrochemical devices are suited for local production at mild operating conditions and are fit for both large and fairly small scale applications [26]. This makes it a promising alternative for decentralized hydrogen peroxide production. Furthermore, combining this system with renewable energy sources would allow to considerably decrease the environmental impact compared to the current production processes.

Both cathodic and anodic hydrogen peroxide production in water have been reported. Research for the Oxygen Reduction Reaction (ORR) is significantly more mature than for Water Oxidation Reaction (WOR) of the product [25]. In 2019, the danish startup HPNow received the SDG TEch Best Startup award for their water electrolyzers to H_2O_2 via ORR, which clearly exemplifies the interest in the field [27]. The best catalysts found so far include noble metal alloys and carbon based materials which respectively present drawbacks regarding costs and degradation [28].

Anodic evolution presents the major advantage that it can be combined to another valuable reaction, for example hydrogen production.

1.2.3. WATER OXIDATION REACTION TO HYDROGEN PEROXIDE

Water oxidation towards hydrogen peroxide was long considered as a negative effect to be suppressed. In the past years however the trend has been shifting as H_2O_2 was proposed as alternative product to oxygen [21]. Most promising results involved Boron-Doped Diamond electrodes (BDD) and a variety of metal oxide anodes [29–32]. The composition of the electrolyte was observed to be central as well. The presence of bicarbonate enabled to reach enhanced peroxide production [33]. Bicarbonate is thought to be involved together with its oxidized form, the peroxymonocarbonate ion. These ions allow to stabilize the peroxide bond, which tends to decompose rapidly in oxidative conditions.

A broad range of materials has been explored for the anodic evolution of hydrogen peroxide. However, a lack of understanding is still visible regarding the actual mechanisms driving enhanced peroxide formation in carbonate and bicarbonate rich electrolytes. Moreover, the research established has focused on selectivity of materials towards hydrogen peroxide rather than materials appropriate for industrial applications.

1.3. RESEARCH QUESTIONS

In this study, the potential of anodic hydrogen peroxide industrial production will be explored. The aim is to assess the added-value of the process thanks to the coupled reaction. To do so, experimental work will delve into design parameters for the operation of a cell at high current density. If this can be achieved, stability of electrode materials should be preserved and the triggering of competitive reactions should be avoided. An optimal cell would operate at high current densities but preserve a high faradaic efficiency. Operation will be performed in a bicarbonate and carbonate environment. The effect of the electrolyte on peroxide formation and stability will be observed.

This leads us to formulating the following research question:

What is the potential for anodic evolution of H_2O_2 at industrial conditions and which forms does the product take?

Several sub-questions were defined to answer the main research question and will be tackled throughout the study:

- What are the performance targets to make the hydrogen peroxide evolution profitable? What are the opportunities for the product combined to hydrogen production, as well as oxygen and carbon dioxide reduction?
- Which materials are the most suitable? What are the effects of different deposition techniques?
- What mechanisms govern the process at low and high current densities? What methods are most appropriate for peroxide detection?

1.4. THESIS OUTLINE

This report consists of 8 chapters including this one. In Chapter 2, some theoretical background and an overview of literature are provided on the topic. Chapter 3 presents a model for the techno-economic evaluation of processes involving the OER and the two-electron WOR coupled to different cathodic reactions. Materials and methods used for experimental work are explored in Chapter 4. The results obtained from Chapter 3 and Chapter 4 are presented in Chapter 5. A discussion on these results in view of the research questions an literature is provided in Chapter 6. Finally, a conclusion and recommendations are provided in Chapter 7.

2

THEORETICAL BACKGROUND

This chapter provides a review of the current knowledge in the field. It aims at providing some background to the research questions and guide the reader in his understanding of the report. Firstly, some characteristics and recent findings on the Water Oxidation Reaction (WOR) towards hydrogen peroxides are explored. Secondly, an overview of promising electrode materials is provided. Finally, reaction mechanisms thought to be involved are delved into.

2.1. WATER OXIDATION REACTION TO HYDROGEN PEROXIDE

The market potential for the anodic hydrogen peroxide evolution reaction is two-fold. First of all, there is a demand for a decentralized, straightforward alternative to the current anthraquinone process [26]. Moreover, the possible combination with a cathodic reaction such as CO_2 reduction, ammonia or hydrogen production makes it a value-added chemical. There are however several hurdles before achievement of a viable anodic hydrogen peroxide process. Water oxidation can lead to several products including hydrogen peroxide. This section first explores competitive oxidation reactions before diving into preferred cell design parameters for enhanced industrial hydrogen peroxide evolution.

2.1.1. AN OVERVIEW OF WATER OXIDATION REACTIONS

Oxidation of water in an electrochemical device can lead to different reactions. The main competitive reactions are the one-, two-, and four-electron pathways shown in Equation (2.1)-(2.3). These respectively lead to the production of hydroxyl radicals, hydrogen peroxide and oxygen [18].

$$H_2O \longrightarrow OH\cdot + H^+ + e^- \qquad E^o = 2.38\,V \textit{ vs } NHE \tag{2.1}$$

$$2\,H_2O \longrightarrow H_2O_2 + 2\,H^+ + 2\,e^- \qquad E^o = 1.76\,V \textit{ vs } NHE \tag{2.2}$$

$$2\,H_2O \longrightarrow O_2 + 4\,H^+ + 4\,e^- \qquad E^o = 1.23\,V \textit{ vs } NHE \tag{2.3}$$

Other deleterious mechanisms oppose the formation of the peroxide product. The latter can indeed undergo oxidation at rather low potentials (Equation (2.4)), but also disproportionate spontaneously (Equation (2.5)) or be subject to homolysis (Equation (2.6)) [25].

$$H_2O_2 \longrightarrow O_2 + 2\,H^+ + 2\,e^- \qquad E^o = 0.68\,V \textit{ vs } NHE \tag{2.4}$$

$$H_2O_2 \longrightarrow H_2O + \frac{1}{2}\,O_2 \tag{2.5}$$

$$H_2O_2 \longrightarrow 2\,OH\cdot \tag{2.6}$$

The oxidation process towards H_2O_2 is a challenging one as reactants, intermediates and products can be subject to redox reactions. However, even though the OER is thermodynamically favourable, it has sluggish kinetics and is hard to catalyse due to the numerous electron transfer steps.

The possible reactions at the electrodes are highly influenced by surface interactions. For the hydrogen peroxide production, it has been observed that interactions between oxygen and the electrode surface play

a crucial role [25]. This can be influenced for example by pH of the electrolyte [18, 34] or crystal orientation of the electrode [35]. Different materials have been explored, which successfully trigger the WOR towards hydrogen peroxide. Moreover, cell design has been shown to have a great influence on production but also degradation of hydrogen peroxide evolution [25, 36].

2.1.2. IMPROVED CELL PARAMETERS FOR H_2O_2 EVOLUTION

Experimental results have shown that H_2O_2 evolution is achievable. Several strategies have been proven to increase peroxide yield, either by tuning of the selectivity, production enhancement or inhibition of product decomposition. Cell design is thought to have a major impact on results obtained. This subsection explores operating condition strategies found so far to improve hydrogen peroxide yield.

ELECTRO-CHEMICAL *vs* PHOTOELECTRO-CHEMICAL DEVICES

Electrolysis can be operated in two types of devices: electro-chemical and photoelectro-chemical cells. These are respectively operated in the dark and under solar irradiation. These both present advantages and disadvantages for electrolysis. A comparative overview is provided in Table 2.1 [33]. Photo-chemistry long aroused interest due to efficiency prospects. Direct conversion from solar to chemical energy would indeed allow circumventing intermediate conversion to electricity hence reducing losses. However, the trend has been shifting back lately as PEC devices are less suited for industrial applications. Intermittence of supply and device sizes are major drawbacks in order to meet on-site hydrogen peroxide demand. Moreover, hydrogen peroxide is a rather unstable component and UV light seems to enable deleterious homolysis of the product [25]. This study being established in the context of industrial application, it will focus on application of the two-electron WOR in the dark.

Table 2.1: Advantages and disadvantages of (photo)electrochemical devices [33]

	EC production of H_2O_2 in the dark	PEC production of H_2O_2 under illumination
Advantages	• Only energy source is electricity • Compact system • Constant utilization possible	• Direct use of solar light • Low applied bias required (> 0.4 V)
Disadvantages	• High applied bias needed (> 2.5 V)	• Two energy sources used • Dependence on weather intermittence • Large surface area required hence cumbersome devices

CELL COMPONENTS

Several cell design strategies have been proven to enhance production of peroxide. First of all, compartmentalization of the electrolysis cell has yielded improved results at high current densities [36]. This is due to the decomposition of hydrogen peroxide at the cathode. Moreover, addition of a stabilizing agent like sodium silicate has been observed to be helpful [37]. The optimal stabilizer concentration was found to be 2 g/L during electrolysis and 4 g/L during storage.

Of course, main components' characteristics such as electrode structure or electrolyte concentration and pH will play a major role. Their influence will be explored in the subsequent sections.

2.2. ELECTRODE MATERIALS

One of the main limitations of the electrolytic hydrogen peroxide production is the inverse relationship between hydrogen peroxide selectivity and current density. Different approaches have been used in order to

find the most adequate materials. In a first part, main findings from computational studies are presented. Experimental results for two promising types of electrodes are explored afterwards.

2.2.1. COMPUTATIONAL STUDIES

Several computational studies based on Density Functional Theory (DFT) calculations have allowed to identify optimal catalysts. DFT calculations allow to investigate electronic structures via quantum mechanical models. They are based on free energies of intermediates that are thought to play an important role in the reactions considered. The key intermediates for the competing reactions explored in Section 2.1 are OH*, O* and OOH*. According to the Sabatier principle for heterogeneous catalysis, the binding between each intermediate should be neither too weak nor too strong. This implies that the binding of the intermediate should be strong enough to bind to the surface of the catalyst but also weak enough to let go. The challenge for multi-electron processes is to find a catalyst suitable according to the Sabatier principle for each of the steps. The WOR towards H_2O_2 is promising compared to the OER as half the amount of electrons is involved.

The Sabatier principle is usually illustrated by the use of a volcano plot. In the latter, the limiting potential for the reaction to occur is plotted against the free energy of the intermediate considered. This results in a characteristic triangular shape hence the name. Materials closest to the extremum are considered the best catalysts. Figure 2.1 presents the results obtained by Shi et al. (2017) for $BiVO_4$, SnO_2, TiO_2 and WO_3 by considering the OH* intermediates [18]. If the bond with the intermediate is too strong, the intermediate will get oxidized further and the oxygen evolution will be favoured (blue region of the graph). On the other hand, if the bond is too weak, bulk water molecules will not get dissociated and the hydroxyl formation will occur (red region). The dashed line in Figure 2.1 represents the equilibrium potential for the oxygen and hydrogen evolution reaction. The practical overpotential, which is the minimum overpotential required to trigger the reaction is defined as the difference between limiting and equilibrium potentials. Note that a rather high theoretical overpotential is needed for the OER due to scaling relations for the four electron steps, in contrary to the two electron reaction.

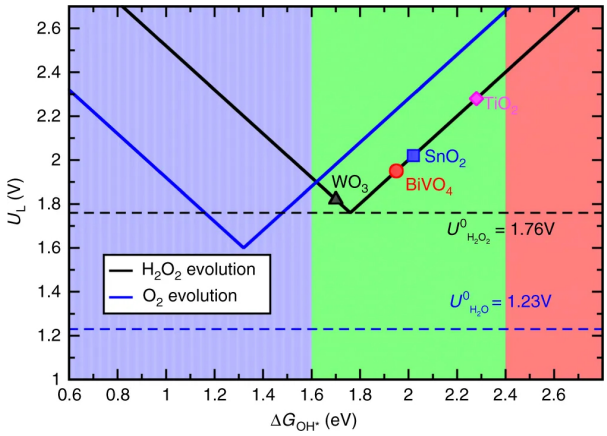

Figure 2.1: Activity volcano plots. It is based on calculated limiting potentials as a function of calculated adsorption energies of OH* (ΔGOH^*) for the two-electron oxidation of water to hydrogen peroxide evolution (black) and the four-electron oxidation to oxygen evolution (blue). The corresponding equilibrium potentials for each reaction have been shown in dashed lines. [18]

It should be noticed that free energies of intermediates scale with each other. Having a good binding energy for the OH* intermediate does not mean that the binding energy of the other intermediates is adequate. Several other drawbacks can be attributed to DFT results. First of all, kinetic barriers are not taken into account while they are of importance. Moreover, the materials considered are monocrystalline. However, for large scale application, synthesis of these type of materials is not realistic. DFT calculations are therefore a method to provide a background for experimental validation.

2.2.2. PARAMETERS FOR PERFORMANCE EVALUATION

Computational models are to be validated via experimental methods. To investigate electrochemical behavior, different tests can be performed. These tests often consists of maintaining one variable constant and observing how the others evolve. Different types of variables may influence the system, namely [38]:

- External variables: *e.g.* temperature, pressure, time

- Electrical variables: *e.g.* potential, current, amount of charge passed
- Electrode variables: *e.g.* material, surface area, geometry
- Mass transfer: *e.g.* diffusion, convection, surface concentrations, adsorption
- Solution variables: *e.g.* bulk concentration of electro-active species, electrolyte, pH, solvent.

In order to compare electrode performances, different parameters are usually defined. This section provides an overview of conventionally used expressions, their definition and interpretation.

FARADAIC EFFICIENCY

As was described by Michael Faraday, a direct proportionality exists between faradaic current and electrolysis rate [39]. The charge Q (Coulombs) passed during electrolysis is described is Equation (2.7). It amounts to the product of the theoretical amount of mol electrolyzed N, z the stoichiometric number of electrons involved in the electrode reaction and the Faraday constant F (Equation (3.11)).

$$Q = \int i\,dt \tag{2.7}$$

$$Q = zNF \tag{2.8}$$

The Faradaic Efficiency (FE) is defined in Equation (2.9) as the amount of moles product generated during experiments divided by the theoretical amount moles produced.

$$\text{FE (\%)} = \left[\frac{n_{H_2O_2}\ \text{experimental (mol)}}{n_{H_2O_2}\ \text{theoretical (mol)}}\right] * 100 = \frac{zNF}{Q} * 100 \tag{2.9}$$

This quantity allows to identify the fraction of the charge passed which actually goes to the desired reaction and therefore provides insights on the selectivity of the reaction.

CURRENT DENSITY

Electrode reactions are more complex than reactions in gas and solution phases as the reaction only occurs locally at the surface and is therefore heterogeneous. This implies that next to the kinetic variables, different surface effects need to be considered [38]. For this reason, parameters are often expressed per unit area.

Current corresponds to the amount of charge per unit of time passed through the system. The current density is defined as the current per unit area. The current density response of a system is of importance as it indicates the feasibility for upscaling a device. Systems with very low current densities will require tremendously large facilities to allow significant production. An acceptable order of magnitude for current density should be in the order of $100\,\text{mA/cm}^2$ in order to be relevant for large scale applications [25]. It has been observed experimentally that high current densities usually result in lower selectivities towards hydrogen peroxide reactions [36], which might be a major bottleneck for industrialization of the process.

OVERPOTENTIAL

The additional potential to the standard potential thermodynamically required to drive the reaction is referred to as the overpotential [38]. This overpotential reflects additional energy requirements from the system to allow electrolysis. A small overpotential is therefore desirable for the design of an efficient system. However, at higher current densities the overpotential tends to increase as described in the *Tafel* equation. This not only results in unwanted losses but may also result in overheating of the system. Overpotentials may be induced by losses at the membrane or by bubble formation for example.

STABILITY

The stability of a catalyst is of major importance for the electrolytic process. It provides an indication on the material's degradation and deactivation over time. This is particularly relevant for anodic applications as many catalysts are not stable in a large pH window at oxidative conditions. The stability of a catalyst is largely influenced by the operating conditions chosen and impurities in the system which makes comparison between different electrochemical set-ups challenging. A good stability is of importance to reduce both capital and operating costs of a process when implemented on industrial scale [40].

2.2.3. PROMISING MATERIALS FOR PEROXIDE EVOLUTION

Different types of materials have been tested so far, yielding interesting prospects for the production of peroxide via the WOR. These include metal oxides and carbon materials, as visible in the overview provided in Table 2.2.

Metal oxides have received a significant amount of attention in the field of energy storage. This is mainly due to their stability, abundance and flexibility in design. Iron and manganese metals for example, are abundant and therefore rather cheap [41]. Metal oxides offer numerous possibilities in terms of choice in metallic atoms but also in terms of structures. The surface of metal oxides (*i.e.* morphology, size, grain orientation) can be rather easily tuned which gives room for flexibility in electrode design. This flexibility in turn results in a great tunability of applications within the energy storage sector. Metal oxides have indeed been investigated for solar cells, photo-catalytic WOR and reduction reactions, electro-catalytic fuel production, battery applications and super-capacitors [42]. However, several drawbacks also characterize these materials. Their usually large band gap results in poor electrical conductivity.

Among the metal oxides tested so far, some stand out by their performance (Table 2.2). These include $BiVO_4$, $CaSnO_3$ and ZnO, for which faradaic efficiencies above 70 % were achieved [18, 30, 43]. However, the latter materials present some drawbacks regarding stability window in different environments (*e.g.* pH) and toxicity. Moreover, best performances have overall been obtained on mono-crystalline facets, which is not realistic for large scale application.

Next to metal oxides, carbon-based materials have shown impressive performances especially regarding current densities. None of the metal oxide-based anodes explored so far has surpassed the 100 mA/cm^2 mark, which makes them far from mature for industrial implementation. Boron-Doped Diamond (BDD) electrodes have been operated at rather high voltages thus enabling high current densities to be achieved. This allowed a production of 19.7 µmol/cm^2/min hydrogen peroxide [44], which is the second highest anodic production reported so far. Though promising, BDD electrodes still have a fairly low faradaic efficiency.

A recent publication by Xia et al. (2020) showed a breakthrough using a Carbon Fiber Paper electrode coated with Teflon. This allowed to reach a production of 23.4 µmol/cm^2/min at a fairly low overpotential and with a faradaic efficiency of 66 % (see Table 2.2). These results clearly surpass findings in the field so far. Figure 2.2 puts the results obtained in perspective with commonly researched materials and illustrate their superior performances.

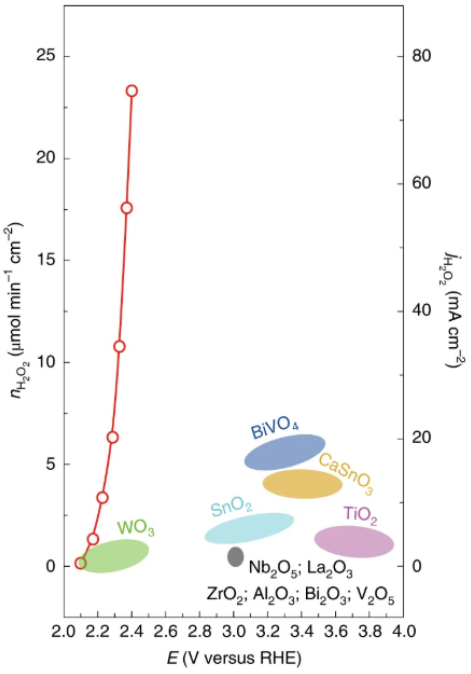

Figure 2.2: Production and current performances for typically reported two-electron water oxidation catalyst and CFP loaded with PTFE (red line) against potential [45]

A striking observation from Table 2.2 is the difference in electrolytes used, namely bicarbonate and carbonate for metal oxides and carbon-based electrodes respectively.

Table 2.2: Electrode materials reported in literature for the two-electron water oxidation. When multiple compositions of doped or mixed metal oxides were studied, the best recorded data is reported. [(a)] Value calculated from chronoamperometry data [(b)] pH was not explicitly recorded but was approximated based on the electrolyte using the online Aqion pH calculator [46] [(c)] Derived from Faradaic efficiency plots [(d)] Derived from CV plots [(e)] Derived from the charge passed through the system

Material	Substrate	E (V *vs* RHE)	j (mA/cm^2)	H_2O_2 production µmol/cm^{2}min	Electrolyte	pH	FE (%)	Ref
Metal oxides								
FTO	Glass	3	0.10[(a)]	0.0045[(a)]	0.5 M $KHCO_3$	8[(b)]	14[(a)]	[33]
La_2O_3	FTO	3	0.053[(a)]	0.014[(a)]		8[(b)]	9[(a)]	
Nb_2O_5	FTO	3	0.091[(a)]	0.0028[(a)]		8[(b)]	10[(a)]	
ZrO_2	FTO	3	0.071[(a)]	0.0026[(a)]		8[(b)]	12[(a)]	
V_2O_5	FTO	3	0.11[(a)]	0.46[(a)]		8[(b)]	13[(a)]	
Al_2O_3	FTO	3	0.081[(a)]	0.0043[(a)]		8[(b)]	17[(a)]	
$BiVO_4$	FTO	3	0.25[(a)]	0.021[(a)]		8[(b)]	26[(a)]	
TiO_2	FTO	3	0.099[(a)]	0.0083[(a)]		8[(b)]	27[(a)]	
TiO_2	FTO	3.3	14[(c)]	0.8	1 M $NaHCO_3$	8.3	18	[18]
WO_3	FTO	2.3	3.5[(d)]	0.5		8.3	46	
SnO_2	FTO	3.1	9.5[(c)]	1.5		8.3	51	
$BiVO_4$	FTO	3.1	27[(c)]	5.8		8.3	70	
ZnO	FTO	2.55	9	n.a.	2 M $KHCO_3$	7.84[(b)]	81	[30]
$CaSnO_3$	FTO	3.2	34	4.5	2 M $KHCO_3$	7.84[(b)]	76	[43]
Mixed metal oxides								
Gd-doped $BiVO_4$	FTO	3.1	50	2.6	2 M $KHCO_3$	7.84[(b)]	78	[47]
FTO	Glass	*n.a.*	0.33	1.24[(c)]	0.5 M $KHCO_3$	8[(b)]	12	[32]
$BiVO_4$	FTO	2.8[(d)]	0.33	2.59[(c)]		8[(b)]	25	
Al_2O_3	FTO	*n.a.*	0.33	2.28[(c)]		8[(b)]	22	
Al_2O_3/$BiVO_4$	FTO	2.9[(d)]	0.33	3.94[(c)]		8[(b)]	38	
Carbon-based materials								
BDD	Si-wafer	*n.a.*	65	2.17[(e)]	0.5 M Na_2CO_3	11.39[(b)]	8.06	[36]
BDD	Si-wafer	7.8	31.2	1.67	2 M Na_2CO_3	11.43[(b)]	25	[29]
BDD	Ti	3.47	295	19.7	2 M $KHCO_3$	7.84[(b)]	28	[48]
CFP	–	2.25	230[(d)]	7.87	1 M Na_2CO_3	11.96	11	[45]
CFP PTFE-loaded	–	2.4	125[(d)]	23.4		11.96	66	

2.2.4. ELECTRODE DESIGN STRATEGIES

As mentioned before, metal oxides present a great flexibility in design, which allows tuning the surface properties of the electro-catalyst. Different strategies have been explored in order to increase performance of water electrolysis on metal oxides.

DOPING

Doping of the materials allows to alter both the chemical and physical properties of the materials. This is mainly obtained by changes in lattice structures and defects and electronic structures [49]. Gd-doping of bismuth vanadate for example (Table 2.2) has enabled improving both faradaic efficiency and current densities reached [47].

MIXED METAL OXIDES

Combination of different metal oxides has also revealed some positive effects. For example, joined application of Al_2O_3 and $BiVO_4$ on FTO resulted in an increase in both faradaic efficiency and current density of more than 50 % of the initial values for the separate metal oxides (Table 2.2) [32]. Similar results have been obtained for WO_3/$BiVO_4$ systems [50]. The effect of these combination is thought to be double by simultaneous enhancement of water oxidation and inhibition of peroxide degradation.

SURFACE DESIGN

Different structures can be obtained from metal oxides. The effect of different surfaces on electro-catalysis, often paired with different preferred orientations, has been explored by different research groups [30, 35]. $BiVO_4$ for example was synthesized as seeds, nano-needles and truncated pyramids on FTO as visible from Figure 2.3 [35]. Each of these materials exhibited different preferred orientations, with the seeds preferring higher index planes compared to the other two structures. Though nano-needles presented least charge transfer resistance, its selectivity towards hydrogen peroxide was not favorable. Best performances, in both selectivity and stability, were obtained for the high index plane seed-like structure. Structural analysis can contribute to improved electrode performance both in selectivity and stability of both the product and the electrode.

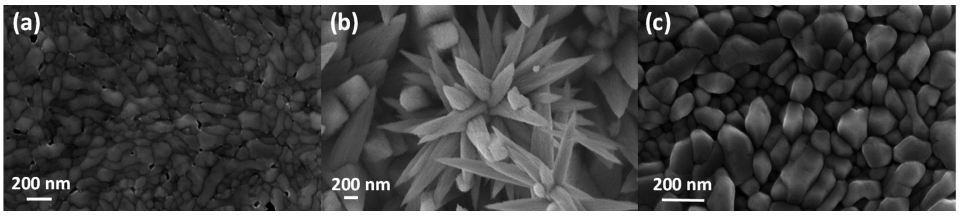

Figure 2.3: TEM images showing different structures for $BiVO_4$ with (a) the formation of seeds (b) the formation of nano-needles and (c) the formation of truncated pyramids [35].

2.3. REACTION PATHWAYS TOWARDS PEROXIDE: THE ROLE OF ELECTROLYTE

The choice in electrolyte for two-electron WOR has been demonstrated to be crucial. For cells operated with metal oxide anodes, bicarbonate was commonly employed as electrolyte (Table 2.2). A study by Fuku et al. (2016) explored different electrolytes and clearly showed the superiority of bicarbonate for their system (Figure 2.4).

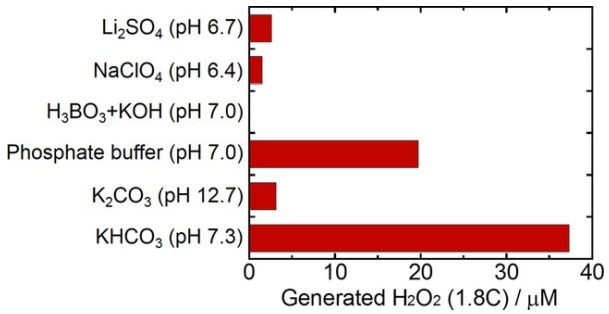

Figure 2.4: Oxidative hydrogen peroxide generation on an FTO substrate at an applied charge of 1.8 C at 3V̇ in various 0.5 M aqueous solutions [33].

On the other hand, carbon-based electrodes were predominantly operated in carbonate-rich environments. Both these electrolytes are thought to be involved in the electrolysis process itself rather than being simple ion carriers. Products such as the peroxymonocarbonate ion (HCO_4^-), and the peroxydicarbonate ion ($C_2O_6^{2-}$) ion are thought to be involved. Most publications so far have used titration for the identification of their peroxide product. However, this method quantifies the peroxide bonds rather than identifying the separate products present [36]. This section delves into the current knowledge on these mechanisms and aims at providing an overview of reaction pathways hypothesized so far. First, mechanisms for direct hydrogen peroxide evolution are presented. Then, potential mechanisms involving bicarbonate for the peroxide formation are explored. Thirdly, an overview of carbonate involving mechanisms is provided. Finally, the peroxycarbonate ion is discussed.

2.3.1. DIRECT PATHWAYS TOWARDS HYDROGEN PEROXIDE

Three different pathways support the hypotheses for a direct water oxidation to hydrogen peroxide. An overview of these pathways is sketched in Figure 2.5. In these three pathways, the OH* intermediate is key,

which corroborates the DFT calculations performed by Shi et al. (2017) [18]. The upper circle in Figure 2.5 shows the attacks by either water or hydroxide at a surface site M. This leads to the adsorbed OH* intermediate which can undergo three different reactions. The coupling of to M-OH sites can directly lead to the formation of hydrogen peroxide. The M-OH intermediate can also be attacked further from the bulk, freeing the occupation site and simultaneously liberating hydrogen peroxide [31]. The lower circle of the sketch shows a third pathway to peroxide starting from the M-OH intermediate [34]. Here, the steps are similar to those for the Oxygen Evolution Reaction (OER). However, this intermediate gets protonated rather than deprotonated thus leading to the desired product. The detailed mechanisms for these reactions are explored in the subsequent sections.

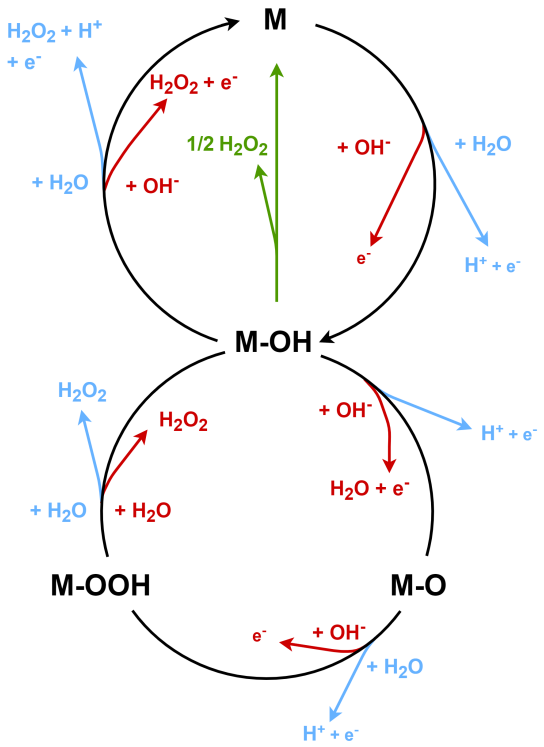

Figure 2.5: Two-electron water oxidation pathways in both basic (red) and acidic (blue) media involving the OH* intermediate.

WATER OXIDATION STARTING FROM AN UNOCCUPIED SITE

For both pathways in the upper half of Figure 2.5, the attack of an empty site starts by the adsorption of the OH* intermediate (Figure 2.6). This steps is referred to as a *Volmer* step [51]. Two different mechanisms can be then be used to describe the attack of the occupied site. Either the *Volmer* step is repeated twice, after which either two OH* intermediates combine, or the OH* intermediate gets attacked from the bulk. These are respectively referred to as *Tafel* and *Heyrovski* steps.

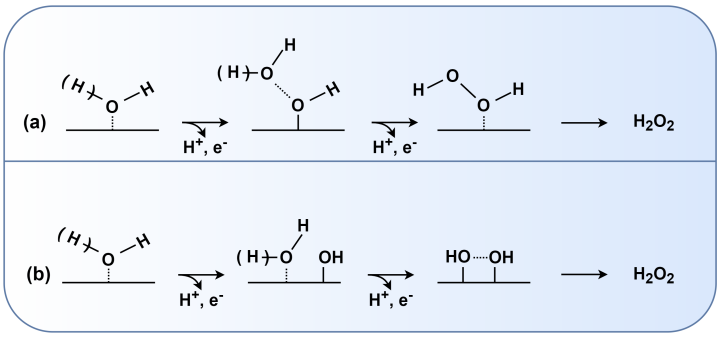

Figure 2.6: Two-electron water oxidation reaction via (a) *Volmer-Heyrovski* and (b) *Volmer-Tafel* pathways in an acidic environment.

DFT calculations based on the OH* intermediate support these mechanisms as they are based on its free energy ΔG_{OH*} [18]. Viswanathan et al. (2015) identified the activation of water as OH* as the limiting step for the two-electron oxidation reaction towards H_2O_2 [31]. Materials with strong OH adsorption energy will tend to the four-electron reaction as OH^* will get oxidized to O^* and OOH^*. Electro-catalysts with weak OH^* free energy will promote the two-electron reaction as long as the adsorption is strong enough to dissociate water.

The importance of the OH intermediate was explored further by Xia et al. (2020). In their study, the binding energy of the OH* intermediate was tuned by local production of oxygen [45]. The confined local O_2 was obtained by creation of an aerophilic surface. A concentration gradient was obtained at the surface thanks to a hydrophobic PTFE layer deposited onto the electro-catalyst. The presence of this layer allowed to create a three-phase boundary at the surface of the catalyst. By applying this onto a Carbon Fiber Paper electrode, they achieved the highest hydrogen peroxide production reported so far. The faradaic efficiency was increased six-fold compared to a pristine CFP electrode. These results were obtained at a fairly low overpotential, as visible on Figure 2.2. Moreover, selectivity towards hydrogen peroxide on a nickel-foam electrode was even obtained. The latter electrode being an OER catalyst clearly demonstrated the potential for PTFE coating.

WATER OXIDATION STARTING FROM THE M-OH INTERMEDIATE

The four-electron water oxidation to oxygen can go subsequently through the following intermediates, with M being a site at the surface: M, M-OH, M-O, M-OOH, M [52]. The M-OOH intermediate may play an important role regarding selectivity towards oxygen or hydrogen peroxide [34] as it can either get deprotonated or protonated. The main hypothesis proposed by Zhu et al. (2019) is that the evolution reaction is influenced by the ease of protonation of OOH intermediates as exemplified in Figure 2.7. Considering an M-OOH system with M the active center for catalytic water splitting, one can predict that deprotonation will favor O_2 formation whereas protonation will lead to H_2O_2 formation. This line of thought was supported by the observed pH dependence of the selectivity towards the different reactions.

Kinetic isotope effects were observed by comparing D_2O_2 and H_2O_2 evolutions [34]. In a D_2O electrolyte, deprotonation is more difficult and protonation easier leading to a higher yield of D_2O_2 in D_2O than of H_2O_2 in H_2O. $-$OOD is more readily protonated than $-$OOH as $pKa_{H_2O_2}$ is lower than $pKa_{D_2O_2}$. The influence of proton transfer in the rate determining step of WOR was highlighted by this study.

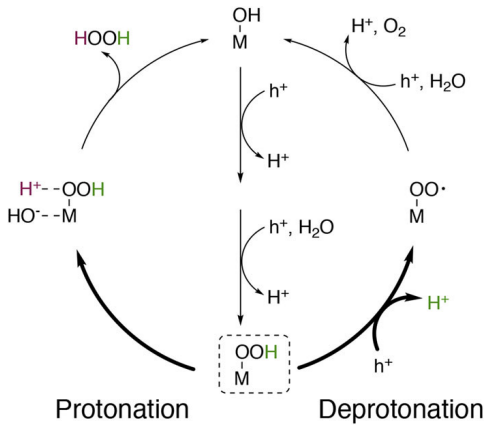

Figure 2.7: Simplified schematic representations of possible water oxidation mechanisms. Right branch: conventional oxygen evolution mechanism with the deprotonation of the —OOH intermediate. Left branch: water oxidation mechanism with the protonation of the —OOH intermediate for two-electron water oxidation reaction [34].

2.3.2. BICARBONATE INVOLVING PATHWAYS

The use of bicarbonate as electrolyte was reported to aid the peroxide evolution on metal oxides as visible in Table 2.2. Both sodium and potassium bicarbonate were reported in literature with slightly superior performances in potassium bicarbonate. Variations in the electrolyte concentration showed improved results for the peroxide evolution as exemplified in Figure 2.8 [32]. Mechanisms behind this have not been clarified yet. Different hypotheses have been advanced which stipulate that the presence of bicarbonate might both enhance the formation and inhibit the degradation of the peroxide product.

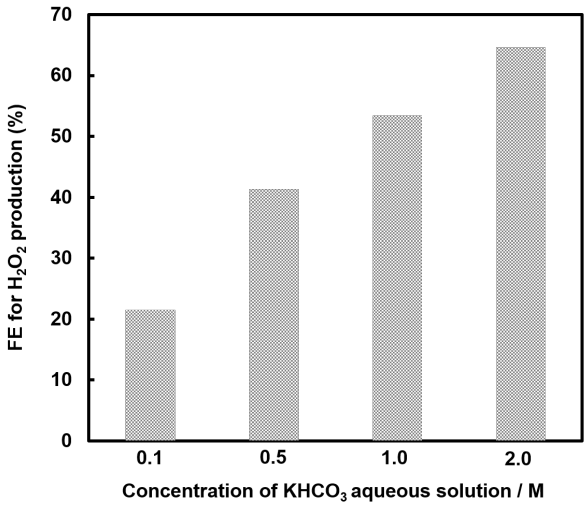

Figure 2.8: FE for H_2O_2 production on $Al_2O_3/BiVO_4$/FTO in a two-electrode set-up with variable $KHCO_3$ concentrations under CO_2 bubbling and stable anodic current of 2 mA [32].

Bicarbonate may be the component getting oxidized towards species encapsulating the peroxide bond. Combined spectroscopy and titration analyses have shown that bicarbonate-derived products containing peroxide bonds cannot be distinguished from H_2O_2 components from titration [36]. However, titration is being used in a majority of the research in the field for hydrogen peroxide quantification [18]. It might therefore very well be that reported hydrogen peroxide produced was in fact peroxymonocarbonate, peroxycarbonate or peroxydicarbonate. This section will explore the different pathways thought to be potentially involved in the peroxide formation via the WOR as well as the inhibition of its degradation. The mechanisms for first peroxymonocarbonate, then peroxydicarbonate and finally peroxycarbonate are explored.

PEROXYMONOCARBONATE FORMATION

Peroxymonocarbonate is formed on metal oxides by oxidation of bicarbonate at a standard potential of 1.8 V vs RHE [22]. The oxidation of bicarbonate to peroxymonocarbonate would be followed by the hydrolysis towards hydrogen peroxide in the bulk, as sketched on the left side of Figure 2.9. This reaction would allow to inhibit the deleterious oxidation of hydrogen peroxide towards oxygen, which occurs already at 0.68 V vs RHE.

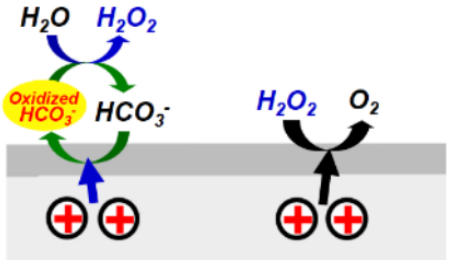

Figure 2.9: Sketch of the peroxide formation via a bicarbonate intermediate (left side) were HCO_3^- oxidizes to HCO_4^- followed by hydrolysis in the bulk, and of the unwanted hydrogen peroxide oxidation [33].

The oxidation reaction is presented in Equation (2.10):

$$HCO_3^- + H_2O \rightleftharpoons HCO_4^- + 2\,H^+ + 2\,e^- \qquad E^o(HCO_3^-/HCO_4^-) = 1.8\,V\ vs\ RHE \tag{2.10}$$

This reaction happens at the surface of the catalyst and may be followed by hydrolysis in the bulk (Equation (2.11)). Hydrolysis of peroxymonocarbonate has been demonstrated via ^{13}C NMR experiments [53]. From these experiments, rate constants in water at pH 7.4 were derived as $K = 0.32 \pm 0.02\,M^{-1}$, $k_f = 1.2 * 10^{-3}\,M^{-1}s^{-1}$ and $k_b = 3.8 * 10^{-4}\,M^{-1}s^{-1}$.

$$HCO_4^- + H_2O \underset{k_b}{\overset{k_f}{\rightleftharpoons}} HCO_3^- + H_2O_2 \tag{2.11}$$

The presence of peroxymonocarbonate ions after water oxidation in bicarbonate electrolytes has been confirmed before [50]. The high occupation of catalyst surface O-bonds due to bicarbonate bonding might explain the reduced hydrogen peroxide decomposition in bicarbonate-rich electrolytes. Due to the occupation of the sites, there are no spots left to bond with the hydrogen peroxide and allow its cleavage [35].

The surface reactions towards HCO_4^- can occur along to different pathways. First, an OH* intermediate can be formed at the surface, liberating an electron (Equation (2.12)). DFT calculations based on ΔG_{OH*} support this hypothesis [18]. The adsorbed intermediate may then be attacked from the bulk by bicarbonate and hydroxide thus releasing a water molecule and electron (Equation (2.13)). Figure 2.10a presents a sketch for this pathway. The reaction are then as follows, with M a site at the surface of the catalyst:

$$M + OH^- \longrightarrow MOH + e^- \tag{2.12}$$

$$HCO_3^- + MOH + OH^- \longrightarrow HCO_4^- + H_2O + e^- + M \tag{2.13}$$

Bicarbonate may also be adsorbed at the catalyst surface via one oxygen atom, liberating one electron via a *Volmer* step (Equation (2.14)) [35]. The adsorbed species may then interact with an adsorbed OH* (Equation (2.12)) via a *Tafel* mechanism to release peroxymonocarbonate (Equation (2.15)). Figure 2.10b illustrates this pathway. Hydroxide - or water depending on the pH - may also attack from the bulk via a *Heyrovski* step (Equation (2.16)), yielding the HCO_4^- ion as shown Figure 2.10c.

$$M + HCO_3^- \longrightarrow MHCO_3 + e^- \tag{2.14}$$

$$MOH + MHCO_3 + OH^- \longrightarrow HCO_4^- + H_2O + 2\,M \tag{2.15}$$

$$2\,OH^- + MHCO_3 \longrightarrow HCO_4^- + e^- + H_2O + M \tag{2.16}$$

Bicarbonate has also been reported to get adsorbed at the surface via two oxygen atoms on (-121) bismuth vanadate [35]. The reaction mechanisms for this pathway have not been demonstrated yet. Bicarbonate might evolve further to peroxymonocarbonate or peroxycarbonate, though no proof for these mechanisms have been advanced yet. Nadar et al. (2020) stipulated that enhanced peroxide evolution was observed for (-121) $BiVO_4$ facets thanks to this two-fold oxygen bonding. They advanced that high concentrations of O-bonded HCO_3^- at the surface reduces the amount of oxygen atoms available for hydrogen peroxide dissociation. High-index surfaces are therefore though to help the peroxide evolution, though the exact product has not been identified yet. Figure 2.10d presents a potential pathway towards peroxymonocarbonate from the double-bonded bicarbonate.

PEROXYDICARBONATE FORMATION

Peroxydicarbonate is a compound which allows stabilization of the characteristic O-O peroxide bond. Peroxydicarbonate formation has been observed during water electrolysis in bicarbonate electrolytes on BDD electrodes [48]. The anodic material is known to catalyze the formation of hydroxyl radicals [36]. Interaction of these radicals can result in direct hydrogen peroxide formation as shown in Figure 2.6b, which does not involve bicarbonate. However, the interaction of two hydroxyl radicals ($OH\cdot$) with two bicarbonate molecules may lead to the formation of peroxydicarbonate [29]. The reaction is then Equation (2.17) in acidic media or Equation (2.18) in alkaline media, followed by Equation (2.19). Hydrolysis might allow regeneration of bicarbonate from peroxydicarbonate in the bulk via Equation (2.20). This reaction has been proposed in literature [54] but no kinetic data has been presented so far.

$$H_2O \longrightarrow OH\cdot + H^+ + e^- \tag{2.17}$$

$$OH^- \longrightarrow OH\cdot + e^- \tag{2.18}$$

$$2\,OH\cdot + 2\,HCO_3^- \longrightarrow C_2O_6^{2-} + 2\,H_2O \tag{2.19}$$

$$C_2O_6^{2-} + 2\,H_2O \rightleftharpoons 2\,HCO_3^- + H_2O_2 \tag{2.20}$$

PEROXYCARBONATE FORMATION

Peroxycarbonate (CO_4^{2-}) is a third compound containing the peroxide bond. No mechanisms involving this compound have been reported in literature so far for the electrochemical formation of peroxide. The product is rather unstable which may explain why it is not thought to be involved.

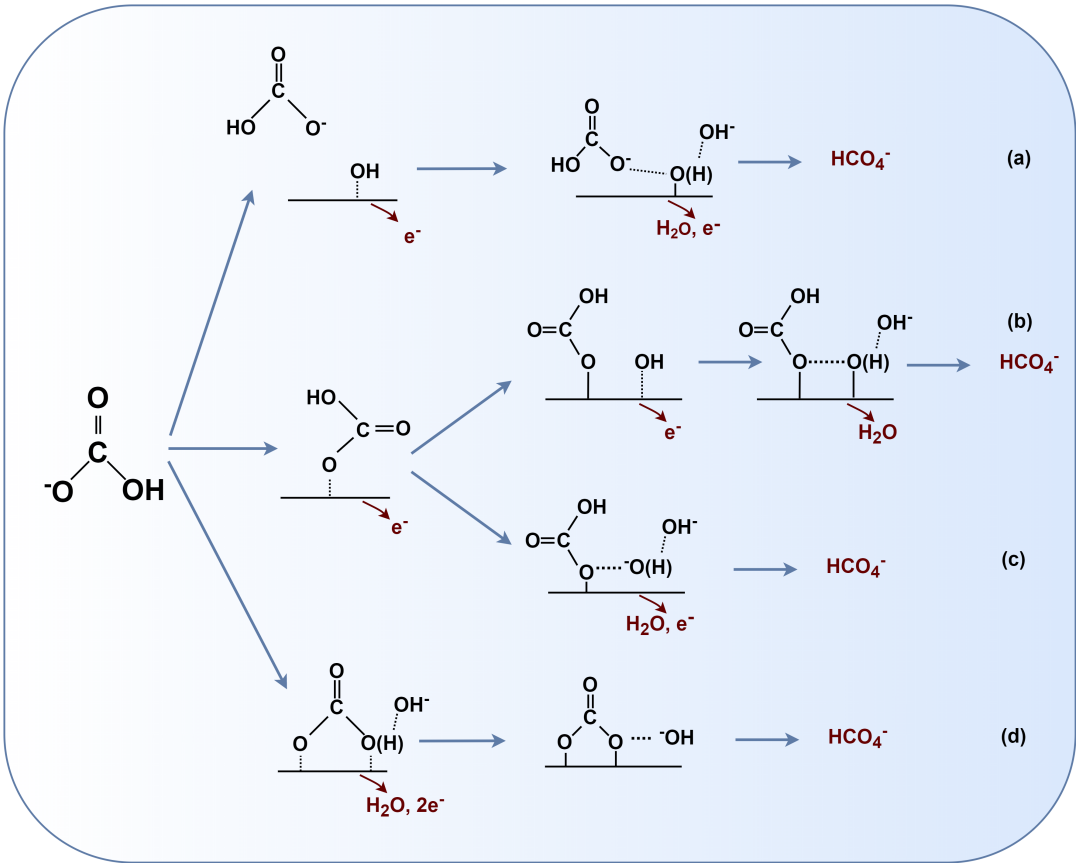

Figure 2.10: Reaction mechanisms proposed for the formation of peroxide compounds in bicarbonate via (a) a *Volmer-Heyrovski* mechanism starting from an OH* intermediate towards peroxymonocarbonate, (b) a *Volmer-Tafel* step starting from a HCO_3* intermediate to form peroxymonocarbonate, (c) a *Volmer-Heyrovski* mechanism starting from a HCO3* intermediate to form peroxymonocarbonate, (d) a double-bonded bicarbonate intermediate attacked by OH^- from the bulk.

2.3.3. CARBONATE INVOLVING PATHWAYS

Just as bicarbonate electrolytes are thought to be involved in the electrolytic peroxide formation on metal oxides, carbonate is thought to be involved for the product evolution on carbon-based electrodes. Improved peroxide yields were observed on both BDD and CFP electrodes in carbonate electrolytes [36, 45, 54]. Concentration studies have demonstrated higher current densities on BDD electrodes when operated in higher concentrations of sodium carbonate [44]. Different mechanisms explaining these performances in carbonate have been conjectured so far. The formation of peroxydicarbonate seems to be at the center of it as it allows to store the peroxide bond in a stable form. Findings on the oxidation of carbonate towards peroxydicarbonate and the formation of hydroxyl radicals for enhanced peroxydicarbonate production are explored in this subsection.

CARBONATE OXIDATION TOWARDS PEROXYDICARBONATE

In the previous section, the bicarbonate oxidation towards peroxymonocarbonate was shown to allow enhanced peroxide formation due to the use of an intermediate oxidizing compound that protects hydrogen peroxide itself from oxidation (Figure 2.9). A similar mechanism may be involved in the enhanced peroxide formation in carbonate. Carbonate may oxidize to peroxydicarbonate according to Equation (2.21) [54]. A possible mechanism for this reaction is illustrated in Figure 2.11. Subsequent hydrolysis in the bulk would then allow for the regeneration of the electrolyte as shown in Equation (2.22). No kinetic data has been reported so far for this reaction.

$$2\,CO_3^{2-} \longrightarrow C_2O_6^{2-} + 2\,e^- \tag{2.21}$$

$$C_2O_6^{2-} + 2\,OH^- \rightleftharpoons H_2O_2 + 2\,CO_3^{2-} \tag{2.22}$$

Even thought these mechanisms have been presented by several groups, no in-depth research was found on the mechanisms behind the interactions of the carbonate with the catalyst surface and the intermediates

involved in these reaction.

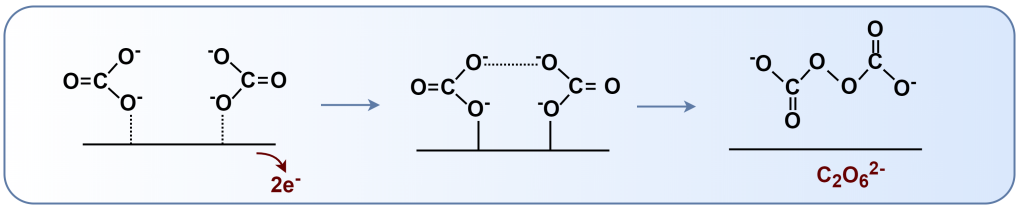

Figure 2.11: Reaction mechanism proposed for the carbonate oxidation towards peroxydicarbonate via two *Tafel* steps.

FORMATION OF HYDROXYL RADICALS FOR ENHANCED PEROXYDICARBONATE FORMATION

The favored formation of hydroxyl radicals has been conjectured on BDD electrodes in carbonate electrolytes [36]. The proposed mechanism for the one-electron WOR at BDD electrodes is [29, 37, 44]:

$$\mathrm{BDD} + \mathrm{OH^-} \longrightarrow \mathrm{BDD}(\cdot\mathrm{OH}) + \mathrm{e^-} \tag{2.23}$$

This reaction would then be followed by Equation (2.24) where carbonate and the formed hydroxyl radicals interact.

$$2\,\mathrm{CO_3^{2-}} + 2\,\mathrm{BDD}(\cdot\mathrm{OH}) \longrightarrow \mathrm{C_2O_6^{2-}} + 2\,\mathrm{OH^-} \tag{2.24}$$

Main competitive reactions to Equation (2.24) are the formation of hydrogen peroxide, which in the end results in a desired product (Equation (2.25)), and the reactions to ozone shown in Equations (2.26) and (2.27).

$$2\cdot\mathrm{OH} \longrightarrow 2\,\mathrm{H_2O_2} \tag{2.25}$$

$$\cdot\mathrm{OH} + \mathrm{OH^-} \longrightarrow \cdot\mathrm{O} + \mathrm{H_2O} + \mathrm{e^-} \tag{2.26}$$

$$\cdot\mathrm{O} + \mathrm{O_2} \longrightarrow \mathrm{O_3} \tag{2.27}$$

Via the reactions presented in this subsection, the presence of carbonate is thought to influence the electrochemical formation of peroxide. Even though these reactions have been presented as potentially involved, little research has been conducted to unveil the actual mechanisms behind them. Xia et al. (2020) for example, who observed enhance peroxide formation on CFP in carbonate electrolyte, proposed a direct synthesis route of hydrogen peroxide as alternative explanation.

In this chapter, an overview of current knowledge in the field of electrochemical hydrogen peroxide evolution was provided. Competitive reactions, preferred materials and reaction mechanisms were investigated. Some knowledge gaps, especially regarding the role of the electrolyte in the peroxide formation, were identified. The relevance of such mechanisms and their consequences for industrial applications of the two-electron WOR will be investigated in this study.

3

A Gross-Margin Model for Defining Technoeconomic Benchmarks in water electrolysis

The study of the anodic peroxide evolution is at this point still at its very beginning. In order to assess the viability of scaling-up the peroxide evolution, it is of importance to assess the link between experimental work and industrial requirements. Verma et al. [55] has recently published a gross margin model that allows the derivation of performance benchmarks for coupled CO_2 reduction and the Oxygen Evolution Reaction (OER). This model links the economic evaluation of large scale processes with electrolytic performance criteria. In this work, the prospects for different CO_2 reduction products such as CH_4, CH_3OH, C_2H_5OH and C_2H_4 were investigated.

A similar study by the same research group implemented their model for CO_2 reduction coupled to the glycerol oxidation instead of the traditional OER [56]. The coupling of this oxidation reaction allowed to decrease the overall Gibbs free energy requirement of the reaction thus the cell potential. In their study, the positive impact of co-electrolysis on process economics is demonstrated by implementing a thermodynamically more favorable reaction.

The techno-economical study presented in this report aims at assessing the impact on process economics for co-electrolysis of different reduction reactions and the two-electron WOR. Though these reactions will be thermodynamically less favorable than when coupled to the OER, the oxidation product will have a higher value than oxygen. This study focuses on assessing the trade-off between these two aspects. In a first part, the scope of the project will be addressed by exploring the processes examined. In a second part, the gross margin model and its derivation towards performance targets will be presented.

3.1. Processes considered and scope of the study

For the analysis of the coupled hydrogen peroxide evolution reaction, four coupled cathodic reactions were explored: the Hydrogen Evolution Reaction (HER), the CO_2 reduction towards carbon monoxide and ethylene and the two-electron Oxygen Reduction Reaction (ORR). The same reactions coupled to the OER were explored as well for the sake of comparison.

This section aims at defining the scope of the study. Firstly, a common cell design and reactions involved in the processes are explored. Secondly, block schemes and battery limits for the industrial processes are presented. Thirdly, an overview of main assumptions for cost estimates is provided.

3.1.1. Common cell design and reactions

Eight processes were considered for the study, divided in four different cathodic reactions and two different anodic reactions. An overview of these reactions can be seen in Figure 3.1.

A common cell design was established in order to ensure similar conditions for the different reactions and enable comparison. The designs can be seen in Figure 3.2. A 3 M Na_2CO_3 electrolyte was chosen. Experiments

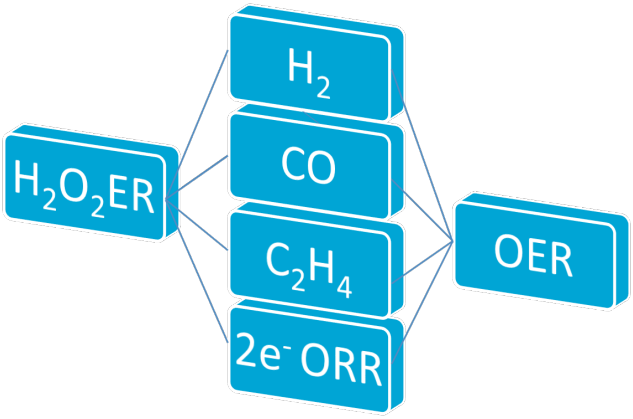

Figure 3.1: Overview of the different processes modelling based on anodic reactions (H_2O_2 Evolution Reaction, Oxygen Evolution Reaction (OER)) and coupled cathodic reactions (H_2 Evolution Reaction, CO_2 reduction to CO and C_2H_4, and two-electron Oxygen Reduction Reaction)

conducted in carbonate have indeed yielded the best results so far for the two-electron WOR (Table 2.2). Sodium carbonate was selected over potassium carbonate based on industrial prices (0.275 \$/kg *vs* 0.9 \$/kg [57, 58]). The 3 M concentration chosen was based on the maximum solubility of soda ash (34.07 g/100 mL [59]) and on downstream equipment requirements. Crystallization of the peroxide product requires an environment below 95 % of Na_2CO_3 saturation [60]. Detailed requirements for these units will be provided in subsequent sections. All electrodes were taken as gas diffusion electrodes onto which the relevant catalyst was coated. Cathodic catalyst materials considered were Pt, Ag and Cu for the HER, CO_2 reduction to carbon monoxide and CO_2 reduction to ethylene respectively [61]. For the two-electron ORR, the addition of a catalyst was not considered because good performances were reported on mesoporous carbon electrodes [25]. On the anodic side, a Ni catalyst and a plain GDE were considered for the OER and two-electron WOR respectively. For all catalysts, a loading of 0.5 mg/cm^{-2} electrode was considered [55, 62]. The product leaving the anolyte in the case of the two-electron WOR was sodium percarbonate ($Na_2CO_3 \cdot 1.5\,H_2O_2$). This product indeed allows improved stability of the peroxide bond. Sodium percarbonate is a widely used chemical with similar applications as hydrogen peroxide. It is mainly used as laundry detergent, but is also implemented for waste water treatment and textile bleaching. In 2019, the revenues generated by sodium percarbonate sales amounted 600 million \$ [63]. A compound annual growth rate of *ca* 3 % is expected until 2029 due to the increasing demand for environmental friendly oxidizing agent. Sodium percabonate has for example gradually been replacing perborate detergents due to environmental concerns [64]. Other shifts towards percarbonate are expected, especially in the textile bleaching industry.

The anodic reactions considered were the OER (Equation (3.1)) and the two-electron WOR (Equation (3.2)). A basic environment is created by the 3 M carbonate electrolyte thus the anodic reaction will be OH^- sinks rather than H^+ sources.

$$4\,OH^- \longrightarrow O_2 + 2\,H_2O + 4\,e^- \qquad E^o = 1.23\,V\ vs\ RHE \tag{3.1}$$

$$2\,OH^- \longrightarrow H_2O_2 + 2\,e^- \qquad E^o = 1.8\,V\ vs\ RHE \tag{3.2}$$

The auxiliairy role potentially played by carbonate in the formation of a stabilized peroxide bond was presented in Section 2.3. The involvement of carbonate may be either in the formation of an adduct thus yielding a chemical percarbonate, or the oxidation of carbonate itself thus yielding an electrochemical percarbonate [54]. In the first case, Equation (3.2) is followed by the coupling of Na_2CO_3 and H_2O_2 molecules. In the second case, the oxidation reaction towards peroxide compounds would be the carbonate oxidation towards percarbonate (Equation (3.3)). This reaction may be followed by hydrolysis to hydrogen peroxide (Equation (3.4)). The equilibrium constant for this reaction was not reported in literature.

$$2\,CO_3^{2-} \longrightarrow C_2O_6^{2-} + 2\,e^- \qquad E^o = 1.09\,V\ vs\ RHE\ [54] \tag{3.3}$$

$$C_2O_6^{2-} + 2\,OH^- \rightleftharpoons 2\,CO_3^{2-} + H_2O_2 \tag{3.4}$$

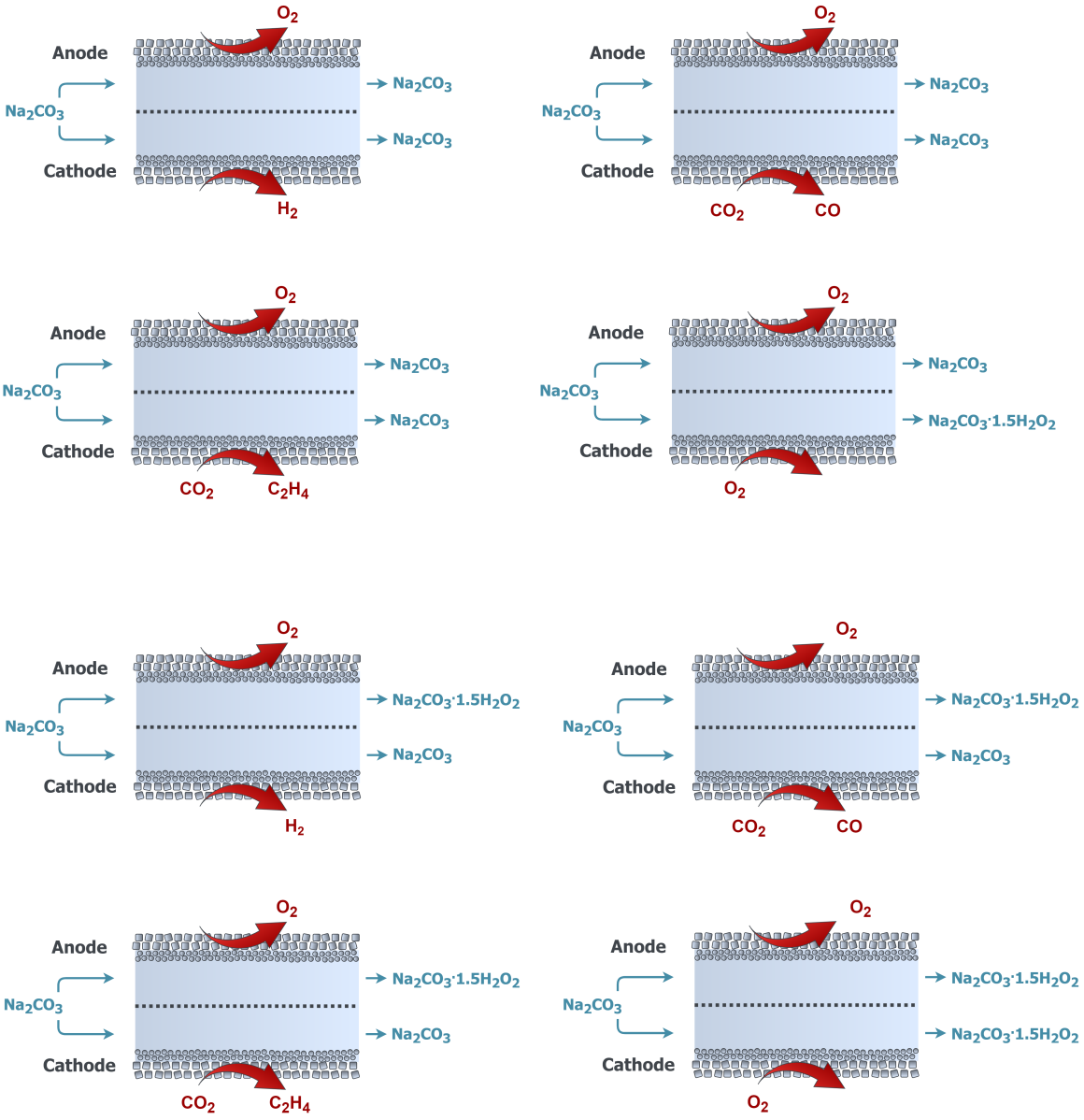

Figure 3.2: Common cell design for the OER couped to H_2, CO, C_2H_4 evolution and O_2 reduction, and the two-electron oxidation towards H_2O_2 coupled to H_2, CO, C_2H_4 evolution and O_2 reduction presented in reading order

Different cathodic products were investigated in order to assess the added-value of the peroxide evolution reaction compared to the OER. These included hydrogen, carbon monoxide, ethylene and hydrogen peroxide. Hydrogen was considered as it is one the most investigated electrochemical product. Alkaline water electrolyzers have been developed for the production of this component. CO_2 reduction products have been subject to several techno-economic studies. For the sake of process design comparability, only gaseous CO_2 products were chosen in this study. Carbon monoxide was observed as one of the most promising gaseous products from CO_2 reduction in terms of viability [40]. The electrochemical production of ethylene on the other hand was computed to be on the verge of feasibility. The final cathodic reaction considered was the oxygen reduction to hydrogen peroxide. This process requires the same type of separation equipment as for the anodic peroxide production. In the past years, interest has been aroused for this reaction and first commercial implementations have emerged [27]. The cathodic reactions considered were the HER (Equation (3.5)), the CO_2 reduction reactions to carbon monoxide and ethylene (Equation (3.6) and Equation (3.7)) and the ORR to hydrogen peroxide (Equation (3.8)).

$$2\,H_2O + 2\,e^- \longrightarrow H_2 + 2\,OH^- \tag{3.5}$$

$$CO_2 + 2\,e^- + H_2O \longrightarrow CO + 2\,OH^- \tag{3.6}$$

$$2\,CO_2 + 8\,H_2O + 12\,e^- \longrightarrow C_2H_4 + 12\,OH^- \tag{3.7}$$

$$O_2 + 2\,H_2O + 2\,e^- \longrightarrow H_2O_2 + 2\,OH^- \tag{3.8}$$

Competing reaction are the HER for the reduction to CO, the HER and the CO production for the reduction to C_2H_4 and the four-electron ORR (Equation (3.9)) for the two-electron ORR.

$$O_2 + 2\,H_2O + 4\,e^- \longrightarrow 4\,OH^- \tag{3.9}$$

3.1.2. BATTERY LIMITS

For processes including the two-electron WOR, a production rate of 100 ton/day anodic product was defined. For processes involving the OER, the cathodic production rate was set equal to the cathodic production rate obtained from the two-electron WOR mass balances. This was done in order to have a common parameter for the two anodic reaction thus enabling comparison.

Battery limits were defined for the eight processes. For all processes, the only utility crossing the battery limit is electricity. For the OER (Figures 3.3 to 3.6), oxygen and water get produced as shown in Equation (3.1). Oxygen leaves via the gas side of the GDE (see Figure 3.2). Water leaves via a purge which will contain water and sodium carbonate in the same ratio leaving the electrolyzer. A make-up of sodium carbonate enters the battery limit to compensate for the purge.

During the two-electron ORR shown in Figures 3.3 and 3.7 water gets consumed as shown in Equation (3.8). Additional water gets produced by the side-reaction, namely the four-electron ORR. Water and soda ash to compensate for the sodium percarbonate product enter the battery limit. Air is also fed to the process to drive the reduction reaction. Unreacted air leaves the battery limit and is not recycled as it is a relatively non-valuable stream.

The HER described in Equation (3.5) consumes water. A water make-up therefore crosses the battery limit to account for this cathodic reaction (Figures 3.4 and 3.8). Due to the absence of competing reaction, the hydrogen evolution Faraday efficiency was considered as 100 % in all cases for this reaction.

The CO_2 reduction towards CO necessitates a CO_2 feed crossing the battery limit (Figures 3.5 and 3.9). Carbon dioxide is recycled after separation from the products. Products leaving the battery limit are the main product CO together with H_2 as by-product. Both cathodic reactions consumed H_2O which results in the need for a water feed entering the battery limit.

The CO_2 reduction towards C_2H_4 presents similar features the reduction towards CO. CO_2 enters the battery limit together with water (Figures 3.6 and 3.10). The product and by-products (C_2H_4, H_2 and CO) leave the battery limit.

For the two-electron WOR, sodium percarbonate and oxygen leave the battery limit. Their production is accounted for by Equations (3.1) and (3.2). Water gets produced by the OER side reaction and leaves the process via a purge containing water and a small amount of sodium carbonate and hydrogen peroxide. A sodium carbonate feed enters the battery limit to compensate for the purge and for the carbonate leaving as product.

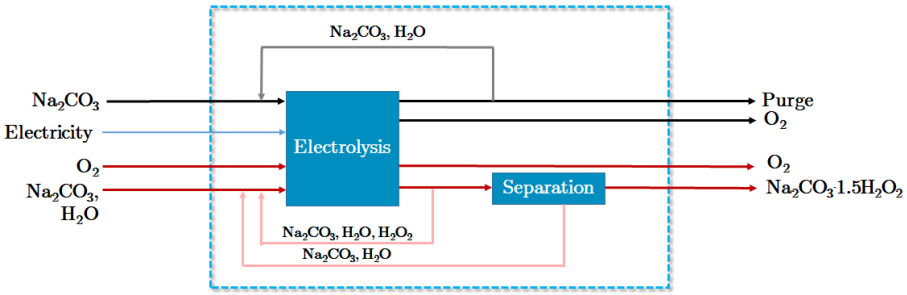

Figure 3.3: Battery limits for the coupled oxygen evolution reaction and two electron oxygen reduction reaction. Black arrows represent the anodic side and red arrows the cathode one.

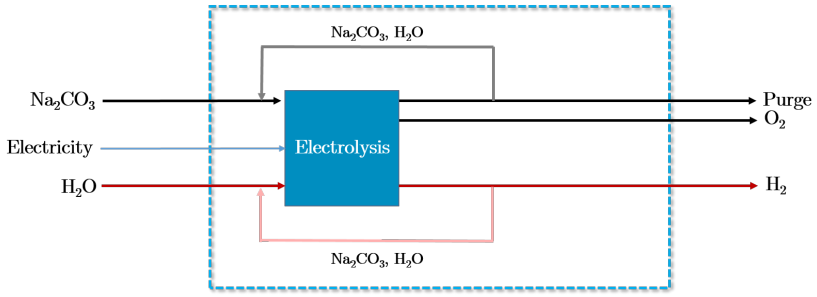

Figure 3.4: Battery limits for the coupled oxygen evolution reaction and hydrogen evolution reaction. Black arrows represent the anodic side and red arrows the cathode one.

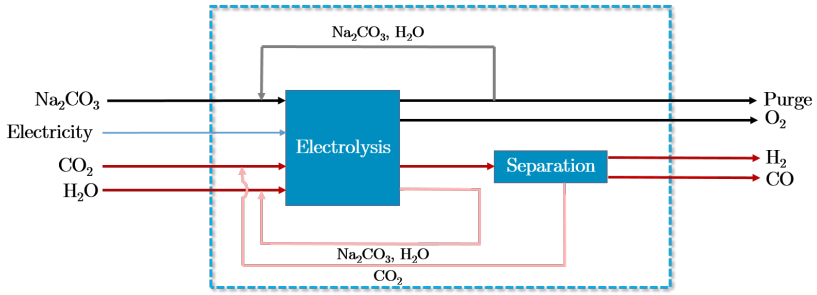

Figure 3.5: Battery limits for the coupled oxygen evolution reaction and CO_2 reaction to CO. Black arrows represent the anodic side and red arrows the cathode one.

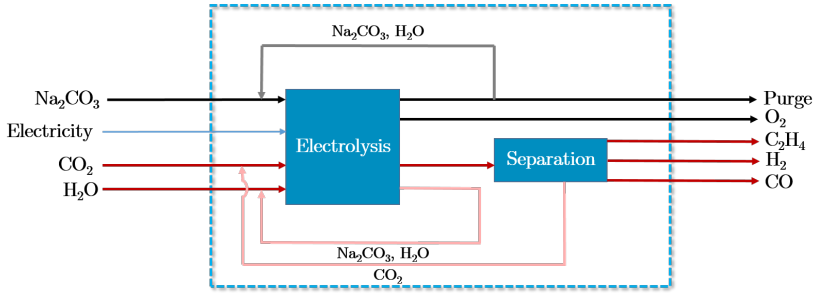

Figure 3.6: Battery limits for the coupled oxygen evolution reaction and CO_2 reaction to C_2H_4. Black arrows represent the anodic side and red arrows the cathode one.

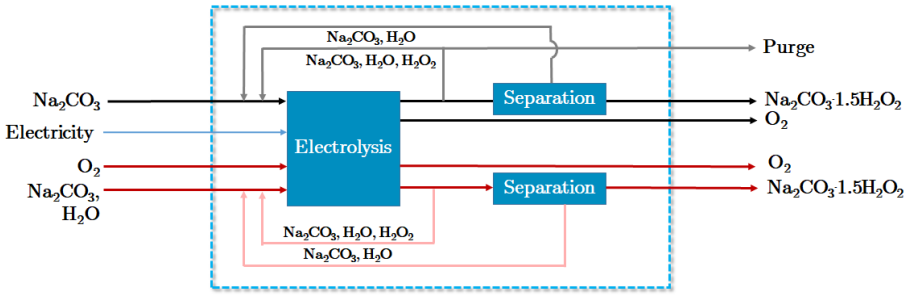

Figure 3.7: Battery limits for the coupled two-electron water oxidation reaction and two electron oxygen reduction reaction. Black arrows represent the anodic side and red arrows the cathode one.

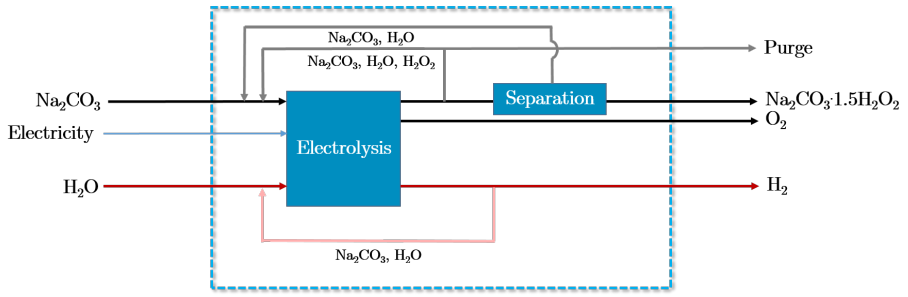

Figure 3.8: Battery limits for the coupled two-electron water oxidation reaction and hydrogen evolution reaction. Black arrows represent the anodic side and red arrows the cathode one.

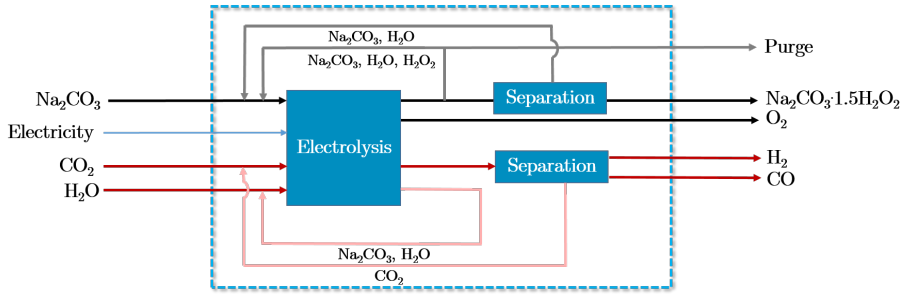

Figure 3.9: Battery limits for the coupled two-electron water oxidation reaction and CO_2 reaction to CO. Black arrows represent the anodic side and red arrows the cathode one.

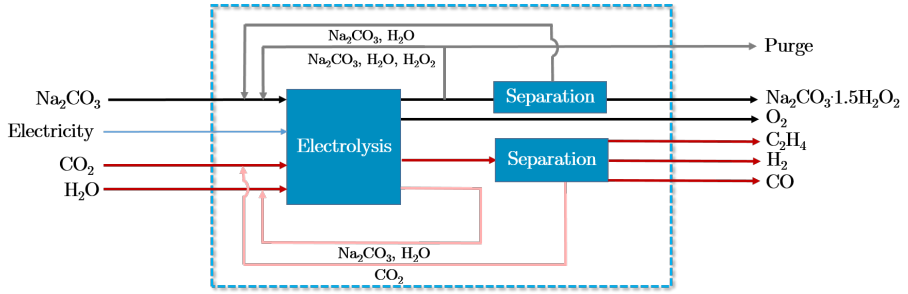

Figure 3.10: Battery limits for the two-electron water oxidation reaction and CO_2 reaction to C_2H_4. Black arrows represent the anodic side and red arrows the cathode one.

3.1.3. MAIN ASSUMPTIONS FOR THE ECONOMIC EVALUATION

The economic evaluation was based on several assumption which are explored in this section.

ELECTROCHEMICAL CELL

Given the current state of research on both electrochemical hydrogen peroxide production and CO_2 reduction, no industrial-scale electrolyzers have been implemented yet for these systems. Furthermore, no standard cell design for electrosynthesis of H_2O_2 have been reported yet [25]. Estimation of electrolyzer capital costs have therefore been based on alkaline water electrolysis systems. This choice was based on several features common to the processes evaluated and alkaline water electrolysis. First of all, no precious metal catalysts are required for the anodic reactions considered. Moreover, alkalinity is induced by the use of carbonate as electrolyte. This will result in similar constructing material criteria for the alkaline water electrolysis and for the processes considered. The main difference between alkaline water electrolysis and cells considered in this study resides in the cell design. For most of the processes, as shown in Figure 3.2, a direct gas feed to the catalyst surface is required. Such a feed was not expected to have a major impact on costs [40]. The capital costs of the electrolyzer were based on the DOE Current Distributed Grid Electrolysis base case for an alkaline electrolyzer.T he uninstalled capital cost linked to the stack component was taken as 250 $/kWh. Stacks are composed of structural rings, PTFE sealings, bipolar plates, pre-electrodes, the anode and cathode, a membrane, flanges and tie rods [65]. A power estimate of 7 MW was taken from the Faraday equation of electrolysis based on a 100 ton/day percarbonate production and an operating voltage of 2 V. The electrolyte flow rate was taken as 880 L/min [40].

The balance of plant, which includes auxiliairy compounds for the electrolyzer such as gas and electrolyte management, control sensors and power electronics was taken as 50 % of the alkaline electrolyzer system capital cost [65]. For a power requirement of 5 MW, 50 stacks of 200 cells each are required. The cell area is taken as 1500 cm^2 [66].

PRODUCT SEPARATION

Two types of outlets require product separation: gas products and liquid products. The gas streams to be separated consist of excess CO_2 fed to the electrolyzer, H_2, CO and C_2H_4. The liquid stream consists of water, sodium carbonate, hydrogen peroxide and sodium silicate, which was reported to enhance stabilization of the product.

Four of the processes considered will require gas separation at the outlet of the electrolyzer. Processes involved are the one with CO_2 reduction. Gas separation can be distinguished for three types of targets: purification of a stream, sharp separation of products and increase in the concentration of one component [67]. For this model, a sharp separation of the product is desired. Different methods allow a sharp separation of products, including physical absorption, adsorption and cryogenic distillation. Adsorption is the most commonly employed method for this type of separation. Pressure Swing Adsorption (PSA) is an industrial process with low equipment volumetric footprint, low energy requirements, low capital investment costs, that is safe and relatively simple [68]. For CO_2 reduction, the output stream is composed of excess CO_2, hydrogen and other gas products. Due to the novelty of the processes considered, no industrial-scale equipment and costs are reported. The upgrading of biogas presents presents similarities in gas composition with the outlet studied [40]. The upgrading of biogas via PSA has been described in several industrial reports [69]. Based on these studies, a capital cost of 1 990 000 $ per 1000 m^3/h was used. In order to account for significant change in equipment sizing for low single pass conversions, a scale factor of 0.7 was implemented. The variable cost, composed of electricity required for pressure changes, was estimated at 0.25 kWh/m^3 [40].

All reactions towards the peroxide product will require a separation unit on the liquid outlet stream. This includes the two-electron WOR and ORR. Hydrogen peroxide in itself is not a very stable product. Combination with bicarbonate or carbonate to yield peroxymonocarbonate (HCO_4^-) and percarbonate ($C_2O_6^{2-}$) respectively has been shown to stabilize the peroxide bond. In view of the sodium carbonate electrolyte used for these reactions, the product considered will be sodium percarbonate. This product can be obtained via crystallization of a carbonate/ hydrogen peroxide mixture, via spraying and via drying methods [70]. The spraying and drying processes described were based on separate hydrogen peroxide and sodium carbonate feeds, as opposed to the crystallization process for which they were mixed beforehand. Based on this and considering the maturity of crystallization technology, the latter was implemented for the obtaining of sodium percarbonate. Crystallization efficiency is often increased with the use of salting-out agents. As visible in Figures 3.7 to 3.10, a recycle of electrolyte is implemented to the inlet of the crystallizer. Salting out agents such as sodium chloride are unwanted in the crystallizer as they will have a deleterious effect on electrolysis

performance. Solvay patented a crystallization process without the use of salting-out agent [60]. The sodium percarbonate product obtained was reported to have enhanced thermal stability [70]. Main requirements for this process include a (1:1) Na_2CO_3:H_2O_2 mole ratio at the inlet of the crystallizer. Sodium carbonate should be used at a concentration below 95 % of a saturated solution concentration. The crystallizer should be operated around room temperature (between 15 and 25 °C. The use of a stabilizing agent such as sodium silicate was recommended in a ratio between 5 and 80 g/kg soda ash. Sodium silicate has been reported to enhance electrolysis performance at concentrations of 2 g/L [37]. As this concentration fell in the range for the recommended crystallizer concentration (9.5 $g_{Na_2SiO_3}/kg_{Na_2CO_3}$), it was implemented for the processes. Based on engineering rules of thumbs, the free-on-board capital cost of a crystallizer with continuous operation can be estimated as 675 000 $ for a capacity of 1 kg/s crystals produced [71]. This value is valid for carbon steel, however, hydrogen peroxide is incompatible with this material [72]. The free-on-board capital cost should be multiplied by a factor 4 to be translated to total fixed capital costs. To account for the use of stainless steel, one should multiply this by 0.75 [71]. In the end, the capital cost of the crystallizer was therefore 3*675 000 $ for a capacity of 1 kg/s crystals produced. A scale factor of 0.53 was used.

BASE CASE OPERATION

Base case operation times were defined for all the processes. The plant lifetime was taken as 20 years. Yearly operation was evaluated at 8000 h to account for downtime needed for maintenance. The catalyst lifetime was taken as 4000 h based on values used for the gross margin model by Verma et al. [55].

PRICES

Different prices were used to assess the techno-economic features of the eight processes considered. Costs used were based on values found from providers and values presented in literature. Variable costs comprise utilities and raw materials. Product prices were used to asses the value created during the process. The price for the catalyst was defined to establish the electrode cost.

Base case electricity costs were taken as 0.06 $/kWh based on industrial electricity prices in both Europe and the United States [73, 74]. Raw materials fed to the process are deionized water, soda ash, sodium silicate, oxygen and carbon dioxide. Prices used were 1.42 [40], 0.275 [57], 0.3 [75], 0.02 [76] and 0.06 $/kg [55]. Sodium percarbonate, carbon monoxide, ethylene and hydrogen leave the processes as added-value compounds. Prices were taken as 0.5 [77, 78], 0.6 [40, 79], 1.2 [55, 80] and 4.5 $/kg [55, 81]. As presented in Section 3.1.1, catalyst materials considered were Pt, Ag, Cu, Ni. Prices used were $2.7 * 10^{-2}$ [82], $5.3 * 10^{-4}$ [83], $5.2 * 10^{-6}$ [84] and $1.21 * 10^{-5}$ $/mg [85] respectively. These materials are to be deposited onto a gas diffusion electrode for which a cost of 0.006 $/$cm^2$ was used [55].

EFFICIENCY AND CONVERSION

Several assumptions were used for the evaluation of the mass balances for the different processes considered. Some base case parameters were defined regarding faradaic efficiencies of cathodic and anodic reactions. Moreover, single pass conversion was taken into account. This is notably relevant for processes involving gas feeds. Other reactions, such as the hydrogen peroxide evolution or the hydrogen evolution have reactants already in large excess. Single pass conversion was therefore not considered of importance for these processes. Energetic efficiency of the system was not taken into account as this would only be relevant at a later stage of the development process for the reactions considered. This study focuses on performance targets at the beginning of the process design thus losses due to cell design were not looked into yet.

The faradaic efficiencies for the OER and two-electron WOR were taken as 100 and 60 % respectively. The OER has been intensively studied over the past years resulting in the design of more and more efficient catalyst. Moreover, oxygen was not considered as a valuable product which is why side reactions were assumed not to impact the results of the techno-economic model. The faradaic efficiency for the anodic hydrogen peroxide formation was taken as 60% based on results presented by Xia et al. [45]. This recently published research has presented the best performances so far in the field. The catalysts chosen were based on this research thus it seems fit to use their reported faradaic efficiency. For the evaluation of faradaic efficiencies on the cathodic side, values were mainly based on literature. The HER is a fairly mature technology and its faradaic efficiency was taken as 100 %. For the two-electron ORR and the CO_2 reduction to CO and C_2H_4, faradaic efficiencies were taken as 90 [25], 80 and 70 % [61].

Single pass conversion was implemented in the mass balances in order to encompass the downstream equipment sizing in the techno-economic study. Single pass conversion was taken into account for the ORR and CO_2 reduction. A base case conversion of 70 % was used based on values reported in literature for CO_2 reduction [86].

Mass balances for the eight processes at base case parameters can be found in Appendix D.

3.2. THE GROSS MARGIN MODEL

A techno-economic analysis based on a gross margin evaluation allows to define performance targets for scientific electrochemistry work. In this section, definitions for different parameters involved in the techno-economic evaluation are first provided. In a second time, definition for revenues and costs are explored. Finally, expressions for performance targets are provided.

3.2.1. GROSS MARGIN PARAMETERS DEFINITION

The gross margin is an economic concept used to assess the profitability of a process for a company. It excludes parameters such as taxes, product distribution and personnel costs [87]. The gross margin is defined as the quotient of the difference between revenue and costs of goods and the revenue as presented in [55]. In Equation (3.10), the term "A" corresponds to the gross margin requirement. The worst case gross margin is chosen to be 15% ($A = 0.15$), the base case scenario 30% ($A = 0.30$) and the best case scenario 45% ($A = 0.45$). A gross margin of 0 % would imply break even over the period of time considered. Taking the worst- and best-case scenarios allows performing a sensitivity analysis.

$$\frac{\text{Revenue} - \text{Cost of goods sold}}{\text{Revenue}} > A \tag{3.10}$$

First, the costs of goods need to be defined. Economic evaluations for process and product design are usually divided in two parts: manufacturing costs and capital costs. Manufacturing costs can be subdivided in three parts: direct costs (raw materials, utilities, operational costs), indirect costs (plant overhead and fixed costs) and general costs (administration and marketing). Raw materials play a major role and usually account for 50-90% of the total manufacturing cost [88]. The electricity consumption being significant for electrolysis, it can be expected that variable costs, which include both raw materials and utilities, will dominate the manufacturing cost. An analysis based on the DOE model for decentralized hydrogen production from alkaline water electrolysis showed that 52 % of the final product market price originates from variable costs and 35 % from capital costs [89]. Studies on PSA showed that operating and maintenance costs are negligible compared to capital costs [90]. Cost of electricity will however be significant as compression is an energy-intensive process. For crystallizers, total annual costs were found to originate mainly from vessel capital cost and heat exchangers [91]. The crystallization of percarbonate operating around room temperature, it is assumed that the major cost factor will be the capital cost of the crystallizer itself. For both separation techniques, no raw materials are fed to the process.

Based on these assumptions, it is considered representative to base the economic evaluation on the following costs:

1. Capital costs for the main pieces of equipment (electrolyzer, product separation)(T_{cap}),
2. Variable costs including raw materials and main utilities entering the battery limit (T_{var}).

The overall capital costs can be further divided in two categories, namely the capital costs for the electrolysis itself (T_{prod}) and the capital costs for the separation (T_{sep}).

The capital costs for the electrolyzer itself can be divided in two categories, each amounting for 50 % of T_{prod} [92]. The first half corresponds to costs related to the electrolyzer ($\lambda_{\text{electroylzer}}$), the second half consists of the balance of plant, including auxiliary components to the electrolyzer such as power electronics, control systems, electrolyte and gas management (λ_{BOP}).

The capital costs for product separation ((T_{sep}) are obtained by multiplying the capital cost of separation per kilogram main product by the production rate of the latter product.

Next to capital costs, the costs of feedstocks crossing the battery limit are accounted for. Main electricity sinks are the electrolysis reactions and the compression of gases during PSA. Raw materials crossing the battery limit are make-up electrolyte, inlet gases and peroxide stabilizer.

Table 3.1 provides the expressions of the different parameters for the estimation of the costs of goods sold. Production rates were evaluated based on Faraday's law on electrolysis with FE the Faraday efficiency in

[%], z the number of electrons required in the reaction towards the product, n the number of moles in [mol] produced, F the Faraday constant which equals 96 485 s A/mol and Q the charge passed in [As]:

$$FE = \frac{znF}{Q} \tag{3.11}$$

Table 3.1: Cost parameters for the gross margin model evaluation, with λ different costs in [$], C_{cat} the cost of catalyst in [$/mg], W_{cat} the catalyst loading in [mg/cm^{-2}], C_{GDL} the cost of the gas diffusion layer in [$/cm^{-2}], A the surface area in [cm^{-2}], j the current density in [mA/cm^{-2}], FE the faradaic efficiency in [%], M the molar mass in [g/mol], C_{cryst} the capital cost of the crystallizer expressed in [$/kg$_{product}$], z the number of electrons transferred in the reaction, C_E the cost of electricity in [$/kWh], V the operating voltage in [V], Q_{gas} the gas flow rate at the inlet of the PSA in [m^3/h], C_{raw} the cost of raw materials in [$/kmol], Q_{raw} the raw material feed to the system in [kmol/h] and t the time in h.

Cost	Parameters	Parameter definition
T_{prod}	Electrolyzer cost	$\lambda_{electrolyzer}$
	Catalyst cost	$\lambda_{cat} = \frac{(\sum(C_{cat,i}W_{cat,i})+2C_{GDL})At}{t_{catdur}}$
	Electrolyzer BOP cost	$\lambda_{BOP} = \lambda_{electrolyzer} + \lambda_{cat}$
T_{sep}	PSA cost	$\lambda_{PSA} = \frac{36}{F} * 10^{-6} * \frac{jAtFE_{product}M_{product}}{z} * C_{PSA}$
	Cystallizer cost	$\lambda_{crystallizer} = \frac{36}{F} * 10^{-6} * \frac{jAtFE_{product}M_{product}}{z} * C_{cryst}$
T_{var}	Electricity cost	$\lambda_{electricity} = C_E[VjAt * 10^{-6} + 0.25Q_{gas}t]$
	Raw materials cost	$\lambda_{raw} = \sum C_{raw}Q_{raw}t$

3.2.2. DEFINITION OF REVENUE AND COST OF GOODS SOLDS

The gross margin was defined as Equation (3.10) based on revenues and costs of goods sold, both expressed in [$]. This subsection present the derivations of both concepts based on parameters defined in the previous section.

The revenue can be derived from the sales prices of different products and the production rate obtained from Faraday's law of electrolysis. In Equation (C.2), a distinction is made between cathodic and anodic product products.

$$\text{Revenue} = \frac{jAt * 36 * 10^{-6}}{F} * \left(\sum \frac{\text{FE}_P^{anodic} C_P M}{z} + \sum \frac{\text{FE}_P^{cathodic} C_P M}{z} \right) \tag{3.12}$$

The cost of goods sold is somewhat more complex. It is indeed composed of capital costs for both the electrolyzer and separation units as well as variable costs for raw materials and utilities (Section 3.2.2).

$$\text{Costs of goods sold} = T_{cap} + T_{var} = T_{prod} + T_{sep} + T_{var}$$

Using the parameters provided in Table 3.1, one can set-up an equation for the costs of goods solds as:

$$\text{CSG} = T_{prod} + \lambda_{raw} + C_E(VJAt * 10^{-6} + 0.25Q_{gas}t) + \frac{36 * 10^{-6} * jAt}{F} \left(\frac{\text{FE}^{anode}_{main\ product} C_{sep} M}{z} + \frac{\text{FE}^{cathode}_{main\ product} C_{sep} M}{z} \right) \tag{3.13}$$

T_{prod} is the capital cost of production [$], T_{sep} the capital cost of product separation [$], λ_{raw} [$] the cost of raw materials , Q_{gas} is the gas inlet to the PSA unit [m^3/h], F is the Faraday constant, C_{sep} is the cost of separation [$/kg$_{product}$].

3.2.3. PERFORMANCE TARGETS FROM THE GROSS MARGIN MODEL

From explored in the previous sections, one can derive expressions for a maximum operating voltage and minimum current density for the system to be economically viable. This subsection provides the highlights for the derivation of these parameters. Detailed derivations can be found in Appendix C.

Combining the gross margin definition (Equation (3.10)) with expression for revenues (Equation (C.2)) and costs of goods sold (Equation (C.4)) gives Equation (C.5):

$$T_{\text{prod}} + \lambda_{\text{raw}} + 0.25 C_E Q_{\text{gas}} t < jAt * 10^{-6} \left[\frac{36}{F} \left[\sum \left(\frac{\text{FE}_P^{cathode} M}{z} \right) (1-A) C_P - \frac{\text{FE}^{\text{cathode}}_{\text{main product}} M}{z} C_{\text{sep}} \right. \right.$$

$$\left. \left. + \sum \left(\frac{\text{FE}_P^{anode} M}{z} \right) (1-A) C_P - \frac{\text{FE}^{\text{anode}}_{\text{main product}} M}{z} C_{\text{sep}} \right] - V C_E \right] \quad (3.14)$$

V_{MAX} DEFINITION

A voltage requirement stems from Equation (C.5). The costs found on the left hand-side will per definition have a positive value. This implies that the right hand-side term in brackets may not be negative. From this requirements, one can derive a maximum operating voltage for the process given its economic characteristics:

$$V_{\text{max}} = \frac{36}{F C_E} \left[\sum \left(\frac{\text{FE}_P^{cathode} M}{z} \right) (1-A) C_P - \frac{\text{FE}^{\text{cathode}}_{\text{main product}} M}{z} C_{\text{sep}} + \sum \left(\frac{\text{FE}_P^{anode} M}{z} \right) (1-A) C_P - \frac{\text{FE}^{\text{anode}}_{\text{main product}} M}{z} C_{\text{sep}} \right] \quad (3.15)$$

If the maximum operating voltage evaluated from this model for a given process is inferior to its standard cell potential, one can conclude that the process is not feasible. One should be careful when considering the opposite situation, which is a maximum operating voltage superior to the standard cell potential. The definition of V_{max} does not explicitly account for raw materials and utilities, which might have a deleterious impact on the accuracy of the process economics' evaluation. The benchmark obtained for V_{max} should be used to quickly eliminate unfeasible processes, but more extensive feasibility analyses should be performed on processes satisfying the V_{max} criterion.

J_{MIN} DEFINITION

Rearranging Equation (C.5) and using the definition for V_{max} provided in Equation (3.15), one can define the minimum operating current density as:

$$j > \frac{T_{\text{prod}} + \lambda_{\text{raw}} + 0.25 Q_{\text{gas}} t C_E}{At * 10^{-6} * C_E [V_{\text{max}} - V]} \quad (3.16)$$

4

MATERIALS AND METHODS

In order to tackle the research questions presented in Chapter 1, experiments were performed in three subsequent phases. First, anodic materials for the electrolysis cell were prepared. In a second time, the cell operation was studied. Finally, products obtained were analyzed.

4.1. ELECTRODE SYNTHESIS AND CHARACTERIZATION METHODS

Electrode materials were prepared via different routes in order to assess the electrochemical parameters of influence for the obtaining of industrially relevant peroxide evolution. The use of DC magnetron sputtering was first investigated. This technique provides good control on sample properties based on conditions applied during the deposition. Examples of parameters that can be controlled include stoichiometry, thickness, crystallinity and substrate. Sputtering, however, tends to yield very uniform and flat surfaces. Spray pyrolysis was investigated as alternative thin film synthesis method to obtain nanostructured surfaces. In this section, some background on the synthesis methods is first provided. Experimental protocols for synthesis are then explored for thin tin oxide films via reactive sputtering, thin indium tin oxide films via sputtering, tin oxide films via spray pyrolysis and carbon-based electrodes. Finally, characterization methods used to analyze the produced samples are presented.

4.1.1. SOME BACKGROUND ON DC MAGNETRON SPUTTERING

Direct Current (DC) magnetron sputtering is a thin film physical vapor deposition technique. It allows production of thin films (semi-)conducting materials onto a surface referred to as *substrate*. In the chamber of the sputtering system, a gaseous plasma is produced. Argon is usually used for this purpose, other gases may be introduced for reactive sputtering. The ions contained in the plasma are accelerated towards the material to be deposited, contained in the *target* [93]. Electron transfer from the projected ions to the target results in erosion of the latter as exemplified in Figure 4.1. The source material indeed liberates neutral particles in the form of atoms or molecule that will be directed towards the substrate. In the case of reactive sputtering, the liberated particles will interact with the gas. An example is the formation of oxides when adding oxygen.

In magnetron sputtering, two magnets are placed behind the target. This allows to trap free electrons from the plasma which prevents overheating and damage to the substrate. Moreover, the number of pathways that electrons can take is reduced due to the magnetic field. This increases the ionization of neutral gas molecules thus increasing the deposition rate.

Targets and substrates are contained in a vacuum chamber. The target is protected by a shutter, which can open during depositions. The substrate is rotating in order to maximize the homogeneity of the deposited film thickness.

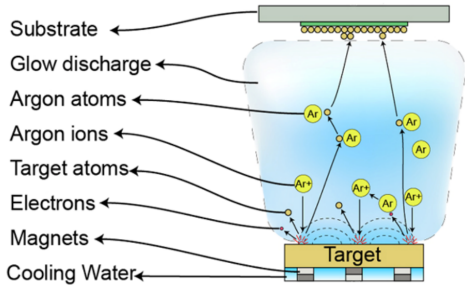

Figure 4.1: Sketch of the elements in a vacuum chamber of a DC magnetron sputtering system [94]

4.1.2. REACTIVE DC MAGNETRON SPUTTERING FOR TIN OXIDE THIN FILM SYNTHESIS

Tin oxide thin films were deposited by reactive DC magnetron sputtering using an AJA system and a Sn target. For each batch, four samples were produced. Two samples were deposited on a 2 by 2 cm and 0.1 mm thick Ti substrate, and two samples were deposited on a microscope grade glass plate. The glass samples were used later for XRD and four point point probe measurements and the Ti samples were destined for SEM imaging and electrochemical experiments. If other substrates were used, this will be mentioned in the description of experiments.

SUBSTRATE CLEANING

Prior to deposition, substrates were cleaned using the following procedure:

- **Ti foils:** Foils were first washed carefully with soap and demineralized water. They were then rinsed three times with milli-Q water. Sonication of the foils was performed for 15 min in subsequently milli-Q water, acetone and isopropanol using an Emmi-30 HC sonicator at 100 % efficiency. In between the sonication steps, samples were rinsed twice with respectively acetone and isopropanol. Samples were stored in isopropanol and dried with nitrogen gas upon retrieval.
- **Glass substrate:** Samples were rinsed subsequently three times with milli-Q water, acetone and isopropanol. They were then dried with high purity nitrogen gas.
- **FTO substrates:** Commercial FTO with a sheet resistance of 15 Ω/sq (TEC-15) was obtained from Hartford Glass Co. Samples were first washed carefully with soap and demineralized water. They were then rinsed three times with milli-Q water. Sonication of the FTO substrates was performed for 15 min in subsequently milli-Q water, acetone and isopropanol using an Emmi-30 HC sonicator at 100 % efficiency. In between the sonication steps, samples were rinsed twice with respectively acetone and isopropanol. Samples were dried with nitrogen gas upon retrieval. They were then treated in a UV-ozone cleaner for 45 min at 60 °C. Samples were stored in sealed containers. Before use, potential dust was blown off with nitrogen gas.

Before initiating the sputtering, substrates were cleaned for 2 min under DC 20 W power a 3 µbar and 20 sccm Ar. Targets were cleaned by pre-sputtering with closed shutter under Ar at the power and pressure used for sputtering. Targets were pre-sputtered for 5 min if they had recently been placed in the AJA system and for 2 min if they had already been used after installation in the chamber.

SPUTTERING PROTOCOLS

During the experiments presented subsequently, gas ratio and pressure were varied in order to obtain the correct stoichiometric ratio for tin oxide. First, a method using a similar AJA Intl. system as the one at the TU Delft MECS group was followed [95]. Stoichiometry of films obtained from reactive sputtering is highly dependent on equipment and equipment used. A more universal method was used in a second time to obtain SnO_2 films [96]. This method was based on oxygen partial pressure and discharge voltage properties. Rates for sputtering were determined with a crystal monitor.

SPUTTERING UNDER 15 SCCM AR : 5 SCCM O_2

Samples were deposited on three Ti substrates and one microscope grade glass substrates based on the method described by Bissig et al. [95].

The effect of heating treatment was investigated. The fixed and varied parameters used were:

- **Fixed parameters**: Sputtering with a tin target was performed for 7 minutes and 14 seconds at 35 W and 5 µbar with 15 sccm Ar and 5 sccm O_2. A deposition rate of 2.05 Å/s was obtained at room temperature. The deposition rate was evaluated with a crystal monitor. A correction factor of 0.89 was determined via profilometry on test samples of 100 nm theoritecial thickness. During deposition, the pressure was maintained constant by fixing the throttle valve.

- **Heating treatment:** Three batches were made. The first one was sputtered at room temperature. The second one was sputtered in the same conditions followed by a post annealing treatment for 5 hours at 500 °C under 100 sccm air using a 5 °C/min ramp. The final batch was sputtered at high temperature. For this batch, the substrates were heated in the vacuum chamber for two hours to 450 °C prior to sputtering.

SPUTTERING UNDER 5 SCCM AR : 15 SCCM O_2 AT 450 °C

The argon to oxygen ratio was varied to observe the effect on film composition. The substrates were heated for two hours to 450 °C. They were subsequently cleaned under DC power as describe in the substrate cleaning procedure explored previously. Sputtering was performed for 7 minutes and 14 seconds at 450 °C, 35 W and 5 µbar with 5 sccm Ar and 15 sccm O_2.

SPUTTERING UNDER 9 SCCM AR : 11 SCCM O_2

The method by Snyders et al. for controlled stoichiometry of SnO_x films based on oxygen partial pressure was used as backbone for the following depositions [96]. The effect of heating treatment was investigated. The fixed and varied parameters used were:

- **Fixed parameters:** Sputtering with a tin target was performed at 120 mA and 13.3 µbar with 9 sccm Ar and 11 sccm O_2. The pressure was maintained constant by fixing the throttle valve. The deposition rate was evaluated based on rate control via a crystal monitor. At the given parameters, the rate of deposition was 0.2 Å/s.

- **Heating treatment:** For each set of sputtering, three batches were made. The first one was sputtered at room temperature. The second one was sputtered in the same conditions followed by a post-annealing treatment for 5 hours at 500 °C under 100 sccm air using a 5 °C/min ramp. The final batch was sputtered at high temperature. For this batch, the substrates were heated in the vacuum chamber for two hours to 500 °C prior to sputtering. Depositions for the heating treatment study were done for 1 h 23 min 20 s thus aiming for samples of 100 nm thickness.

- **Thickness variation:** The experiments were repeated three times for the samples sputtered at high temperature in order to obtain samples of *ca.* 100, 200 and 300 nm thickness. Sputtering times were respectively 1 hour 23 min 20 s, 2 hours 46 min 40 s and 4 hours 10 min.

  Additional samples of *ca.* 275 nm were deposited onto two glass and two FTO substrates of 3 by 3 cm at room temperature. The deposition was done for 3 hours 49 min 10 s under the same conditions as the previous samples. The samples obtained were post-annealed for 5 h at 500 °C using a ramp of 5 °C/min.

4.1.3. SPUTTERING FOR INDIUM OXIDE THIN FILM SYNTHESIS

ITO thin films were deposited by reactive DC magnetron sputtering using an AJA system and In_2O_3/SnO_2 target with respectively 90 and 10 wt % of each component. For each batch, four samples were produced. The parameters used for the deposition were based on a study by Tuna et al. [97]. For each batch, two samples were deposited on a 2 by 2 cm and 0.1 mm thick Ti substrate, and two samples was deposited on a microscope grade glass plate. If other substrates were used, this will be mentioned in the description of experiments.

Prior to deposition, the substrates were cleaned using the same procedure as described in Section 4.1.2. A 60 seconds ramp was used for ignition of the target to avoid its rupture.

SPUTTERING UNDER 15 SCCM AR: 5 SCCM O_2

Heating treatment and thickness of the films deposited were varied. The fixed and varied parameters are presented below:

- **Fixed parameters:** Sputtering was performed for 73 minutes and 24 seconds at 15 W and 3 µbar under 20 sccm Ar. The deposition rate amounted 0.23 Å/s and was evaluated via profilometry on a test sample deposited at room temperature for 30 min.

- **Heating treatment:** Three batches were made. The first one was sputtered at room temperature. The second one was sputtered in the same conditions followed by a post annealing treatment for 5 hours at 400 °C under 100 sccm air using a 5 °C/min ramp. The final batch was sputtered at high temperature (350 °C). For this batch, the substrates were heated in the vacuum chamber for two hours to 350 °C prior to sputtering.

- **Thickness variation:** Samples of *ca.* 275 nm were deposited onto two glass and two FTO substrates of 3 by 3 cm at room temperature. The deposition was done for 4 hours 30 min under the same conditions as the previous samples. The samples obtained were post-annealed for 5 h at 400 °C using a ramp of 5 °C/min.

4.1.4. SPRAY PYROLYSIS FOR TIN OXIDE FILM SYNTHESIS

Thin films of *ca.* 80, 100 and 160 nm SnO_2 were deposited via spray pyrolysis onto Ti, microscope grade glass and fluorine-doped tin dioxide coated glass. Prior to deposition, the substrates were cleaned according to the procedures described in Section 4.1.2.

The precursor solution composed of 0.1 M $SnCl_4$ (99 %, Acros Organics) in ethyl acetate (99.8 %, Sigma-Aldrich). The substrates were heated to 450 °C prior to the deposition. Temperature control was ensured by a thermocouple pressed onto the ceramic support where the substrates were disposed. An automated spray set-up with Quickmist air atomizing spray nozzle was used. More detailed specifications of the set-up can be found in the supplementary information of [98]. The spraying is driven by an overpressure of 0.06 MPa of nitrogen gas. A distance of 20 cm separated the nozzle and the substrate. The precursor solution was kept 30 cm above the nozzle. The precursor solution flow was engendered by a siphoning effect created by the nitrogen gas flow. Cycles of 5 s spraying and 55 s solvent evaporation time were repeated 5, 6 and 10 times for the 80, 100 and 160 nm samples respectively. Samples were maintained in position by a mask. After the depositions, the setup was cleaned by cycling ethanol spaying 30 times.

The samples were annealed for 5 h at 500 °C under 100 sccm compressed air. A ramp of 5 °C/min was used to reach the required temperature.

4.1.5. PREPARATION OF CARBON-BASED ELECTRODES

Several carbon-based electrodes were prepared based on methods described by Xia et al. [45]. CFP and GDE were used as substrates.

CARBON FIBER PAPER ELECTRODES

CFP was used as electrode material. Sheets of 190 µm thick with 5 % Polytetrafluoroethylene (PTFE) loading were cut in 2 by 2 cm pieces. The preparation procedure for different CFP anodes is described below:

- **Cleaning procedure:** The CFP samples were rinsed with milli-Q water. They were then sonicated for 15 min subsequently in a 0.1 M H_2SO_4 solution and in milli-Q using an Emmi-30 HC sonicator at 100 % efficiency. Between sonication steps, the samples were rinsed three times with milli-Q. A Novascan UV-ozone treatment was performed to enhance hydrophilic behaviour for 30 min at 60 °C.

- **Sample coating:** Some CFP samples were coated with PTFE following experiments described by Xia [45]. For these experiments, a 60 % dispersion in H_2O (CAS number 9002-84-0) ordered from Sigma-Aldrich was used. The samples were dipped for 10 min in the dispersion and left to dry for 30 min at ambient conditions. They were dried for 1 h under ambient conditions at 120 °C followed by 30 min at 350 °C under 20 sccm Ar.

GAS DIFFUSION ELECTRODES

Gas Diffusion Electrode (GDE) of type Sigracet 39BC were obtained from the Fuel Cell Store. These electrodes are 325 µm thick and have a microporous layer coated with 5 % PTFE. Samples of 2 by 2 cm were cut with a cleaned Stanley knife. Prior to use, potential dust was cleaned with compressed nitrogen.

4.1.6. CHARACTERIZATION METHODS

Different characterization methods were used in order to observe and compare the different samples produced. These methods include imaging methods such as Scanning Electron Microscopy (SEM), Atomic Force

Microscope (AFM) as well as crystal characterization with X-Ray Diffraction (XRD) and conductivity performance via four point probe measurements. The following sections aim at providing the reader some background to understand the potential and shortcomings of each of these characterization methods. This is done in order to provide the reader with the tools to understand the results obtained.

SCANNING ELECTRON MICROSCOPY

Scanning Electron Microscopy (SEM) is a non-destructive imaging technique to obtain high resolution images of surfaces [99]. It not only reveals the external morphology but also allows chemical composition analysis [100]. The use of an electron beam in vacuum allows to achieve visualization up to the nanometer. This improved resolution compared to a classic microscope is due to the shorter wavelength of the electron beam compared to light.

A Scanning Electron Microscope is composed of different elements such as an electron source, referred to as the *electron gun*, lenses which focus the electron beam onto the sample surface and detector (Figure 4.2a). The electron gun is situated at the top of the column. Liberated electrons travel through the vacuum and are focused by lenses onto the sample. Depending on the voltage applied, the beam will penetrate the surface of the sample more or less. When the electrons hit the sample, their kinetic energy is dissipated. This dissipation engenders different signals due to interactions with the samples. These include secondary electrons, which are the main signals used for SEM imaging, back-scattered electrons and X-rays. The provenance of these signals is illustrated in Figure 4.2b.

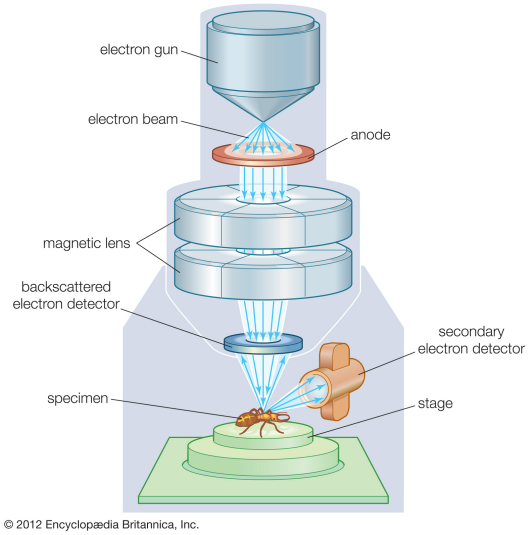

(a) Sketch of a SEM [101]

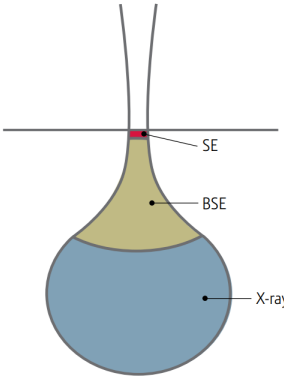

(b) Sketch of the electron beam penetration and origin of Secondary Electrons (SE), Back-Scattered Electrons (BSE) and X-Rays [99]

Figure 4.2: Sketches of (a) the layout of a Scanning Electron Microscope and (b) the penetration of the electron beam onto the surface

Energy-Dispersive X-Ray Spectroscopy (EDS) can be performed with a Scanning Electron Microscope to analyze the x-rays emitted by the sample upon exposure to the electron beam. Different chemical elements emit characteristic x-rays which are detected during the measurement. The energy spectrum detected is analyzed by the software and reflects the abundance of different elements.

SEM is an advantageous analysis method at it is easy to operate and non-destructive. It should be noted that not only surface characteristics will be reflected by SEM as the beam penetrates the sample to a certain extent (Figure 4.2b). Another shortcoming, which is mainly relevant for EDS stems from the fact that x-ray detectors implemented have a poor energy resolution. This implies that chemical element analysis will be moderately accurate.

ATOMIC FORCE MICROSCOPE

An Atomic Force Microscope (AFM) allows high resolution imaging of surfaces. Three-dimensional topography images can be obtained with resolution on the height scale in the order of Å.

AFM readings are performed with a probe. This probe consists of a cantilever and a very sharp tip as illustrated in Figure 4.3 [102]. Upon scanning the surface of a sample, the tip will move due to interactions with the atoms of the sample. A laser beam is reflected onto the cantilever. All movements induced by the interactions of the tip and the sample surface induce a change in the reflection of the laser beam. A detector tracts the laser response and the change in reflection is used to compute the surface of the sample.

A Bruker Dimension Icon AFM with RTESPA 300 tip was used in tapping in air mode with a scan rate of 0.388 Hz and a force constant of 40 N/m.[1]

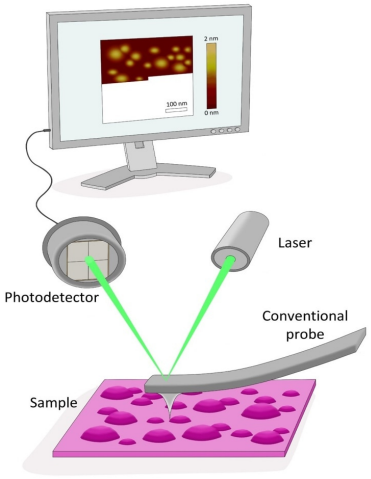

Figure 4.3: Sketch of an AFM [102]

X-RAY DIFFRACTION

XRD is a technique used to characterize the crystallinity of materials as well as to assess the presence of certain elements in a sample. The analysis is based on the diffraction of waves emitted onto the surface of the considered sample. The diffraction pattern formed by the sample provides information on the arrangement within the crystal, but also on the size of the crystal [103].

The diffractometer is composed of several elements presented in Figure 4.4). An x-ray source provides the waves that will be diffracted. The most commonly used material for the x-ray tube is copper. The XRD used for this study was a Bruker D8 ADVANCE diffractometer (Co, $\lambda = 1.789$ Å). Diffraction datasets obtained during this research were therefore translated using Bragg's law in order to allow comparison with literature. The derivation for the conversion can be found in Appendix A. The detector receives the diffraction pattern created by the sample. The signal obtained is plotted as a function of 2θ, the detector angle.

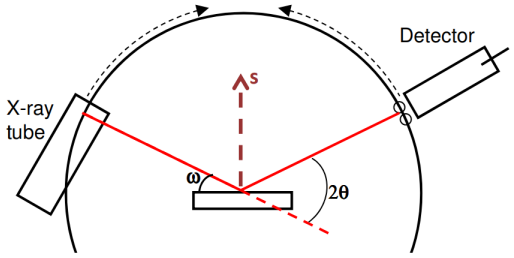

Figure 4.4: Simplified sketch of a diffractometer [103]

Information about the arrangement and size of the crystal can be deduced from the data obtained. The crystallite grain size can be derived from the Scherrer equation 4.1. This equation relates crystallite grain size D to wavelength λ, Scherrer constant K, diffraction angle θ and full width at half maximum β.

$$D = \frac{K\lambda}{\beta \cos\theta} \tag{4.1}$$

The plane of the system can be determined with Miller indices [103]. The distance between planes of atoms is given by Bragg's law (equation A.1).

$$\lambda = 2d \sin\theta \tag{4.2}$$

Even though XRD provides a broad range of information on the structure and nature of the sample, it also has its limitations. When analysis thin films, penetration of x-rays too deep into the sample might provide

[1] Atomic Force Microscope measurements were made by Ir. Anirudh Venugopal, PhD student at the TU Delft in the MECS research group.

information only on the substrate rather than the film itself. Moreover, rotation of films was rather inconvenient in the set-up used. For this reason, samples were analyzed at a fixed position. The lack of variety in the angle of emission might have allowed for some structures to be overlooked.

VAN DER PAUW METHOD

In this subsection, some background on the four point probe method and sample requirements are presented. The application of the latter for this study are then shortly explored.

The sheet resistance of a thin film is of importance in order to characterize electrodes. A low sheet resistance indeed implies less losses. During electrode operation, a current flows to the contacts. It is of importance for the scaling-up of such processes that losses across the electrode are minimized.

Van Der Pauw has derived a method that allows determining the specific resistivity without knowing current patterns if the following requirements are fulfilled [104]:

- Contacts are placed at the periphery of the samples,
- Contacts are small,
- Thickness of the sample is homogeneous,
- The sample surface is uniform, *i.e.* there are no holes.

For this study, the simplified case of thin square samples is considered. To determine the resistivity of the thin film via the van der Pauw method, the four small ohmic contacts are deposited approximately equidistantly on the corners of the sample. Four probes are placed on top of these contacts as shown in Figure 4.5. Conventionally, contacts are numbered counter-clockwise from 1 to 4. A current is passed from probe 1 to probe 2 and the voltage across probes 3 and 4 is measured, which gives a resistance $R_{12,34}$. The same can be done with a current between probes 2 and 3 and a voltage measurement across probes 1 and 4, yielding $R_{23,41}$. These two resistances are related to the sheet resistance R_S via the Van der Pauw equation. Solving the van der Pauw equation, one can express the resistivity as Equation (4.3) for uniform and symmetric samples with $R_{12,34} = R_{23,41}$.

$$\rho = \frac{\pi d R_{12,34}}{\ln 2} \tag{4.3}$$

The sheet resistance R_S in [Ω or Ω/sq] can then be computed as Equation (4.4) with ρ the resistivity in [Ω m] and d the thickness of the sample in [m] [105].

$$R_S = \frac{\rho}{d} = \frac{\pi}{\ln 2} R_{12,34} \tag{4.4}$$

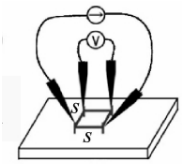

Figure 4.5: Sketch of the four point probe method [106]

This technique was applied for sputtered samples. Samples on Ti substrates were first analyzed, but soon probe contacts appeared to be made with the Ti thus influencing the results. Glass substrates were therefore used for subsequent measurements. Contacts were sputtered using a DC magnetron sputtering system. A plastic mask was placed on top of the samples in order to only sputter at the edges of the samples. A thin layer of Sn (*ca.* 10 nm) was first sputtered in order to prevent the formation of Schottky contact between the semi-conductor and gold. This first layer also allows the top contact to stick better. The Sn layer was deposited for 42 s at 35 W under 20 sccm Ar and 5 µbar. A top layer of *ca.* 100 nm gold was then deposited for 1 min 43 s at 200 W, 3 µbar under 20 sccm Ar. Pre-sputtering of the substrate was implemented at DC power 20 W for 5 min at 3 µbar under 20 sccm Ar. Pre-sputtering of the Sn and Au targets was done for 5 min at respectively 5 µbar, 35 W and 3 µbar, 200 W[2].

[2]The method for contact deposition was suggested by Ir. Diana Chaykina, PhD student at the TU Delft in the MECS research group

4.2. ELECTROCHEMICAL EXPERIMENTS

Electrochemical experiments were performed in order to assess the performance of the synthesized electrodes. First, the equipment and type of measurements performed are described. Secondly, the experimental set-up and protocol for validation are explored. Finally, experiments performed are described.

4.2.1. ELECTROCHEMICAL METHODS

Different types of electrochemical methods are commonly used to assess electrochemical performances of devices such as electrolyzers. Measurements are usually performed with a potentio/galvanostat. An overview of the most commonly used methods is presented below.

1. **Chronoamperometry**, measured with a potentiostat. A current response to a potential applied is measured as a function of time (Figure 4.6).

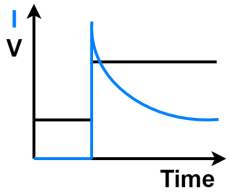

Figure 4.6: Typical chronoamperometry graph with current response to a potential step *vs* time

Chronoamperometry is often employed for:

- Evaluation of electrode reactions with know redox potential,
- Focusing on a material and one reaction,
- Analysis of mass transfer limitations.

2. **Chronopotentiometry**, measured with a galvanostat. A potential response to a current density applied is measured as a function of time (Figure 4.7).

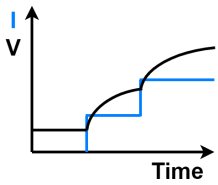

Figure 4.7: Typical chronopotentiometry graph with voltage response to a current step *vs* time

Chronopotentiometry is often used for:

- Cases dominated by mass transport,
- Controlling the production rate to asses industrial relevance.

3. **Cyclic Voltammetry (CV)**: a current response is reported as a function of potential (Figure 4.8).

   CV is often used for:

   - Redox potential analysis,
   - Looking at reversibility of reactions,
   - Analysis of reaction kinetics based on the Tafel plot.

4. **Electrochemical Impedance Spectroscopy (EIS)**: this type of measurement allows to decompose and analyze the ohmic resistances and reactance playing a role in the cell. Impedance is often represented in a Nyquist plot with the real part of the impedance against its imaginary part (Figure 4.9). The half-circles obtained allow to translate and model the behaviour of the system with electrical circuit elements [108].

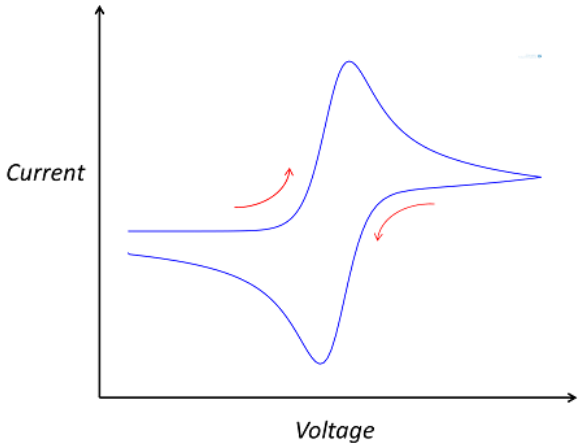

Figure 4.8: Typical cyclic voltammetry graph with current as a function of potential [107]

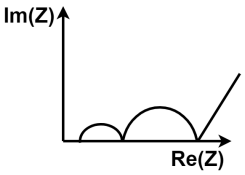

Figure 4.9: Typical Nyquist plot

4.2.2. ELECTROCHEMICAL EXPERIMENTAL SET-UP

In this subsection, the electrolytic cell set-up and cleaning routines used for all electrochemical experiments are described. Configurations used to assess the good functioning of the set-up are described.

CELL DESIGN

The cell itself consisted of four main components:

- PTFE blocks, composing the main body of the cell. These blocks allow separated entrance and flow of the anolyte and catholyte as illustrated in Figure 4.10. A hole at the top allows inserting of a reference electrode. The blocks allow flexibility of design with the possible addition of gas compartments;
- Viton gaskets, ensuring that the cell is leak-tight and separating components such as the electrodes and the membrane;
- Metal protections, meant to make the design sturdier and prevent damage to the Teflon blocks due to the tightening of the screws;
- Screws to hold the pieces tight together.

The cell used was 6 by 6 cm with an exposed electrode area of 1.5 by 1.5 cm. The body of the cell was made of Polytetrafluoroethylene (PTFE) and the attachments for catholyte and anolyte tubings were made of polypropylene. A platinum coil was used as cathode.

The anolyte and catholyte were contained in 100 mL amber glass bottles from Duran in order to minimize light-induced decomposition of products. A GL45 screw cap with air-tight tube connectors was used in order to isolate the system. A valve was placed on the anolyte tubing in order to permit sample retrieval for product testing.

CELL PREPARATION

The following cleaning procedure was followed before starting to use the cell. The Teflon blocks, valve, T-junction and caps were rinsed with milli-Q water. The Viton rubber gaskets were washed with soap and demineralized water, and rinsed with milli-Q water. The whole was left overnight in 20 % H_2SO_4. The Pt coil

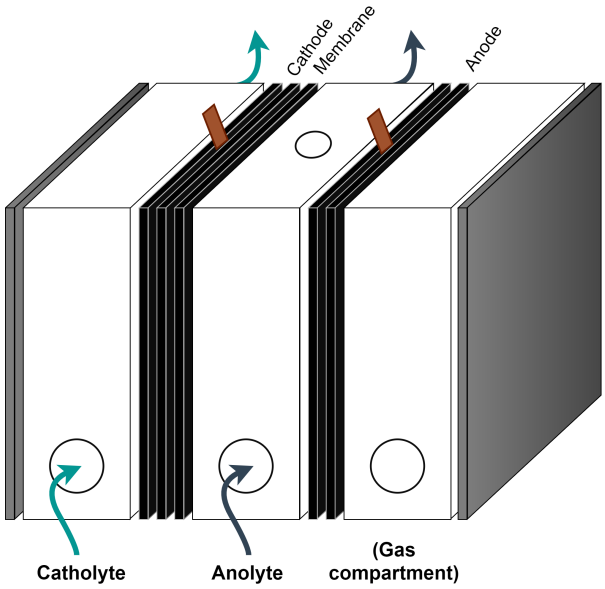

Figure 4.10: Sketch of the electrolysis cell used for experimental work

used as cathode was soaked for 15 min in 97 % H_2SO_4. Beakers were rinsed with 97 % H_2SO_4. The whole was rinsed twice with milli-Q, and potential sulfuric acid left-overs were boiled off for 15 min.

A Nafion 115 Proton Exchange Membrane was used for the experiments. It was replaced *ca.* every 20 set of runs. Prior to use, it was treated as to enhance its properties. Samples of 2.5 by 2.5 cm were cut and separated from the cover sheet. They were left an hour in lightly boiling 3 % H_2O_2 after which they were rinsed with milli-Q water. They were then left for 2 h in lightly boiling H_2O and subsequently for 1 h in lightly boiling 0.5 M H_2SO_4. They were then rinsed 3 times with lightly boiling H_2O. The membranes were stored in milli-Q water.

DESIGN VALIDATION

Some experiments were performed in order to assess the correct functioning of the cell. These include calibration of the reference electrode and testing of the membrane.

- **Reference electrode calibration:** The Ag/AgCl reference electrode of type XR300 radiometer analytical used for experiments was calibrated against another Ag/AgCl standard reference electrode. Open circuit values were measured with a potentiostat/galvanostat. Values obtained were within ± 10 mV of each other thus the electrode was considered as well calibrated.

- **Membrane tests:** Some experiments were carried on in order to ensure that no significant limitations, in particular due to the membrane, were impeding the performance of the cell.

  The cell was tested in a Pt/ Pt configuration with a Ag/AgCl reference electrode. The Pt working electrode and the reference electrode were separated from the Pt counter electrode by a Nafion 115 PEM. The experiments were performed in 0.5 M $KHCO_3$ with 50 mL of anolyte and catholyte respectively. The electrolyte was pumped at a rate of 18.5 mL/min through the system.

4.2.3. ELECTROCHEMICAL TESTS

The anodes produced as described in the previous section were tested in the electrolytic cell using the methods presented below. A standard protocol and cleaning procedures were followed for all experiments. The type of electrolyte was varied as to observe the role of the latter in the peroxide evolution reaction. As explored in Section 2.3, mechanisms involved in bicarbonate and carbonate on metal oxide and carbon-based electrodes respectively are not fully understood. The superiority of a bicarbonate environment for metal oxide electrode performance has already been shown in literature thus tests for tin oxide-based electrodes were performed in $KHCO_3$. The effect of both bicarbonate and carbonate electrolytes on carbon-based electrodes was investigated. An overview of the tests performed is provided here:

- **Standard protocol:** Different sets of experiments were performed, some in bicarbonate and others in carbonate electrolytes. For the electrochemical experiments, the following standard procedure was followed unless specified otherwise. The electrolyte bottles were both filled with 40 mL electrolyte. A magnetic stirrer was inserted in the anolyte. connection tubes were mounted going from the electrolyte container via the pump to the cell and from the cell back to the electrolyte container. At the anolyte GL45 cap, gas tubes were inserted in order to bubble nitrogen through. The design allows for a connection of the gas outlet to a GC. It was however not used in these experiments. The cell was mounted as shown in Figure 4.10 with a Pt coil as cathode, a Nafion 115 PEM, a Ag/AgCl reference electrode and the test sample as anode. Copper tape was used to fix the anode to the gaskets and make electrical contact. The electrolyte was pumped through the system at 37 mL/min, nitrogen gas was bubbled through the anolyte at *ca.* 10 mL/min to prevent interaction of the electrolyte with CO_2. The anolyte was stirred at 100 rpm.

- **Cleaning procedure:** After usage of the cell, a standard cleaning procedure was used. Milli-Q water was pumped for 5 min through the system at 37 mL/min. This was repeated 3 times. After disassembly, cell components were rinsed 3 times with milli-Q water and dried with nitrogen if stored dry.

- **Tests in different electrolytes:** All sputtered samples and samples prepared by spray pyrolysis were tested in 0.5 M bicarbonate. CFP samples were tested in 2 M $KHCO_3$ and in 2 M K_2CO_3. The GDE sample was tested in 2 M K_2CO_3. A series of standard tests was run unless specified otherwise. These tests included, in the following order: chronoamperometry at 2 V *vs* RHE, cyclic voltammetry from 0 V *vs* OC to 3 V *vs* RHE, chronoamperometry at 3 V *vs* RHE, cyclic voltammetry from 0 V *vs* OC to 3 V *vs* RHE and finally chronoamperometry at 4 V vs RHE.

Figure 4.11 shows the assembled experimental set-up with at (1) the cell, (2) the anolyte with magnetic stirrer bar, (3) the catholyte, (4) the valve for anolyte sample retrieval, (5) the Ag/AgCl reference electrode, (6) the connection at the working electrode and counter electrode with the potentiostat, (7) the flow controller for nitrogen gas bubbled through the anolyte and (8) the pump.

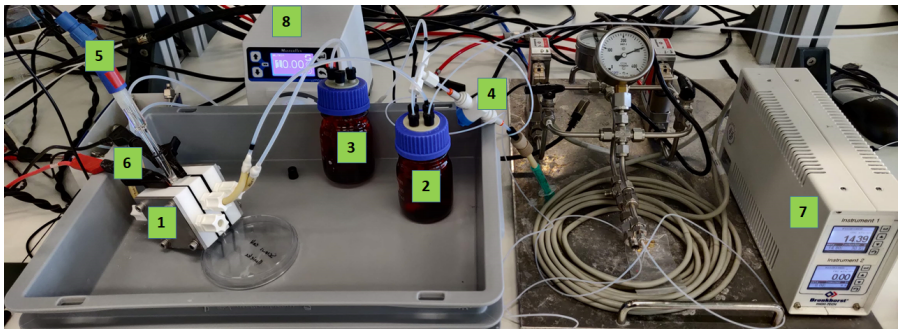

Figure 4.11: Experimental set-up as used for the elctrochemical tests with (1) the electrolysis cell, (2) the anolyte with magnetic stirrer bar, (3) the catholyte, (4) the valve for anolyte sample retrieval, (5) the Ag/AgCl reference electrode, (6) the connection at the working electrode and counter electrode with the potentiostat, (7) the flow controller for nitrogen gas bubbled through the anolyte and (8) the pump.

4.3. PRODUCT CHARACTERIZATION AND QUANTIFICATION

Different methods were used for the identification and quantification of peroxide products. These include test sticks, titration and NMR spectroscopy.

4.3.1. QUANTOFIX STRIPS

Quantofix® test sticks (Sigma-Aldrich) with application ranges 0.5-25, 1-100 and 50-1000 mg/L were used for quick estimates of peroxide concentration. The lowest range sticks were used for experiments in bicarbonate, the highest concentration range sticks were used for the experiments in carbonate.

4.3.2. TITRATION

The use of permanganate titration has been reported in several studies for the quantification of peroxide electrochemical production [18, 29]. The permanganate ion has a strong purple color which disappears as it reacts with hydrogen peroxide according to the reaction in Equation (4.5):

$$2\,MnO_4^- + 5\,H_2O_2 + 6\,H^+ \longrightarrow 2\,Mn^{2+} + 5\,O_2 + 8\,H_2O \tag{4.5}$$

Addition of an acid is important to prevent the formation manganese dioxide which induces the decomposition of H_2O_2 [109].

Several methods were found in the literature and followed for calibration experiments of the permanganate titration. For all experiments, a 0.02 M (0.1 N) $KMnO_4$ solution was used as titrant. A Tritrino Plus Metrohm titrator was used. Volume addition was done manually at steps of 0.5 mL. Sulfuric acid was used as proton source. The analyte used for the calibrations contained hydrogen peroxide, electrolyte (potassium bicarbonate or carbonate), water and acid in different concentrations.

Different titration methods were used:

1. Titation with direct addition of acid to the peroxide and electrolyte containing analyte (4 mL H_2SO_4/ 100 mL analyte) [109],

2. Titration with dilution of the analyte before addition of dilute acid [110]: 100 g samples of hydrogen peroxide at known concentration in bicarbonate or carbonate were diluted to 250 mL. An aliquot of 25 mL of the diluted solution was mixed with 250 mL H_2O and 10 mL H_2SO_4 to form the analyte.

3. Titration followed by UV-vis spectroscopy to quantify the excess permanganate [109]: calibration curves of absorbance for solutions of permanganate and bicarbonate at different concentrations were made. Measurements were done in the 400-600 nm range in 2 and 10 mm cuvettes depending on the bicarbonate concentration. The peak for permanganate is found at 525 nm.

4.3.3. NMR SPECTROSCOPY

Nuclear Magnetic Resonance (NMR) spectroscopy was explored as analysis method to distinguish different types of peroxide products. Firstly, some background on NMR spectroscopy and its functioning are provided in order to guide the reader in its understanding of the usage of the method. Secondly, the use of benzene capillaries for the experiments is explored in light of the theory presented. Thirdly, NMR calibration experiment protocols are explored.

SOME BACKGROUND ON THE FUNCTIONING OF NMR

Nuclear Magnetic Resonance (NMR) spectroscopy is a powerful structure determination tool used widely in analytical organic chemistry and biochemistry. In this technique, magnetic properties of atomic nuclei and electron clouds allow to unveil molecular structures. NMR spectroscopic features correlate with individual atoms which makes this a powerful technique. In the following paragraphs, some insights will be given on the working of NMR spectroscopy in the scope of peroxide analysis.

The phenomenon of nuclear magnetic resonance occurs due to the spin that certain nuclei of atoms possess [111]. Nuclei with zero spin can therefore not be observed via NMR spectroscopy. However, most elements possess at least one isotope that presents a nuclear spin. As example, one may consider C^{12} which is the most abundant form of carbon. Its nucleus does not possess any spin. It does nonetheless have a less abundant isotope (1.1 %), C^{13} which does have a spin thus enabling carbon NMR spectroscopy. The most commonly studied nucleus in NMR is H^1, which has a 99.98 % abundance and therefore allows goods sensitivity.

When nuclei with a spin are subjected to a strong magnetic field, their axis of rotation will enter a precession motion around the field as exemplified in Figure 4.12. This motion occurs at a frequency which is proportional to the applied field. This frequency is called the Larmor frequency. The amount of energy absorbed by the nucleus will influence the angle of precession [112]. After the excitation of the nucleus, a relaxation will take place. The latter is usually characterized by the time it takes for the nuclei to return to their lower energy states.

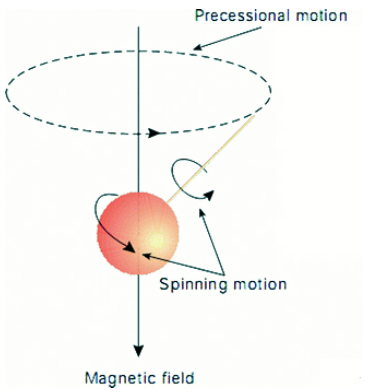

Figure 4.12: Sketch of a spinning nucleus precess in an external field [113]

NMR INSTRUMENTATION

This subsection explores data acquisition and its interpretation. First, the main components of an NMR instrument are presented. Secondly, data acquisition and important features of the instrument are shortly dived into.

Samples are inserted in cylindrical glass tubes. A tube is placed in the sample holder, which is inserted in a magnet. A coil of wire surrounds the sample. The frequency emitted by the sample as a response to the pulse signal is received by the coil as an emitted voltage. This induced voltage plotted against time is called the free induction decay. The Fourier transform of this plot will give the final NMR spectrum.

One of the main challenges of NMR spectroscopy is its low sensitivity, implied by the very small response of nuclei. Frequency differences below 1 Hz are fairly common. For this reason, uniformity of the field applied is of importance. To palliate this, superconducting magnets are used, as represented in Figure 4.13. An additional *shimming* is used to remove left-over inhomogeneities. Moreover, in order to reduce the effect of diffusional motion in the sample, the latter is spun during measurements.

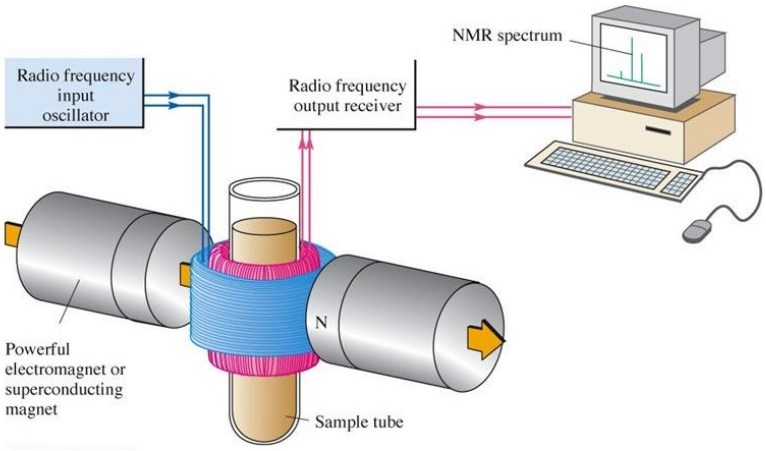

Figure 4.13: Sketch of the main components in an NMR instrument [114]

To prevent magnetic drift from affecting the spectra, a *field-frequency* lock is usually used. To do so, the resonance of a well-known specie is recorded and correction is applied if necessary. Species used for locking are usually deuterated solvents such as chloroform. The main advantage of using deuterium is that it will not appear in the H^1 spectrum.

NMR SPECTRA

As explored above, spectra are obtained via Fourier transform of the free induction decay plot. The transformed plot used for this study will solely be one-dimensional. The x-axis is a relative frequency axis and peak positions are referred to as *chemical shift*. This value is dimensionless and usually in the order of 10^{-6}, which is why the units "ppm"is often found beneath the x-axis. A reference coumpound, conventionally tetramethylsilane (TMS), is used to define the 0.0 ppm chemical shift.

Characteristic peaks at a known chemical shift will allow to identify different atoms analyzed. The nuclei considered are shielded to a certain extent by electron clouds. Different shieldings will result in different frequencies of resonance, which is how NMR spectroscopy will allow to relate to overall chemical structures.

Though the spectra obtained are one dimensional, some quantitative information can be derived from the peaks. The resonance intensity indeed scales with the number of nuclei that originated it. This implies that the area under peaks will be proportional to the quantity behind it.

LOCKING FOR PEROXIDE COMPOUNDS

The peroxide compounds that are to be differentiated are the following:

- Bicarbonate (HCO_3^-)
- Carbonate (CO_3^{2-})
- Peroxymonocarbonate (HCO_4^-)
- Peroxydicarbonate ($C_2O_6^{2-}$).

NMR might be a powerful technique to differentiate these products. The compounds are in solution, namely an aqueous bicarbonate or carbonate electrolyte. This solution contains water, which will saturate H^1 NMR spectra. Luckily, the spectra processing software allows for water suppression.

Some issues are faced regarding locking of the measurements, a notion that was explored in the previous subsection. The addition of a deuterated solvent is usually used for this purpose. However, as the peroxide products are unstable and a powerful oxidizing agent, it is desired to leave the samples taken from electrolysis untouched. Moreover, to make the data reliable, measurements should be made quickly. An additional step would therefore be cumbersome.

Benzene is an alternative to deuterium for locking. It has two characteristic peaks in the H^1 chemical shift range and in the C^{13} range. As mentioned previously, a proportionality rule relates areas beneath characteristic peaks. For the experiment, 16 capillary pyrex tubes of 2.5 mm diameter were filled with benzene (spectrophotometric grade, ≥ 99 %, Sigma Aldrich) and sealed with a bunsen burner. The obtained capillaries are shown in Figure 4.14. The concentration of benzene contained in the capillaries remaining the same, the calibration experiments aim at relating the peak areas of the peroxide compounds at different concentrations with the peak area of benzene.

Figure 4.14: Benzene-containing capillaries used for locking of the NMR spectroscopy measurements

Quantification NMR spectroscopy is prone to error and requires a lot of precision and consistence in protocols followed. Before using the capillaries, they were tested by using a maleic acid solution. Maleic acid offers a sharp peak at a chemical shift of 6.2 ppm and is often used as reference for quantitative NMR experiments.

One batch of 0.0244 M maleic acid was prepared and distributed over 15 tubes with inserted capillary. The use of one solution is important to minimize sources of error. The different capillaries were tested with maleic acid. The relative areas below the peaks for maleic acid and benzene were obtained and analyzed in the MestReNova software. Surprisingly, a large deviation was found for the different capillaries. The relative standard deviation for the experiments was 12 %. A more in-depth study of the distribution can be found in Appendix B.1. Duplicating experiments for constant capillary-tube combinations yielded a much lower relative standard deviation of 2 % (Appendix B.2). From this, it was observed that each capillary-tube combination had a characteristic signature on the signal. For the rest of the experiments, tubes and capillaries were labelled and always used in the same duos. A correction to all further measurements was made to translate results to a maleic acid reference and eliminate this effect.

CALIBRATION EXPERIMENTS

Calibration experiments were performed in order to define the proportionality between the maleic acid peak area and different components at known concentration. The components measured were hydrogen peroxide,

potassium bicarbonate, sodium bicarbonate, potassium carbonate, sodium percarbonate and peroxymonocarbonate.

Measurements were taken with a 400 MHz Agilent NMR. For the calibration experiments, hydrogen peroxide (spec & origin), potassium bicarbonate, sodium bicarbonate (99.5 %, Sigma-Aldrich), potassium carbonate (analysis grade, Merck Millipore) and sodium percarbonate (available H_2O_2 20-30 %, Sigma-Aldrich) were used. Before each measurement, the NMR instrument was tuned to prevent influence of the high salt content of the solutions. For each sample, 16 scans were taken. C^{13} measurements were run at a pulse angle of 45°. All tests were performed at room temperature. The following concentration ranges were investigated for calibration experiments:

- Hydrogen peroxide: 0.005–10 M,
- Potassium bicarbonate: 0.01–2 M,
- Sodium bicarbonate: 0.005–1 M,
- Potassium carbonate: 0.001–5 M,
- Sodium percarbonate: 0.1–0.9 M.

Peroxymonocarbonate is a compound that can be formed with water by the equilibrium reaction between bicarbonate and hydrogen peroxide as presented earlier in Equation (2.11). It cannot be obtained commercially. In order to obtain a calibration curve for the HCO_4^- ion, bicarbonate and hydrogen peroxide were mixed at known concentration. Their evolution over time was tracked via NMR spectroscopy together with the apparition of a new peak caused by the reaction towards peroxymonocarbonate.

Spectra were processed in MestReNova. A Gaussian apodization of 1 GB was used to reduce the noise. The zero filling from the free induction decay size was increased to 256144. A Bernstein polynomial fit of order 3 was used as baseline correction. The benzene peaks with chemical shift 7.16 ppm in the H^1 range and 128 ppm in the C^{13} range were used as reference and later on translated to the maleic acid reference. The auto-integration tool was used when possible.

5

RESULTS

This chapter explores results obtained from the economic model presented in Chapter 3 and from materials and methods shown in Chapter 4. First, techno-economic results are presented. Results from electrochemical experiments are then explored. Finally, results on peroxide product quantification are dived into.

5.1. TECHNO-ECONOMIC MODEL

The techno-economic model described in Section 3.2 was used to evaluate eight processes. Several processes were investigated in order to assess the added-value of the peroxide evolution reaction compared to the OER. The coupled cathodic products considered included hydrogen, carbon monoxide, ethylene and hydrogen peroxide. Hydrogen was chosen as it is one of the most vastly investigated electrolysis product. Two gaseous CO_2 reduction products were chosen. No liquid CO_2 reduction products were investigated in order to keep a comparable process design basis. Carbon monoxide was observed as one of the most promising gaseous products from CO_2 reduction in terms of viability [40]. The electrochemical production of ethylene on the other hand was computed to be on the verge of feasibility. This makes it additionally interesting to evaluate the potential of the coupled peroxide evolution reaction. The final cathodic reaction considered was the oxygen reduction to hydrogen peroxide. Recently, interest has been aroused for this reaction and first commercial implementations have emerged.

This section presents the performance targets for the processes to be viable that were obtained from the model. Firstly, results regarding maximum operating voltage are presented. Secondly, minimum operating current density targets and effect of different parameters are explored. Finally, the use of the model in a broader context is shown to assess its potential.

5.1.1. MAXIMUM OPERATING VOLTAGE (V_{MAX})

Thanks to the gross margin model, performance targets could be defined for the eight processes considered. The maximum operating voltage corresponds to the maximum voltage at which electrolysis can be run with the process still being viable. If the maximum operating potential drops below the standard potential for the reactions to occur then the process will not be feasible for the parameters used. In this subsection, the model is first validated with a known industrial process. Then, the effect of coupling an added-value anodic reaction is investigated. Finally, the feasibility of different processes is looked into.

VALIDATION OF THE MODEL

The model was first computed for the coupled OER and HER. Alkaline water electrolysis is indeed a commercial process for which the hydrogen product is sold at 4.5 \$/kg [81]. The maximum operating voltage was evaluated for a cost of electricity of 0.06 \$/kWh and a gross margin of 30%, which were considered base case parameters (Section 3.1.3). For these values, a V_{max} of 1.96 V was obtained. Commonly used electrolyzers for electrochemical hydrogen production operate at 1.6 V, which is below the value predicted by the gross margin model [55]. The model therefore seems to provide a realistic upper value for the maximum operating potential of a cell.

It is interesting to note that a hydrogen price of 4.5 \$/kg is the price for H_2 produced by water electrolysis. Other methods, such as coal gasification or natural gas reforming, produce hydrogen for 1 \$/kg [81]. Evalu-

ation of the maximum operating voltage via the gross margin model shows that the electrochemical process for the HER coupled to the OER is not viable anymore for such a low product price. Figure 5.1 shows the calculated maximum operating voltages for both the OER and two-electron WOR at different gross margins and costs of electricity. For an average price of electricity of 0.06 \$/kg, even the worst gross margin case of 15 % did not allow to surpass the standard cell potential threshold of 1.23 V. On the other hand, coupling of the HER to the hydrogen peroxide evolution reaction did allow to surpass the 1.8 V standard cell potential for all gross margin and electricity cases considered. The unfeasibility of the HER/OER process at such a low price reflects that the current electrochemical price of hydrogen is not competitive with other production processes due to technical limitations. The much higher potentials obtained for the H_2O_2 evolution reaction unveil the prospectives for this added-value anodic reaction to make electrochemical processes viable. One should however remain careful when interpreting a maximum operating voltage superior to the standard cell potential. The definition of V_{max} does not explicitly account for raw materials and utilities, which might have a deleterious impact on the process economics (Equation (3.15)). The benchmark obtained for V_{max} may be used to quickly eliminate unfeasible processes, but more extensive feasibility analyses should be performed on processes satisfying the V_{max} criterion.

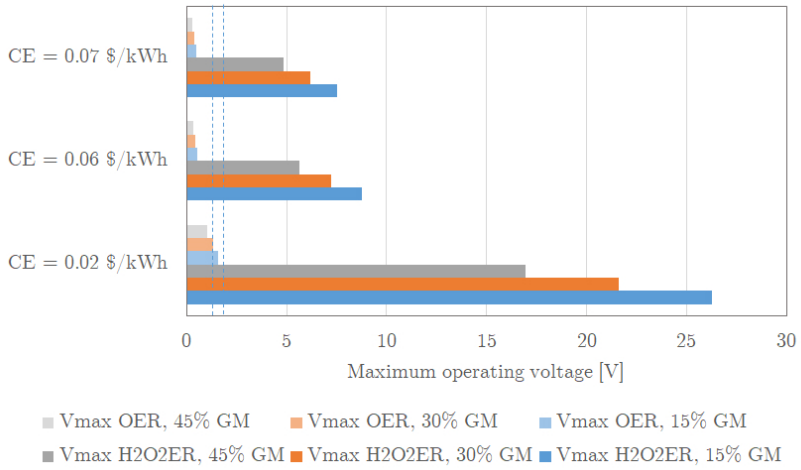

Figure 5.1: Maximum operating voltage for the HER combined to the OER and the hydrogen peroxide evolution reaction as computed by the gross margin model for gross margins of 15, 30 and 45% at different electricity costs (CE, \$/kWh) and for a product price of 1 \$/kg. For the other parameters, base case values presented in Section 3.1.3 were used. The blue dotted lines show the standard cell potentials for the HER coupled to the OER (1.23 V vs RHE) and coupled to the two-electron WOR (1.8 V vs RHE).

OER *vs* TWO-ELECTRON WOR

For all processes considered, the coupling to the added-value two-electron WOR yielded higher maximum operating voltages for the four cathodic reactions considered. In fact, all maximum operating voltages obtained for the worst case gross margin of the hydrogen peroxide evolution reaction exceeded the maximum operating voltages computed for the best case gross margin of the OER. A more detailed overview of all computed maximum operating voltages can be found in Appendix E. This implies that even though the oxygen evolution reaction has more favourable thermodynamics, the addition of a valuable anodic product enables to boost the economical performance for the process. This is extremely promising as fields such as carbon dioxide reduction or electrochemical ammonia production are meeting severe economical constraints. The coupling to an added-value anodic product may allow these processes to compete on the market thus enabling faster penetration of green energy in the chemical sector.

FEASIBILITY OF THE PROCESSES

The maximum operating voltage is a good first step in the economic feasibility evaluation of a process. From the eight processes considered and for worst, base and best case scenarii of gross margin and electricity costs, only one case yielded an unfeasible process. The rest parameters were set at base case values as defined in Section 3.1.3. The only unfeasible process computed was the ethylene evolution coupled to the OER at a gross margin of 45 % and a cost of electricity of 0.07 \$/kWh. Figure 5.1 shows the calculated maximum operating voltages for the reaction towards ethylene coupled to both the OER and two-electron WOR at different gross

margins and costs of electricity. Maximum operating voltage values obtained for the OER were very close to the standard cell potential, leaving little room for other losses in the electrochemical cell design. Processes are usually operated at an overpotential of *ca* 0.4 V. This is due to the fact that catalysts will often not present the ideal binding energy for all intermediates. Moreover, other losses may occur due to cell design. The gross margin model does indeed not take energetic efficiency into account. For the coupled OER/C_2H_4 processes and at base case values for gros margin (30 %) and electricity cost (0.06 \$/kWh), values obtained for V_{max} are were very close to the 1.17 V standard cell potential threshold. This leaves little room for losses and will most likely make the CO_2 reduction towards ethylene unfeasible if coupled to the OER. Similar results were already presented by different research groups [40]. The results obtained in this study for the coupled hydrogen peroxide evolution reaction seem promising to make the electrochemical ethylene production feasible.

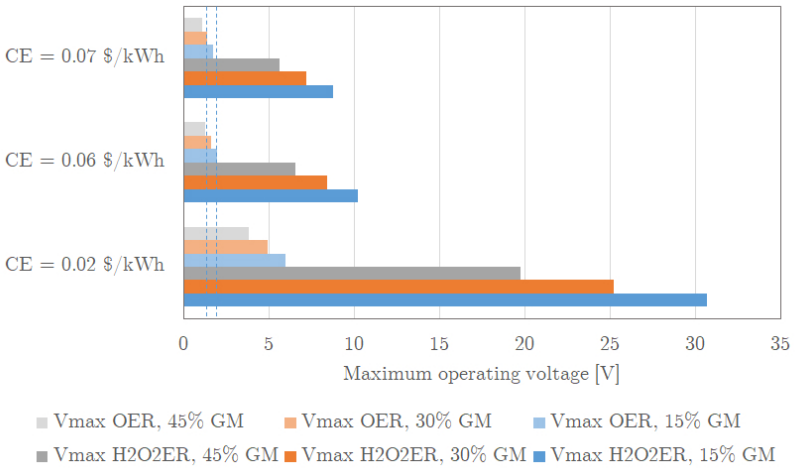

Figure 5.2: Maximum operating voltage for the CO_2 reduction to ethylene combined to the OER and the hydrogen peroxide evolution reaction as computed by the gross margin model for gross margins of 15, 30 and 45% at different electricity costs (CE, \$/kWh). For the other parameters, base case values presented in Section 3.1.3 were used. The blue dotted lines show the standard cell potentials for the CO_2 reduction to ethylene coupled to the OER (1.17 V) and coupled to the two-electron WOR (1.74 V).

5.1.2. MINIMUM OPERATING CURRENT DENSITY

Minimum current density targets could be defined for the eight processes considered using the gross margin model. The minimum operating current density for the process corresponds to the minimum current density for which electrolysis can be ran while keeping the process viable. A minimum operating current density were obtained from Equation (3.16) for the eight processes considered. These processes comprise the OER and the two-electron WOR respectively combined to the HER, two-electron ORR and CO_2 reduction to CO and to C_2H_4. This subsection first present results obtained for base case parameters as defined in Section 3.1.3. The effects of faradaic efficiency, catalyst lifetime and single pass conversion on minimum operating current density are then explored.

IDENTIFYING SUITABLE OPERATING CURRENT DENSITY

The eight processes were evaluated using base case parameters. This enabled to compute a minimum operating current densities for each of the processes considered. Section 5.1.2 provides an overview of current densities in [mA/cm^2] according to the process considered and value taken for the gross margin.

It is of importance to first evaluate the validity of the model. The minimum operating current density computed for the coupled OER and HER amounted 1162 mA/cm^2 at a gross margin of 30 %. This falls within the range of state-of-the-art alkaline water electrolyzers which operate around 1 A/cm^2 [55]. The minimum operating current density for this process to break even over 20 years (which corresponds to a gross margin of 0 %) was 348 mA/cm^2. This value is lower than the one obtained from a previous gross margin model by Verma et al., who calculated a j_{min} of 465 mA/cm^2 [55]. This difference is mainly induced by the fact that the authors based their economic evaluation of the model on the costs for a PEM electrolyzer. Even though they corrected for the addition of electrolyte flow channels to approximate the cost of an alkaline water electrolyzer, other parameters significantly differ for the two electrolyzer types. This includes the number of

stacks and cells involved as well as the electrode area per cell [81]. The major differences in electrolyzer costs and electrode area accounted for the difference in modeled current densities.

Some blanks can be observed in Section 5.1.2. These represent the processes for which no minimum current density could be evaluated due to voltage requirements. Some maximum operating voltage requirements computed by the model were very close to the standard potential of the reactions in question. Operating voltages for the computation of j_{min} were taken from literature or approximated as the standard cell potential together with an overpotential. If the standard potential was too close to the maximum operating voltage requirement, then the process was unfeasible as the operating voltage would exceed the maximum operating voltage for the process to be viable. This was the case for the ethylene production coupled to the OER at gross margins of 15, 30 and 40 %. It was also the case for the coupled OER/HER at a gross margin of 45 %. Ethylene was shown as an unfeasible process if coupled to the OER. However, once coupled to the added-value hydrogen peroxide evolution reaction, it allowed reaching feasibility at fairly low current densities (in the range of 200 to 400 mA/cm^2).

The hydrogen peroxide evolution coupled to different cathodic reactions was showed to have a positive impact on process economics and reduce the technical requirements compared to the OER. Xia et al. (2020) have recently published ground breaking results for the coupled and two-electron WOR. In their study ,they achieved a current density of 75 mA/cm^2 at an anodic faradaic efficiency of 66 % and an overpotential of 0.57 V [45]. Using the parameters reported in their study and a gross margin of 30 %, a minimum current density target of 231 mA/cm^2 was computed by the gross margin model. The difference between the experimental results and the targets set from the gross margin model shows that some progress is still to be made before making the process commercially interesting. Some limitations of the implemented should here be kept in mind. The cost of the electrolyzer was fixed to a constant value based on its size at base case power. The processes were defined based on an anodic production rate of 100 ton/day. Changing the anodic faradaic efficiency for the peroxide evolution reaction therefore does not impact any of the results in the model. The by-product is indeed oxygen which is simply vented out. This is one of the limitations of the model. Further research on the effect of faradaic efficiency on the electrolyzer size and cost should be done and implemented in the model.

Table 5.1: Minimum operating current density [mA/cm^2] for eight processes as computed from the gross margin model at base case parameters defined in Section 3.1.3 for gross margins of 0 (break even), 15, 30 and 40 %.

Process	Gross margin = 0 %	Gross margin = 15 %	Gross margin = 30 %	Gross margin = 45 %
OER/ORR	173	206	256	338
OER/H_2	348	535	1162	-
OER/CO	209	297	513	1900
OER/C_2H_4	-	-	-	-
H_2O_2ER/ORR	156	186	230	303
H_2O_2ER/H_2	168	210	279	416
H_2O_2ER/CO	142	174	224	315
H_2O_2ER/C_2H_4	162	199	258	369

EFFECT OF FARADAIC EFFICIENCY

The effect of cathodic faradaic efficiency variations on the minimum operating current density were observed. Other parameters were kept constant at their base case value (Section 3.1.3). A grosss margin of 30 % was considered. Figure 5.3 presents the minimum operating current density target as a function of cathodic faradaic efficiency for the coupled OER and CO_2 reduction to CO. The competitive reaction considered here was the HER. The computed values seem to follow an inverse quadratic or exponential trend with faradaic efficiency. Computed current density targets for the processes to be viable are above 3000 mA/cm^2 at a cathodic faradaic efficency of 30 %. At low faradaic efficiencies, the change in minimum current density requirement is very steep. After a given faradaic efficiency threshold, minimum operating current density targets reach a plateau. Between 30 and 75 % faradaic efficiency, values for current density decrease from 3138 to 575 mA/cm^2. Above this, minimum operating current density is comprised between 575 and 434 mA/cm^2. This shows that experimental work should focus on exceeding a threshold in faradaic efficiency for the process to be viable. After this, further improvements will only have a minor impact on the process economics.

It may be interesting to look at the minimum current density evolution trend as a function of cathodic faradaic efficiency for different reaction. Tools such as Matlab can be used to fit the data with trendlines.

Perhaps some common trends can be identified and modeled.

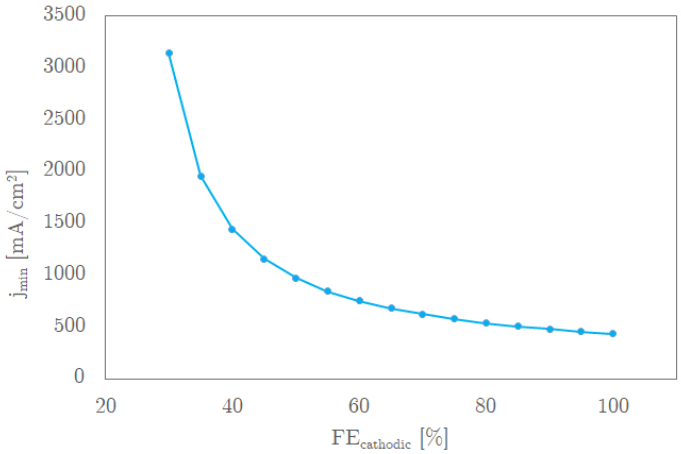

Figure 5.3: Minimum operating current density computed by the gross margin model for the coupled OER/CO evolution as a function of cathodic faradaic efficiency. Apart from faradaic efficiency variations, a gross margin of 30 % and parameters defined in Section 3.1.3 were used for the computation.

EFFECT OF CATALYST LIFETIME

Catalyst lifetime was taken into account in the model by adding the overall capital costs for new catalysts over a plant lifetime of 20 years. The effect of catalyst lifetime on the computed minimum operating current density was monitored. Other parameters were set to base case values. The lower limit for catalyst lifetime was taken as 210 h, which is the catalyst lifetime for which the environmental impact of electrode fabrication becomes negligible for CO_2 reduction processes [115].

Figure 5.4 present the evolution of the computed minimum operating current density for the two-electron WOR coupled to four different cathodic reactions. The minimum operating current density can be seen to significantly increase at low catalysts lifetimes. This is especially the case for the hydrogen evolution reaction as platinum was the most expensive of the catalysts considered. After a lifetime of 2000 h, the minimum operating current density starts to reach a plateau for all processes between 310 and 224 mA/cm^2. Lab-scale experiments usually report stability in the order of tens of hours [30, 55] thus important steps in catalyst stability are to be achieved in order to improve economic performance. It is important to note that the model does not account for down-time due to catalyst replacement. These losses together with operational costs for the replacement may have an impact on the results provided above. The results presented here only aim at providing a first rough estimate for the processes. It should be kept in mind that values presented underestimate the actual impact of catalyst lifetime.

EFFECT OF SINGLE PASS CONVERSION

The single pass conversion corresponds to the amount of reactants consumed divided by the amount of reactant entering the electrolyzer. Single pass conversion was accounted for only in reactions including gas streams. Other reactions, such as the OER, two-electron WOR and HER have reactants already present in excess due to other process requirements. The OER/C_2H_4 process was not considered as it was previously determined as unfeasible for the base case parameters. For the ORR, pure oxygen entered and left the system thus a recycle was put in place. No down-streams units were handling the gas streams thus it was not considered in this analysis.

Figure 5.5 presents the minimum operating current density for the reactions considered at different single pass conversions. The effect on current density is significantly lower than for the previously explored parameters such as faradaic efficiency and catalyst lifetime. The largest difference in minimum operating current density amounted 100 mA/cm^2 and was observed between 30 and 100 % single pass conversion for the combined OER and CO production. For the coupled two-electron WOR and CO production it amounted to 9 mA/cm^2 and for the C_2H_4 production 6 mA/cm^2. A significant difference is seen on the effect of single pass conversion for CO production coupled to the OER and to the two-electron WOR. In the case of the coupled OER, the only revenue comes from the cathodic production. The cost of separation, which increases

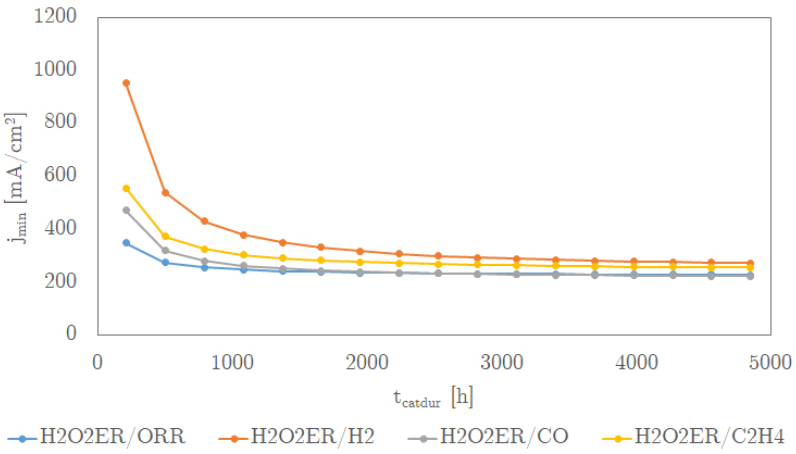

Figure 5.4: Minimum operating current density computed by the gross margin model for the coupled hydrogen peroxide evolution reaction and the HER, CO_2 reduction to CO and C_2H_4 and the two-electron ORR as a function of catalyst lifetime (t_{catdur} in [h]). Apart from catalyst lifetime variations, parameters defined in Section 3.1.3 were used for the computation.

for lower single pass conversion, therefore affect the economics more than if coupled to the anodic peroxide evolution. In the case of peroxide, the additional revenue from the anodic product act diminishes the effect of cathodic separation costs on the overall economics. From Figure 5.5, single pass efficiency does not seem to have a major impact on the process performance for the process to be viable. The changes in minimum operating current density are indeed minimal over the range of conversions considered. It should be noted that the only variations in costs taken into account for larger gas streams regarded the downstream separation units. As mentioned previously, the model should be improved by adding the effect of electrolyzer sizing on the costs.

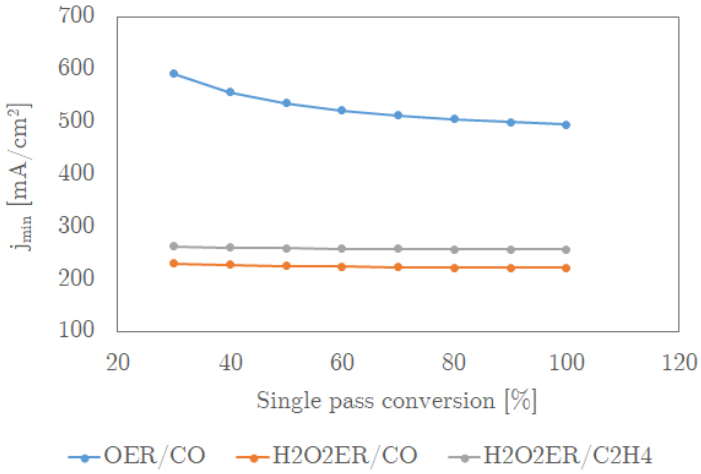

Figure 5.5: Minimum operating current density computed by the gross margin model for the OER and the hydrogen peroxide evolution reaction coupled to CO_2 reduction products as a function of single pass conversion. Apart from single pass conversion variations, parameters defined in Section 3.1.3 were used for the computation.

5.1.3. COUPLING TO RENEWABLE ENERGY SOURCES

The coupling to different renewable energy sources was investigated. Photovoltaic (PV) systems have gone through important technical advances in recent years which have pushed the solar energy prices down. A recent energy auction in Portugal has reached the historic solar energy price of 0.016 $/kWh [116]. However, the amount of full load hours per year is only of 1500 h [117]. Off-shore wind energy is on the other side rather

costly (0.07 $/kWh in the Netherlands) [118]. The amount of full load hour is nonetheless higher than for PV energy with 3800 h per year. The trade-off between energy price and operating hours was evaluated using the gross margin model. For comparison, the case for grid electricity was implemented with an electricity cost of 0.06 $/kWh and 8000 operating hours for the electrolysis plant.

Figure 5.6 represents the calculated minimum operating current densities for the eight processes considered powered by different energy sources. Operating hours were set to 1500, 3800 and 8000 for PV generated energy, off-shore wind energy and grid energy respectively. The cost of electricity was taken as 0.02, 0.07 and 0.06 $/kWh for these three respective energy sources. As expected, the case of off-shore wind energy results in the least favorable minimum operating current densities in all cases. The case of the OER coupled to the CO_2 reduction to C_2H_4 is not feasible if powered by off-shore wind. Off-shore wind is the most costly from the three sources considered. It has lower operation time than grid electricity, which makes it less advantageous. Progress needs to be made to drive its costs down and make it a competitive source. PV generated energy on the other hand is competitive with the grid powered base case. Even though the amount of operating hours is significantly reduced, the cost difference allows it to be competitive. Minimum operating current densities are still higher for the PV case than for grid electricity for the coupled OER and HER and OER and CO production. The OER coupled to ethylene production is not feasible due to the maximum operating voltage criterion. This shows the added-value of anodic hydrogen peroxide production as it allows to generate more revenue on the same period of time thus decreasing the minimum current density requirement.

The presented results were used to draw a quick sketch of possibilities for the coupling of electrolysis with renewable sources. It is important to note that intermittent availability of energy has consequences for the electrolysis and separation equipment. The separation processes can not easily be started up and shut down. Electrolysis will need to be coupled to a buffer storage on the short term to allow continuous operation. The main advantage of electrolysis over batteries will be the conversion of energy for long term storage. This could be for example on the seasonal scale, something that cannot be achieved by using current technologies. Another major advantage would be replacing traditional CO_2 intensive manufacturing techniques for the production of valuable chemicals.

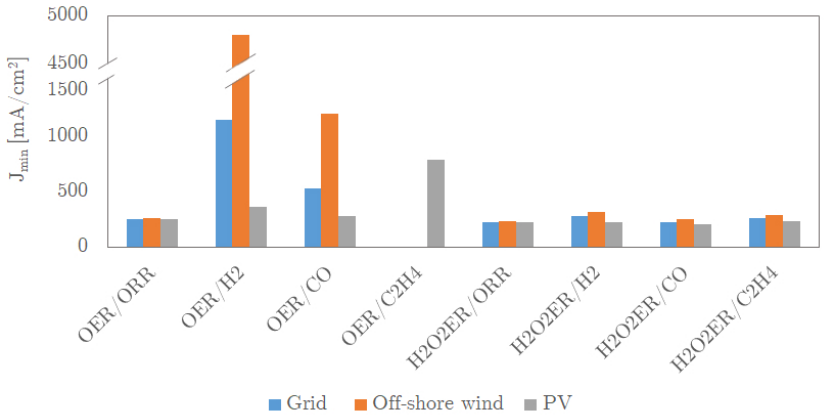

Figure 5.6: Minimum operating current density computed by the gross margin model for the OER and the hydrogen peroxide evolution reaction coupled to the two-electron ORR, CO_2 reduction products and the HER for different energy sources. Base case parameters defined in Section 3.1.3 were used for the computation.

Cathodic product prices were calculated for the different energy sources based on base case parameters determined in Section 3.1.3 and for a current density of 300 mA/cm^2. The prices were computed by rearranging Equation (C.5). Table 5.2 presents an overview of the computed prices for cathodic products obtained from different energy sources. This shows the potential of the gross margin model to link electrochemical performance and economics. Take for example the case of ethylene. Different results presented in previous sections showed that the coupled OER and ethylene production are not viable. This has been also supported by literature [40]. Thanks to the gross margin model, a needed price to reach 30 % gross margin for the product can be computed. This corresponds to 3.87 $/kg for the grid electricity case. Looking at the hydrogen case, for which the current electrochemically generated product costs 4.5 $/kg instead of the 1 $/kg market price, allows to put this results in perspective. This table also highlights the advantage of coupling an added-value reaction at the anode. All product prices have been decreased compared to OER case due to the increased

process value produced. The cost for the two-electron WOR coupled to ethylene production and driven by solar energy results in a negative product price. This implies that revenues from the anodic product and cathodic by-products were higher than the production and separation costs. The separation costs were lower than for CO production as the flow rate was less than half of it for the CO reaction. This also results in less energy requirement for compression.

Table 5.2: Cathodic product price C_P [$/kg] for eight processes as computed from the gross margin model at base case parameters defined in Section 3.1.3 for solar energy (1500 operating hours, 0.02 $/kWh), grid energy (8000 operating hours, 0.06 $/kWh) and off-shore wind energy (3800 operating hours, 0.07 $/kWh). Current market prices as presented in Section 3.1.3 are provided as reference.

Process	C_P solar [$/kg]	C_P grid [$/kg]	C_P off-shore wind [$/kg]	Current market price [$/kg]
OER/ORR	0.43	0.44	0.46	0.5
OER/H_2	5.44	7.40	8.31	4.5
OER/CO	0.56	0.68	0.79	0.6
OER/C_2H_4	3.00	3.87	4.51	1.2
H_2O_2ER/ORR	0.31	0.33	0.35	0.5
H_2O_2ER/H_2	0.04	2.23	3.52	4.5
H_2O_2ER/CO	0.07	0.22	0.36	0.6
H_2O_2ER/C_2H_4	-0.32	0.70	1.57	1.2

5.2. ELECTROCHEMISTRY

This section provides an overview of electrochemistry related work and results obtained. The goal of the electrochemical experiments was to assess the parameters of importance to achieve industrially relevant performances for the anodic peroxide evolution and evaluate the mechanisms behind the peroxide formation. Tin oxide-based materials were first investigated as they present a broad stability window in the Pourbaix diagram. From previous results in literature, the main challenge for these materials concerned reaching high current densities while maintaining high selectivity towards hydrogen peroxide. Carbon-based materials were then explored as they presented groundbreaking performances. The initial goal was to identify a material allowing operation at industrially relevant conditions and to use it for subsequent detailed electrochemical studies. These would have included systematic pH, electrolyte and electrolytic concentration variations. However, due to restrained time for lab experiments, these systematic studies could not be performed. In this section, production and characterization of tin oxide materials are first explored. Secondly, the working of the cell without and with membrane was assessed. Thirdly, electrochemical tests with tin oxide-based electrodes are presented, followed by electrochemical tests with carbon-based materials.

5.2.1. ANODE SYNTHESIS

As described in Section 4.1, different types of electrodes were synthesized for anodic use in electrolysis cells. This subsection present the materials produced and their main features. Firstly, sputtered tin oxide thin films are presented. Secondly, sputtered Indium Tin oxide (ITO) thin films are explored. Tin (IV) oxide films deposited via spray pyrolysis are then considered.

TIN OXIDE SPUTTERED THIN FILMS

Experimental work on tin oxide thin film synthesis via reactive DC magnetron sputtering was divided into two parts. Firstly, adequate sputtering conditions to obtain the right stoichiometric of tin (IV) oxide were investigated. Secondly, once the right parameters were determined, effect of temperature variation on tin (IV) oxide thin film synthesis was explored. Influence of thin film thickness was finally considered.

Material identification

Tin oxide materials were first produced via reactive DC sputtering. The properties and stoichiometry of the films produced are known to be strongly influenced by the sputtering conditions [96]. Conditions obtained in the vacuum chamber may vary depending on the type of equipment used. A range of deposition parameters were tested in order to obtain crystalline SnO_2. Deposition parameters including temperature, pressure and oxygen partial pressure were varied. The crystalline planes of the deposited samples obtained were characterized via XRD measurements. Their morphology was observed via SEM imaging.

Different samples were deposited. The pressure was first set at 5 µbar and the argon to oxygen volume ratio to 15:5. For this set, depositions were performed at room temperature (Figure 5.7a), at room temperature followed by post annealing at 500 °C (Figure 5.7b) and at high temperature (450 °C, Figure 5.7c). Another high temperature deposition (450 °C) was done with this time a volume ratio of 5:15 Ar:O_2 (Figure 5.7d). All samples seemed homogeneously distributed onto the titanium substrate, apart for the post annealed sample for which some irregularities could be observed. Colors varied from light blue and yellow (Figure 5.7a), dark blue (Figure 5.7b), blue and yellow (Figure 5.7c) to brown (Figure 5.7d).

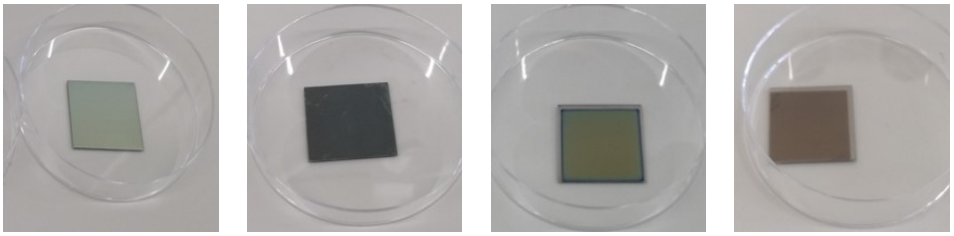

(a) Room temperature deposition

(b) Room temperature deposition followed by post annealing at 500 °C

(c) High temperature deposition at 450 °C

(d) High temperature deposition at 450 °C, 5:15 Ar:O_2

Figure 5.7: Pictures of thin films deposited onto titanium substrates via reactive DC magnetron sputtering to investigate parameters for tin (IV) oxide deposition. Deposition were done at 5 µbar, (a, b, c) 15:5 Ar:O_2 ratio and (d) 5:15 Ar:O_2 ratio with different temperature treatments.

XRD measurements were first used to determine the thin films' crystallinity and crystalline orientations. The measurements were first done for samples deposited on titanium. The observed signal only reflected characteristic peaks for the substrate. For this reason, samples were deposited onto glass substrates. Figure 5.8 shows XRD spectra for reactive deposition of Sn under 15 sccm Ar and 5 sccm O_2 at (a) room temperature, (b) room temperature with post annealing at 500 °C and (c) high temperature (500 °C). Figure 5.8d shows the spectrum for deposition under 5 sccm Ar and 15 sccm O_2. The detailed parameters used for the sputtering can be found in Section 4.1.2. All 2Θ data obtained from literature was translated to a Co source standard using Bragg's law Appendix A.

The room temperature deposition (Figure 5.8a) resulted in an amorphous sample. The spectrum is presented without background subtraction. An XRD measurement for a plain glass sample showed that the trend observed is due to the substrate and not to the sample. The absence of peaks shows the absence of crystalline material.

The post annealed sample shown in Figure 5.8b presented several peaks of tin oxide crystalline material. Peaks were matched with components using the DIFFRAC.SUITE EVA Bruker library. Three characteristic peaks could be attributed to triclinic Sn_3O_4 material: 2Θ = 12.57, 31.45 and 38.38 ° corresponding to crystalline planes (0 0 1), (1 1 1) and (0 0 3) respectively [119]. The strongest line was the one for the (0 0 3) plane. Four peaks were matched to tin (IV) oxide cassiterite peaks at 2Θ = 30.50, 39.14,44.74 and 60.71 corresponding to the (1 1 0), (1 0 1), (2 0 0) and (2 1 1) planes respectively. It seems that the crystalline structure obtained is a mix between Sn_3O_4 and SnO_2.

The sample deposited at high temperature under 15 sccm argon and 5 sccm oxygen showed very sharp peaks (Figure 5.8c). Five of the eight visible peaks were attributed to a romarchite structure of tin (II) oxide [120].

The fourth sample was also deposited at high temperature but this time under 5 sccm Ar and 15 sccm O_2 (Figure 5.8d). Different peaks could be attributed to Sn.

Is should be noted that matching of peaks via the Bruker software may lead to erroneous results if not used wisely. The immense amount of existing and reported crystalline material sometimes makes the identification of materials tricky. The software allow for inclusion of a selected amount of atoms to be comprised in the peak matching process. This implies that potential impurities cannot be taken into account in the system and will not be taken into consideration. This matching tool should therefore be used carefully. It is highly useful to assess the presence of a given compound. The limitations of the tools should however always be kept in mind.

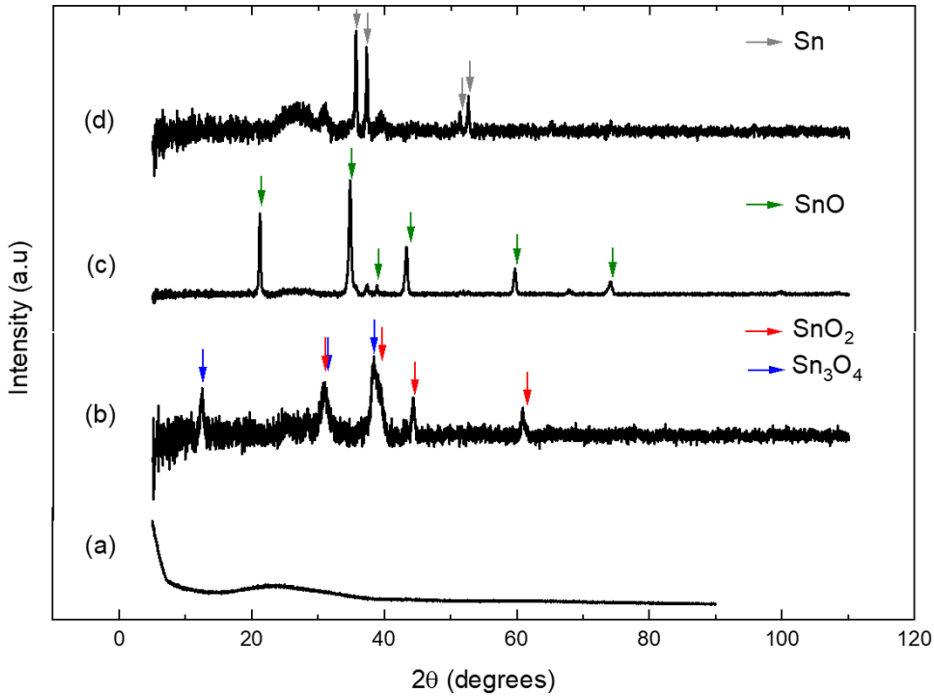

Figure 5.8: XRD spectra for samples deposited under 15 sccm Ar and 5 sccm O_2 at (a) room temperature, (b) room temperature with post annealing at 500 °C, (c) high temperature (450 °C) and (d) under 5 sccm Ar and 15 sccm O_2 via reactive DC sputtering of Sn. XRD spectra were taken with a Co source (λ = 1.789 Å) using an increment of 0.02 ° and a scan speed of 10 s/step.

From the previous results, it seemed that a decrease in the oxygen fraction would yield a stoichiometry closer to SnO_2. Four test samples were sputtered at 5 µbar for 7 min 14 s. For the first three samples, the power was set to 25 W. Gas flows of different gases was varied in order to alter Ar/ O_2 ratios. The gas flow rates used were 19 to 1 sccm Ar and O_2, 18 to 2, 17 to 3. A fourth sample was sputtered at the same conditions but with a lower power, namely 20 W, to observe the effect of this parameter. None of the synthesized samples showed a clear SnO_2 structure. Some peaks characteristic of the (1 0 1) romarchite crystal plane were identified around $2\Theta = 35°$ found in both samples sputtered under 17 sccm Ar and 3 sccm O_2 [120]. The peaks which overlap characteristic romarchite peaks are indicated by green arrows in Figure 5.9. Other peaks characteristic of cassiterite were identified around 40° for the samples deposited at 19 sccm Ar and 1 sccm O_2 (25 W), 18 sccm Ar and 2 sccm O_2 (25 W) and 17 sccm Ar and 3 sccm O_2 (20 W). The lack of additional characteristic peaks for both SnO and SnO_2 makes is tricky to draw conclusions on the exact structure of the crystal phases synthesized. The evidence was in no case strong enough to assess the presence of either tin (II) or (IV) oxide. Moreover, it should be noted that a multitude of compounds may have one characteristic peak around the 2Θ values considered. This implies that the presence of the crystal can only be deduced by a complete spectrum of characteristic peaks.

A study on the gas composition during sputtering and stoichiometry of obtained tin oxide thin films was presented by Snyders et al. [96]. The authors of this research explored how oxygen partial pressures relates to the obtaining of SnO_2 from reactive DC magnetron sputtering. It appeared that the stoichiometry was dependent on oxygen partial pressure only and not of overall pressure. Tin (IV) oxide could be synthesized for an oxygen partial pressure of 5 mTorr and for overall pressures between 5 and 20 mTorr. Rates of deposition were observed with a crystal monitor in the vacuum chamber of the sputtering set-up for overall pressures of 6.7 and 13.3 µbar. At a flow rate of 9 sccm argon and 11 sccm oxygen, which corresponds to an oxygen partial pressure of 7.3 µbar, a deposition rate of 0.2 Å/s was found. This was used as basis for the deposition time required for samples of 100 nm. The deposition of the correct stoichiometry was confirmed via XRD measurements (Figure 5.10). Characteristic peaks for the cassiterite crystal structure were observed at 2θ = 30.5, 39.1, 44.7 and 60.7°. These respectively originate from the (1 1 0), (1 0 1), (2 0 0) and (2 1 1) crystal planes [120].

The successfully synthesized tin (IV) oxide sample was observed via SEM in order to assess its surface

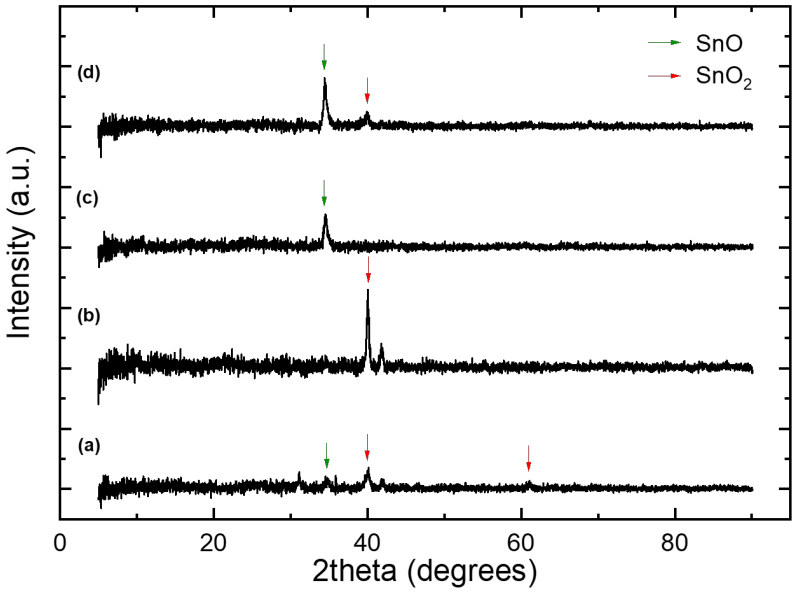

Figure 5.9: XRD spectra for samples deposited under (a) 19 sccm Ar and 1 sccm Ar at 25 W, (b) 18 sccm Ar and 2 sccm Ar at 25 W, (c) 17 sccm Ar and 3 sccm Ar at 25 W and (d) 17 sccm Ar and 3 sccm Ar at 20 W via reactive DC sputtering of Sn. Chamber pressure was kept at 5 µbar during the 7 min 14 s long deposition. Green arrows show peaks characteristic for romarchite and red arrows show peaks characteristic for cassiterite. XRD spectra were taken with a Co source (λ = 1.789 Å) using an increment of 0.02 ° and a scan speed of 1 s/step.

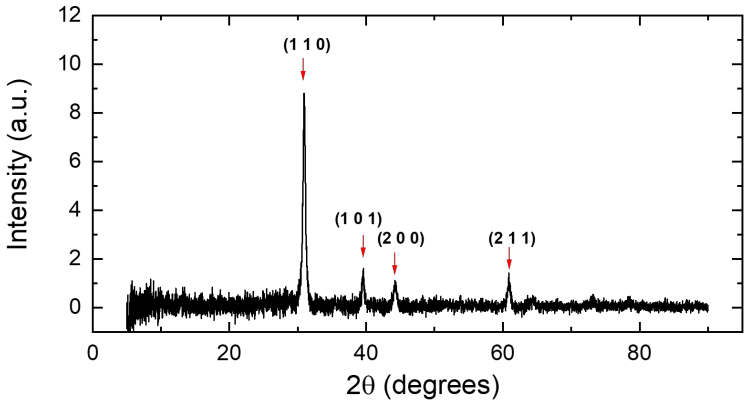

Figure 5.10: XRD spectrum for deposition of a tin (IV) oxide film under 9 sccm Ar and 11 sccm Ar at 500 °C via reactive DC sputtering deposition of Sn. The spectrum was taken with a Co source (λ = 1.789 Å) using an increment of 0.02 ° and a scan speed of 1 s/step.

morphology. On the images obtained (Figure 5.11), the deposition can be seen to be homogeneously distributed over the substrate. The surface of the material is mainly characterized by the roughness of the titanium substrate. Small irregularities of the deposition can be distinguished. One should be careful when considering SEM images. As mentioned in Section 4.1.6, the electrons detected for the imaging will be reflected from different depths of the sample. The titanium substrate seems to have a significant contribution to the morphology observed on Figure 5.11. this could be the result of electrons penetrating the substrate and contributing to the analyzed signal.

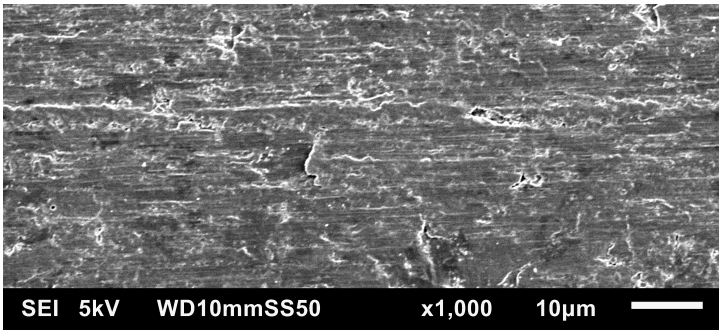

Figure 5.11: SEM image of a SnO_2 thin film deposited via reactive DC magnetron sputtering at 500 °C onto a titanium substrate. SEM measurements were taken by SEI under magnification 1000 using a voltage of 5 kV, a spot size of 50 and a working distance of 10 mm.

Effect of temperature variation

A study was done on the characteristic peaks observed depending on the temperature treatment applied. Depositions were performed under three different conditions: room temperature (Figure 5.13a), room temperature followed by annealing treatment at 500 °C (Figure 5.13b) and under high temperature (500°, Figure 5.13c). New crystal planes were developed due to heat treatment. Sputtering at high temperature seems to yield more crystalline material than when annealing the sample after the deposition. The (1 1 0) crystal plane seems especially dominant by high temperature deposition. A new peak around 2Θ = 45° appeared for the latter sample.

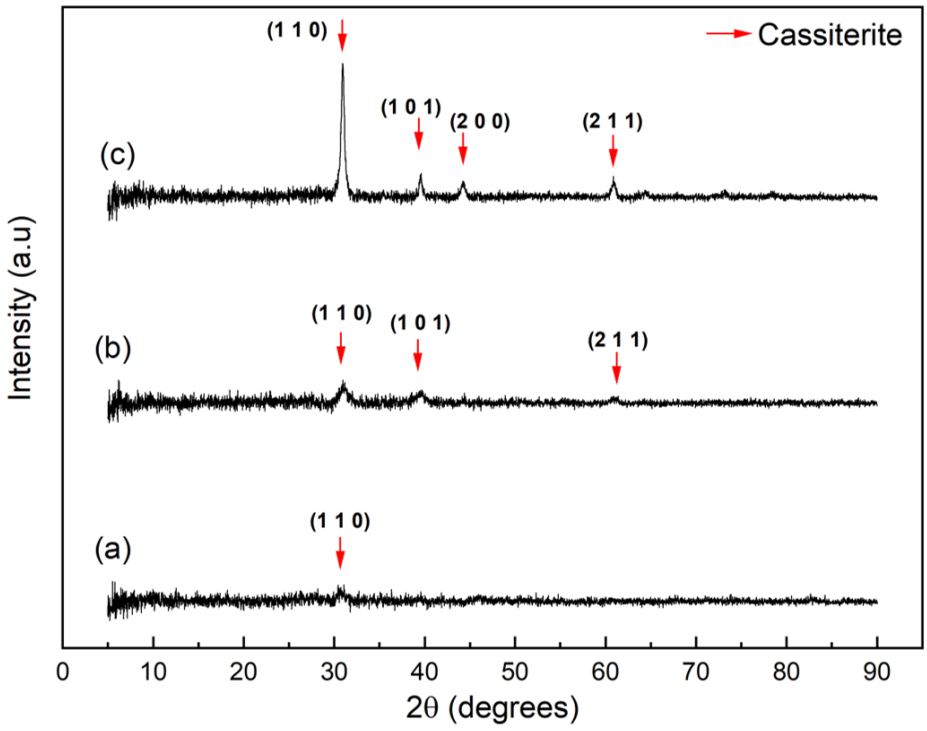

Figure 5.12: XRD spectra for deposition of a tin (IV) oxide film under 9 sccm Ar and 11 sccm Ar for (a) room temperature, (b) room temperature with post annealing at 500 °C, (c) high temperature (500 °C) via reactive DC sputtering deposition of Sn. The spectrum was taken with a Co source (λ = 1.789 Å) using an increment of 0.02 ° and a scan speed of 1 s/step.

Effect of thickness variation

The favored crystalline phases were tracked for different deposited thin film thicknesses. Samples of *ca* 100, 200 and 300 nm were deposited. All spectra showed cassiterite characteristic peaks. The thicker the samples, the sharper the peaks observed. This showed that some crystal planes were dominant in the case of thicker sample. Relative intensities of seemed to scale between the 100 and 200 nm samples. Peaks around 2θ = 30.5,

39.1, 44.7 and 60.7° representative respectively for the (1 1 0), (1 0 1), (2 0 0) and (2 1 1) crystal orientations were identified. The ratio between the (1 1 0) and (1 0 1) peak intensities shifted towards (1 0 1) for the thicker sample. It can be concluded that thickness of the sample will influence the crystal orientation.

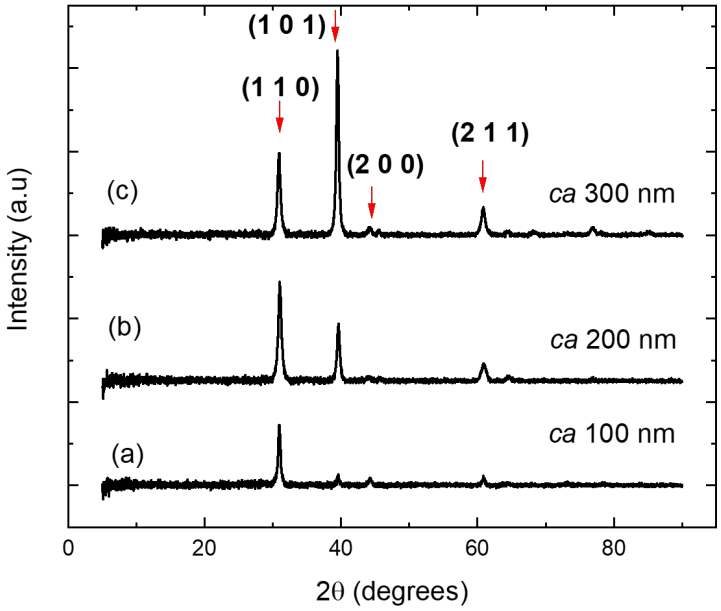

Figure 5.13: XRD spectra for deposition of a tin (IV) oxide film under 9 sccm Ar and 11 sccm Ar at 500 °C via reactive DC sputtering deposition of Sn for (a) 1 hour 23 min 20 s (*ca* 100 nm), (b) 2 hours 46 min 40 s (*ca* 200 nm) and (c) 4 hours 10 min (*ca* 300 nm). The spectrum was taken with a Co source (λ = 1.789 Å) using an increment of 0.02 ° and a scan speed of 1 s/step.

It is important to note that all XRD measurements were done on glass substrates. A difference of crystalline phases present may be induced by the substrate used. For this reason, care should be taken when drawing conclusions on performance of thin films on titanium substrates. The crystallinity may differ from what was observed during measurements.

ITO SPUTTERED THIN FILMS

ITO was deposited via DC magnetron sputtering. Three depositions of four samples each were performed: one at room temperature, one at room temperature followed by post annealing at 400 °C and one at high temperature (350 °C). Depositions were performed on both Ti and glass substrates. Samples deposited onto Ti substrates were used for SEM and electrochemical measurements, samples deposited onto glass substrates were used for XRD measurements and four point probe measurements.

Material features

Figures 5.14a to 5.14c show pictures of samples from the three depositions sets. For each set, one Ti and one glass sample are shown on the left and right of each picture respectively. As visible from the glass samples, ITO thin films are transparent. Profilometry was performed by taking six measurements along the length of the sample. This was done for the room temperature deposited sample and the post annealed one. The deposited height were 108 ± 19 and 73 ± 14 nm respectively. Just as the change in color of the samples on Ti (from left to right: light yellow, dark yellow, blue) seems to indicate a change in crystal structure. Reordering of the crystal may explain the decrease in height for the post annealed sample. The large error in height measured stems from different factors. First, during sputtering, a gradient in thickness deposited exists between the center and the edges of the substrate holder. This difference is usually around 10 % of the total thickness deposited. To measure the thickness, a tape was placed on the glass prior to the deposition. Removing it allows to create a sharp edge of the deposited sample. However, some of the material may have been removed with the tape resulting in lower heights at some points. This may explain off-range measurements.

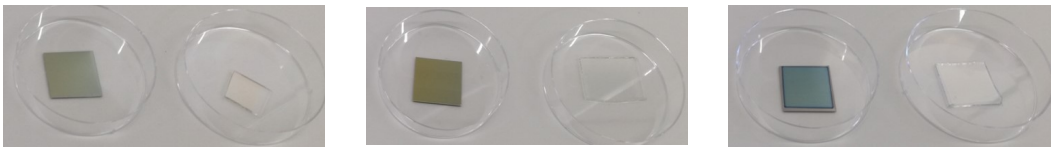

(a) Room temperature deposition, no heat treatment

(b) Room temperature deposition followed by post annealing at 400 °C

(c) High temperature deposition at 350 °C

Figure 5.14: Pictures of ITO thin films deposited onto Ti (left) and glass (right) substrates via DC magnetron sputtering for 73 min 24 s at 3 µbar and 15 W under 20 sccm Ar

Dominant crystallographic orientation

In order to characterize the ITO thin films produced, XRD measurements were taken. The sample sputtered at room temperature seems amorphous, no sharp peaks can be observed (Figure 5.15a). All samples observed featured characteristic peaks for indium tin oxide. Two characteristic peaks can be observed for the room temperature sputtered sample. These peaks originate from the (2 2 2) and the (4 0 0) crystalline planes [97]. At higher substrate temperatures, new peaks appeared around values for 2Θ of 25, 60 and 71 °. These are characteristic for the (2 1 1), (4 4 0) and (6 2 2) crystalline planes respectively. The peak intensities for the (2 2 2) and (4 0 0) planes changed with temperature treatment. At room temperature, these peaks are of similar size. For a post annealing treatment represented in Figure 5.15b, the peak representative of the (2 2 2) plane is significantly intenser. For the sputtering at high temperature shown in Figure 5.15c, the peak for the (4 0 0) plane dominates. It was observed by previous studies that sputtering with particles at higher energies favors a growth according to the (4 0 0) orientation [97]. This seems to corroborate the obtained results. It should be noted that sample thickness has been observed in literature to play an influence on dominant crystalline plane for ITO. It should therefore be kept in mind that other parameters than heat treatment may influence crystal orientation.

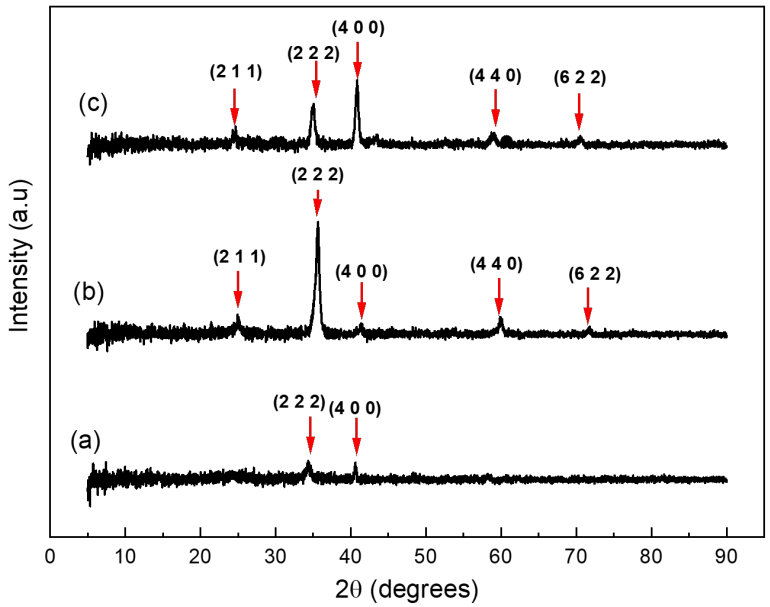

Figure 5.15: XRD spectra for (a) room temperature, (b) room temperature with post annealing at 400 °C, (c) high temperature (350 °C) DC sputtering deposition of ITO (In_2O_3:SnO_2). XRD spectra were taken with a Co source (λ = 1.789 Å) using an increment of 0.02 ° and a scan speed of 1 s/step.

Surface morphology

Samples deposited onto titanium substrates were observed via SEM. On the images obtained (Figure 5.16), the deposition can be seen to be homogeneously distributed over the sample. The surface of the material is mainly characterized by the roughness of the titanium substrate.

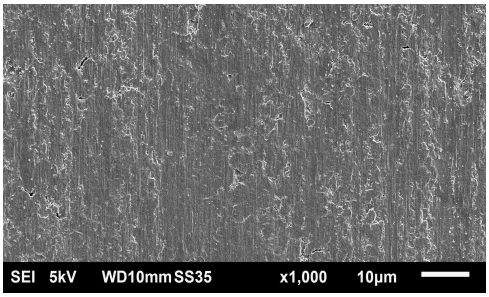

(a) Room temperature deposition, post annealing at 400 °C

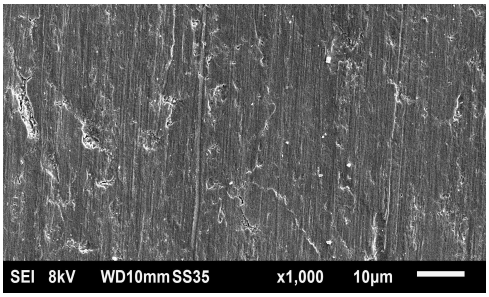

(b) High temperature deposition at 350 °C

Figure 5.16: SEM pictures of ITO thin films deposited onto Ti substrates via DC magnetron sputtering (a) at room temperature with post annealing treatment at 400 °C and (b) at high temperature (350 °C). SEM measurements were taken by SEI using a voltage of (a) 5 and (b) 8 kV under magnification 1000.

Thin film resistivity

The van der Pauw method described in Section 4.1.6 was used to evaluate the thin film resistivity of the deposited ITO samples. Thin films studied were deposited on glass in order to prevent contact of the probes with the metal substrate. The resistance within the titanium substrate could then indeed be measured instead of the thin film resistance itself. Gold contact were deposited at the edges according to the protocol presented in Section 4.1.6.

As visible from Table 5.3, the room temperature sample has the highest resistivity. This seems logical as the sample was the least crystalline (Figure 5.15) thus will impede the electron flow the most. The lowest resistivity was obtained from the sample deposited at high temperature. Though the post annealing temperature (400 °C) was higher than the temperature used for heated sputtering (350 °C), the resistivity obtained was higher for the post annealed sample. This shows that film synthesis at high temperature yields better conductivity than post treatment to re-arrange crystals. The difference in resistivities may also be induced by differences in sample thicknesses. The samples that were subject to a heat treatment had better organized lattices which resulted in thinner samples. All resistivities obtained were in the range of 10^{-4} which falls within the range of characteristic resistivities for ITO [121].

Table 5.3: Resistivity measurements via van der Pauw method for three ITO thin films deposited via DC magnetron sputtering with different temperature treatments.

Sample	Resistivitity [Ω cm]	Percentage error	Current range studied
Room temperature deposited ITO	$8.48 * 10^{-4}$	±2%	$3\text{-}7 * 10^{-6}$
Room temperature deposited, post annealed ITO	$6.14 * 10^{-4}$	±0.2%	$3\text{-}7 * 10^{-5}$
High temperature deposited ITO	$1.16 * 10^{-4}$	±1.17%	$3\text{-}7 * 10^{-5}$

TIN OXIDE THIN FILMS VIA SPRAY PYROLYSIS

Tin oxide films were deposited via spray pyrolysis as described in Section 4.1.6. Thicknesses of *ca.* 80, 100 and 160 nm were obtained by cycling the deposition process 5, 6 and 10 times respectively.

The materials were first characterized by XRD. Characteristic peaks of cassiterite [120] were found around 2θ = 30.5, 39.1, 44.7 and 60.7° (Figure 5.17). Relative peak intensities did not seem to be influenced by the thickness of the sample. The thinner sample, deposited via 5 cycles spray pyrolysis showed an odd sharp peak around 39°. This may be due to an impurity. It should also be kept in mind that a background subtraction was performed for all spectra, and that such a peak may be caused by a software error.

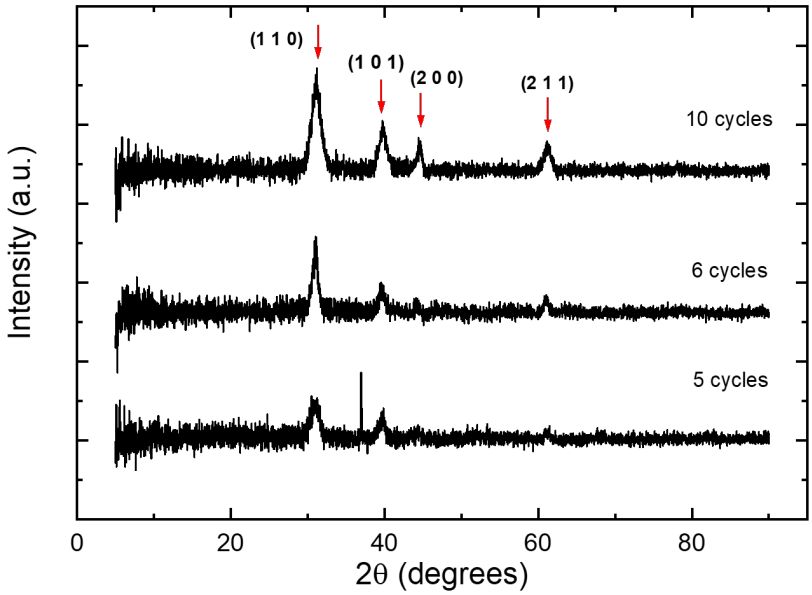

Figure 5.17: XRD spectra of thin SnO_2 films deposited on glass by 5, 6 and 10 cycles spray pyrolysis.

The aim of the spray pyrolysis depositions was to obtain a different morphology than the one obtained for the samples sputtered. Those samples were indeed very homogeneous and flat, which may lead to poor catalytic activity. The structure of the sprayed samples on titanium substrates was observed via SEM.

SEM images were taken for different samples prepared by spray pyrolysis. They were prepared in the same conditions, the only variables were the number of cycles and the number of samples sputtered in one batch. In the first batch, four samples were sprayed at a time. This led to a non-homogeneous deposition across the sample. The center of the samples was covered by a film but not the edges. Spraying with two samples at a time allowed to palliate this problem. SEM images were taken for all samples. The 10 layer sample is shown in Figure 5.18. The main part of the surface looked similar to samples deposited via DC magnetron sputtering. This was unexpected as a nanostructure was aimed for by spray pyrolysis deposition. As mentioned previously, the lack of visible nanostructure could be due to the fact that secondary electrons used for the imaging may be originated from beneath the actual surface of the sample. The electron beam indeed penetrates the sample to a certain extent (Section 4.1.6). Some other peculiar features could be observed from the SEM images. White dots can namely be observed on the surface of the sample. Element analysis was performed via EDS and showed a high Sn content at the white dots. The gray background however was predominantly titanium, again showing the limitations of SEM for surface morphology analysis.

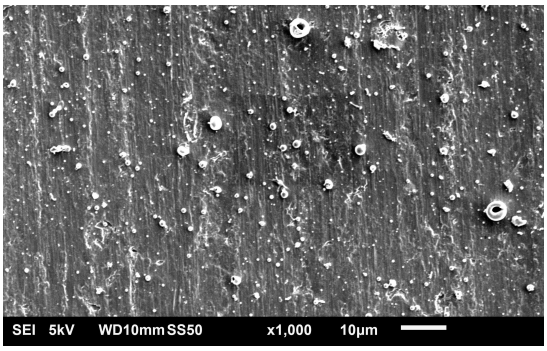

Figure 5.18: SEM image of the 10 cycle spray pyrolysis sample deposited at 5 kV and 1000 magnitude, viewed by SEI at a working distance of 10 mm and with a spot size of 50.

5.2.2. CELL DESIGN VALIDATION

The cell was tested in a platinum/platinum configuration with and without membrane in order to validate the proper working of the cell. The methods used can be found in Section 4.2.2. A chronoamperometry was run for 1300 s at 2.5 V vs RHE in 0.5 M $KHCO_3$ (Figure 5.20). The electrolyte was pumped at a flow rate of 37 mL/min through the cell. Both current responses follow an inverse quadratic trend with time, which is in accordance with the Cottrell equation (Equation (5.1)) [38]. This equation presents the relation between n the number of electrons involved in the reaction, F the Faraday constant, c_o the bulk concentration, D_o the diffusion constant and t the time. The depletion of electroactive species at the surface of the electrode leads to the inverse square relation with time.

$$I_{\text{diff}}(t) = \frac{nFAc_o\sqrt{D_o}}{\sqrt{\pi t}} \tag{5.1}$$

The high current at the start of the measurement is explained by the availability of surface accumulated species. Once these are consumed, species need to be transported from the bulk. With convection, a plateau is reached as the only limitation is diffusion at the boundary layer. Figure 5.20 shows that the flow cell used

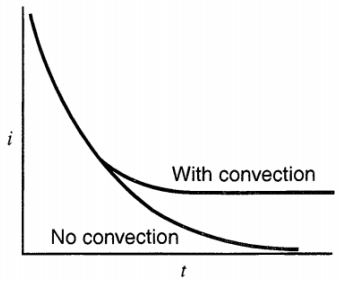

Figure 5.19: Typical chronoamperometry current-time response to a potential step with and without convection. [38]

for experiments presents a typical response for convection. Diffusion limitations will therefore have a minor impact on results obtained for the measurements. The current response plateau for the set-up without membrane is 1.6 times higher than with membrane. This can be explained by ohmic losses at the membrane. The order of magnitude of the two responses is however similar for the two set-ups. The use of a membrane is of importance for the electrochemical processes considered in this study. It allows to keep products separated and to prevent the decomposition of some products at the other electrode.

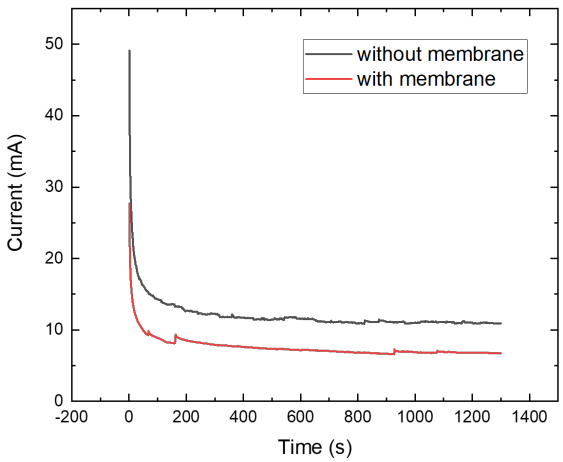

Figure 5.20: Chronoamperometry with and without membrane for a Pt/Pt configuration with a Ag/AgCl reference electrode at an applied potential of 2.5 V vs RHE in 0.5 M$KHCO_3$ and a flow rate of 37 mL/min.

5.2.3. ELECTROCHEMICAL TESTS FOR TIN-BASED ELECTRODES

Different tin-based electrodes were used for electrochemical tests. These include SnO_2, Sn_3O_4, ITO and FTO. Different substrates, namely glass, FTO and titanium were investigated. Experiments were built around five possible effects on performance for hydrogen peroxide evolution: sample crystallinity, sample thickness, sample morphology, thin film composition and substrate variation.

EFFECT OF HEATING TREATMENT

As presented in Section 5.2.1, different heating treatments yielded different crystalline phases and thicknesses for the deposited thin films. SnO_2 samples were deposited via reactive DC magnetron sputtering at room temperature with post annealing at 500 °C and at high temperature (500 °C, Section 4.1.2). ITO samples were deposited via DC magnetron sputtering at room temperature with post annealing at 400 °C and at high temperature (350 °C, Section 4.1.3). These samples were tested as anodes in the electrolysis cell described in Section 4.2.2. A series of electrochemical measurements were taken in the following order: chronoamperometry for 30 min at 2 V vs RHE, cyclic voltammetry from 0 V vs OC to 3 V vs RHE, chronoamperometry for 30 min at 3 V vs RHE, cyclic voltammetry from 0 V vs OC to 3 V vs RHE, cyclic voltammetry from -2 V vs RHE to 3 V vs RHE and chronoamperometry for 30 min at 4 V vs RHE. A full overview of data-sets can be found in Appendix F.1.

Overall, ITO samples allowed to reach higher current densities than SnO_2 samples. Figure 5.21) shows the current density response *vs* applied potential. For the same potentials, current density responses were obtained from high to low from high temperature deposited ITO, post annealed ITO, high temperature deposited SnO_2 and finally post annealed SnO_2. Sputtering at high temperature can therefore be concluded to yield improved results for both tin-based materials. Doping of tin(IV) oxide to ITO allows to enhance electrochemical properties of the material. Current densities obtained were however very low compared to literature. No peroxide was detected using Quantofix® strips. Current densities were especially low towards the end of the experiments. For the second cyclic voltammetry, the peak reached for post annealed ITO at 3 V vs RHE was at 0.18 mA/cm^2. This is 44 times lower than for the first cyclic voltammetry. This either reflects the deactivation of the catalyst material or the oxidation of for example the titanium substrate.

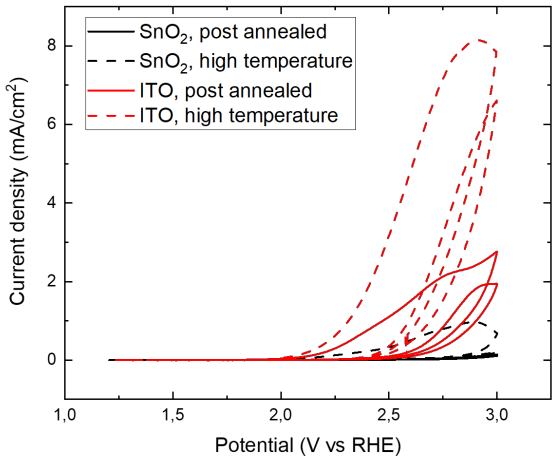

Figure 5.21: Cyclic Voltammetry tests for SnO_2 anodes deposited via reactive DC magnetron sputtering at room temperature with post annealing at 500 °C and at high temperature (500 °C), and ITO anodes deposited via DC magnetron sputtering at room temperature with post annealing at 400 °C and at high temperature (350 °C). Tests were done in 0.5 M $KHCO_3$ pumped through the system at a flow-rate of 37 mL/min.

EFFECT OF SAMPLE THICKNESS

SnO_2 samples were deposited under 9 sccm Ar and 11 sccm O_2 at 13.3 µbar, 500 °C and 120 mA. Depositions were for 1 hour 23 min 20 s, 2 hours 46 min 40 s and 4 hours 10 min in order to obtain batches of *ca* 100, 200 and 300 nm respectively. The samples were placed as anode in the electrochemical cell described in Section 4.2.2. A 0.5 M $KHCO_3$ electrolyte was pumped through the system at 37 mL/min. 50 mL of anolyte and

catholyte were used. A series of electrochemical measurements were taken in the following order: chronoamperometry for 30 min at 2 V vs RHE, cyclic voltammetry from 0 V vs OC to 3 V vs RHE, chronoamperometry for 30 min at 3 V vs RHE, cyclic voltammetry from 0 V vs OC to 3 V vs RHE and chronoamperometry for 30 min at 4 V vs RHE. A detailed overview of data-sets can be found in Appendix F.2.

The behavior of samples of different thicknesses seemed to evolve with the measurements taken. At first, the thinnest sample seemed to yield better results. In the first CV (Figure 5.22a), the current response was in the same range for the thinner sample and the thicker sample. This can be explained by a lower sheet resistivity for thinner films which enables the electrons to be transported more freely. However, after this measurement, this trend seemed to shift. For the second CV (Figure 5.22b), current densities obtained were significantly higher for the thicker sample. This may indicate that along with the experiments, substrate oxidation has occured. This is indeed more likely for the thinner sample as the titanium is more readily exposed to the electrolyte. The 200 nm sample, for which both CV measurements yielded low current density responses may have been deactivated or oxidized during the first chronoamperometry.

A singular sharp peak can be observed on both CV at 2.8 V vs RHE for both the 300 and 200 nm samples. Such a peak was observed in several tests, also on carbon-based electrodes. In subsequent experiments, after changing the current filters for the potentiostat, these peaks were not seen anymore. They were therefore considered as noise from the potentiostat.

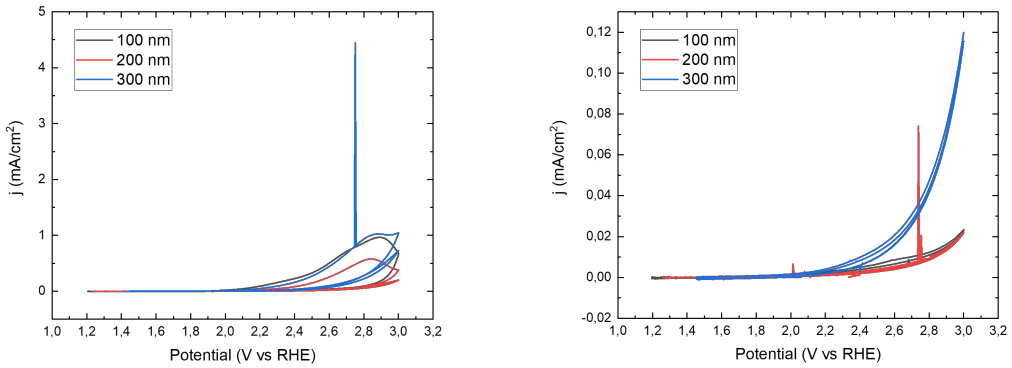

(a) CV from 0 V vs OC to 3 V vs RHE

(b) Second CV at 3 V vs RHE

Figure 5.22: Cyclic Voltammetry (CV) tests performed in the electrolysis cell with as anode SnO_2 sputtered at high temperature (500 °C) as thin layers of *ca* 100, 200 or 300 nm. Current density was evaluated for a potential varying between 0 V vs OC and 3 V vs RHE. Tests were done in 0.5 M $KHCO_3$ pumped through the system at a flow-rate of 37 mL/min.

EFFECT OF SAMPLE MORPHOLOGY

As tin (IV) oxide samples deposited via sputtering did not yield any promising results, spray pyrolysis was considered as alternative deposition technique to create a nanostructured surface. Having such a structure may allow to enhance catalytic activity and prevent catalyst deactivation. A sample deposited via 10 cycles of spray pyrolysis was tested in the electrolysis cell described in Section 4.2.2. A series of electrochemical measurements were taken in the following order: chronoamperometry for 30 min at 2 V vs RHE, cyclic voltammetry from 0 V vs OC to 3 V vs RHE, chronoamperometry for 30 min at 3 V vs RHE, cyclic voltammetry from 0 V vs OC to 3 V vs RHE and chronoamperometry for 30 min at 4 V vs RHE. A detailed overview of data-sets can be found in Appendix F.3.

During the first chronoamperometry measurement, the sputtered sample yielded a a higher initial current density than the sprayed sample. However, after half an hour measurement, both current densities amounted around 0.0035 mA/cm^2 (Figure 5.23a). These values are extremely low, even for the potential step applied (2 V vs RHE). At a higher potential applied of 3 V vs RHE, somewhat higher current densities were obtained from the sprayed sample (0.060 vs 0.020 mA/cm^2 for the sprayed and sputtered sample respectively, see Figure 5.23b). At 4 V vs RHE and after 20 min chronoamperometry, the run for the sputtered sample had reached a plateau at 0.053 mA/cm^2. The current density for the sprayed sample reached 0.39 mA/cm^2 at the end of the

measurement. However, it still seemed to decrease. This might indicate that the sprayed sample is somewhat less sensible to deactivation but will be on the long run. It should be kept in mind that these samples were compared based on the assumption that they have a similar thicknesses. Care should be taken when drawing conclusions as thickness may also play a role in the performance of each sample.

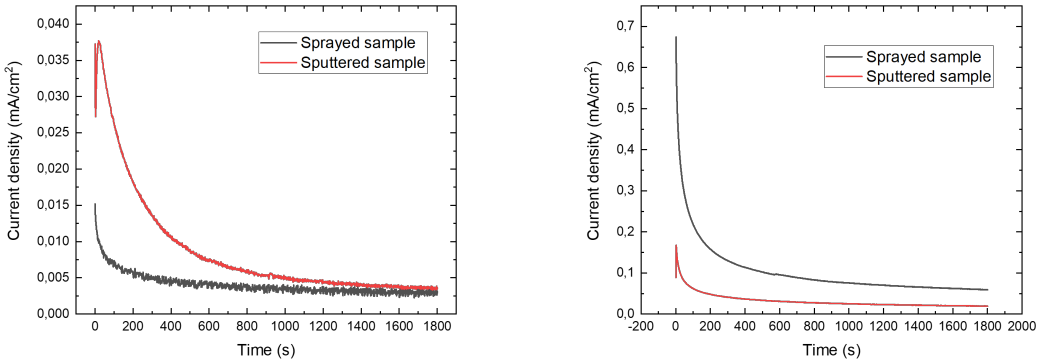

(a) Chronoamperometry at 2 V vs RHE, 30 min (b) Second chronoamperometry at 3 V vs RHE, 30 min

Figure 5.23: Chronoamperometry tests performed in the electrolysis cell with as anode SnO_2 deposited via reactive DC magnetron sputtering at high temperature for 2 hours 46 min 40 s and via spray pyrolysis in 10 cycles. Tests were done in 0.5 M $KHCO_3$ pumped through the system at a flow-rate of 37 mL/min.

A similar behavior was observed via cyclic voltammetry between 0 V vs OC and 3 V vs RHE (Figure 5.24). First, both samples seemed to follow the same trend. At 2.8 V vs RHE however, the current density dropped suddenly for the sputtered sample. This observed peak may be caused by a change of structure of the anode material for the sputtered sample. In the second cycle of the measurement, values obtained for the sputtered sample are significantly lower than for the sprayed sample. In the second cyclic voltammetry test, both current density responses are an order of 10 lower than for the previous one. This shows that the chronoamperometry run in between at 3 V vs RHE has contributed importantly to the degradation of the catalyst. The difference between sprayed and sputtered sample is still observable. A peak can again be observed at 2.8 V vs RHE for the sputtered sample, this time very sharp. This is attributed to noise in the potentiostat. Some smaller peaks can be seen at 2 and 2.1 V vs RHE.

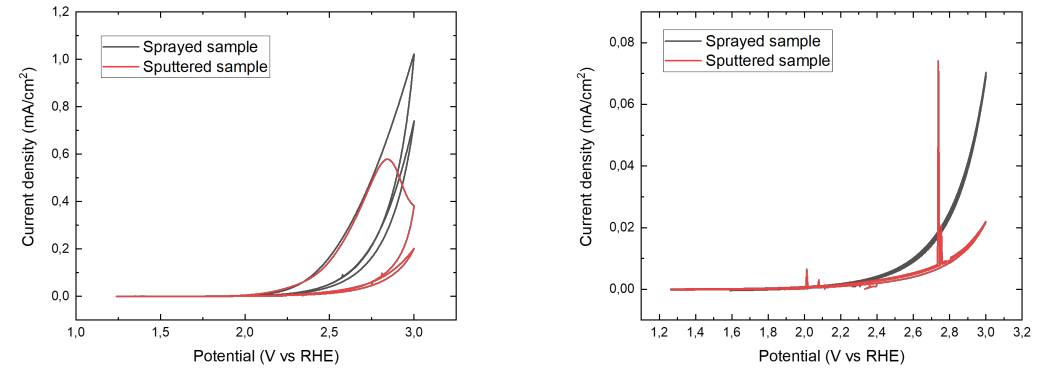

(a) Chronoamperometry at 2 V vs RHE, 30 min (b) Second chronoamperometry at 3 V vs RHE, 30 min

Figure 5.24: Cyclic voltammetry tests performed in the electrolysis cell with as anode SnO_2 deposited via reactive DC magnetron sputtering at high temperature for 2 hours 46 min 40 s and via spray pyrolysis in 10 cycles. Tests were done in 0.5 M $KHCO_3$ pumped through the system at a flow-rate of 37 mL/min.

All values obtained from these samples are extremely low and by far not competitive with results obtained from literature (Table 2.2). Moreover, neither sputtered or sprayed samples yielded any hydrogen peroxide as

measured by Quantofix® strips. The titanium substrate may have a major effect on the governing processes at the electrode. It is highly probable that the substrate is exposed to the electrolyte and undergoes oxidation to TiO_2. This layer will create an insulating barrier and limit the oxidation process towards hydrogen peroxide.

EFFECT OF DIFFERENT COMPOSITIONS

The performance of different tin-derived material was evaluated by comparing SnO_2, ITO and FTO thin films. FTO was used as substrate in order to create a nanostructured support for the deposited material thus influencing the structure of the sputtered material. Obtained ITO thin films were confirmed to be nanostructured by AFM measurements. Both SnO_2 and ITO samples were deposited via DC magnetron sputtering. The samples were deposited at room temperature and post annealed with the parameters described in Section 4.1.2. Deposition times were chosen to create thin films of *ca* 275 nm. This was chosen as to provide a comparable thickness to the commercial FTO and prevent the substrate to be exposed and influence the results. The samples were tested in the electrolysis cell set-up described in Section 4.2.2. A series of electrochemical measurements were taken in the following order: chronoamperometry for 30 min at 2 V vs RHE, cyclic voltammetry from 0 V vs OC to 3 V vs RHE, chronoamperometry for 30 min at 3 V vs RHE, cyclic voltammetry from 0 V vs OC to 3 V vs RHE and chronoamperometry for 20 min at 4 V vs RHE. A detailed overview of datasets can be found in Appendix F.4.

Significantly improved results were obtained for two-electron WOR on FTO. At the end of this measurement, H_2O_2 was detected via Quantofix® strips in the range of 5 to 10 mg/L. This was not the case for SnO_2 and ITO. For a chronoamperometry at an applied potential of 3 V vs RHE, a plateau seemed to be reached around 4 mA/cm^2 (Figure 5.25a). The other two sample were well below 1 mA/cm^2. It should be noted that all measurements for SnO_2 yielded a current response in the order of pA. This is even lower than results obtained for SnO_2 deposited onto glass (Appendix F.5). For this reason, it seems very likely that a contact in the testing set-up was not proper which yielded erroneous results. It would therefore be wise to reiterate these measurements. Current densities up to 28 mA/cm^2 were obtained during chronoamperometry at 4 V vs RHE for the FTO samples, again far above performances obtained for ITO and SnO_2 samples (Figure 5.25b). However, no plateau was reached during the measurement for FTO. A steep descent brought the current density response to 14 mA/cm^2 after 20 min. This measurement should be repeated for a longer time span. Oscillations can also be seen in the response signal. These may account for bubble formation in the system.

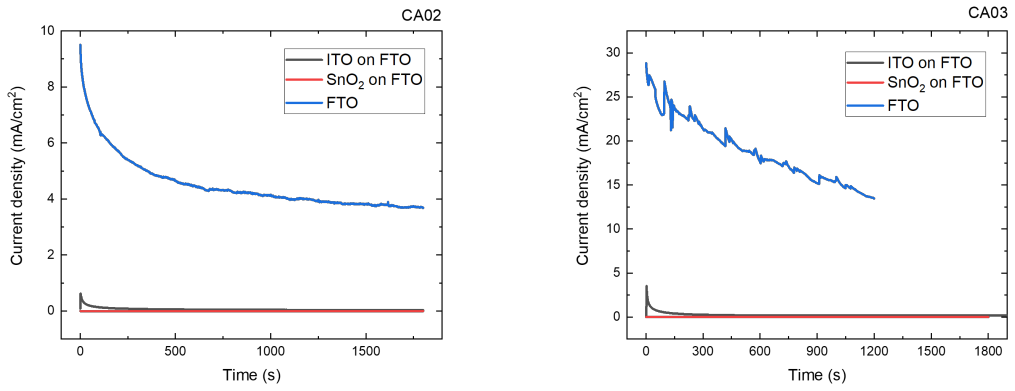

(a) Second chronoamperometry at 3 V vs RHE, 30 min (b) Third chronoamperometry at 4 V vs RHE, 30 min

Figure 5.25: Chronoamperometry tests performed in the electrolysis cell with as anode SnO_2, ITO deposited onto FTO via DC magnetron sputtering at room temperature and post annealed at 500 and 400 °C respectively as well as for a plain commercial FTO sample. Depositions of SnO_2 and ITO were done for 3 hours 49 min 10 s and 4 hours 30 min respectively via the methods described in Section 4.1.2 and Section 4.1.3. Tests were done in 0.5 M $KHCO_3$ pumped through the system at a flow-rate of 37 mL/min.

The Sn_3O_4 containing material presented in Section 5.2.1 was also tested in the electrochemical set-up. Surprisingly enough, it was the only sample next to FTO that yielded H_2O_2. The samples were deposited under 15 sccm Ar and 5 sccm O_2 at 5 µbar and 15 W at room temperature with post annealing treatment at 500 °C as described in Section 4.1.2. Deposition times was 7 min 14 s. The samples were tested in the electrolysis cell set-up described in Section 4.2.2. A series of electrochemical measurements were taken in the following order: chronoamperometry for 30 min at 2 V vs RHE, cyclic voltammetry from 0 V vs OC to 3 V vs

RHE, chronoamperometry for 30 min at 3 V vs RHE, cyclic voltammetry from 0 V vs OC to 3 V vs RHE and chronoamperometry for 20 min at 4 V vs RHE. A detailed overview of data-sets can be found in Appendix F.4.

Current density responses during both chronoamperometry and cyclic voltammetry measurements were higher for the Sn_3O_4 sample. Figure 5.26a shows the second chronoamperometry recording at an applied potential step of 3 V vs RHE. The current response is more than 10 times higher for the Sn_3O_4 sample. At the end of all electrochemical tests, 0.5-2 mg/L peroxide was detected using Quantofix® strips.

The final chronoamperometry at 4 V vs RHE is presented in Figure 5.26b. The initial current density response obtained is at 14 mA/cm^2. However, no plateau is reached within the 20 min measurement. This may indicate that the sample was not stabilized yet. Longer measurements should be performed to assess the performance of the electrode once it reached a plateau.

The performance for peroxide yield, which was not observed for any of SnO_2 material, may be due to the availability of additional oxygen vacancies. Those may allow adsorption with the right binding energies of intermediates favoring the WOR towards peroxide. The current densities obtained were still very low, which implies that this material needs improvements before being relevant for large scale implementations or will not be suitable. The mechanisms behind the formation of peroxide and the stability of the material should be investigated.

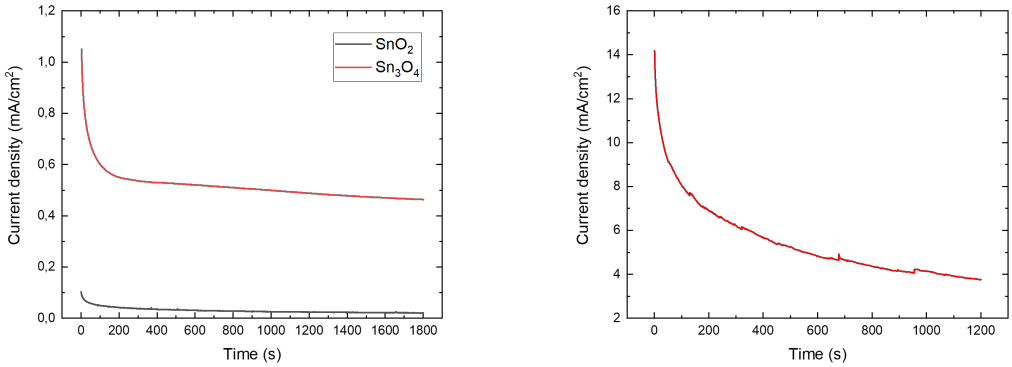

(a) Second chronoamperometry at 3 V vs RHE, 30 min (b) Third chronoamperometry at 4 V vs RHE, 30 min

Figure 5.26: Chronoamperometry tests performed in the electrolysis cell with as anode SnO_2 and Sn_3O_4 deposited onto Ti via reactive DC magnetron sputtering at room temperature and post annealed at 500 °C. Depositions were done for 1 hour 23 min 20 s and 7 min 14 s respectively. Parameters used for SnO_2 deposition were 120 mA, 13.3 µbar under 9 sccm argon and 11 sccm oxygen. Parameters used for Sn_3O_4 deposition were 15 W, 5 µbar under 15 sccm argon and 5 sccm oxygen. Tests were done in 0.5 M $KHCO_3$ pumped through the system at a flow-rate of 37 mL/min.

5.2.4. ELECTROCHEMICAL TESTS FOR CARBON-BASED ELECTRODES

A recent paper published by Xia et al. (2020) [45] showed ground breaking results for the two-electron WOR. The study was based on carbon electrodes coating with PTFE. More details on the working principles for these materials are presented in Section 2.3. Different carbon-based electrodes were tested in the electrolysis set-up described in Section 4.2.2. The tests were performed in 2 M $KHCO_3$ and 2 M K_2CO_3 with different materials as anode. First, Carbon Fiber Paper (CFP) samples were tested with and without PTFE coating. In a second time, samples were tested in bicarbonate and carbonate electrolytes. Finally, a GDE was tested as anode and compared to CFP.

CREATION OF AN AEROPHILIC SURFACE

CFP electrodes were prepared as described in Section 4.1.5. A pristine sample and a CFP with 60 % PTFE loading were tested in 2 M $KHCO_3$ with a flow rate of 37 mL/min. Figure 5.27 shows the current density response as a function of potential for the two samples. Interestingly enough, the pristine sample showed a higher current density response than the loaded sample for the same applied potential. Both materials show a good stability over the two CV cycles. A sharp peak can be observed for both materials around 1.9 V vs RHE. As

mentioned before, this peak was considered as noise from the potentiostat as it was not observed anymore after changing the settings of the current filter.

Both results are significantly better than tin (IV) oxide materials previously tested. However, they are still far from the 75 mA/cm^2 described by Xia et al. (2020). It is striking that current densities obtained are higher for the pristine sample. This was probably due to the inhomogeneity of the PTFE coating obtained for the other sample. A thick layer of PTFE had accumulated at the edges of the sample. This probably resulted in higher contact resistance with the current collector during the electrochemical tests. Several overload errors indeed accompanied the start of the experiments. The method of PTFE deposition should therefore be adapted in order to properly assess the effect of this layer.

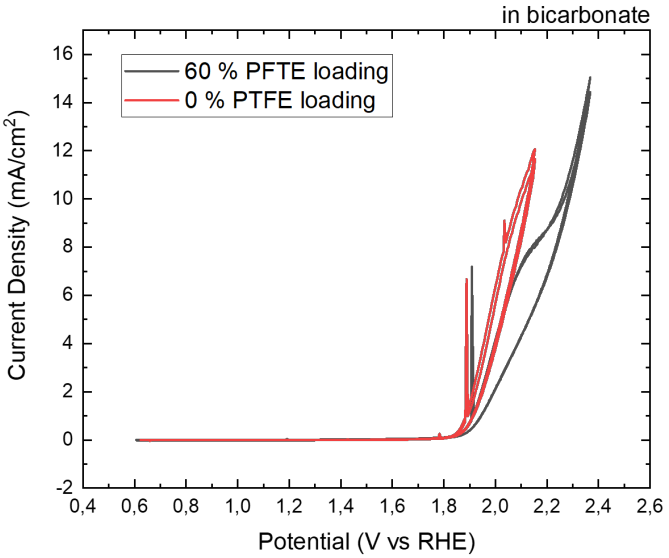

Figure 5.27: Cyclic voltammetry from 0 V vs OC to 2.4 V vs RHE for a pristine and a 60% PTFE loaded CFP sample

EFFECT OF ELECTROLYTE

The pristine CFP electrode from the set of experiments described above was re-used to observe its behavior in 2 M K_2CO_3. The electrolysis set-up was used in the same configuration and with the same parameters as in the previous experiments.

Figure 5.28 presents the current density response to a potential step of 2.4 V vs RHE. The chronoamperometry data was plotted together with the current density response in bicarbonate at the same applied potential. The response obtained in carbonate was more than four times higher than the response in bicarbonate. It thereby approached results presented in literature [45]. Oscillations were obtained in the current *vs* time plot, these are most likely induced by the formation of bubbles. For the measurement in K_2CO_3, three breaks can be seen in the data: around 1500, 2750 and 3200 s. These were due to a failure of the measurement, which was immediately restarted. At the end of the experiment, 5-10 mg/L peroxide was detected in the bicarbonate electrolyte using Quantofix® strips. In carbonate, 1000 mg/L was detected. It should be noted that the CFP had already been used before the measurement in carbonate. The current density response may have been even higher if a new sample had been used. Xia et al. (2020) suggested in their study that the pathway obtained with this type of electrode was a direct one thus that the (bi)carbonate ions were not involved. The important difference between the two responses as well as between the amount of peroxide produced seems to indicate the contrary.

GAS DIFFUSION ELECTRODES

Gas Diffusion Electrodes (GDEs) are usually made of carbon based materials combined with hydrophobic materials. The anodic performance of a GDE was tested in a 2 M K_2CO_3 electrolyte in the set-up described in

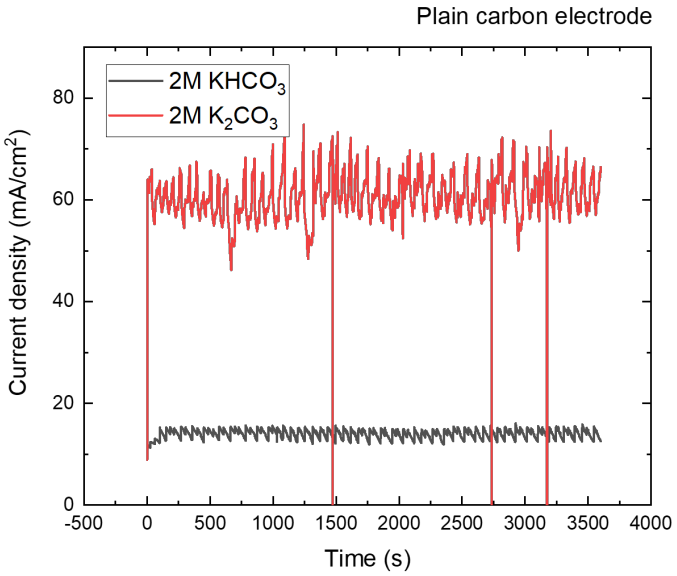

Figure 5.28: Chronoamperometry at 2.4 V vs RHE for a pristine CFP in 2 M $KHCO_3$ and 2 M K_2CO_3 for one hour. 40 mL anolyte and 40 mL catholyte were pumped through the system at 37 mL/min. The anolyte was stirred at 100 rpm.

Section 4.2.2.

Figure 5.29 presents the current density response of the GDE containing cell to a potential step of 2.4 V vs RHE. The chronoamperometry data was plotted together with the current density response of CFP at the same applied potential and in the same electrolyte. The response obtained for the GDE was around 15 mA/cm^2 lower than for the CFP. An increase in current response was observed for the set-up with GDE. The increase may stem from a slow activation of the material. It might be interesting to observe which methods prior to electrochemical tests allow to get the most out of the material.

At the end of the experiments with a GDE anode, the amount of peroxide detected was in the same range as for the CFP sample namely 1000 g/mL. This was detected by using Quantofix® strips. A lower current density for the same production of peroxide would imply a higher Faraday efficiency for the GDE. A more precise quantification method should be used in order to quantify these phenomena and allow rigorous comparison between the different materials.

5.3. PRODUCT QUANTIFICATION

Different methods were calibrated for the identification and quantification of peroxide produced during electrochemical experiments. First, results from titration calibration are presented. Then, NMR calibration results are explored.

5.3.1. TITRATION

The protocols followed for titration calibration are presented in Section 4.3.2. Next to different concentrations of acid added, the use of UV-vis spectroscopy for more precise results was investigated. In this subsection, main results and conclusions regarding the titration of peroxide in bicarbonate and carbonate are presented.

TITRATION WITH DIRECT ADDITION OF 4 ML ACID/ 100 ML ANOLYTE

Following the procedure described by Klassen et al. [109], 4 mL H_2SO_4 (97 %) was added for 100 mL of peroxide-containing sample tested. This was first tested for a 0.5 M bicarbonate solution. A strong reaction between the bicarbonate and the acid took place. The formation of CO_2 as $HCO_3^- + H^+ \longrightarrow CO_2 + H_2O$ was observed. This method was therefore considered inadequate for the titration of peroxide in the samples measured.

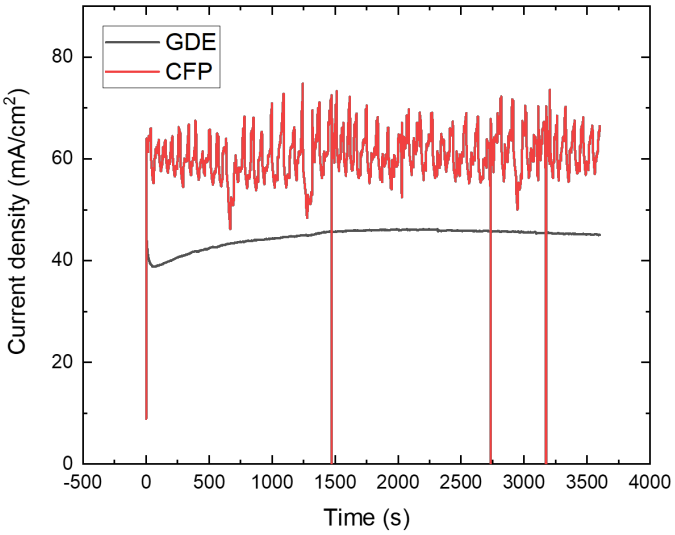

Figure 5.29: Chronoamperometry at 2.4 V vs RHE for a pristine CFP and a GDE in 2 M K_2CO_3 for one hour. 40 mL anolyte and 40 mL catholyte were pumped through the system at 37 mL/min. The anolyte was stirred at 100 rpm.

TITRATION WITH DILUTED ACID

In this procedure [110], the peroxide containing test sample was diluted prior to titration as described in Section 4.3.2. Dilute acid was then added and an aliquot of solution was titrated. Tests were ran in water, 2 M $KHCO_3$ and 2 M K_2CO_3. For a known test concentration of 1.7 mM, concentrations of 1.3, 1.0 and 0.35 mM were measured for the peroxide in water, bicarbonate and carbonate respectively. These experiments were only performed once and should be repeated to assess the error. The important differences observed may be due to several factors. First, the titrator used was a Tritrino Plus Metrohm titrator. This is an automated titrator, which was here used in manual mode. The cleaning of this titrator is very cumbersome and some solution seems to be kept in the reservoir of the machine. The five cleaning and flushing cycles with permanganate may not have been enough. The titrations were performed in the following order: in carbonate, in water and in bicarbonate. This may explain why the measurement in carbonate is so far from the actual concentration. It is recommended for further experiments to use a more traditional set-up with a burette. The deviations from the actual concentration may be caused by other problems. The permanganate or the hydrogen peroxide may have been too old and be at a lower concentration than thought. If the peroxide and bicarbonate or carbonate have formed peroxymonocarbonate or percarbonate, then these components may have interacted with he acid and deteriorated. Reproducing these calibration experiments should allow to obtain more information thus to identify the causes of the observed discrepancies.

UV-VIS CALIBRATION

Excess of permanganate added during the titration can be quantified by UV-vis spectroscopy [109]. The implementation of this method was investigated. The Beer-Lambert law (Equation (5.2)) provides a linear relationship for the absorbance A and concentration c [mol/L] at constant path length b [cm] and absorptivity ϵ [L/mol/cm].

$$A = \epsilon b c \tag{5.2}$$

Calibration experiments were first done in water to assess the functioning of the spectrometer. $KMnO_4$ concentrations of 1, 3, 10, 20 and 45 µM were tested in 10 mm cuvettes at 525 nm. A linear relationship was obtained between absorbance and concentration. A linear trendline with $r^2 = 0.9999$ could be fitted.

The same was done in 0.5 M $KHCO_3$ with similar $KMnO_4$ concentrations. Absorbance for the 45 µM $KMnO_4$ jumped to upper limit values for the spectrometer. This may be due to the addition of salt which decreases transmittance. The absorbance is defined as:

$$A = log^{10} \frac{1}{T} \tag{5.3}$$

This implies that low transmittance will induce large absorbance. For low transmittance, a small error may result in a large change in computed absorbance. Usually, absorbance is considered relevant if inferior or equal to 1. The absorbance found for the 45 µM sample being at 300, it was therefore discarded. For the other data points, a linear trendline could be fitted with an r^2 value of 0.9926.

Experiments were repeated for 2 M $KHCO_3$ samples with different permanganate concentrations (1, 3, 10, 20 and 45 µM). The same behavior was observed as for the 0.5 M batch. The absorbance for the 45 µM sample was discarded. A linear trendline with $r^2 = 0.995$ was fitted between the four remaining data points.

The use of UV-vis spectroscopy encounters challenges regarding detection limits with salty solutions. If combined to permanganate titration, the excess amount added should be in the range of measurable $KMnO_4$ concentration by UV-vis. It is advised to first fine-tune the titration method before carrying on with the coupled UV-vis analysis. If titration methods reach an acceptable precision for the experiments considered, it may not be needed to add this step. The UV-vis step requires calibration at the start of each measurement as the lamp may vary in intensity with time. If the advantages of added precision are not significant, it is preferable to leave out this time consuming analysis.

5.3.2. NMR SPECTROSCOPY

As explored in Section 2.3, different compounds are thought to be involved in the electrochemical formation of hydrogen peroxide from water oxidation. NMR spectroscopy is a powerful technique to distinguish and quantify individual molecules. Its use for peroxides and (bi)carbonate derivatives was therefore investigated. Calibration experiments were performed for hydrogen peroxide (H_2O_2), bicarbonate (HCO_3^-), carbonate (CO_3^{2-}), percarbonate ($C_2O_6^{2-}$) and peroxymonocarbonate (HCO_4^-). This section presents results obtained for each of these compounds.

HYDROGEN PEROXIDE CALIBRATION

Calibration of NMR spectroscopy for quantitative estimation of hydrogen peroxide concentration was carried out via H^1 NMR in the concentration range 0.005 to 1 M and 1 to 10 M. Benzene capillaries were used for locking and all measurements were translated back to the maleic standard defined in Section 4.3.3. Hydrogen peroxide was stored at 4 °C and measured immediately after removal from the refrigerator.

According to a study by Stephenson et al. [122], characteristic peaks for hydrogen peroxide are found around 10 to 11 ppm. For concentrations above 10^{-3} and below 0.1 M, a linear relationship relates the area under the peak and the hydrogen peroxide concentration. The peak is then found at 11.1 ppm. The authors also observed that at a concentration above 1 M and up to 10 M, the water peak found at 4.7 ppm and the hydrogen peroxide peak start to merge. For this concentration range, they observed a linear relationship between the product concentration and the broadened peak position.

0.005 to 1 M H_2O_2 range

Figure 5.30a shows the linear fit for H_2O_2 concentration as a function of relative peak area between the H_2O_2 peak and the maleic acid standard peak. An r^2 value of 0.98936 was obtained for the $y = 0.01618(\pm 0.000838)x + 0.00482(\pm 0.00182)$ fit. A residuals plot *vs* fit plot is provided in Figure 5.30b. This scatter plot shows the residuals *vs* predicted values. The residual points seem randomly distributed around the zero line which would support the validity of the fit. The residuals are fairly low, showing that the data points are close to the fit. It should be noted that the small amount of data points makes this analysis incomplete. Even though the fit seems adequate from the r^2 values, more measurements should be performed to assess the distribution of the residuals and obtain better calibration fits.

During measurements, it was observed that a too long waiting time before a measurement would provide data points off the linear fit. Those were discarded in this analysis as they did not go through the same protocol as other samples. This observed discrepancy could be due to either decomposition of hydrogen peroxide, which is known for being an unstable compound. It could also be induced by temperature differences. If this is the case, then the calibration curve might be erroneous for samples of unknown concentration at room temperature. If electrochemically produced samples are analyzed using this calibration, concentration should first be cross-checked with another analysis method such as peroxide strips.

Due to low signal-to-noise ratio, no accurate integration could be performed for samples at low concentrations. The lowest concentration that could be measured was 0.005 M. The highest hydrogen peroxide production reported so far in literature amounted 23.4 µmol/(min cm^2). This corresponds to 6.21 mM for electrolysis in the cell described in Section 4.2.2 for a 2 h run and with 40 mL anolyte. Some detection prob-

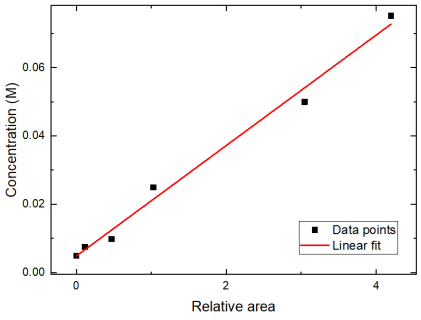

(a) Calibration plot for low H_2O_2 concentrations.

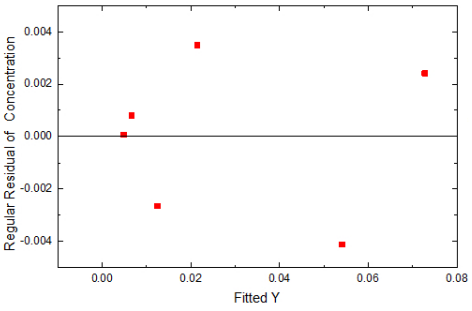

(b) Residuals *versus* fit plot for the fit in Figure 5.30a.

Figure 5.30: Calibration for six hydrogen peroxide samples at different concentrations measured by 1H NMR spectroscopy. (a) shows the linear fit for the H_2O_2 concentration as a function of relative H_2O_2 to 0.0244 M maleic acid peak area. The linear fit obtained was $y = 0.01618(\pm 0.000838)x + 0.00482(\pm 0.00182)$. (b) shows the error analysis.

lems can be predicted due to low concentrations. Alternatives to palliate this problem, such as the use of a lower volume electrolyte should therefore be investigated.

1 to 10 M H_2O_2 range

Figure 5.31a shows the linear fit for high H_2O_2 concentration as a function of relative peak area between the H_2O_2 peak and the maleic acid standard peak. An r^2 value of 0.74793 was obtained for the $y = 7.75616(\pm 2.2514)x - 35.60607(\pm 11.85136)$ fit. The r^2 values is on the low side. Data points can be seen not to be distributed closely to the fit. As can be read from the y-axis of Figure 5.31b, large residuals are found. This illustrates that data points are not grouped closely to the linear fit. The method presented by Richardson et al. [122] seems prone to error and hard to reproduce. Measurements should however be replicated to allows better statistical analysis and assess whether an appropriate and reliable fit can be obtained.

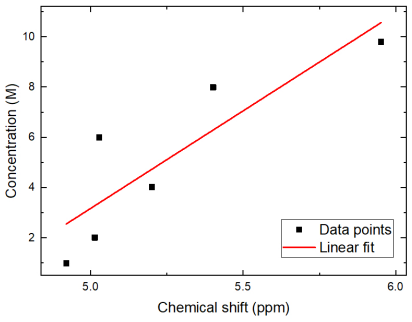

(a) Calibration plot for high H_2O_2 concentrations.

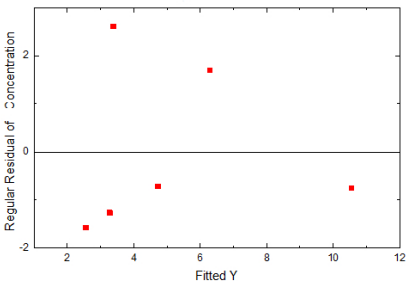

(b) Residuals *versus* fit plot for the fit in Figure 5.31a.

Figure 5.31: Calibration for six hydrogen peroxide samples between 1 and 10 M measured by 1H NMR spectroscopy. (a) shows the linear fit for the H_2O_2 concentration as a function of chemical shift of the coalesced hydrogen peroxide and water peaks. The linear fit obtained was $y = 7.75616(\pm 2.2514)x - 35.60607(\pm 11.85136)$ with $r^2 = 0.74793$. (b) shows the error analysis.

BICARBONATE CALIBRATION

Calibration of NMR spectroscopy for quantitative estimation of bicarbonate concentration was done via C^{13} NMR in the concentration range 0.5 to 2 M. Benzene capillaries were used for locking and all measurements were translated back to the maleic standard defined in Section 4.3.3. Calibration was done in both $KHCO_3$ and $NaHCO_3$ to assess whether the cation had an impact on the bicarbonate peak, found at 161 ppm.

Figure 5.32a shows the linear fit for HCO_3^- concentration as a function of relative peak area between the HCO_3^- peak and the maleic acid standard peak. A linear fit $y = 7.53(\pm 0.253)x - 0.01646(\pm 0.03321)$ was ob-

tained by linear regression. An r^2 value of 0.99437 was obtained for the fit. This seems to indicate that the calibration fit provides a rather reliable model to derive concentrations of unknown samples. The concentration residuals are plotted *vs* values predicted by the fit Figure 5.32b. The residuals are rather small which shows a good distribution. The randomness of the distribution seems good but is hard to assess for the small number of data points. Additional measurements should be performed to confirm this.

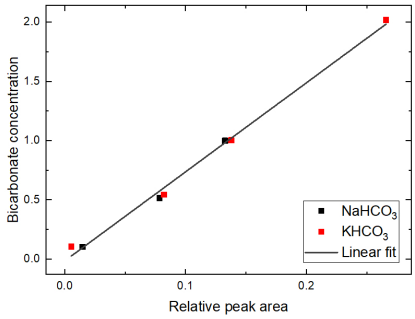

(a) Calibration plot of the HCO_3^- concentration.

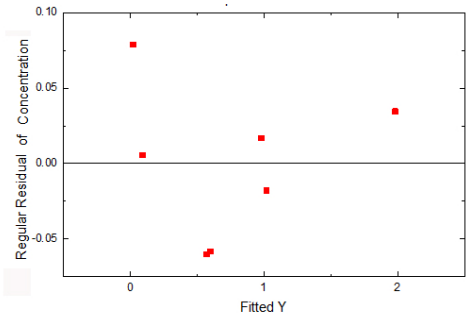

(b) Residuals *versus* fit plot for the fit in Figure 5.32a.

Figure 5.32: Calibration for four potassium bicarbonate and three sodium bicarbonate samples at different concentrations measured by 13C NMR spectroscopy. (a) sows the linear fit for the HCO_3^- concentration as a function of relative HCO_3^- to 0.0244 M maleic acid peak area. The linear fit obtained was $y = 7.53(\pm 0.253)x - 0.01646(\pm 0.03321)$. (b) shows the error analysis for the fit.

The detection limit was reached for measurements below 0.5 M due to low signal-to-noise ratio. This should not be a problem for experiments targeted by this calibration. Bicarbonate is indeed used as electrolyte between 0.5 and 2 M concentration in electrochemical experiments thus its concentration should not go below the detection threshold.

CARBONATE CALIBRATION

Calibration of NMR spectroscopy for quantitative estimation of potassium carbonate concentration was done via C^{13} NMR in the concentration range 0.05 to 5 M. Benzene capillaries were used for locking and all measurements were translated back to the maleic standard defined in Section 4.3.3. The percarbonate peak peak can be found at 167.2 ppm. A detection limit was reached at 0.05 M below which low signal-to-noise ratio prevented integration or even visibility of the signal.

Figure 5.33a shows the linear fit for CO_3^{2-} concentration as a function of relative peak area between the CO_3^{2-} peak and the maleic acid standard peak. A linear fit $y = 4.50(\pm 0.398)x - 0.0591(\pm 0.218)$ was obtained by linear regression. An r^2 value of 0.91418 was obtained for the fit. This value is lower than values obtained for other calibration curves. Figure 5.33b presents the concentration residuals *vs* the predicted values. One outlier can be identified, the one corresponding to the 5 M sample. The residuals are fairly large, illustrating that the fit is not optimal. A calibration curve should provide a very accurate and precise prediction of the concentration/ relative peak area relation. Samples of unknown concentration will indeed be characterized using this model, thus it is of importance not to propagate the error. The deviations noted are thought to be due to tuning problems of the NMR instrument used. High salt contents tend to deregulate the automatic tuning performance of the machine and software. Experiments should be repeated using manual tuning to obtain more reliable calibration results. Two data points at low concentration were also observed to deviate more from the fit. These deviation are thought to be due to faulty dissolution of carbonate prior to acquisition. Samples measured subsequently were stirred before analysis and seem to adhere better to the fit.

PERCARBONATE CALIBRATION

Calibration of NMR spectroscopy for quantitative estimation of sodium percarbonate concentration was done via C^{13} NMR in the concentration range 0.1 to 0.9 M. Benzene capillaries were used for locking and all measurements were translated back to the maleic standard defined in Section 4.3.3. The percarbonate peak peak can be found at 167.2 ppm.

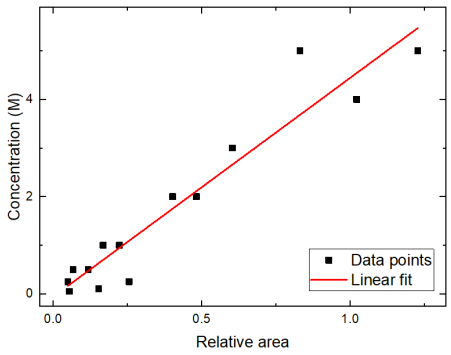

(a) Calibration plot of the $K_2CO_3^{2-}$ concentration.

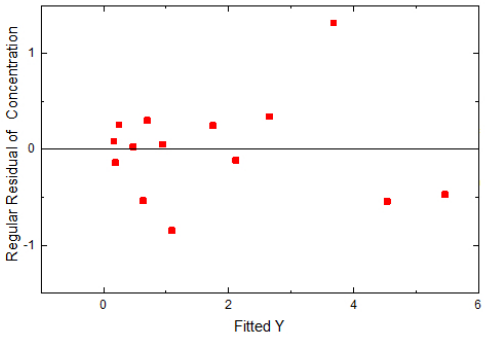

(b) Residuals *versus* fit plot for the fit in Figure 5.33a.

Figure 5.33: Calibration plot of the CO_3^{2-} concentration as a function of relative CO_3^{2-} to 0.0244 M maleic acid peak area. The linear fit obtained in (a) was $y = 4.50(\pm 0.398)x - 0.0591(\pm 0.218)$. Data points were acquired by ^{13}C NMR spectroscopy. (b) shows the error analysis for the fit.

Figure 5.34a shows the linear fit for $C_2O_6^{2-}$ concentration as a function of relative peak area between the $C_2O_6^{2-}$ peak and the maleic acid standard peak. A linear fit $y = 4.70(\pm 0.346)x + 0.0697(\pm 0.0386)$ was obtained by linear regression. An r^2 value of 0.98397 was obtained for the fit. This seems to indicate that the calibration fit provides a rather reliable model to derive concentrations of unknown samples. A residual *vs* fit plot is shown in Figure 5.34b. This scatter plot shows the residuals *vs* predicted values. The residual points seem randomly distributed around the zero line which would support the validity of the fit. However, the small number of data points make it hard to assess the validity of the fitted line in Figure 5.34a. Additional measurements should be performed to obtain more reliable calibration fits. No lower concentrations than 0.1 M were tested. The detection limit still is to be investigated. It should also be noted that calibration experiments were performed with commercial sodium percarbonate, which is actually an adduct of sodium carbonate and hydrogen peroxide. Even if not expected, deviations in NMR spectra may occur for electrochemically produced percarbonate and the commercial one.

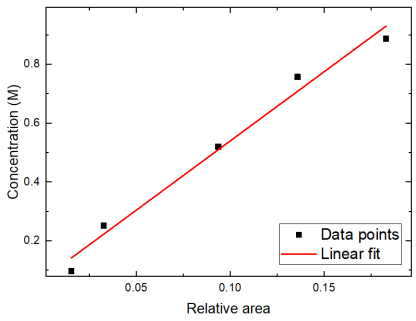

(a) Calibration plot of the $C_2O_6^{2-}$ concentration.

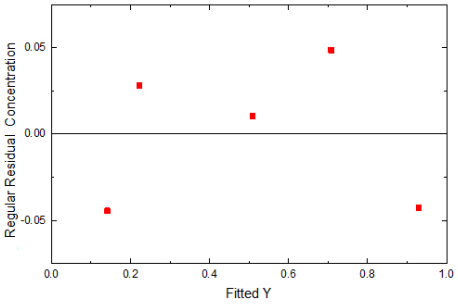

(b) Residuals versus fit plot for the fit in Figure 5.34a.

Figure 5.34: Calibration plot of the $C_2O_6^{2-}$ concentration as a function of relative $C_2O_6^{2-}$ to 0.0244 M maleic acid peak area. The linear fit obtained in (a) was $y = 4.70(\pm 0.346)x + 0.0697(\pm 0.0386)$. Data points were acquired by ^{13}C NMR spectroscopy. (b) shows the error analysis.

PEROXYMONOCARBONATE CALIBRATION

Calibration of NMR spectroscopy for quantitative estimation of peroxymonocarbonate concentration was explored via C^{13} NMR. Benzene capillaries were used for locking and all measurements were translated back to the maleic standard defined in Section 4.3.3. The peroxymonocarbonate peak can be found between 158 and 159 ppm.

Peroxymonocarbonate can not be obtained commercially as such. It can however be formed via the equilibrium reaction presented in Equation (5.4)

$$H_2O_2 + HCO_3^- \rightleftharpoons HCO_4^- + H_2O \tag{5.4}$$

Richardson et al. [53] followed the evolution of peroxymonocarbonate in water with 2 M H_2O_2 and 0.1 M $H^{13}CO_3^-$ via NMR and determined an equilibrium constant $K = 0.32 \pm 0.02\ M^{-1}$ for the reaction.

Calibration experiments were started by mixing and bicarbonate at known concentrations in water. Performing C^{13} and H^1 NMR spectroscopy measurements allows to track the peaks formed. Integrating the peaks obtained and using the previously presented calibrations for hydrogen peroxide and bicarbonate should allow to determine the amount of peroxymonocarbonate formed thus to calibrate the relative peak areas to concentrations for this product. The first step of the calibration was to determine the time needed for the system to reach equilibrium. Components were mixed, immediately inserted in the NMR instrument and measured at different times overnight.

2 M H_2O_2 - 0.5 M $KHCO_3$

The first batch contained 2 M hydrogen peroxide and 0.5 M potassium bicarbonate. No peroxymonocarbonate peak could be observed via C^{13} NMR. The difference with the study by Richardson et al. who observed peaks at already 0.1 M $KHCO_3$ is induced by the fact that they used C^{13} enriched bicarbonate.

2 M H_2O_2 - 2 M $KHCO_3$

The second and third batch contained 2 M hydrogen peroxide and 2 M potassium bicarbonate. First, C^{13} experiments were performed under air. Figure 5.35 presents the results obtained. The peaks obtained for bicarbonate were translated to concentrations using the previously defined calibration fit. The peaks for peroxymonocarbonate are represented in relative area to the maleic acid standard. Oddly, both concentration seem to increase. From Equation (5.4), it was expected that the increase of one component would be induced by the consumption of the other. Therefore, opposite trends were expected. Instrumental drift over time cannot be the cause of the increases observed as locking with benzene prevents the latter. The increase of both components' concentration may be due to equilibrium of the solution with the CO_2 contained in air (Equation (5.5)). However, this equilibrium reaction is not expected to cause an increase in the concentration of bicarbonate by 1 M. To investigate this effect, the same C^{13} experiments were repeated under nitrogen. The tube was first flushed with nitrogen. While flushing, components were added. The tube was then closed and loaded in the NMR instrument. Similar trends were observed, as shown in Figure 5.35, even though both concentration and relative area for bicarbonate and peroxymonocarbonate were lower than for the previous set of measurements. The lid of normal NMR tubes is not entirely air tight. The experiments should be repeated in an airtight tube to be able to draw conclusions. Another possibility for the unexpected trend may be incorrect tuning by the instrument prior to measurement. Automatic tuning is known to be prone to error for salty solutions. Even though tuning was done before each measurement, it may have been erroneous. Repeating the measurements with manual tuning would allow checking whether this has any effect.

$$CO_2 + H_2O \rightleftharpoons H_2CO_3 \rightleftharpoons HCO_3^- + H_2O \tag{5.5}$$

1 M H_2O_2 - 2 M $KHCO_3$

A fourth sample with 1 M hydrogen peroxide and 2 M potassium bicarbonate was investigated to observe the effect of concentration. Both H^1 and C^{13} spectrum acquisition were done under air. Figure 5.36 presents the C^{13} results obtained. The peaks obtained for bicarbonate were translated to concentrations using the previously defined calibration fit. The peaks for peroxymonocarbonate are represented in relative area to the maleic acid standard. Again, both HCO_3^- and HCO_4^- concentrations followed the same trend which goes against what is expected from Equation (5.4). The hydrogen peroxide concentration was tracked by looking at the water peak position shift [122]. Results were not yet translated to concentration as the calibration described previously for hydrogen peroxide was not considered satisfactory. The analysis will therefore be qualitative rather than quantitative. It is known that an increase in chemical shift of the water peak reflects an increase in hydrogen peroxide concentration. Figure 5.37 presents the evolution of hydrogen peroxide with time. Until 146 min, concentrations of bicarbonate, peroxymonocarbonate and hydrogen peroxide seemed to be increasing. At 234 min, the bicarbonate concentration dived from 3.78 M at the previous measurement to 1.4 M. The peroxymonocarbonate concentration also decreased. At that point, the hydrogen peroxide concentration was still increasing. A small decrease in hydrogen peroxide concentration at t = 277 min occurred

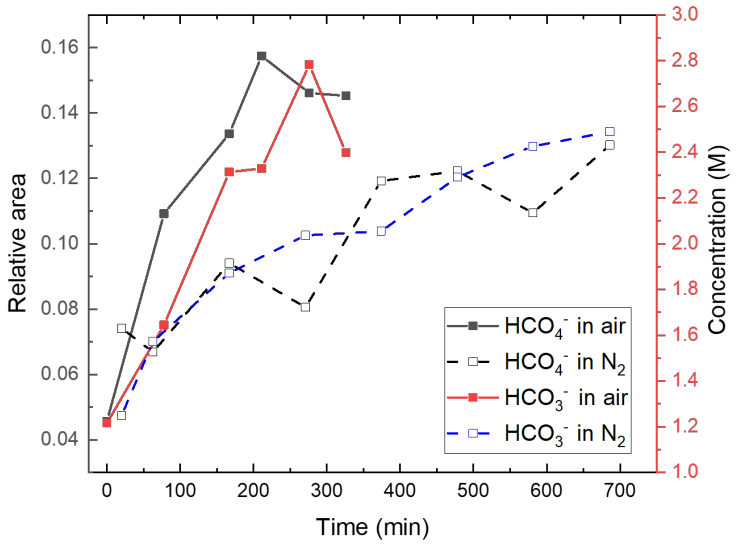

Figure 5.35: Relative area and concentration evolution over time under air and nitrogen for peroxymonocarbonate and bicarbonate obtained from a solution with 2 M H_2O_2 and 2 M $KHCO_3$ mixed at time = 0 min and followed by C^{13} NMR. Times reported refer to the completion of acquisition from the time of mixing.

parallel to an increase in peroxymonocarbonate and bicarbonate. Such unexplained behavior carried on until the final measurement at 495 min. No trend related to expected reactions can be derived from the obtained data. Tuning manually and using a sealed tube under nitrogen are needed to provide more insights on the reliability of this data.

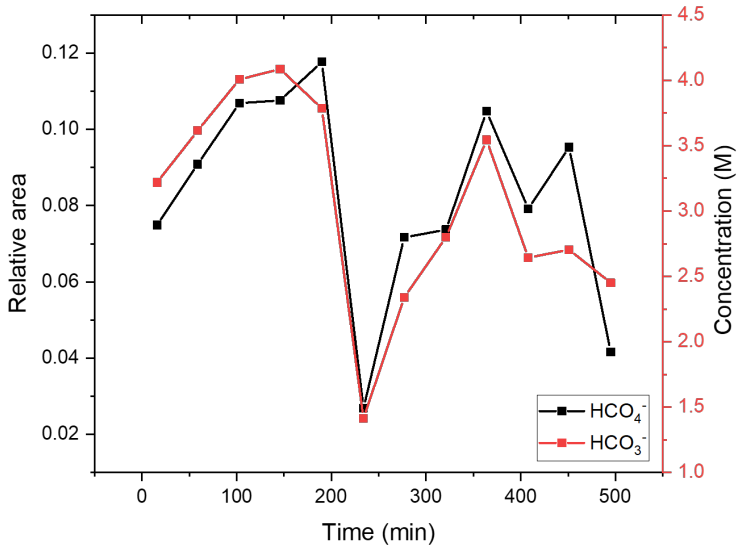

Figure 5.36: Relative area and concentration evolution over time for peroxymonocarbonate and bicarbonate obtained from a solution with 1 M H_2O_2 and 2 M $KHCO_3$ mixed at time = 0 min and followed by C^{13} NMR. Times reported refer to the completion of acquisition from the time of mixing.

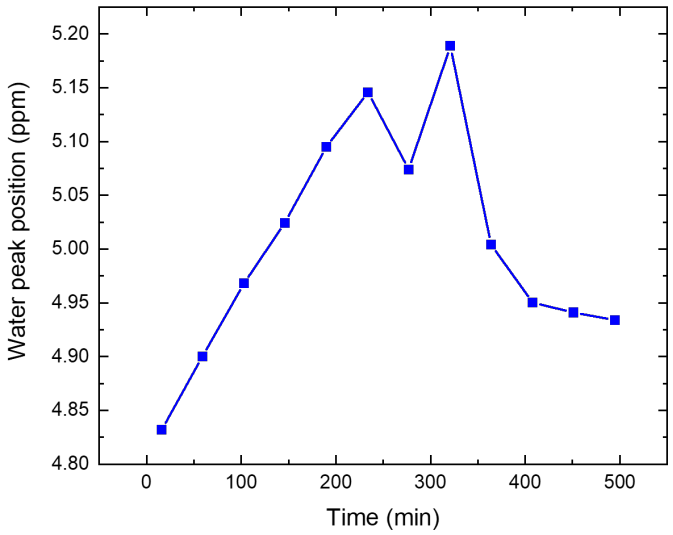

Figure 5.37: Water peak chemical shift evolution over time for peroxymonocarbonate and bicarbonate obtained from a solution with 1 M H_2O_2 and 2 M $KHCO_3$ mixed at time = 0 min and followed by H^1 NMR. Times reported refer to the completion of acquisition from the time of mixing.

6

DISCUSSION

The research questions defining this study encompass three main themes: the large scale implementation of the anodic peroxide evolution, the electrochemical performance for the reaction and the understanding of mechanisms behind the peroxide formation. The adequacy of methods used and the results obtained are assessed in this section and put in perspective with regard to findings in literature. Firstly, the techno-economic model used to explore the large scale implementation of the processes is discussed. Secondly, electrochemical methods and results obtained are reviewed. Finally, the product characterization methods and their outcomes for the understanding of electrochemical peroxide formation are assessed.

6.1. TECHNO-ECONOMIC MODEL

A techno-economic model was built in order to address the opportunities for large scale implementation of the anodic peroxide evolution. This model was based on the gross margin definition of eight processes: the Oxygen Evolution Reaction (OER) and the two-electron Water Oxidation Reaction (WOR) respectively coupled to the Hydrogen Evolution Reaction (HER), the CO_2 reduction to CO and C_2H_4 and the two-electron Oxygen Reduction Reaction (ORR). This section first discusses the results obtained in view of the research goals defined by the research sub-questions. Then, the model is put in perspective with previous models found in literature. Finally, the shortcomings and outlooks of the model are discussed.

6.1.1. OUTPUTS OF THE MODEL WITH RESPECT TO THE SCOPE OF THE STUDY

The feasibility of anodic hydrogen peroxide production has been proven on lab-scale by several research groups (Table 2.2). One of the core goals of this study was to evaluate the feasibility of upscaling the peroxide evolution to industrially relevant conditions. Three main threads were followed for this evaluation. The added-value of the coupled two-electron WOR was first gauged. Performance targets were then defined for the eight processes considered in order to establish a concrete link between theoretical work and commercial implementation. The influence of different technical parameters on final costs was finally evaluated with a sensitivity analysis.

ASSESSING THE ADDED-VALUE OF COMBINED PEROXIDE EVOLUTION

Most of the electrolytic processes produces a valuable cathodic product and oxidize water to oxygen on the anodic side. The OER is however a slow reaction with sluggish kinetics. Alternatives such as the coupling of thermodynamically more favorable anodic reaction have been investigated previously [56]. This study however focused on a thermodynamically less favorable product. The advantage of this study lies the production of an added-value product at the anode thus resulting in the output of two rather than one valuable streams from the electrolytic processes. The trade-off between thermodynamic disadvantage and added-value advantage was investigated using the gross margin model.

Based on the gross margin definition (Equation (C.5)), the costs of cathodic products were determined. Anodic product prices were kept constant and other parameters were fixed at base case values for all processes considered. As presented in Chapter 5, prices for all cathodic products considered (hydrogen, hydrogen peroxide, carbon monoxide and ethylene) decreased once coupled to the hydrogen peroxide evolution

rather than the OER (Table 5.2). This demonstrates that it is indeed of interest to couple an added-value reaction to cathodic processes. For the case of the two-electron WOR, the economical advantage even weights out the thermodynamic constraints. This observation is of great importance for emerging fields such as CO_2 reduction and electrochemical ammonia production. These processes are of interest as they allow the penetration of renewable sources of energy into the chemical sector. Moreover, long-term storage of renewable energy is currently an unanswered challenge to which electrolysis may contribute. The environmental prospects for these processes are tremendous however lack of economic feasibility alienates them from realistic large-scale implementation. The entrance of these processes on the market could significantly be boosted by coupling with the added-value peroxide evolution. The electrochemical production of ethylene from CO_2 for example, which was considered unfavorable when coupled to the OER [40, 55], became interesting when coupled to the two-electron WOR. It is important to note that choices in reaction to be coupled with the peroxide evolution should not only take the techno-economic parameters explored in this study. For example, the global demand for both anodic and cathodic products should be in the same range. An overproduction of on chemical would be counterproductive and may even lead to an unwanted decrease in price of the product.

The added-value of the process was further assessed by considering the case of hydrogen. The HER is a well-studied reaction implemented in state-of-the-art alkaline water electrolyzers. The current cost of electrochemically produced hydrogen is however still 4.5 times higher than from fossil-based production methods. Thanks to coupling of the HER to the added-value peroxide evolution, the electrochemical process may be made competitive with more traditional production methods.

All in all, the gross margin model was used as a tool to demonstrate the economic superiority of two-electron WOR based processes. Its potential role in the energy transition was established.

PERFORMANCE TARGETS

The link between experimental work and large-scale applications was drawn by defining performance targets for lab-scale research. To that effect, benchmarks for maximum operating voltage and minimum operating current density were defined and are presented in Section 5.1.1 and Section 5.1.2.

To illustrate the use of the model, the best results presented in literature for the two-electron WOR are used. Xia et al. showed groundbreaking anodic peroxide evolution coupled to the two-electron ORR at 1.7 V with a faradaic efficiency of 66 % [45]. These parameters were entered in the gross margin model for the considered process. Based on an anodic production of 100 ton/day hydrogen peroxide, a current density of 140 mA/cm^2 was needed for the process to break even over a period over 20 years, and 207 mA/cm^2 for a 30 % gross margin to be achieved over the same period of time. Experiments by Xia et al. reached current densities of 120 mA/cm^2. Even though these results are significantly superior to results obtained from previous studies (Table 2.2), some progress still needs to be made to obtain industrially significant results. The gross margin model allows to put experimental work in perspective on a scale of commercial implementation.

SENSITIVITY ANALYSIS

In order to assess which parameters are of main influence on the process profitability computed by the gross margin model, a sensitivity analysis was performed. The price of cathodic products was derived based on Equation (C.5). Different parameters thought to influence the final product price were varied between a worst case, base case and best case value (Section 6.1.1).

Table 6.1: Range of values for the sensitivity analysis

Sensitivity parameters	Worst case	Base case	Best case
Electricity price [$/kWh]	0.07	0.06	0.02
Current density [mA/cm^2]	100	300	500
Electrolyzer cost [$/h]	13.8	11.5	9.19
Overpotential [V]	0.8	0.6	0.4
Cathodic faradaic efficiency [%]	40	70	100
Single pass conversion [%]	30	50	70
CO_2 cost [$/ton]	150	60	20

For all processes considered apart from the coupled OER and C_2H_4, improvements in current density and electricity cost had the most impact on decreasing the product price (Figure 6.1). Overall, electricity price was of main importance for OER coupled cathodic products while current density was of main importance for the hydrogen peroxide evolution. As described by the Faraday law of electrolysis, the charge passed during

electrolysis directly relates to the amount of product produced. Electricity is the driver of the reaction which explains why its costs has such an influence. In the expression for the cathodic product price, derived from Equation (C.5), the current density divides the electrolyzer capital costs and the variable costs. The difference in effect of current density for the OER and the two-electron WOR on cathodic product prices is induced by the higher cost of raw materials for the anodic production of percarbonate. A significant share of electrolyte indeed leaves the system in percarbonate crystals. At a fixed voltage, a higher current density implies a smaller capital cost for production. The current passed through a system corresponds to the amount of charge passed per second thus relates to the amount of product that can be produced at a time. As the anodic peroxide evolution has two valuable product stream, this had a greater influence than for the OER. For all processes, a decrease in current density performance resulted in a more important negative impact on price than an increase resulted in a positive impact. This shows that it is important to reach a given threshold in current density after which improvements will only have a minor impact on process economics. These observations can be extended to other parameters as presented in Section 5.1.2 for catalyst lifetime and cathodic faradaic efficiencies.

Cathodic faradaic efficiency mainly had an influence on OER coupled processes with gas streams. The influence of separation equipment sizing was thereby confirmed. For the anodic peroxide evolution, the same separation processes were required for the cathodic products. The limited influence of cathodic faradaic efficiency on cathodic price when combined to the two-electron WOR is due to the added-value of the anodic product. This reduces the impact of the cathodic separation costs on the overall process economics.

The capital cost of the electrolyzer seemed to have an only limited impact on the overall economics. Variations in ± 20 % costs did not significantly affect the computed product prices. One of the limitations of the model mentioned previously was that it did not comprise scaling of the electrolyzer. This limitations is here shown to have only a minor impact on the results from the model. Voltage overpotential variations, CO_2 cost and single pass conversion did not induce large cost variations either.

6.1.2. A NOVEL GROSS MARGIN MODEL

In order to assess the model presented in this study, it is of importance to situate it in the scope of the field. The model was based on a study by Verma et al. on CO_2 reduction processes [55]. Appropriate changes were made to allow the study of the eight processes presented. This subsection provides some insights into knowledge gaps filled with this study and improvements made to the model.

Different gross margin studies have been used to assess the techno-economic feasibility of emerging processes. The goals for these studies included assessing the feasibility of different CO_2 reduction products [55]. The coupling to novel anodic reactions was also previously investigated. Valuable cathodic reactions were coupled to thermodynamically more favorable reactions than the OER. The superiority of glycerol oxidation as anodic product alternative was thereby demonstrated [56]. The focus of this study however laid in the energy savings due to thermodynamic improvements rather than the economic savings due to the added-value principle. The study presented in this report, therefore, fills a knowledge gap in the literature.

The gross margin model allows to investigate processes which are far from entering the market. Its main goal was to define targets to link experimental work and economic requirements thus to provide a road-map to lab-scale studies. It stems from this aspect that multiple assumptions were needed to estimate the process economics. Modelling choices which differ from the gross margin by Verma et al. are presented and defended here.

In the model by Verma et al., the electrolyzer was based on a 25 kW direct hydrogen PEM fuel cell stack. Their model comprised 70 stacks, which results in a total power of 1.75 MW for a daily production of 1500 kg hydrogen. Back of the envelope calculations from the faradaic law of electrolysis (Equation (3.11)) and for their assumed operating voltage of 1.6 V result in a power requirement of 2.8 MW. The power difference found nearly amounts a factor 2. Another striking aspect is the choice for a fuel cell stack as a model for the electrolyzer. CO_2 reduction electrolyzers are shifting towards Membrane Electrode Assembly (MEA) designs, which present similar characteristics to fuel cells. However, these types of cells are mostly relevant for gaseous products. For liquid products on the other hand, a catholyte is needed. In their model, Verma et al. transformed the cost of their electrolyzer to account for an electrolyte feed thus to approach an alkaline water electrolyzer design. It seems cumbersome to choose fuel cell stacks as a model and transform it to an alkaline water electrolyzer model. A multitude of commercial reports are available to assess the alkaline water electrolyzer economics. Inherent differences characterize PEM and alkaline water electrolyzers, such as the use of only a membrane instead of liquid electrolytes. Even though they corrected the cost of the electrolyte for the feed of electrolyte, it seems extremely prone to error to base the model on fundamentally different

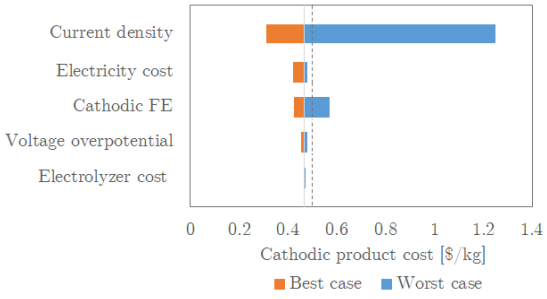

(a) OER/ORR

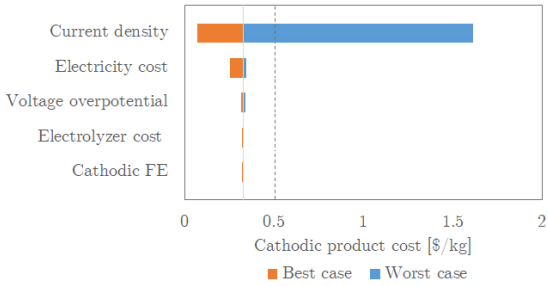

(b) H_2O_2ER/ORR

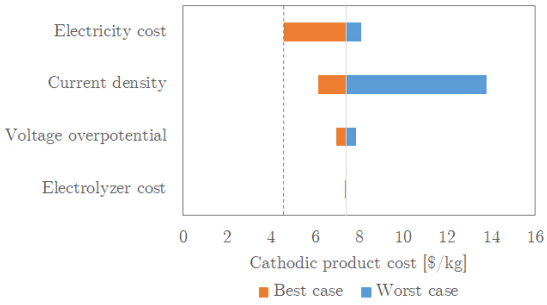

(c) OER/HER

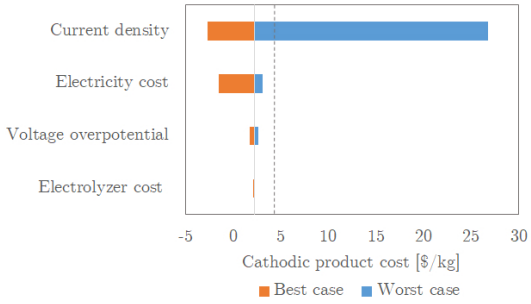

(d) H_2O_2ER/HER

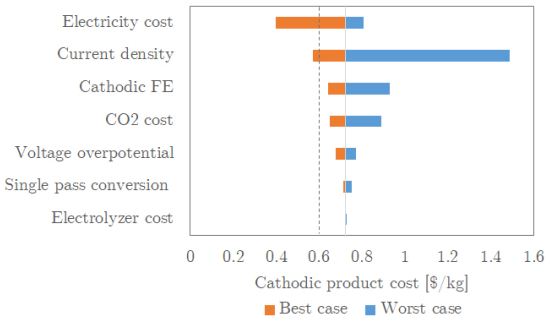

(e) OER/CO

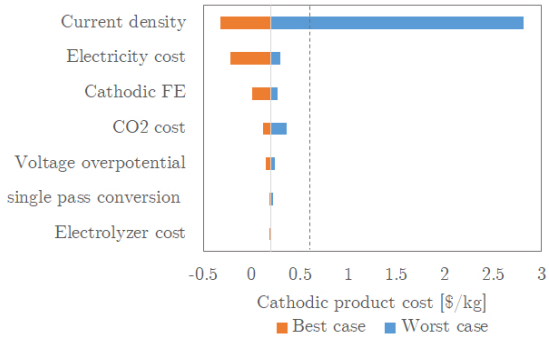

(f) H_2O_2ER/CO

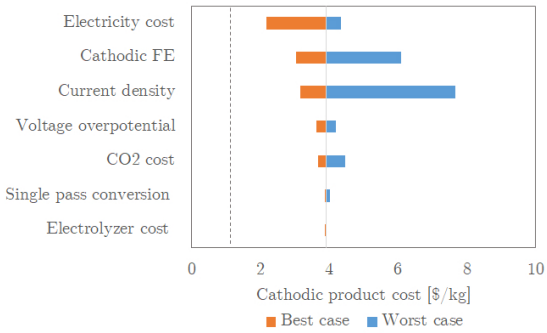

(g) OER/C_2H_4

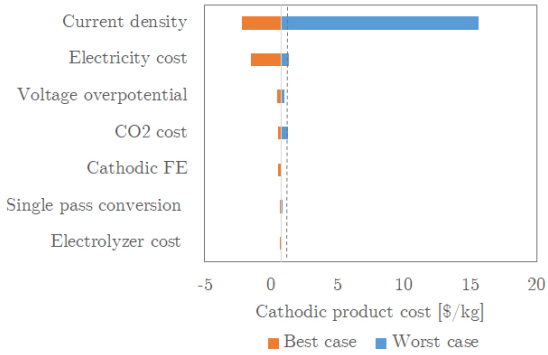

(h) H_2O_2ER/C_2H_4

Figure 6.1: Sensitivity analysis of the cathodic product price [$/kg] for the OER and H_2O_2 evolution reaction coupled to the HER, the CO_2 reduction to CO and ethylene and the two-electron ORR

equipment. Examples of other differences that were not accounted for are the active area per cell, which is approximately 25 times higher for alkaline water electrolysis [81]. This will have a major impact on the

minimum operating current density as defined in Equation (3.16). For these reasons, a new model was implemented in this study for the electrolyzer. The new model was based on alkaline electrolyzer costs from the National Renewable Energy Laboratory H2A Current Forecourt Hydrogen Production from Grid Electrolysis (1500 kg per day) model.

Another important change was implemented for the computation of separation costs. The model for separation by Verma et al. is based on the Sherwood plot for the separation of dilute streams. This model provides an *"empirical relationship between the market price [...] and its typical concentration [before it is] extracted"* [123]. On the other hand, they estimated the manufacturing costs by including capital costs for production (electrolyzer, catalyst, balance of plant) and variable costs (bill of materials, main utilities). It seems unbalanced to add separation costs which include all costs to electrolyzer costs which only take into account variable and capital costs (Figure 5.16). For this reason, separation costs in the new model were estimated using the same criteria as for the electrolyzer. Commercial equipment prices and process heuristics were used to determine the capital cost of the equipment, and utilities were accounted for. This all was translated in a price in $/kg of product output. Equipment scaling was taken into account for variations in efficiency.

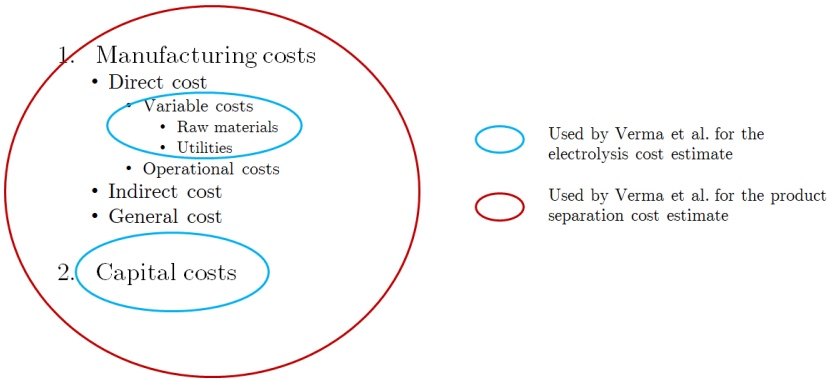

Figure 6.2: Cost decomposition for process cost evaluation during process design [88]

LIMITATIONS OF THE MODEL

Even if the model presents adaptations compared to previously presented gross margin models, some features can still be improved. First of all, the electrolyzer cost was determined based on a fixed power at base case parameters. This implies that changes in efficiency will not be translated in scale-up/ scale-down of the electrolyzer. The impact of this is however thought to be limited, as presented in the sensitivity analysis. In the latter, 20 % variations in electrolyzer costs did not significantly affect the final product price. Moreover, the implementation of catalyst costs can be improved. The catalyst lifetime was indeed not decoupled for the anode and cathode, which means that the individual effects of each side cannot be observed. Moreover, the downtime and operating costs for catalyst replacement were not taken into account, which may have a major impact. Another drawback of the implemented model is its lack of flexibility. As mentioned before, the economic evaluation will be very different for PEM electrolyzers for example. The model does not allow for quick changes in electrolyzer type.

Overall, the gross margin model aims at providing a design tool for emerging processes. It establishes the link between experimental work and large scale implementation. This implies that the development of processes considered is at a very early stage and that many assumptions will be required for the economic evaluation. For this reason, it seems fit to use a not too in-depth model, which will be required only at a later stage of the design process. This will be for example an analysis of the Net Present Value, which looks at detailed manufacturing and capital costs.

6.2. ELECTROCHEMISTRY

With the previously defined techno-economic performance targets in mind, experimental work was performed. Improvements of electrochemical performance for the upscaled peroxide production were investigated. For this purpose and in order to tackle the research sub-questions, three main paths were followed.

The synthesis and characterization of electrode materials with adequate properties were first investigated. The assembly of an appropriate set-up for electrochemical testing was then looked into. The electrochemical performance towards peroxide was finally investigated. This was done for two main types of materials: tin oxide based anodes and carbon-based ones. In the following subsections, these materials will be discussed with regard to the three main goals derived from the research sub-questions.

6.2.1. TIN-BASED MATERIALS

Tin (IV) oxide is a semi-conductor which is stable in a large pH window of the Pourbaix diagram against anodic dissolution [124]. The catalytic properties of SnO_2 for anodic peroxide evolution were demonstrated both via computational and experimental methods [18, 31]. The potential of the material for upscaled hydrogen peroxide production from the two-electron WOR was therefore explored. Different synthesis methods for the material were first explored. Synthesized samples were subsequently tested in the electrochemical set-up. This subsection provides a discussion on the results obtained for tin oxide based materials and their performance regarding the two-electron WOR.

SYNTHESIS

Different methods were used for the synthesis of tin (IV) oxide. Parameters such as heating treatment, thickness, surface morphology, composition and substrates were varied. Both the use of sputtering and spray pyrolysis were explored.

From the reactive DC magnetron sputtering experiments, it appeared that the oxygen partial pressure was the major factor in obtaining crystalline SnO_2. High temperature in the chamber during sputtering was observed to increase crystallinity for both SnO_2 and ITO and decrease resistivity for ITO. Spray pyrolysis was used in order to obtain nanostructured surfaces which were expected to lead to lower catalytic deactivation. From spray pyrolysis experiments, it appeared that small deposition batches were needed to obtain a homogeneous distribution across the sample. Increasing the number of cycles yielded an increase in crystallinity observed via XRD. Some tin oxide clusters were observed on the surface via EDS. The surface sprayed samples was studied via SEM. However, the electron beam emitted during SEM penetrates the sample to a certain extent thus reflects the upper layer of the surface rather than the surface itself. In order to provide a full assessment of the samples' surface, AFM acquisitions should be done.

ELECTROCHEMICAL PERFORMANCE

Overall, little peroxide production was observed and current density responses were very low. Parameters that did increase current density responses were high temperature depositions, thicker samples, spray deposition and doping. The use of a titanium substrate seemed to somewhat improve the current density response.

The only samples for which hydrogen peroxide was detected via Quantofix® strips were FTO and Sn_3O_4. It could however be that peroxide was produced but not above the detection limit. A previous study on tin (IV) oxide indeed reported a production of 1.5 µmol/(cm^2 min) at 3.1 V vs RHE and 9.5 mA/cm^2 [18]. Translated to the electrode area, electrolyte volume and duration of the experiments in this study, it amounts to a concentration of 0.23 mg/L . This is below the detection limit of the strips used, which starts at 0.5 mg/L. The lower current density nonetheless indicates that the set-up or materials used were not optimal. Moreover, in view of the previously presented techno-economical targets, tin (IV) and its derivatives do not seem very promising for industrial applications.

The peroxide production on Sn_3O_4 was unexpected as not reported previously by the field. The sample was first actually used for test runs as it was considered as a failed sample. After observing hydrogen peroxide production, experiments were reproduced and yielded the same result. Characterization and mechanisms behind this were not investigated as the scope of this study was to focus on the potential for large scale applications. SnO_2 was at that time thought to be more promising due to its stability in a large pH window while little was known on the Sn_3O_4 material produced. However, it may be interesting to try and understand the mechanisms favoring peroxide evolution on this material.

Several shortcomings of the study should be pointed out in order to put the results obtained in perspective and allow improvements in further studies. Some experiments should be repeated in order to draw conclusions on different parameters. The testing of SnO_2 deposited on FTO is for example most likely to have failed due to bad contact during cell assembly. Current density responses were indeed even lower than for tin (IV) oxide deposited on glass, which does not seem very likely. This sample is key in assessing the impact of different substrates such as titanium and FTO. Moreover, the SnO_2 deposited on FTO was expected to be

nanostructured, which may allow to conclude on the impact of surface morphology as well. The use of other characterization methods than SEM may allow to draw better conclusions regarding surface morphology.

6.2.2. CARBON-BASED MATERIALS

Moving away from metal oxides for the anodic peroxide evolution has yielded promising results so far [45, 48]. Carbon-based materials combined with the use of PTFE coatings have been shown to enhance the peroxide yield and current densities. This subsection puts in perspective results obtained with findings in literature and discusses a view for further experiments. First, conclusions presented in literature are challenged in view of the results obtained. Alternative explanations of the phenomena observed are then explored. A view on how future research in the field should be tackled is then exposed.

ELECTROCHEMICAL PERFORMANCE IN VIEW OF LITERATURE

As described in Section 4.1.5, different anodic samples were synthesized. Supports used were either Carbon Fiber Paper (CFP) or Gas Diffusion Electrode (GDE). One of the CFP samples was coated with PTFE in order to reproduce results obtained by Xia et al. [45].

In their study, novel effects were observed and thought to boost hydrogen peroxide production. A PTFE coating was applied on CFP. The samples were annealed, making the coating rough and more hydrophobic [125]. Due to this additional polymer layer, local oxygen gas formation was observed. This formation can be explained by the creation of a concentration gradient in the electrolyte at the surface of the aerophilic PTFE (Figure 6.3). The oxygen concentration becomes locally increased until it results in bubble formation. The authors asserted that the local oxygen concentration tuned the binding energy of the OH* intermediate. As presented in Section 2.3, this intermediate is central to the competitive water oxidation reactions towards oxygen, hydrogen peroxide or hydroxyl radicals. The confined oxygen presence would allow to favor catalysis towards the hydrogen peroxide product.

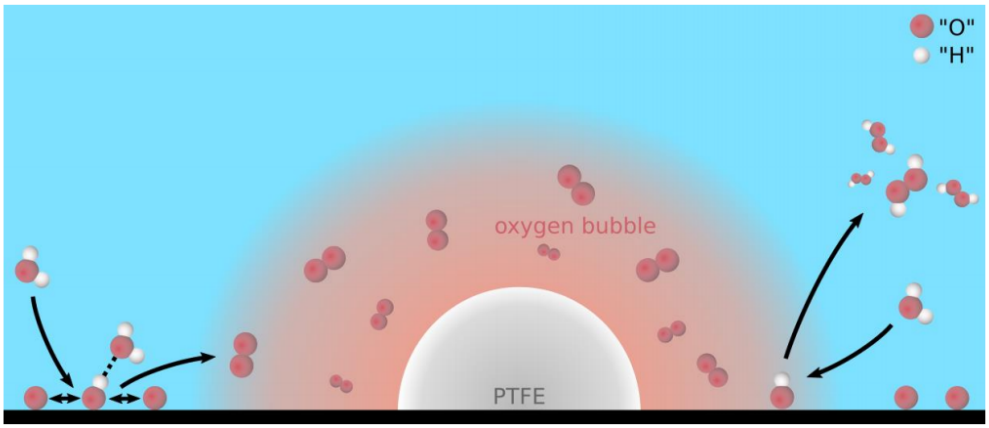

Figure 6.3: Schematic drawing of the coated catalyst surface, its effect on local oxygen concentration and assumed enhanced reaction pathways towards hydrogen peroxide [45].

Another novel finding presented by the authors concerns the effect of electrolyte. So far, bicarbonate was thought to be involved in the peroxide evolution on metal oxides and carbonate was thought to be involved for evolution on Boron-Doped Diamond (BDD) electrodes(Section 2.3). Xia et al. claim to have reached enhanced hydrogen peroxide yield via a direct synthesis route which does not involve the electrolyte ions as intermediates. To support this, they quantified peroxide evolution in sodium bicarbonate, sodium carbonate, sodium metaborate and tripotassium phosphate. Carbonate yielded the best results thus they excluded the effect of higher pH. An isotope study was performed in which O^{18} contents were followed via isotope mass spectroscopy. The isotope contents were followed for electrolyzed and unelectrolyzed Na_2CO_3. If percarbonate was an important intermediate, a difference in isotope content was expected at the end of the electrolysis due to chemical bond reconfiguration. However, during the study, they did not observe any difference in O^{18} ratio thus concluded that no intermediates were involved. According to their study, this would explain the superior performance in carbonate compared to bicarbonate.

Even though their results were indisputably groundbreaking, several question marks arise regarding the interpretation of the results and the validity of the direct synthesis hypothesis. The reproduction of experiments in this study was performed in order to delve into the mechanisms behind the enhanced peroxide formation for the used CFP materials.

First of all, experiments in carbonate and bicarbonate yielded significant current density responses during chronoamperometry, namely 60 and 15 mA/cm^2 respectively on CFP (Section 5.2.4). Large difference were also seen in the study by Xia et al, with *ca* 20 mA/cm^2 in 1 M $NaHCO_3$ and 40 mA/cm^2 in 1 M Na_2CO_3 on 60 % loaded CFP at a potential of 2.3vs RHE. If the difference is not explained by the involvement of ions in the oxidation reactions, then an effect influencing the current density could be ionic transport. The transference number of an ion provides the fraction of total current carried by a given ion in the solution [38]. It is defined as:

$$t_j = \frac{i_j}{i_{total}} = \frac{|z_j| u_j C_j}{\sum |z_k| u_k C_k} \tag{6.1}$$

where z is the charge, C the concentration and u the mobility. The mobility can be either found from tabulated data or computed with the Einstein-Schmoluchowski equation (Equation (6.2)) using the diffusion coefficient D of the ion, its charge z, the Faraday constant, the ideal gas constant and the temperature.

$$u_j = \frac{|z_j| F D_j}{RT} \tag{6.2}$$

Transference numbers were computed for the ions in the four systems studied: HCO_3^- in 2 M $KHCO_3$ and 1 M K_2CO_3 and CO_3^{2-} in 2 M K_2CO_3 and 1 M Na_2CO_3. Mobility for Na^+, K^+ and HCO_3^- was taken from tabulated data-sets [38]. The mobility for CO_3^{2-} was calculated using the Einstein-Schmoluchowski equation using a diffusion coefficient from literature [126]. The computed transference numbers were respectively 0.38 and 0.44 for HCO_3^- and CO_3^{2-} in 2 M $KHCO_3$ and K_2CO_3, and 0.47 and 0.55 for HCO_3^- and CO_3^{2-} in 1 M $NaHCO_3$ and Na_2CO_3. These transference numbers show that even though the fraction of current carried by CO_3^{2-} is higher than by HCO_3^-, it is not large enough to explain the differences in current density responses observed. This seems to indicate that carbonate is somehow involved and not only a charge carrier. All electrolytes tested by Xia et al. (bicarbonate, carbonate, perborate and phosphate) can enclose peroxide bonds to form for example peroxymonocarbonate, percarbonate and peroxymonophosphate. Next to mobility, pH variation between the electrolytes used may be another factor to explain the current density differences obtained. It would be interesting to look at the behaviour of the PTFE coated electrodes in a specie that does not stabilize peroxide, such as KOH for example.

Another noteworthy remark can be made regarding the assessment of the role of binding energy at the catalyst surface. In order to support the hypothesis for the role of oxygen in tuning the binding energy, Xia et al. followed the normalized partial current density of oxygen under different potentials (Figure 6.4). The results obtained were similar for pristine and for PTFE coated samples. An oxygen excess could, according to Le Châtelier principle, drive the reaction towards hydrogen peroxide. By showing that the partial current density of oxygen remained similar, they exclude the role of oxygen in such a mechanism. The very same result could however be used against their hypothesis on the binding energy of intermediates. If the binding energy was tuned to favor hydrogen peroxide evolution, then the selectivity towards oxygen would be expected to decrease thus decrease the partial current density.

ALTERNATIVE EXPLANATIONS FOR THE ENHANCED PEROXIDE PRODUCTION

Several discrepancies between hypotheses and results for the peroxide evolution on PTFE coated samples have been pointed out. A view on other mechanisms to explain the results obtained is discussed here.

It seems very unlikely that carbonate is not involved in the reaction when looking at the tremendous difference in current density obtained for different electrolytes. On metal oxide anodes, bicarbonate is thought to oxidize to peroxymonocarbonate and hydrolyze back in the bulk. It could be that in a similar fashion, carbonate would oxidize to percarbonate and hydrolyze back in the bulk:

$$2\,CO_3^{2-} \longrightarrow C_2O_6^{2-} + 2\,e^- \tag{6.3}$$

$$C_2O_6^{2-} + 2\,OH^- \rightleftharpoons 2\,CO_3^{2-} + H_2O_2 \tag{6.4}$$

Perhaps the potential for carbonate oxidation or the equilibrium reaction for carbonate regeneration is more favorable than for the bicarbonate system. Little literature could be found on the topic. Additional research on these parameters would provide some useful insights.

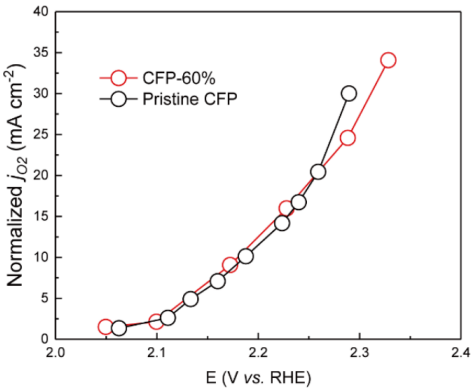

Figure 6.4: ECSA-normalized partial current of oxygen under different applied potentials [45].

It is striking that both BDD and carbon-based electrodes present performances towards peroxide that are in the same range. Moreover, for both types of electrodes, significantly improved results were obtained in carbonate electrolytes. The link between the two systems may lead to a better understanding of the working behind PTFE coated CFP. BDD electrodes have been investigated for peroxide evolution by different groups [29, 36, 37, 44]. The enhanced peroxide production on BDD is thought to be linked to the formation of hydroxyl radicals. The proposed mechanisms on these electrodes are as follow: catalyzed one-electron water oxidation to hydroxyl radicals (Equation (6.5)) followed by reaction with carbonate (Equation (6.6)).

$$\mathrm{BDD} + \mathrm{OH^-} \longrightarrow \mathrm{BDD}(\cdot\mathrm{OH}) + \mathrm{e^-} \tag{6.5}$$

$$2\,\mathrm{CO_3^{2-}} + 2\,\mathrm{BDD}(\cdot\mathrm{OH}) \longrightarrow \mathrm{C_2O_6^{2-}} + 2\,\mathrm{OH^-} \tag{6.6}$$

Similar mechanisms have been reported for BDD electrodes in bicarbonate, which would explain why peroxide was also formed in the latter electrolyte.

A noteworthy observation can be made on the role of PTFE. It has been asserted by Xia et al. (2020) that PTFE is involved in tuning the binding energy of WOR intermediates due to the local oxygen production. Polymer coating on a nickel electrode even resulted in enhanced peroxide production while nickel is an OER catalyst. It may be, however, that the formation of oxygen is not at the origin of the improved catalytic performance observed. A study by Ngene et al. (2014) has demonstrated that PTFE deposition on Pd catalysts improved the catalytic performance towards hydrogen [127]. Chemical structure modification of the catalyst surface atoms was induced by the application of the polymeric layer. An XPS study allowed to demonstrate that the electron binding energy of surface catalyst atoms was indeed altered compared to bulk properties of the same materials. These modifications resulted in changes in the binding energies of the surface atoms. This resulted in preferred hydrogen evolution for the Pd catalysts studied by Ngene et al. The PTFE layer may have induced changes in binding energies on CFP and nickel in the same fashion as it did for Pd and not due to the local oxygen formation.

OUTLOOKS FOR THE FIELD

The novel findings on carbon-based electrodes and PTFE are undeniably very promising for the field of anodic hydrogen peroxide evolution. The main goal for researchers in the field should be to aim for the techno-economic performance targets that allow the industrial implementation of the process. To do so, it is of importance to understand the underlying mechanisms behind the enhanced peroxide formation. In light of the previously presented hypotheses which challenge statements by Xia et al., the author of this study provides a view on how to tackle the verification of these hypotheses.

One of the main statements by Xia et al. is that the three-phase boundary between electrolyte, catalyst and oxygen formed induces the changes in binding energy thus improves peroxide yields. Gas Diffusion Electrode (GDE) were successfully tested in this study (Section 5.2.1). They present similar properties to coated CFP, which is a carbon support and PTFE. Moreover, they enable the formation of a three-phase boundary system. Passing different gases at the GDE may allow to assess the actual effect of the oxygen gas itself. A novel method to obtain extended three-phase boundaries from GDE has been published by Pelayo García de Arquer et al. A thin ionomeric layer of Nafion was added onto the surface of a GDE by the authors. This allowed creating

an architecture that further decoupled gas, ion and electron transport [128]. Such a system allowed to reach current densities superior to 1 A/cm^2 for CO_2 reduction. The implementation of such a system may allow to achieve improved results as well for peroxide evolution.

The use of a zero-gap type of set-up may allow to solve the matter of direct synthesis *vs* carbonate involvement. By sputtering the catalyst and PTFE layer on top of the membrane, one circumvents the use of an electrolyte.

6.3. PRODUCT CHARACTERIZATION

As explored in the previous section and in Section 2.3, different mechanisms involving bicarbonate and carbonate are thought to affect the electrochemical performances of the two-electron WOR. The role of these components both as intermediates and as stabilizing agents for the peroxide product is not fully understood yet. Unveiling these mechanisms is key in choosing, designing and optimizing adequate electrode materials and cells. From the research sub-questions of this study, three main product characterization themes of importance can be derived. First, the quantification of the product allows to assess the performance of different materials. Identifying the different peroxide-containing compounds and quantifying them individually and rapidly would allow to follow their evolution during electrolysis. Based on these results, one could assess the electrolytic production mechanisms. This would allow to determine the factors that matter and provide tools to reach for the techno-economic targets that make the process viable.

To tackle these goals, different methods were implemented. These included the use of Quantofix® strips for quick quantification, the use of titration for more accurate quantification, and finally the use of NMR spectroscopy to discern the different products. This section explores the calibration results obtained in this study and their potential in enlightening the mechanisms behind the anodic hydrogen peroxide evolution.

6.3.1. QUANTITATIVE PRODUCT EVALUATION

Different methods were used for the quantification of produced peroxide. Quantofix® strips are a quick method to assess the presence of hydrogen peroxide in solution. The lack of precision is however inconvenient thus it should be used only for quick estimates or to cross-check results obtained. It would be wise to test the strips in electrolyte solutions containing known hydrogen peroxide concentrations. This would allow to check whether the electrolyte somehow interferes with the result.

Quantification was also explored via permanganate titration. This method was the most widely reported one for electrochemically produced peroxide quantification. The addition of diluted acid is needed to allow the correct titration reaction to take place and prevent the formation of MnO_2 [109]. One of the concerns is the interaction between the acid and (bi)carbonate compounds towards CO_2. If peroxymonocarbonate reacts with the acid, then the result from the titration may actually be an underestimate of the hydrogen peroxide concentration. This could be cross-checked by using Quantofix® strips.

The use of UV-vis spectroscopy combined with titration for enhanced precision of the analysis was investigated. It appeared that calibration in carbonate and bicarbonate solutions was made difficult due to low transmittance. The use of this method appeared cumbersome. For a well-calibrated set-up, additional precision may not be needed.

6.3.2. QUALITATIVE PRODUCT EVALUATION

Even though titration is a good method to observe the quantity of peroxide present in a sample, it only reflects the oxidation ability of the solution. In order to understand the reaction mechanisms behind electrochemical peroxide formation, it is of importance to discern these compounds. NMR provides a tool to qualitatively analyze the evolution of the separate compounds during electrolysis. The calibration of different peroxide concentrations and their respective acquired spectrum was investigated in this study.

C^{13} NMR allows the identification of different (bi)carbonate containing compounds within *ca* 10 min. No additional compounds are to be added to allow the analysis, which prevents deleterious interactions with the sample. Most of the compounds studied yielded a linear relationship between the concentration inserted and the relative peak area measured. Relative peak areas for the peroxymonocarbonate ion could however not be calibrated for concentration. The compound is not available commercially. Its formation can be obtained via the equilibrium reaction for the addition of bicarbonate and hydrogen peroxide. Observed responses did however not match the expected reaction (Section 5.3.2). Further studies are required to understand the acquired spectra and their unexpected data.

If the calibration of peroxymonocarbonate fails, the method can still be used in combination with titration. All other compounds have indeed been calibrated. Ratios of relative peak areas are proportionally related to the concentration of compounds. One can therefore calculate the concentration of peroxymonocarbonate back by using the total concentration of oxidant gotten from titration. One of the main drawbacks is however the problem of detection limits. It may be that some products are produced in very small amounts. These will then not appear on the NMR spectra, and would be accounted for as peroxymonocarbonate.

Overall, the detection limit is one of the main concerns for the use of NMR spectroscopy to quantify the peroxide compounds individually. If the concentration is to be followed quasi-live during electrolysis (samples measured periodically), then the concentration will be very low at the start of the experiments. This can be tackled by diminishing the volume of electrolyte. However, a trade-off has to be made as liquid will be collected for the measurements and electrolyte is required for the proper running of the electrolysis. If the concentration ratios for different do not vary along electrolysis time then taking NMR measurements only at the end of the experiments and titration at regular intervals would be fine.

Another important limitation is the time between collection of the sample and data acquisition. C^{13} NMR spectra are acquired in the order of 10 min. Due to this, if detection limits are not an issue and peroxymonocarbonate can be calibrated, the spectrum will provide an overview of compounds contained in the bulk. This however will not reflect surface mechanisms thus will only provide a limited understanding of the reaction mechanisms involved.

6.4. A VIEW ON PROSPECTS AND CHALLENGES FOR THE FIELD

The prospects for the anodic peroxide evolution were highlighted with the techno-economic study performed. Some recent experimental work on carbon-based electrodes has shown that performance targets are getting closer to realization. However, some important progress still is to be made. In this section, a vision on the work that is to be performed and how it should be tackled by researchers is laid down.

6.4.1. A WORD ON EXPERIMENTAL WORK FOR IMPROVED PEROXIDE EVOLUTION

New possibilities have opened the field of anodic peroxide evolution with the testing of PTFE-coated carbon electrodes. Due to these exciting novel findings, the field now finds itself at a crossroads full of opportunities.

It can not be stressed enough how important it is that all the experimental work keeps final targets in mind. The main advantage of the anodic peroxide evolution reaction is its added-value compared to the OER. The reaction explored in this study can be a tool in helping the large scale implementation of electrolysis. By doing so, important openings can be created for the field of renewable energies. Those include long-term energy storage in the form of chemical bonds, but also allowing renewables to enter the chemical sectors in which they are currently underrepresented. Next to their technological enthusiasm for novel findings, researchers should bear these applications in mind when making choices in the turn their projects take. Scientists play a central role in the development of solutions for societal challenges such as the energy problem and should be aware of that responsibility.

The design of new electrodes and cells for enhanced peroxide production should be explored keeping techno-economic targets in mind. Choices of materials should be guided not only by performance but also by availability and cost. Carbon-based electrodes therefore provide exciting prospects for electrochemical applications as carbon is one of the most abundant elements on earth. Further research should focus on reaching industrial applications by looking into realistic materials. Moreover, understanding the mechanisms behind the peroxide evolution should be delved into as informed material and cell design will most certainly lead to better results than shooting in the dark.

6.4.2. A PAMPHLET FOR CROSS-POLLINATION OF IDEAS

It is compelling to note that scientists, such as Xia et al. with their study on the effect of PTFE for enhanced peroxide production, manage to come up with groundbreaking ideas. Several factors, such as the pressure for publication, push the researcher towards safe options. These often include reproducing and building on results obtained by colleagues. However, the generation and testing of out-of-the-box ideas is essential for progress. So what does it take to stay innovative without losing oneself in speculation?

Over the ages, humans have developed a full-blown language capacity. Communication should be a central tool in the scientific community. Events such as conferences already ensure the exchange of ideas between different groups and countries. However, the idea exchange should also be present between fields. The

anodic peroxide evolution is a good example of this communication desideratum. The coupling to cathodic reactions is inherent to the peroxide evolution reaction. If no one in the CO_2 reduction field hears about it, its advantages may never get explored. If techno-economic studies are not involved in the design process, then necessary conditions for viable industrial implementation may be overseen. The cross-pollination of ideas between fields is central to keep an open mind in the idea generation. After years of working in a field, it is natural to get enclosed in the topic. The exchange of ideas with other people can ensure the flow of ideas keeps going and may help people to come up with exceptional, groundbreaking ideas.

To conclude this discussion, it is important to stress how communication and exchange of ideas can and should play a central role in the scientific community. Not only can it allow to learn from each other and come up with innovative ideas, but it is also a great way to share one's enthusiasm for the topic. Bearing these tools in mind, I have good confidence that the community will continue to come up with incredible solutions to the challenges we face.

7

CONCLUSIONS AND RECOMMENDATIONS

To conclude the techno-economic assessment of the peroxide evolution reaction, the three main themes encompassed in the main research question and the outcomes from this study are conflated. The main research question was: *"What is the potential for anodic evolution of H_2O_2 at industrial conditions and which forms does the product take?"* The aim of the study was to investigate the potential industrial relevance of the anodic peroxide evolution, both from an economic point of view as from an electrochemical one. Electrochemical parameters of influence were investigated experimentally, keeping in mind the performance targets obtained from the economic study. Methods to assess the mechanisms behind the peroxide production were investigated in order to improve electrochemical design strategies. A retrospective look is taken here at the research sub-questions. The outcomes of this study with respect to the latter and to the knowledge gaps identified are recapitulated. Recommendations for further studies on the topic are provided.

1. "What are the performance targets to make the hydrogen peroxide evolution profitable? What are the opportunities for the product combined to hydrogen production, as well as oxygen and carbon dioxide reduction?"

The industrial relevance of the study was first assessed by developing a gross margin model. This model provides a first rough estimate of process economics based on electrochemical criteria. This model is particularly relevant to assess the viability of emerging processes. It indeed allows to link early-stage experimental work to commercial applications. The gross margin model developed allowed to evaluate the potential of the coupled two-electron water oxidation reaction over the oxygen evolution reaction. The coupling of four cathodic reaction was investigated based on the gross margin model. These reactions included the hydrogen evolution reaction, the two-electron oxygen reduction reaction and the carbon dioxide reduction to carbon monoxide and ethylene respectively.

The water oxidation reaction towards hydrogen peroxide is thermodynamically less favorable than towards oxygen. The gross margin model allowed to first assess the trade-off between thermodynamic disadvantage and economic advantage due to the production of an added-value chemical. For each of the cathodic reactions observed, the product price calculated was lower when coupled with the hydrogen peroxide evolution reaction than with the oxygen evolution reaction. Performance targets in maximum operating voltage and minimum operating current density were defined for the eight processes considered.

The CO_2 reduction to ethylene coupled to the oxygen evolution reaction was demonstrated to be only economically feasible at low overpotentials. This corroborated previous techno-economical results presented in literature. The coupling to the anodic peroxide evolution reaction enabled to significantly decrease performance targets required for the viability of the process. In the same way, prices computed from the model for electrochemically produced hydrogen were significantly decreased when coupled to the two-electron water oxidation reaction thus enabling competition with more traditional fossil-based synthesis methods. These results highlighted the opportunities for the anodic peroxide evolution. The added-value reaction may play an important role in boosting the implementation of electrochemical processes. This in turn may allow to favor the penetration of renewable energies in the chemical sectors, in which they are underrepresented.

Moreover, it may provide solutions to long-term storage of energy in the from of chemical bonds. New processes, such as the reduction of carbon dioxide investigated in this study, but perhaps also other reactions such as electrochemical ammonia production, may be made feasible thanks to the peroxide evolution. Not only would the anodic peroxide evolution improve economics for cathodic processes, it would also circumvent the need for centralized and energy intensive peroxide production processes. On-site production at low concentrations enabled by the electrochemical process would allow to tackle transport and safety concerns that accompany traditional peroxide production processes.

The gross margin model is a tool that may be implemented on a way broader scale. It is highly flexible and should be explored for various processes. The model provides guidelines for experimental work that provide industrial context to more fundamental research.

2. "Which materials are the most suitable? What are the effects of different deposition techniques?"

Two main types of materials were investigated to evaluate the electrochemical production of peroxide for industrial applications. The materials chosen were tin oxide based and carbon-based. Due to time constraints, depositions techniques were mainly investigated. Results for carbon-based materials were however significantly more promising.

Tin oxide presents stability in a large pH window of the Pourbaix diagram, which is why its investigation was chosen in view of industrial application goals. Tin oxide-based materials had been previously investigated in literature, but only at low potentials. Modifications to achieve higher current densities were looked at in this study. Effects such as heating treatments for higher crystallinity and doping positively affected the current density responses. Different substrates were investigated, including glass, FTO and titanium. Due to missing data-sets, no clear conclusions could be drawn from these experiments. Two deposition techniques were investigated: DC magnetron sputtering and spray pyrolysis. The goals of using these techniques was to evaluate the effect of surface morphology on stability of the catalyst. Sprayed samples yielded somewhat higher current density responses than sputtered samples of the same material.

Overall, performances obtained on tin oxide and tin oxide derivatives were extremely low. In most cases, results were lower than studies reported in literature. This may have been induced by the experimental set-up. Out of all samples tested, only two resulted in detectable peroxide evolution. These were a commercial FTO sample on glass and a sputtered Sn_3O_4 sample on titanium. Evolution of peroxide may have occurred on other samples but have been too low to allow detection. It may be interesting to explore the properties of the synthesized Sn_3O_4 and understand the mechanisms behind the enhanced peroxide production.

Carbon-based electrodes yielded significantly higher current density responses and peroxide yields than tin oxide-based materials. The effect of Teflon coating could not be assessed due to deposition problems. The methods for the electrode preparation still are to be improved in order to evaluate and understand the effect of the polymeric layer. Gas diffusion electrodes, based on a microporous layer and a polymeric layer, yielded similar results to carbon fiber paper electrodes reported in literature. An important knowledge gap was identified regarding mechanisms behind the improved peroxide production on carbon-based electrodes. Time constraints did not allow to delve into the latter, however, several experiments can be recommended for further research. First, it seems essential to determine the role played by carbonate in the reaction. A systematic concentration study should allow to establish the influence of the electrolyte on the performance and on the product. Comparison with a different electrolyte such as potassium hydroxide may allow to assess the potential formation of enclosed peroxide bonds such as percarbonates. The use of gas diffusion electrodes combined with different gases may allow to assess the role of Teflon in the reaction. So far, the formation of oxygen at the aerophilic surface was thought to influence the binding energy of intermediates towards hydrogen peroxide. It may however be that Teflon simply influences the electronic configuration of the catalyst's surface. The use of a zero-gap type of electrolysis cell could enable the determination of the role of the electrolyte at carbon-based materials. By sputtering the catalyst directly onto the membrane, the use of the electrolyte is circumvented.

From the electrochemical study of materials for the anodic peroxide evolution, it appeared that carbon-based materials offer greater possibilities than tin oxide materials. Even though the latter were thought to

be more stable, performances obtained remained very low and little peroxide production was observed. Carbon-based materials on the other end presented results in the range of boron-doped diamond electrode performances, which approach techno-economic targets for industrial applications. These performances were thought to be linked to the use of carbonate electrolytes. The influence of the latter should be explored in order to make informed design choices for the material and the electrolytic cell.

3. "What mechanisms govern the process at low and high current densities? What methods are most appropriate for peroxide detection?"

Understanding the mechanisms behind the peroxide production is of importance to improve electrochemical materials and cell design and thereby to aim for industrial application targets. The calibration of different methods was investigated for both quantitative and qualitative purposes. Due to reduced time for experiments, these methods could not be implemented for the analysis of electrochemical products.

The quantification of the products was investigated via both Quantofix® strips and permanganate titration methods. These methods are used widely in literature for peroxide quantification. Even though calibration experiments could not be finished, no challenges are expected for these methods.

An important knowledge gap was identified in literature regarding the exact reaction mechanisms behind the anodic peroxide production. C^{13} NMR spectroscopy experiments were investigated to identify and quantify different peroxide compounds individually. During calibration experiments, the possibility of identifying different compounds was established. Calibration fits for the quantification of H_2O_2, HCO_3^-, CO_3^{2-} and $C_2O_6^{2-}$ were successfully obtained. The calibration of HCO_4] was not achieved yet. This calibration can be achieved by following the equilibrium reaction between hydrogen peroxide and bicarbonate. Data acquired for the evolution of these compounds was not understood. This may be due to interactions with CO_2 or tuning problems of the equipment. Additional experiments are required to complete the calibration.

Some concerns arise regarding the implementation of NMR analysis for electrochemical production of peroxide compounds. Firstly, detection limits may be a challenge to follow the evolution of the different compounds. The coupling to other methods, such as titration, may allow to obtain a broader picture. Another challenge concerns the opportunities for the understanding the mechanisms behind the peroxide production based on NMR spectra. A C^{13} measurement with the parameters used for calibration took around 10 min. The time between the retrieval of the aliquot and its analysis may not reflect the electrochemical mechanisms but rather the equilibria in the bulk. Perhaps the use of operando spectroscopic methods should be looked into.

To summarize, industrial application targets have been defined for the anodic peroxide evolution based on a gross margin model. The broad application possibilities for this reaction make its potential role within the field of electrochemistry tremendous. Two types of electrocatalysts were investigated, namely tin oxide and carbon-based materials. The latter yielded the most promising results. The mechanisms behind these results are not understood yet thus some product characterization methods to palliate this have been investigated. Future research should focus on improving these anodes and understanding the mechanisms behind the peroxide formation, bearing industrial targets in mind.

List of Figures

List of Tables

ABBREVIATIONS

AFM Atomic Force Microscope.

BDD Boron-Doped Diamond.

BOP Balance of Plant.

CFP Carbon Fiber Paper.

CV Cyclic Voltammetry.

DC Direct Current.

DFT Density Functional Theory.

EC electro-chemical.

EDS Energy-Dispersive X-Ray Spectroscopy.

FE Faradaic Efficiency.

FTO Fluorine-doped Tin Oxide.

GC Gas Chromatograph(y).

GDE Gas Diffusion Electrode.

HER Hydrogen Evolution Reaction.

ITO Indium Tin oxide.

MEA Membrane Electrode Assembly.

MECS Materials for Energy Storage and Conversion.

NMR Nuclear Magnetic Resonance.

OC Open Circuit.

OER Oxygen Evolution Reaction.

ORR Oxygen Reduction Reaction.

PEC photoelectro-chemical.

PEM Proton Exchange Membrane.

PSA Pressure Swing Adsorption.

PTFE Polytetrafluoroethylene.

PV Photovoltaic.

RHE Reversible Hydrogen Electrode.

SEM Scanning Electron Microscopy.

TMS tetramethylsilane.

WOR Water Oxidation Reaction.

XPS X-ray Photoelectron Spectroscopy.

XRD X-Ray Diffraction.

REFERENCE LIST

[1] *World population: Past, present, and future,* https://www.worldometers.info/world-population/, accessed: 2020-03-04.

[2] H. Ritchie and M. Roser, *Energy,* https://ourworldindata.org/energy (2018), accessed: 2020-03-04.

[3] *IEA: data and statistics,* https://www.iea.org/data-and-statistics (2017), accessed: 2020-03-04.

[4] *The european green deal,* https://ec.europa.eu/info/sites/info/files/european-green-deal-communication_en.pdf (2020), accessed: 2020-03-04.

[5] S. T. Revankar, *Chapter 6: Chemical energy storage,* in *Storage and Hybridization of Nuclear Energy* (Elsevier, 2019) pp. 177–227.

[6] K.-D. Jäger, O. Isabella, A. H. Smets, R. A. van Swaaij, and M. Zeman, *Solar energy: fundamentals, technology and systems* (UIT Cambridge, 2016).

[7] O. Schmidt, A. Gambhir, I. Staffell, A. Hawkes, J. Nelson, and S. Few, *Future cost and performance of water electrolysis: An expert elicitation study,* International Journal of Hydrogen Energy **42**, 30470 (2017).

[8] A. van Wijk, *The green hydrogen economy in the Northern Netherlands* (Noordelijke Innovation Board, 2017).

[9] C. B. Robledo, L. B. van Leeuwen, and A. J. van Wijk, *Hydrogen fuel cell scooter with plug-out features for combined transport and residential power generation,* International Journal of Hydrogen Energy **44**, 29648 (2019).

[10] M. Wang, Z. Wang, X. Gong, and Z. Guo, *The intensification technologies to water electrolysis for hydrogen production–a review,* Renewable and Sustainable Energy Reviews **29**, 573 (2014).

[11] F. M. Mulder, *Electrolytic cell for the production of ammonia,* (2019), uS Patent App. 10/309,020.

[12] S. Giddey, S. Badwal, and A. Kulkarni, *Review of electrochemical ammonia production technologies and materials,* International Journal of Hydrogen Energy **38**, 14576 (2013).

[13] A. J. Martín, G. O. Larrazábal, and J. Pérez-Ramírez, *Towards sustainable fuels and chemicals through the electrochemical reduction of CO_2: lessons from water electrolysis,* Green Chemistry **17**, 5114 (2015).

[14] T. Burdyny and W. A. Smith, *CO_2 reduction on gas-diffusion electrodes and why catalytic performance must be assessed at commercially-relevant conditions,* Energy & Environmental Science **12**, 1442 (2019).

[15] M. Götz, J. Lefebvre, F. Mörs, A. M. Koch, F. Graf, S. Bajohr, R. Reimert, and T. Kolb, *Renewable power-to-gas: A technological and economic review,* Renewable energy **85**, 1371 (2016).

[16] N.-T. Suen, S.-F. Hung, Q. Quan, N. Zhang, Y.-J. Xu, and H. M. Chen, *Electrocatalysis for the oxygen evolution reaction: recent development and future perspectives,* Chemical Society Reviews **46**, 337 (2017).

[17] S. K. Ghosh and H. Rahaman, *Noble metal–manganese oxide hybrid nanocatalysts,* in *Noble Metal-Metal Oxide Hybrid Nanoparticles* (Elsevier, 2019) pp. 313–340.

[18] X. Shi, S. Siahrostami, G.-L. Li, Y. Zhang, P. Chakthranont, F. Studt, T. F. Jaramillo, X. Zheng, and J. K. Nørskov, *Understanding activity trends in electrochemical water oxidation to form hydrogen peroxide,* Nature communications **8**, 701 (2017).

[19] Y. Jiao, Y. Zheng, M. Jaroniec, and S. Z. Qiao, *Design of electrocatalysts for oxygen-and hydrogen-involving energy conversion reactions,* Chemical Society Reviews **44**, 2060 (2015).

[20] J. Weidner, S. Barwe, K. Sliozberg, S. Piontek, J. Masa, U.-P. Apfel, and W. Schuhmann, *Cobalt–metalloid alloys for electrochemical oxidation of 5-hydroxymethylfurfural as an alternative anode reaction in lieu of oxygen evolution during water splitting,* Beilstein journal of organic chemistry **14**, 1436 (2018).

[21] Y. Ando and T. Tanaka, *Proposal for a new system for simultaneous production of hydrogen and hydrogen peroxide by water electrolysis,* International journal of hydrogen energy **29**, 1349 (2004).

[22] J. Liu, Y. Zou, B. Jin, K. Zhang, and J. H. Park, *Hydrogen peroxide production from solar water oxidation,* ACS Energy Letters (2019).

[23] S. Wang, R. J. Lewis, D. E. Doronkin, D. J. Morgan, J.-D. Grunwaldt, G. J. Hutchings, and S. Behrens, *The direct synthesis of hydrogen peroxide from H_2 and O_2 using Pd–Ga and Pd–In catalysts,* Catalysis Science & Technology (2020).

[24] A. Sehrish, R. Manzoor, K. Dong, Y. Jiang, and Y. Lu, *Recent progress on electrochemical production of hydrogen peroxide,* Chemical Reports **1**, 81 (2019).

[25] S. C. Perry, D. Pangotra, L. Vieira, L.-I. Csepei, V. Sieber, L. Wang, C. P. de León, and F. C. Walsh, *Electrochemical synthesis of hydrogen peroxide from water and oxygen,* Nature Reviews Chemistry **3**, 442 (2019).

[26] J. M. Campos-Martin, G. Blanco-Brieva, and J. L. Fierro, *Hydrogen peroxide synthesis: an outlook beyond the anthraquinone process,* Angewandte Chemie International Edition **45**, 6962 (2006).

[27] *HPNow: On-site generation of hydrogen peroxide,* https://www.hpnow.eu/, accessed: 2020-03-17.

[28] Y. Sun, L. Silvioli, N. R. Sahraie, W. Ju, J. Li, A. Zitolo, S. Li, A. Bagger, L. Arnarson, X. Wang, *et al.*, *Activity–selectivity trends in the electrochemical production of hydrogen peroxide over single-site metal–nitrogen–carbon catalysts,* Journal of the American Chemical Society **141**, 12372 (2019).

[29] E. Ruiz-Ruiz, Y. Meas, R. Ortega-Borges, and J. J. Baizabal, *Electrochemical production of peroxocarbonate at room temperature using conductive diamond anodes,* Surface Engineering and Applied Electrochemistry **50**, 478 (2014).

[30] S. R. Kelly, X. Shi, S. Back, L. Vallez, S. Y. Park, S. Siahrostami, X. Zheng, and J. K. Nørskov, *ZnO as an active and selective catalyst for electrochemical water oxidation to hydrogen peroxide,* Acs Catalysis **9**, 4593 (2019).

[31] V. Viswanathan, H. A. Hansen, and J. K. Nørskov, *Selective electrochemical generation of hydrogen peroxide from water oxidation,* The journal of physical chemistry letters **6**, 4224 (2015).

[32] Y. Miyase, S. Iguchi, Y. Miseki, T. Gunji, and K. Sayama, *Electrochemical H_2O_2 production and accumulation from H_2O by composite effect of Al_2O_3 and $BiVO_4$,* Journal of The Electrochemical Society **166**, H644 (2019).

[33] K. Fuku, Y. Miyase, Y. Miseki, T. Gunji, and K. Sayama, *Enhanced oxidative hydrogen peroxide production on conducting glass anodes modified with metal oxides,* ChemistrySelect **1**, 5721 (2016).

[34] S. Zhu, Y. Zhao, Y. He, and D. Wang, *Selectivity of H_2O_2 and O_2 by water oxidation on metal oxide surfaces,* The Journal of chemical physics **150**, 041712 (2019).

[35] A. Nadar, S. S. Gupta, Y. Kar, S. Shetty, A. P. van Bavel, and D. Khushalani, *Evaluating the reactivity of $BiVO_4$ surfaces for efficient electrocatalytic H_2O_2 production: A combined experimental and computational study,* The Journal of Physical Chemistry C (2020).

[36] S. Velazquez-Pena, C. Sáez, P. Canizares, I. Linares-Hernández, V. Martínez-Miranda, C. Barrera-Díaz, and M. Rodrigo, *Production of oxidants via electrolysis of carbonate solutions with conductive-diamond anodes,* Chemical Engineering Journal **230**, 272 (2013).

[37] E. J. Ruiz, R. Ortega-Borges, J. L. Jurado, T. Chapman, and Y. Meas, *Simultaneous anodic and cathodic production of sodium percarbonate in aqueous solution,* Electrochemical and Solid-State Letters **12**, E1 (2009).

[38] A. J. Bard, L. R. Faulkner, J. Leddy, and C. G. Zoski, *Electrochemical methods: fundamentals and applications*, Vol. 2 (Wiley New York, 1980).

[39] F. Walsh, *Faraday and his laws of electrolysis: an appreciation,* Bulletin of Electrochemistry **7**, 481 (1992).

[40] M. Jouny, W. Luc, and F. Jiao, *General techno-economic analysis of CO_2 electrolysis systems,* Industrial & Engineering Chemistry Research **57**, 2165 (2018).

[41] J. Jiang, Y. Li, J. Liu, X. Huang, C. Yuan, and X. W. Lou, *Recent advances in metal oxide-based electrode architecture design for electrochemical energy storage,* Advanced materials **24**, 5166 (2012).

[42] A. R. Bredar, A. L. Chown, A. R. Burton, and B. H. Farnum, *Electrochemical impedance spectroscopy of metal oxide electrodes for energy applications,* ACS Applied Energy Materials (2020).

[43] S. Y. Park, H. Abroshan, X. Shi, H. S. Jung, S. Siahrostami, and X. Zheng, *$CaSnO_3$: an electrocatalyst for two-electron water oxidation reaction to form H_2O_2,* ACS Energy Letters **4**, 352 (2018).

[44] M. S. Saha, T. Furuta, and Y. Nishiki, *Electrochemical synthesis of sodium peroxycarbonate at boron-doped diamond electrodes,* Electrochemical and solid-state letters **6**, D5 (2003).

[45] C. Xia, S. Back, S. Ringe, K. Jiang, F. Chen, X. Sun, S. Siahrostami, K. Chan, and H. Wang, *Confined local oxygen gas promotes electrochemical water oxidation to hydrogen peroxide,* Nature Catalysis , 1 (2020).

[46] *ph calculator,* http://www.aqion.onl/, accessed: 2020-03-30.

[47] J. H. Baek, T. M. Gill, H. Abroshan, S. Park, X. Shi, J. Nørskov, H. S. Jung, S. Siahrostami, and X. Zheng, *Selective and efficient Gd-doped $BiVO_4$ photoanode for two-electron water oxidation to H_2O_2,* ACS Energy Letters **4**, 720 (2019).

[48] S. Mavrikis, M. Göltz, S. Rosiwal, L. Wang, and C. Ponce-de Leon, *Boron-doped diamond electrocatalyst for enhanced anodic H_2O_2 production,* ACS Applied Energy Materials (2020).

[49] Y. Liu, W. Wang, X. Xu, J.-P. M. Veder, and Z. Shao, *Recent advances in anion-doped metal oxides for catalytic applications,* Journal of materials chemistry A **7**, 7280 (2019).

[50] K. Fuku and K. Sayama, *Efficient oxidative hydrogen peroxide production and accumulation in photoelectrochemical water splitting using a tungsten trioxide/bismuth vanadate photoanode,* Chemical Communications **52**, 5406 (2016).

[51] J. Spivey, Y.-F. Han, and D. Shekhawat, *Catalysis*, Vol. 32 (Royal Society of Chemistry, 2020) p. 63.

[52] H. Dau, C. Limberg, T. Reier, M. Risch, S. Roggan, and P. Strasser, *The mechanism of water oxidation: from electrolysis via homogeneous to biological catalysis,* ChemCatChem **2**, 724 (2010).

[53] D. E. Richardson, H. Yao, K. M. Frank, and D. A. Bennett, *Equilibria, kinetics, and mechanism in the bicarbonate activation of hydrogen peroxide: oxidation of sulfides by peroxymonocarbonate,* Journal of the American Chemical Society **122**, 1729 (2000).

[54] J. Zhang and C. W. Oloman, *Electro-oxidation of carbonate in aqueous solution on a platinum rotating ring disk electrode,* Journal of applied electrochemistry **35**, 945 (2005).

[55] S. Verma, B. Kim, H.-R. Jhong, S. Ma, and P. J. Kenis, *A gross-margin model for defining technoeconomic benchmarks in the electroreduction of CO_2,* ChemSusChem **9**, 1972 (2016).

[56] S. Verma, S. Lu, and P. J. Kenis, *Co-electrolysis of CO_2 and glycerol as a pathway to carbon chemicals with improved technoeconomics due to low electricity consumption,* Nature Energy **4**, 466 (2019).

[57] S. Smith and B. Bowen, *Soda ash,* https://www.icis.com/explore/commodities/chemicals/soda-ash/ (2014), accessed: 2020-05-22.

[58] ICIS, *Potassium carbonate swings into balance as player exits market,* https://www.icis.com/explore/resources/news/2003/05/16/195939/potassium-carbonate-swings-into-balance-as-player-exits-market/ (2013), accessed: 2020-06-01.

[59] A. Seidell, *Solubilities of inorganic and organic compounds c. 2* (D. Van Nostrand Company, 1919).

[60] A. James, G. R. Horne, and R. Rosler, *Process for producing a percarbonate,* (Patent WO 9735806, Oct. 1997).

[61] P. De Luna, C. Hahn, D. Higgins, S. A. Jaffer, T. F. Jaramillo, and E. H. Sargent, *What would it take for renewably powered electrosynthesis to displace petrochemical processes?* Science **364** (2019).

[62] Battelle Memorial Institute, *Manufacturing cost analysis of 10 kw and 25 kw direct hydrogen polymer electrolyte membrane (PEM) fuel cell for material handling application,* https://www.energy.gov/sites/prod/files/2014/06/f16/fcto_battelle_cost_analysis_mhe_mar2013.pdf (2013), accessed: 2020-05-14.

[63] *Sodium percarbonate market forecast, trend analysis competition tracking: Global market insights 2019 to 2029,* https://www.factmr.com/report/2527/sodium-percarbonate-market (2019), accessed: 2020-06-01.

[64] *Switch to percarbonate could be completed by 2005,* https://www.icis.com/explore/resources/news/2002/03/11/158723/switch-to-percarbonate-could-be-completed-by-2005/ (2002), accessed: 2020-06-01.

[65] O. Schmidt, A. Gambhir, I. Staffell, A. Hawkes, J. Nelson, and S. Few, *Future cost and performance of water electrolysis: An expert elicitation study,* International Journal of Hydrogen Energy **42**, 30470 (2017).

[66] M. Ruth, A. Mayyas, and M. Mann, *Manufacturing competitiveness analysis for PEM and alkaline water electrolysis systems,* https://www.nrel.gov/docs/fy19osti/70380.pdf (2017), accessed: 2020-05-14.

[67] A. B. de Haan and H. Bosch, *Industrial separation processes: Fundamentals* (Walter de Gruyter, 2013).

[68] T. Van Gerven and A. Stankiewicz, *Structure, energy, synergy, time the fundamentals of process intensification,* Industrial & engineering chemistry research **48**, 2465 (2009).

[69] F. Bauer, C. Hulteberg, and D. T. Persson Tobias, *Biogas upgrading - review of commercial technologies (biogasuppgradering-granskning av kommersiella tekniker),* SGC rapport **270**, 83 (2013).

[70] H. Jakob, S. Leininger, T. Lehmann, S. Jacobi, and S. Gutewort, *Peroxo coumpounds, inorganic,* in *Ullmann's encyclopedia of industrial chemistry* (VCH publishers, 2007) pp. 19–27.

[71] D. R. Woods, *Rules of thumb in engineering practice* (John Wiley & Sons, 2007) p. 396.

[72] *Hydrogen peroxide material compatibility chart,* https://www.industrialspec.com/images/files/hydrogen-peroxide-material-compatibility-chart-from-ism.pdf (2020), accessed: 2020-05-15.

[73] Centre for European Policy Studies, *Composition and drivers of energy prices and costs in energy intensive industries,* https://op.europa.eu/en/publication-detail/-/publication/424dac0a-ec77-11e8-b690-01aa75ed71a1/language-en (2020), accessed: 2020-05-22.

[74] U.S. Energy Information Administration, *Electric power monthly,* https://www.eia.gov/electricity/monthly/ (2020), accessed: 2020-05-22.

[75] *Sodium silicate,* https://www.alibaba.com/product-detail/Sodium-Silicate-Solid-Sodium-Silicate-Lu62046694162.html?spm=a2700.7724857.normalList.230.1d764d48BQ0Ep5 (2020), accessed: 2020-05-22.

[76] *Current forecourt hydrogen production from grid electrolysis (1,500 kg per day) version 3.0,* https://www.nrel.gov/hydrogen/h2a-production-archive.html (2020), accessed: 2020-05-22.

[77] *Kemcore sodium percarbonate,* https://www.kemcore.com/sodium-percarbonate-coated-oxygen-13-min (2020), accessed: 2020-05-22.

[78] *Boholy sodium percarbonate uncoated,* https://boholy.en.alibaba.com/product/60758648558-.html (2020), accessed: 2020-05-22.

[79] *Zero-carbon cement production with solar thermal,* https://cleantechnica.com/2012/04/10/zero-carbon-cement-production-with-solar-thermal/ (2012), accessed: 2020-05-22.

[80] *Platts global ethylene price index,* https://www.spglobal.com/platts/en/our-methodology/price-assessments/petrochemicals/pgpi-ethylene (2018), accessed: 2020-05-22.

[81] M. David, C. Ocampo-Martínez, and R. Sánchez-Peña, *Advances in alkaline water electrolyzers: a review,* Journal of Energy Storage **23**, 392 (2019).

[82] *Platinum commodity,* https://markets.businessinsider.com/commodities/platinum-price (2020), accessed: 2020-05-06.

[83] *Silver commodity,* https://markets.businessinsider.com/commodities/silver-price (2020), accessed: 2020-05-06.

[84] *Copper,* https://tradingeconomics.com/commodity/copper (2020), accessed: 2020-05-06.

[85] *Nickel,* https://tradingeconomics.com/commodity/nickel (2020), accessed: 2020-05-06.

[86] D. S. Ripatti, T. R. Veltman, and M. W. Kanan, *Carbon monoxide gas diffusion electrolysis that produces concentrated C_2 products with high single-pass conversion,* Joule **3**, 240 (2019).

[87] A. Bloomenthal and M. James, *Gross margin definition,* https://www.investopedia.com/terms/g/grossmargin.asp (2020), accessed: 2020-05-15.

[88] J. Harmsen, A. B. de Haan, and P. L. Swinkels, *Product and process design: Driving innovation* (Walter de Gruyter GmbH & Co KG, 2018).

[89] M. Ruth, *Current hydrogen production from distributed grid alkaline electrolysis,* (2012), https://www.nrel.gov/hydrogen/h2a-production-archive.html.

[90] A. Wiheeb, Z. Helwani, J. Kim, and M. Othman, *Pressure swing adsorption technologies for carbon dioxide capture,* Separation & Purification Reviews **45**, 108 (2016).

[91] K.-L. Wu, H.-Y. Wang, and J. D. Ward, *Economic comparison of crystallization technologies for different chemical products,* Industrial & Engineering Chemistry Research **57**, 12444 (2018).

[92] L. Bertuccioli, A. Chan, D. Hart, F. Lehner, B. Madden, and E. Standen, *Development of water electrolysis in the european union,* Fuel cells and hydrogen joint undertaking **83** (2014).

[93] *AJA international inc: what is sputtering?* http://www.ajaint.com/what-is-sputtering.html, accessed: 2020-05-14.

[94] MicroMagnetics, *Magnetron sputtering technology,* http://www.directvacuum.com/pdf/what_is_sputtering.pdf, accessed: 2020-05-14.

[95] B. Bissig, T. Jäger, L. Ding, A. Tiwari, and Y. Romanyuk, *Limits of carrier mobility in Sb-doped SnO_2 conducting films deposited by reactive sputtering,* APL materials **3**, 062802 (2015).

[96] R. Snyders, M. Wautelet, R. Gouttebaron, J. Dauchot, and M. Hecq, *Correlation between the gas composition and the stoichiometry of SnO_x films prepared by DC magnetron reactive sputtering,* Surface and Coatings Technology **142**, 187 (2001).

[97] O. Tuna, Y. Selamet, G. Aygun, and L. Ozyuzer, *High quality ITO thin films grown by dc and RF sputtering without oxygen,* Journal of Physics D: Applied Physics **43**, 055402 (2010).

[98] B. J. Trześniewski, I. A. Digdaya, T. Nagaki, S. Ravishankar, I. Herraiz-Cardona, D. A. Vermaas, A. Longo, S. Gimenez, and W. A. Smith, *Near-complete suppression of surface losses and total internal quantum efficiency in $BiVO_4$ photoanodes,* Energy & Environmental Science **10**, 1517 (2017).

[99] P. Beniac and C. Barnes, *An introduction to electron microscopy*, www.fei.com (FEI^{TM}, 2010).

[100] S. Swapp, *Scanning electron microscopy,* https://serc.carleton.edu/research_education/geochemsheets/techniques/SEM.html (2017), accessed: 2020-05-14.

[101] D. C. Joy, B. J. Ford, and S. Bradbury, *Encyclopaedia britannica: Scanning electron microscope,* https://www.britannica.com/technology/scanning-electron-microscope (2012), accessed: 2020-05-14.

[102] H. Wang and P. K. Chu, *Surface characterization of biomaterials,* in *Characterization of biomaterials* (Elsevier, 2013) pp. 105–174.

[103] S. A. Speakman, *Basics of x-ray powder diffraction,* the Center for Materials Science and Engineering at MIT, Tech. Rep. Massachusetts-USA (2011).

[104] L. J. van der Pauw, *A method of measuring specific resistivity and hall effect of discs of arbitrary shape,* Philips Res. Rep **13**, 1 (1958).

[105] N. Ngo, H. Niu, P. Bharadwaj, H. Bhatti, and S. Adhikari, *Van der Pauw resisitivity measurement,* Technical Report (2017).

[106] S. Hasegawa, *Surface one-dimensional structures,* Chinese Journal of Physics **45**, 385 (2007).

[107] E. Dickinson, *COMSOL modeling electroanalysis: Cyclic voltammetry,* https://www.comsol.com/blogs/modeling-electroanalysis-cyclic-voltammetry/ (2013), accessed: 2020-05-14.

[108] *Gamry instruments: Basics of electrochemical impedance spectroscopy,* https://www.gamry.com/application-notes/EIS/basics-of-electrochemical-impedance-spectroscopy/, accessed: 2020-05-14.

[109] N. V. Klassen, D. Marchington, and H. C. McGowan, *H_2O_2 determination by the I_3^- method and by $KMnO_4$ titration,* Analytical Chemistry **66**, 2921 (1994).

[110] *USP technologies: Permanganate titration procedure,* http://www.h2o2.com/technical-library/analytical-methods/default.aspx?pid=68&name=Permanganate-Titration, accessed: 2020-05-12.

[111] L. M. Harwood and T. D. Claridge, *Introduction to organic spectroscopy* (Oxford University Press New York, 1997).

[112] *Nuclear magnetic resonance spectroscopy: Theoretical principles,* https://teaching.shu.ac.uk/hwb/chemistry/tutorials/molspec/nmr1.htm (), accessed: 2020-05-13.

[113] H. Liu, *Principles and applications of well logging* (Springer, 2017) pp. 161–179.

[114] *Chemical shift and coupling constant,* https://slideplayer.com/slide/7480590/ (), accessed: 2020-05-13.

[115] M. Rumayor, A. Dominguez-Ramos, and A. Irabien, *Environmental and economic assessment of the formic acid electrochemical manufacture using carbon dioxide: Influence of the electrode lifetime,* Sustainable Production and Consumption **18**, 72 (2019).

[116] *Photovoltaic auction analysis portugal 2019,* https://www.tsolar.com/en/news/photovoltaic-auction-analysis-portugal-2019.html (2019), accessed: 2020-05-24.

[117] I. Graabak and M. Korpås, *Variability characteristics of european wind and solar power resources—a review,* Energies **9**, 449 (2016).

[118] S. Lensik and I. Pisca, *Costs of offshore wind energy 2018,* https://www.pbl.nl/sites/default/files/downloads/pbl-2019-costs-of-offshore-wind-energy-2018_3623.pdf (2019), accessed: 2020-05-10.

[119] F. Lawson, *Tin oxide — Sn_3O_4,* Nature **215**, 955 (1967).

[120] J. Hanawalt, H. Rinn, and L. Frevel, *Chemical analysis by x-ray diffraction,* Industrial & Engineering Chemistry Analytical Edition **10**, 475 (1938).

[121] Y. Shigesato and D. C. Paine, *A microstructural study of low resistivity tin-doped indium oxide prepared by dc magnetron sputtering,* Thin solid films **238**, 44 (1994).

[122] N. A. Stephenson and A. T. Bell, *Quantitative analysis of hydrogen peroxide by 1H NMR spectroscopy,* Analytical and bioanalytical chemistry **381**, 1289 (2005).

[123] K. Z. House, A. C. Baclig, M. Ranjan, E. A. van Nierop, J. Wilcox, and H. J. Herzog, *Economic and energetic analysis of capturing CO_2 from ambient air,* Proceedings of the National Academy of Sciences **108**, 20428 (2011).

[124] T. El Moustafid, H. Cachet, B. Tribollet, and D. Festy, *Modified transparent SnO_2 electrodes as efficient and stable cathodes for oxygen reduction,* Electrochimica Acta **47**, 1209 (2002).

[125] P. Glaris, J.-F. Coulon, M. Dorget, and F. Poncin-Epaillard, *Thermal annealing as a new simple method for PTFE texturing,* Polymer **54**, 5858 (2013).

[126] R. E. Zeebe, *On the molecular diffusion coefficients of dissolved CO_2, HCO_3^-, and CO_3^{2-} and their dependence on isotopic mass,* Geochimica et Cosmochimica Acta **75**, 2483 (2011).

[127] P. Ngene, R. J. Westerwaal, S. Sachdeva, W. Haije, L. C. de Smet, and B. Dam, *Polymer-induced surface modifications of Pd-based thin films leading to improved kinetics in hydrogen sensing and energy storage applications,* Angewandte Chemie International Edition **53**, 12081 (2014).

[128] F. P. G. de Arquer, C.-T. Dinh, A. Ozden, J. Wicks, C. McCallum, A. R. Kirmani, D.-H. Nam, C. Gabardo, A. Seifitokaldani, X. Wang, *et al., CO_2 electrolysis to multicarbon products at activities greater than 1 A cm^{-2},* Science **367**, 661 (2020).

APPENDICES CONTENTS

A

XRD PATTERN CONVERSION FROM CO-K ALPHA SOURCE TO CU-K ALPHA

The XRD measurements were done with a cobalt source using a Bruker ADVANCE D8. The data can be translated to copper source values in order to allow comparison with literature. This was done by using Bragg's law:

$$n\lambda = 2d\sin\theta \tag{A.1}$$

with n an integer, λ the wavelength of the incident radiation, d the inter-planar spacing and θ the scattering angle in radians.

The inter-planar spacing d remains constant between the copper and the cobalt value for one sample, hence equation A.2 can be set-up:

$$d = \frac{n\lambda_1}{2\sin\theta_1} = \frac{n\lambda_2}{2\sin\theta_2} \tag{A.2}$$

$$\sin\theta_2 = \frac{\lambda_2}{\lambda_1}\sin\theta_1 \tag{A.3}$$

$$\theta_2 = \arcsin\frac{\lambda_2}{\lambda_1}\sin\theta_1 \tag{A.4}$$

$2\theta_1$ cobalt source measurements were taken in degrees, hence the copper source value $2\theta_2$ in degrees will be:

$$2\theta_2 = 2 * \frac{360}{2\pi} * \arcsin(\frac{\lambda_2}{\lambda_1}\sin(\frac{2\pi}{360} * \theta_1)) \tag{A.5}$$

One can compute the new 2θ value of each point by filling in equation A.5 with:
λ_1 = 1.788965 Å (Cobalt source wavelength)
λ_2 = 1.540562 Å (Copper source wavelength)

B

CALIBRATION OF CAPILLARY-TUBE DUOS WITH RESPECT TO MALEIC ACID

B.1. RELATIVE MALEIC ACID - BENZENE PEAK AREAS FOR DIFFERENT TUBE - CAPILLARIES

Table B.1: Area under the benzene peaks (δ = 7.16 ppm) relative to maleic peaks (δ = 6.42 ppm) normalized to 1 for a 0.0244 M maleic acid solution in tube and capillaries nr 0-15.

Tube number	Capillary number	Relative intensity
0	0	1.57
1	1	1.53
2	2	Tube broken
3	3	1.1
4	4	1.61
5	5	1.46
6	6	1.51
7	7	1.53
8	8	1.57
9	9	1.13
10	10	1.47
11	11	1.83
12	12	1.56
13	13	1.63
14	14	1.56
15	15	1.58
	Average	1.51

The standard deviation is $\sigma = 0.1815$, which corresponds to a relative standard deviation of 12 %.

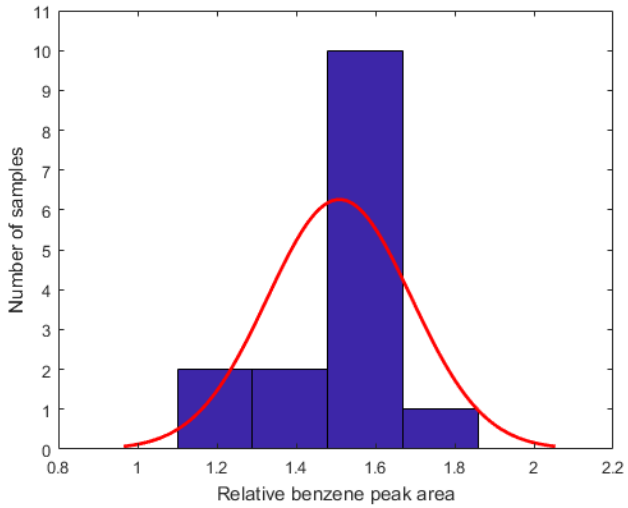

Figure B.1: Distribution of relative benzene peak areas with respect to the maleic acid standard normalized to one for 15 different tubes - capillary combinations

B.2. Relative maleic acid - benzene peak areas for a fixed tube - capillary combination

Table B.2: Area under the benzene peaks (δ = 7.16 ppm) relative to maleic peaks (δ = 6.42 ppm) normalized to 1 for 5 different measurements of 0.0244 M maleic acid in tube 15 - capillary 15.

Measurement	Tube - capillary number	Relative intensity
1	15	1.42
2	15	1.35
3	15	1.1
4	15	1.61
5	15	1.46
	Average	1.38

The standard deviation is $\sigma = 0.0286$, which corresponds to a relative standard deviation of 2 %.

Note that the factor between the benzene and maleic acid peak areas is different in Table B.1 and Table B.2 for the tube - capillary combination 15. This is due to the fact that a new solution of maleic acid was prepared for the second batch of experiments. The exact concentration might therefore have been somewhat different due to weighing and diluting errors. For the rest of the experiments, all data was translated back to the values in Table B.1 as they were all measured with the same batch of solution. That solution therefore corresponds to the standard for the rest of this study.

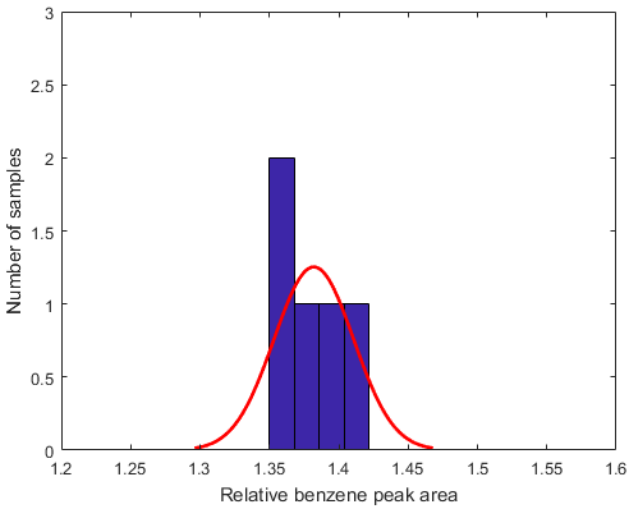

Figure B.2: Distribution of relative benzene peak areas with respect to the maleic acid standard normalized to one for 5 different measurements in the same capillary - tube combination

C

DERIVATIONS FOR THE GROSS MARGIN MODEL

This appendix provides some more detailed calculations for the derivation of the gross margin model explored in Section 3.2.

As defined in Equation (3.10), the gross margin for a process can be defined as:

$$\frac{\text{Revenue} - \text{Cost of goods sold}}{\text{Revenue}} > A \tag{C.1}$$

The revenue are derived from the sales prices and the production rate, yielding:

$$\text{Revenue} = \frac{jAt * 36 * 10^{-6}}{F} * \left(\sum \frac{\text{FE}_P^{anodic} C_P M}{z} + \sum \frac{\text{FE}_P^{cathodic} C_P M}{z} \right) \tag{C.2}$$

The cost of goods sold is composed of capital costs for the electrolyzer and separation units as well as variables costs for raw materials and utilities.

$$\text{Costs of goods sold} = T_{\text{prod}} + T_{\text{sep}} + T_{\text{feed}} \tag{C.3}$$

$$= T_{\text{prod}} + \lambda_{\text{raw}} + C_E(VJAt * 10^{-6} + 0.25 Q_{\text{gas}} t) + \frac{36 * 10^{-6} * jAt}{F} \left(\frac{\text{FE}^{\text{anode}}_{\text{main product}} C_{\text{sep}} M}{z} + \frac{\text{FE}^{\text{cathode}}_{\text{main product}} C_{\text{sep}} M}{z} \right) \tag{C.4}$$

where T_{prod} is the capital cost of production [\$], T_{sep} the capital cost of product separation [\$], λ_{raw} [\$] the cost of raw materials , Q_{gas} is the gas inlet to the PSA unit [m^3/h], F is the Faraday constant, C_{sep} is the cost of separation [\$/kg_{product}].

Entering these values into the definition of the gross margin given in Equation (3.10) gives:

$$\left[\frac{jAt * 36 * 10^{-6} * \sum \frac{\text{FE}_P^{anode} C_P M}{z} + \sum \frac{\text{FE}_P^{cathode} C_P M}{z}}{F} - \left(T_{\text{prod}} + \lambda_{\text{raw}} + C_E(VJAt * 10^{-6} + 0.25 Q_{\text{gas}} t) \right.\right.$$

$$\left.\left. + \frac{36 * 10^{-6} * jAt}{F} \left(\frac{\text{FE}_P^{anode} C_{\text{sep}} M}{z} + \frac{\text{FE}_P^{cathode} C_{\text{sep}} M}{z} \right) \right) \right] * \frac{F}{jAT * 36 * 10^{-6} * \left(\sum \frac{\text{FE}_P^{anode} C_P M}{z} + \sum \frac{\text{FE}_P^{cathode} C_P M}{z} \right)} > A$$

Rearranging gives:

$$-\frac{F}{jAT*36*10^{-6}*\left(\sum\frac{\mathrm{FE}_P^{anode}C_PM}{z}+\sum\frac{\mathrm{FE}_P^{cathode}C_PM}{z}\right)}\Bigg[T_{\mathrm{prod}}+\lambda_{\mathrm{raw}}+C_E(VJAt*10^{-6}+0.25Q_{\mathrm{gas}}t)$$

$$+\frac{36*10^{-6}*jAt}{F}\left(\frac{\mathrm{FE}_P^{anode}C_{\mathrm{sep}}M}{z}+\frac{\mathrm{FE}_P^{cathode}C_{\mathrm{sep}}M}{z}\right)\Bigg]>A-1$$

$$\Leftrightarrow T_{\mathrm{prod}}+\lambda_{\mathrm{raw}}+0.25C_EQ_{\mathrm{gas}}t+jAt*10^{-6}\left(VC_E+\frac{36}{F}*\left(\frac{\mathrm{FE}_P^{anode}C_{\mathrm{sep}}M}{z}+\frac{\mathrm{FE}_P^{cathode}C_{\mathrm{sep}}M}{z}\right)\right)$$

$$<(1-A)*\frac{jAT*36*10^{-6}}{F}*\left(\sum\frac{\mathrm{FE}_P^{anode}C_PM}{z}+\sum\frac{\mathrm{FE}_P^{cathode}C_PM}{z}\right)$$

$$\Leftrightarrow T_{\mathrm{prod}}+\lambda_{\mathrm{raw}}+0.25C_EQ_{\mathrm{gas}}t<jAt*10^{-6}\Bigg[(1-A)*\frac{36}{F}*\left(\sum\frac{\mathrm{FE}_P^{anode}C_PM}{z}+\sum\frac{\mathrm{FE}_P^{cathode}C_PM}{z}\right)-VC_E$$

$$-\frac{36}{F}\left(\frac{\mathrm{FE}_P^{anode}C_{\mathrm{sep}}M}{z}+\frac{\mathrm{FE}_P^{cathode}C_{\mathrm{sep}}M}{z}\right)\Bigg]$$

Hence filling in revenue and costs of goods first condition for gross margin gives

$$T_{\mathrm{prod}}+\lambda_{\mathrm{raw}}+0.25C_EQ_{\mathrm{gas}}t<jAt*10^{-6}\Bigg[\frac{36}{F}\Big[\sum\Big(\frac{\mathrm{FE}_P^{cathode}M}{z}\Big)(1-A)C_P-\frac{\mathrm{FE}^{\mathrm{cathode}}_{\mathrm{main\ product}}M}{z}C_{\mathrm{sep}}$$

$$+\sum\Big(\frac{\mathrm{FE}_P^{anode}M}{z}\Big)(1-A)C_P-\frac{\mathrm{FE}^{\mathrm{anode}}_{\mathrm{main\ product}}M}{z}C_{\mathrm{sep}}\Big]-VC_E\Bigg] \quad \text{(C.5)}$$

D

STREAM SUMMARIES FOR THE PROCESSES EVALUATED VIA THE GROSS MARGIN MODEL

Streams summaries present the mass balances for the eight processes evaluated using the gross margin model. Streams were numbered in the processes' block schemes which can be found in this appendix. Two anodic reactions were considered, namely the Oxygen Evolution Reaction (OER) and the anodic peroxide evolution. Both were coupled to the Hydrogen Evolution Reaction (HER), the CO_2 reduction to CO and C_2H_4 and the two-electron Oxygen Reduction Reaction (ORR). An anodic production of 100 ton/day sodium percarbonate was used as common parameter for all reactions coupled to the anodic peroxide evolution. The cathodic product outputs from these mass balances were used as starting point for the OER coupled cathodic reactions. The stream summaries presented in this appendix are for the base case parameters defined in Section 3.1.3.

D.1. OER COUPLED TO THE HER

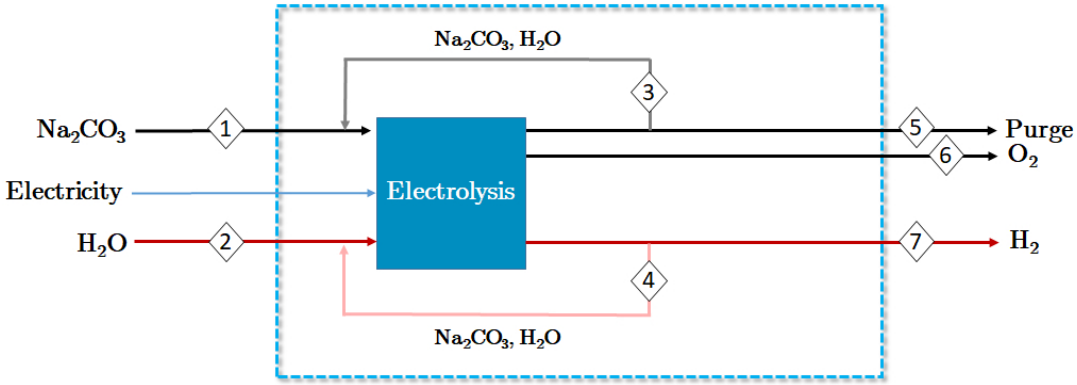

Figure D.1: Block scheme and battery limits for the coupled OER/HER

Table D.1: Stream summary for the OER/HER process as defined in Figure D.1 for a production of 68.85 kmol/h hydrogen at base case performance parameters.

Stream number		**1**		**2**		**3**		**4**		**5**		**6**		**7**	
Name		**Anolyte feed**		**Catholyte feed**		**Anolyte recycle**		**Catholyte recycle**		**Purge**		**Anodic product**		**Cathodic product**	
Component	MW	kg/h	kmol/h	kg/h	kmol/h	kg/h	kmol/h	kg/h	kmol/h	kg/h	kmol/h	kg/h	kmol/h	kg/h	kmol/h
Na_2CO_3	106	380.54	3.59			8014.66	75.61	8395.20	79.20	380.54	3.59				
H_2O	18			2478.60	137.70	26136.00	1452.00	23657.40	1314.30	1239.30	68.85				
O_2	32											1101.76	34.43		
$Na_2CO_3 \cdot 1.5\,H_2O_2$	157														
H_2O_2	34														
H_2	2													137.70	68.85
CO_2	44														
CO	28														
C_2H_4	28														
Total		380.54	3.59	2478.60	137.70	34150.66	1527.61	32052.60	1393.50	1619.84	72.44	1101.76	34.43	137.70	68.85

D.2. OER COUPLED TO THE CO_2 REDUCTION TO CO

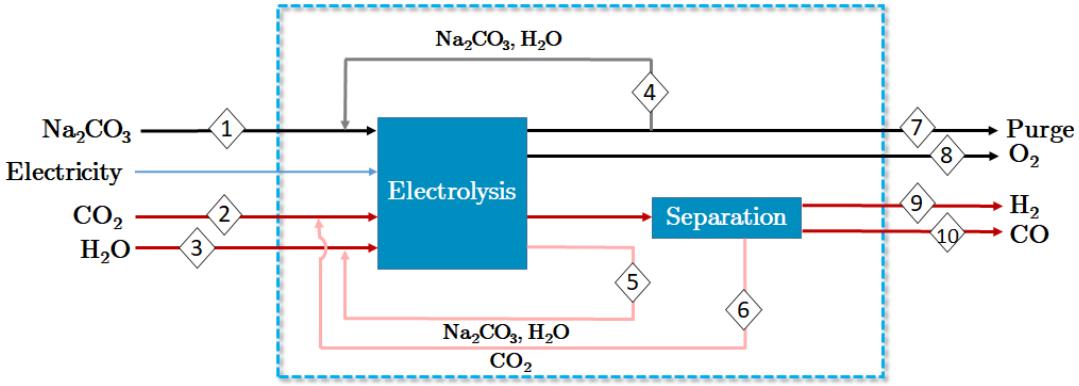

Figure D.2: Block scheme and battery limits for the coupled OER/CO_2 reduction to CO

Table D.2: Stream summary for the first 6 streams of the OER/CO process as defined in Figure D.2 for a production of 55.08 kmol/h carbon monoxide at base case performance parameters.

Stream number		**1**		**2**		**3**		**4**		**5**		**6**	
Name		**Anolyte feed**		**Catholyte gas feed**		**Catholyte liquid feed**		**Anolyte recycle**		**Catholyte recycle**		**Gas recycle**	
Component	MW	kg/h	kmol/h	kg/h	kmol/h	kg/h	kmol/h	kg/h	kmol/h	kg/h	kmol/h	kg/h	kmol/h
Na_2CO_3	106	380.33	3.59					8014.66	75.61	8395.20	79.20		
H_2O	18					1487.16	82.62	26136.00	1452.00	24648.84	1369.38		
O_2	32												
$Na_2CO_3 \cdot 1.5\,H_2O_2$	157												
H_2O_2	34												
H_2	2												
CO_2	44			2423.52	55.08							1038.84	23.61
CO	28												
C_2H_4	28												
Total		380.33	3.59	2423.52	55.08	1487.16	82.62	34150.66	1527.61	33044.04	1448.58	1038.84	23.61

Table D.3: Stream summary for 4 outlet streams of the OER/CO process as defined in Figure D.2 for a production of 55.08 kmol/h carbon monoxide at base case performance parameters.

Stream number		**7**		**8**		**9**		**10**	
Name		**Purge**		**Anodic product**		**Cathodic by-product**		**Cathodic product**	
Component	MW	kg/h	kmol/h	kg/h	kmol/h	kg/h	kmol/h	kg/h	kmol/h
Na_2CO_3	106	380.33	3.59						
H_2O	18	1239.30	68.85						
O_2	32			1101.76	34.43				
$Na_2CO_3 \cdot 1.5\,H_2O_2$	157								
H_2O_2	34								
H_2	2					27.54	13.77		
CO_2	44								
CO	28							1542.24	55.08
C_2H_4	28								
Total		1619.63	72.44	1101.76	34.43	27.54	13.77	1542.24	55.08

D.3. OER COUPLED TO THE CO_2 REDUCTION TO C_2H_4

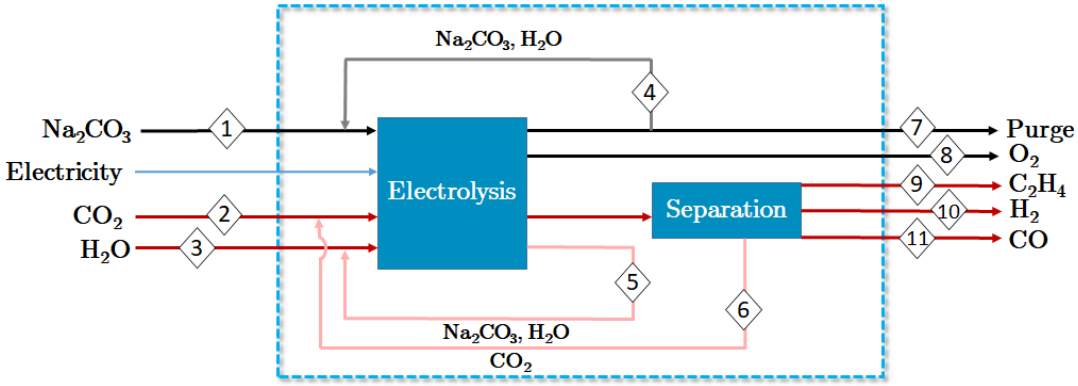

Figure D.3: Block scheme and battery limits for the coupled OER/CO_2 reduction to C_2H_4

Table D.4: Stream summary for the first 6 streams of the OER/C_2H_4 process as defined in Figure D.3 for a production of 8.03 kmol/h ethylene at base case performance parameters.

Stream number		**1**		**2**		**3**		**4**		**5**		**6**	
Name		**Anolyte feed**		**Catholyte gas feed**		**Catholyte liquid feed**		**Anolyte recycle**		**Catholyte recycle**		**Gas recycle**	
Component	MW	kg/h	kmol/h	kg/h	kmol/h	kg/h	kmol/h	kg/h	kmol/h	kg/h	kmol/h	kg/h	kmol/h
Na_2CO_3	106	380.33	3.59					8014.66	75.61	8395.20	79.20		
H_2O	18					1714.50	95.25	26136.00	1452.00	24421.50	1356.75		
O_2	32												
$Na_2CO_3 \cdot 1.5\,H_2O_2$	157												
H_2O_2	34												
H_2	2												
CO_2	44			1161.60	26.40							497.64	11.31
CO	28												
C_2H_4	28												
Total		380.33	3.59	1161.60	26.40	1714.50	95.25	34150.66	1527.61	32816.70	1435.95	497.64	11.31

Table D.5: Stream summary for 4 outlet streams of the OER/C_2H_4 process as defined in Figure D.3 for a production of 8.03 kmol/h carbon monoxide at base case performance parameters.

Stream number		**7**		**8**		**9**		**10**		**11**	
Name		**Purge**		**Anodic product**		**Cathodic product**		**Cathodic by-product 1**		**Cathodic by-product 2**	
Component	MW	kg/h	kmol/h	kg/h	kmol/h	kg/h	kmol/h	kg/h	kmol/h	kg/h	kmol/h
Na_2CO_3	106	380.33	3.59								
H_2O	18	1239.30	68.85								
O_2	32			1101.76	34.43						
$Na_2CO_3 \cdot 1.5\,H_2O_2$	157										
H_2O_2	34										
H_2	2							20.66	10.33		
CO_2	44										
CO	28									289.24	10.33
C_2H_4	28					224.84	8.03				
Total		1619.63	72.44	1101.76	34.43	224.84	8.03	20.66	10.33	289.24	10.33

D.4. OER COUPLED TO THE TWO-ELECTRON ORR

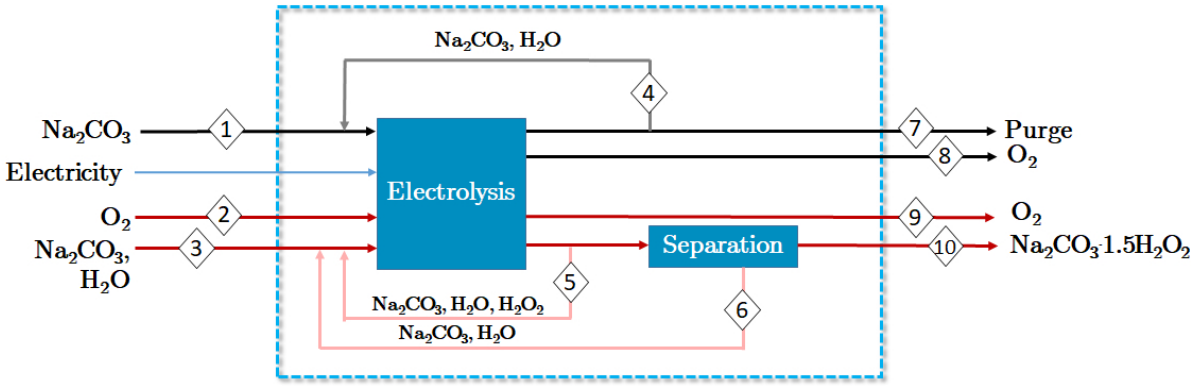

Figure D.4: Block scheme and battery limits for the coupled OER/two-electron ORR

Table D.6: Stream summary for the first 6 streams of the OER/ORR process as defined in Figure D.4 for a cathodic production of 41.31 kmol/h sodium percarbonate at base case performance parameters.

Stream number		**1**		**2**		**3**		**4**		**5**		**6**	
Name		**Anolyte feed**		**Catholyte gas feed**		**Catholyte liquid feed**		**Anolyte recycle**		**Recycle (electrolyzer)**		**Recycle (crystallizer)**	
Component	MW	kg/h	kmol/h	kg/h	kmol/h	kg/h	kmol/h	kg/h	kmol/h	kg/h	kmol/h	kg/h	kmol/h
Na_2CO_3	106	380.54	3.59			4378.86	41.31	8014.66	75.61	6568.82	61.97	2189.96	20.66
H_2O	18					2354.58	130.81	26136	1452	20449.08	1136.06	20449.08	1136.06
O_2	32			2990.08	93.44								
$Na_2CO_3 \cdot 1.5\,H_2O_2$	157												
H_2O_2	34									2106.98	61.97		
H_2	2												
CO_2	44												
CO	28												
C_2H_4	28												
Total		380.54	3.59	2990.08	93.44	6733.44	172.12	34150.66	1527.61	29124.88	1260	22639.04	1156.72

Table D.7: Stream summary for 4 outlet streams of the OER/ORR process as defined in Figure D.4 for a cathodic production of 41.31 kmol/h sodium percarbonate at base case performance parameters.

Stream number		**7**		**8**		**9**		**10**	
Name		**Purge**		**Anodic product**		**Gas excess**		**Cathodic product**	
Component	MW	kg/h	kmol/h	kg/h	kmol/h	kg/h	kmol/h	kg/h	kmol/h
Na_2CO_3	106	380.54	3.59						
H_2O	18	1239.3	68.85						
O_2	32			1101.76	34.43	896.96	28.03		
$Na_2CO_3 \cdot 1.5\,H_2O_2$	157							6485.67	41.31
H_2O_2	34								
H_2	2								
CO_2	44								
CO	28								
C_2H_4	28								
Total		1619.84	72.44	1101.76	34.43	896.96	28.03	6485.67	41.31

D.5. ANODIC PEROXIDE EVOLUTION REACTION COUPLED TO THE HER

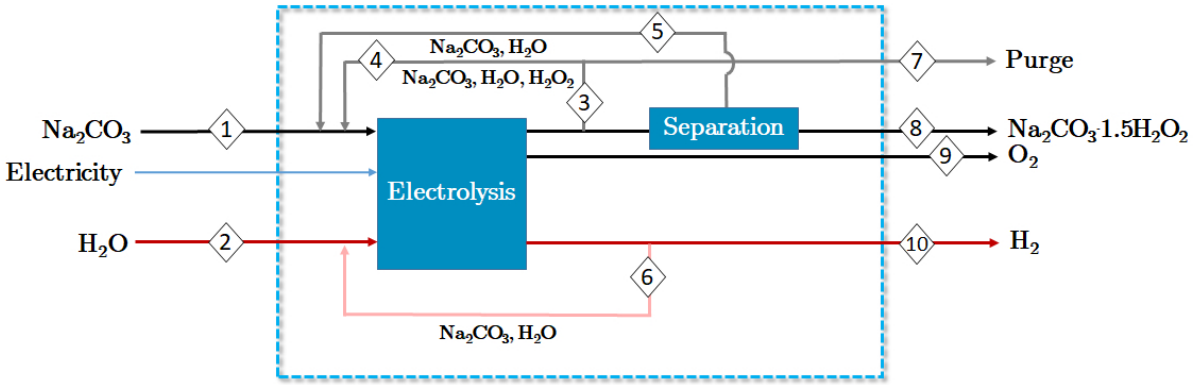

Figure D.5: Block scheme and battery limits for the coupled anodic peroxide evolution reaction/HER

Table D.8: Stream summary for the first 6 streams of the H_2O_2ER/HER process as defined in Figure D.5 for an anodic production of 26.54 kmol/h sodium percarbonate at base case performance parameters.

Stream number		**1**		**2**		**3**		**4**		**5**		**6**	
Name		**Anolyte feed**		**Catholyte feed**		**Split recycle/purge**		**Recycle (electrolyzer)**		**Recycle (crystallizer)**		**Recycle catholyte**	
Component	MW	kg/h	kmol/h	kg/h	kmol/h	kg/h	kmol/h	kg/h	kmol/h	kg/h	kmol/h	kg/h	kmol/h
Na_2CO_3	106	2972.24	28.04			4378.86	41.31	4219.86	39.81	1406.62	13.27	8395.2	79.2
H_2O	18			2478.6	137.7	13632.66	757.37	13136.94	729.83	13136.94	729.83	23657.4	1314.3
O_2	32												
$Na_2CO_3 \cdot 1.5\,H_2O_2$	157												
H_2O_2	34					1404.54	41.31	1353.54	39.81				
H_2	2												
CO_2	44												
CO	28												
C_2H_4	28												
Total		2972.24	28.04	2478.6	137.7	19416.06	839.99	18710.34	809.45	14543.56	743.1	32052.6	1393.5

Table D.9: Stream summary for 4 outlet streams of the H_2O_2ER/HER process as defined in Figure D.5 for an anodic production of 26.54 kmol/h sodium percarbonate at base case performance parameters.

Stream number		**7**		**8**		**9**		**10**	
Name		**Purge**		**Anodic product**		**Anodic by-product**		**Cathodic product**	
Component	MW	kg/h	kmol/h	kg/h	kmol/h	kg/h	kmol/h	kg/h	kmol/h
Na_2CO_3	106	159.00	1.50						
H_2O	18	495.72	27.54						
O_2	32					440.64	13.77		
$Na_2CO_3 \cdot 1.5\,H_2O_2$	157			4166.78	26.54				
H_2O_2	34	51.00	1.50						
H_2	2							137.70	68.85
CO_2	44								
CO	28								
C_2H_4	28								
Total		705.72	30.54	4166.78	26.54	440.64	13.77	137.70	68.85

D.6. ANODIC PEROXIDE EVOLUTION REACTION COUPLED TO THE CO_2 REDUCTION TO CO

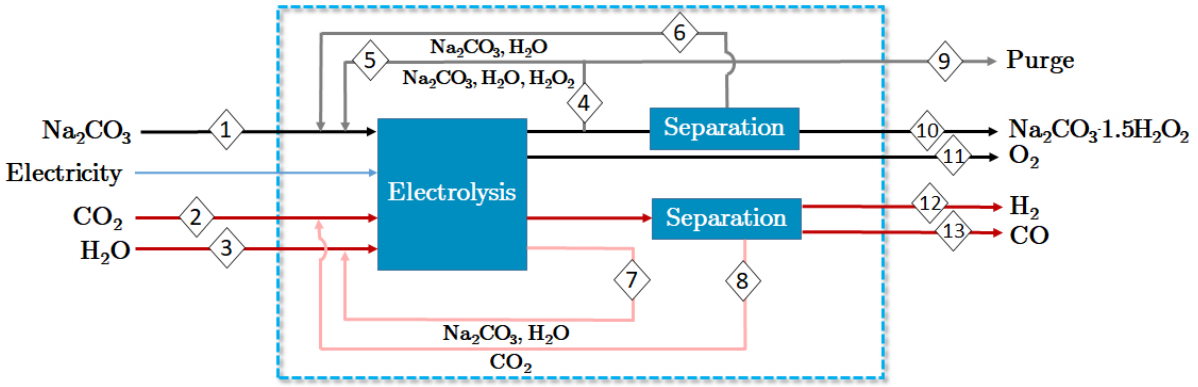

Figure D.6: Block scheme and battery limits for the coupled anodic peroxide evolution reaction/CO evolution

Table D.10: Stream summary for the first 6 streams of the H_2O_2ER/CO process as defined in Figure D.6 for an anodic production of 26.54 kmol/h sodium percarbonate at base case performance parameters.

Stream number		**1**		**2**		**3**		**4**		**5**		**6**	
Name		**Anolyte feed**		**Catholyte gas feed**		**Catholyte liquid feed**		**Split recycle/purge**		**Recycle (electrolyzer)**		**Recycle (crystallizer)**	
Component	MW	kg/h	kmol/h	kg/h	kmol/h	kg/h	kmol/h	kg/h	kmol/h	kg/h	kmol/h	kg/h	kmol/h
Na_2CO_3	106	2972.24	28.04					4378.86	41.31	4219.86	39.81	1406.62	13.27
H_2O	18					1487.16	82.62	13632.66	757.37	13136.94	729.83	13136.94	729.83
O_2	32												
$Na_2CO_3 \cdot 1.5\,H_2O_2$	157												
H_2O_2	34							1404.54	41.31	1353.54	39.81		
H_2	2												
CO_2	44			2423.52	55.08								
CO	28												
C_2H_4	28												
Total		2972.24	28.04	2423.52	55.08	1487.16	82.62	19416.06	839.99	18710.34	809.45	14543.56	743.10

Table D.11: Stream summary for the final 7 streams of the H_2O_2ER/CO process as defined in Figure D.6 for an anodic production of 26.54 kmol/h sodium percarbonate at base case performance parameters.

Stream number		**7**		**8**		**9**		**10**		**11**		**12**		**13**	
Name		**Catholyte liquid recycle**		**Catholyte gas recycle**		**Purge**		**Anodic product**		**Anodic by-product**		**Cathodic by-product**		**Cathodic product**	
Component	MW	kg/h	kmol/h	kg/h	kmol/h	kg/h	kmol/h	kg/h	kmol/h	kg/h	kmol/h	kg/h	kmol/h	kg/h	kmol/h
Na_2CO_3	106	8395.20	79.20			159.00	1.50								
H_2O	18	24648.84	1369.38			495.72	27.54								
O_2	32									440.64	13.77				
$Na_2CO_3 \cdot 1.5\,H_2O_2$	157							4166.78	26.54						
H_2O_2	34					51.00	1.50								
H_2	2											27.54	13.77		
CO_2	44			1038.84	23.61										
CO	28													1542.24	55.08
C_2H_4	28														
Total		33044.04	1448.58	1038.84	23.61	705.72	30.54	4166.78	26.54	440.64	13.77	27.54	13.77	1542.24	55.08

D.7. ANODIC PEROXIDE EVOLUTION REACTION COUPLED TO THE CO_2 REDUCTION TO C_2H_4

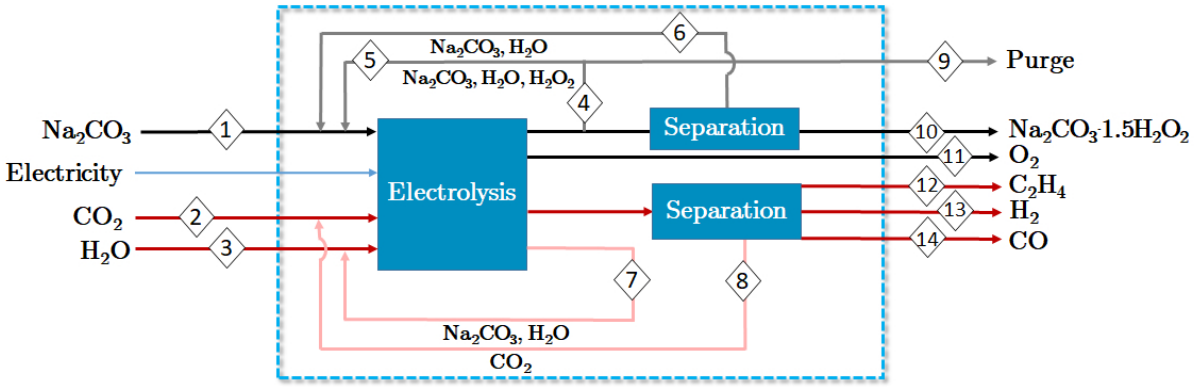

Figure D.7: Block scheme and battery limits for the coupled anodic peroxide evolution reaction/C_2H_4 evolution

Table D.12: Stream summary for the first 7 streams of the H_2O_2ER/C_2H_4 process as defined in Figure D.7 for an anodic production of 26.54 kmol/h sodium percarbonate at base case performance parameters.

Stream number		**1**		**2**		**3**		**4**		**5**		**6**		**7**	
Name		**Anolyte feed**		**Cathodic gas feed**		**Catholyte liquid feed**		**Split recycle/purge**		**Recycle (electrolyzer)**		**Recycle (crystallizer)**		**Recycle catholyte**	
Component	MW	kg/h	kmol/h	kg/h	kmol/h	kg/h	kmol/h	kg/h	kmol/h	kg/h	kmol/h	kg/h	kmol/h	kg/h	kmol/h
Na_2CO_3	106	2972.24	28.04					4378.86	41.31	4219.86	39.81	1406.62	13.27	8395.2	79.2
H_2O	18					1714.32	95.24	13632.66	757.37	13136.94	729.83	13136.94	729.83	24421.68	1356.76
O_2	32														
$Na_2CO_3 \cdot 1.5\,H_2O_2$	157														
H_2O_2	34							1404.54	41.31	1353.54	39.81				
H_2	2														
CO_2	44			1161.16	26.39										
CO	28														
C_2H_4	28														
Total		2972.24	28.04	1161.16	26.39	1714.32	95.24	19416.06	839.99	18710.34	809.45	14543.56	743.1	32816.88	1435.96

Table D.13: Stream summary for the final 7 streams of the H_2O_2ER/C_2H_4 process as defined in Figure D.7 for an anodic production of 26.54 kmol/h sodium percarbonate at base case performance parameters.

Stream number		**8**		**9**		**10**		**11**		**12**		**13**		**14**	
Name		**Cathodic gas recycle**		**Purge**		**Anodic product**		**Anodic by-product**		**Cathodic product**		**Cathodic by-product 1**		**Cathodic by-product 2**	
Component	MW	kg/h	kmol/h	kg/h	kmol/h	kg/h	kmol/h	kg/h	kmol/h	kg/h	kmol/h	kg/h	kmol/h	kg/h	kmol/h
Na_2CO_3	106			159.00	1.50										
H_2O	18			495.72	27.54										
O_2	32							440.64	13.77						
$Na_2CO_3 \cdot 1.5\,H_2O_2$	157					4166.78	26.54								
H_2O_2	34			51.00	1.50										
H_2	2											20.66	10.33		
CO_2	44	497.64	11.31												
CO	28													289.24	10.33
C_2H_4	28									224.84	8.03				
Total		497.64	11.31	705.72	30.54	4166.78	26.54	440.64	13.77	224.84	8.03	20.66	10.33	289.24	10.33

D.8. ANODIC PEROXIDE EVOLUTION REACTION COUPLED TO THE TWO-ELECTRON ORR

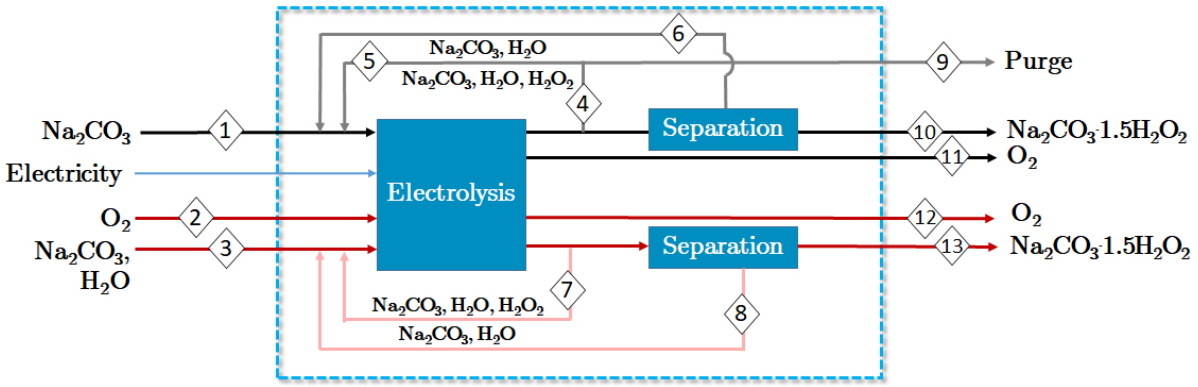

Figure D.8: Block scheme and battery limits for the coupled anodic peroxide evolution reaction/two-electron ORR

Table D.14: Stream summary for the first 6 streams of the H_2O_2ER/ORR process as defined in Figure D.8 for an anodic production of 26.54 kmol/h sodium percarbonate at base case performance parameters.

Stream number		**1**		**2**		**3**		**4**		**5**		**6**	
Name		**Anolyte feed**		**Cathodic gas feed**		**Catholyte feed**		**Split recycle/purge**		**Recycle (electrolyzer)**		**Recycle (crystallizer)**	
Component	MW	kg/h	kmol/h	kg/h	kmol/h	kg/h	kmol/h	kg/h	kmol/h	kg/h	kmol/h	kg/h	kmol/h
Na_2CO_3	106	2972.24	28.04			4378.86	41.31	4378.86	41.31	4219.86	39.81	1406.62	13.27
H_2O	18					2354.76	130.82	13632.66	757.37	13136.94	729.83	13136.94	729.83
O_2	32			2990.08	93.44								
$Na_2CO_3 \cdot 1.5\,H_2O_2$	157												
H_2O_2	34							1404.54	41.31	1353.54	39.81		
H_2	2												
CO_2	44												
CO	28												
C_2H_4	28												
Total		2972.24	28.04	2990.08	93.44	6733.62	172.13	19416.06	839.99	18710.34	809.45	14543.56	743.1

Table D.15: Stream summary for the final 7 streams of the H_2O_2ER/ORR process as defined in Figure D.8 for an anodic production of 26.54 kmol/h sodium percarbonate at base case performance parameters.

Stream number		**7**		**8**		**9**		**10**		**11**		**12**		**13**	
Name		**Catholyte recycle 1**		**Catholyte recycle 2**		**Purge**		**Anodic product**		**Anodic by-product**		**Gas excess**		**Cathodic product**	
Component	MW	kg/h	kmol/h	kg/h	kmol/h	kg/h	kmol/h	kg/h	kmol/h	kg/h	kmol/h	kg/h	kmol/h	kg/h	kmol/h
Na_2CO_3	106	6568.82	61.97	2189.96	20.66	159.00	1.50								
H_2O	18	20449.08	1136.06	20449.08	1136.06	495.72	27.54								
O_2	32									440.64	13.77	896.96	28.03		
$Na_2CO_3 \cdot 1.5\,H_2O_2$	157							4166.78	26.54					6485.67	41.31
H_2O_2	34	2106.98	61.97			51.00	1.50								
H_2	2														
CO_2	44														
CO	28														
C_2H_4	28														
Total		29124.88.88	1260	22639.04	1156.72	705.72	30.54	4166.78	26.54	440.64	13.77	896.96	28.03	6485.67	41.31

E

PERFORMANCE TARGETS FROM THE TECHNO-ECONOMIC MODEL

MAXIMUM OPERATING VOLTAGE STUDY

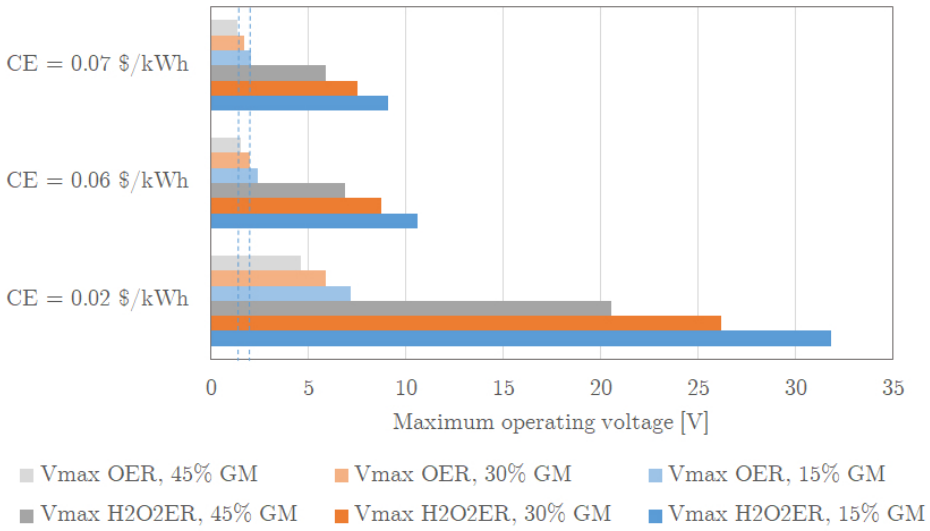

Figure E.1: Maximum operating voltage for the HER combined to the OER and the hydrogen peroxide evolution reaction as computed by the gross margin model for gross margins of 15, 30 and 45% at different electricity costs (CE, $/kWh). Base parameters presented in Section 3.1.3 were used.

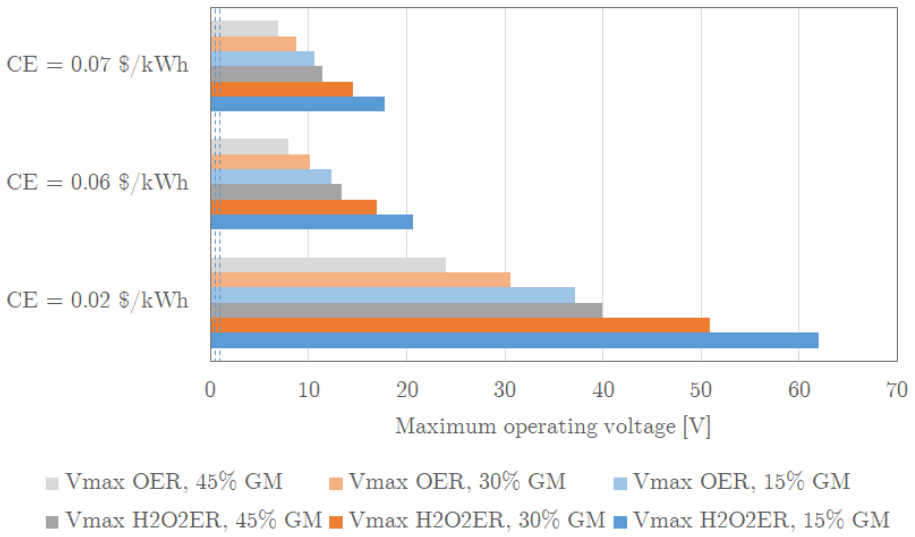

Figure E.2: Maximum operating voltage for the ORR combined to the OER and the hydrogen peroxide evolution reaction as computed by the gross margin model for gross margins of 15, 30 and 45% at different electricity costs (CE, $/kWh). Base parameters presented in Section 3.1.3 were used.

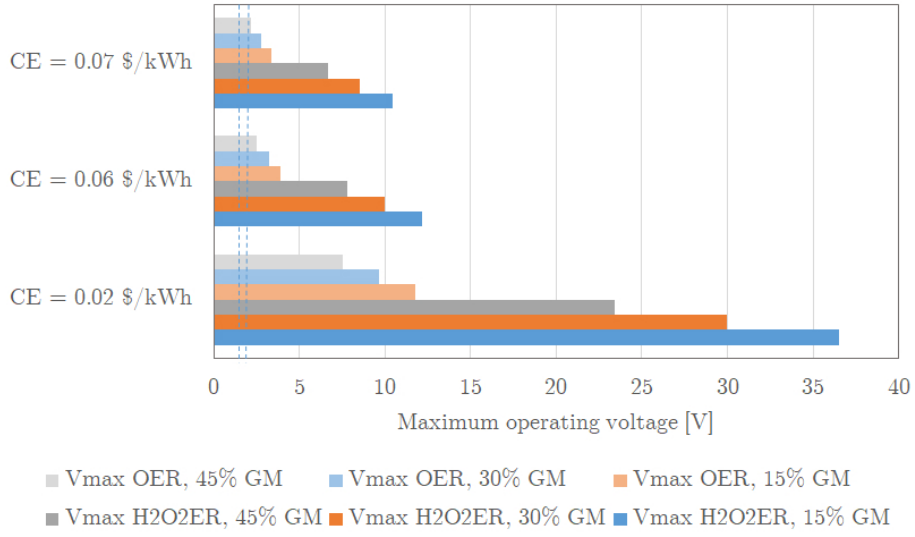

Figure E.3: Maximum operating voltage for the CO_2 reduction to CO combined to the OER and the hydrogen peroxide evolution reaction as computed by the gross margin model for gross margins of 15, 30 and 45% at different electricity costs (CE, $/kWh). Base parameters presented in Section 3.1.3 were used.

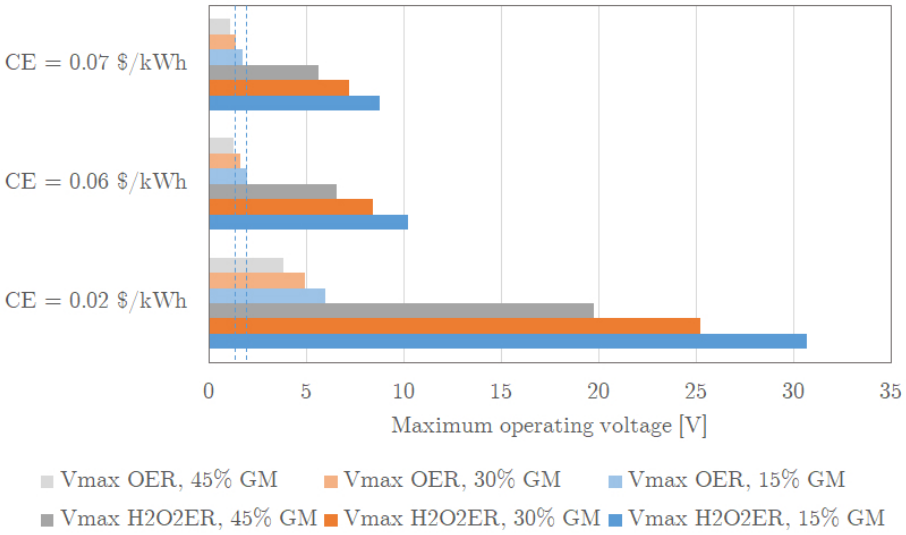

Figure E.4: Maximum operating voltage for the CO_2 reduction to C_2H_4 combined to the OER and the hydrogen peroxide evolution reaction as computed by the gross margin model for gross margins of 15, 30 and 45% at different electricity costs (CE, $/kWh). Base parameters presented in Section 3.1.3 were used.

F

ELECTROCHEMICAL DATA-SETS FOR TIN-BASED ELECTRODE TESTING

F.1. DIFFERENT HEAT TREATMENTS

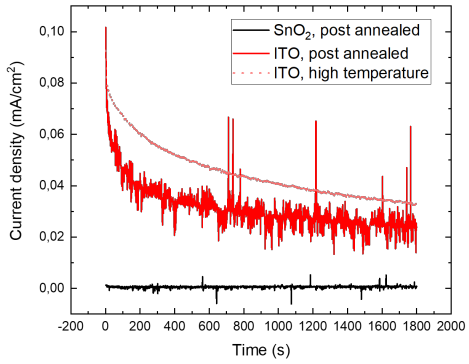

(a) Chronoamperometry at 2 V vs RHE, 30 min

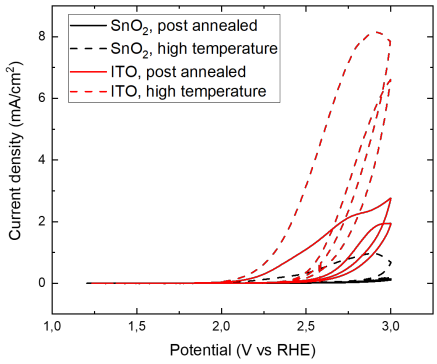

(b) CV from 0 V vs OC to 3 V vs RHE

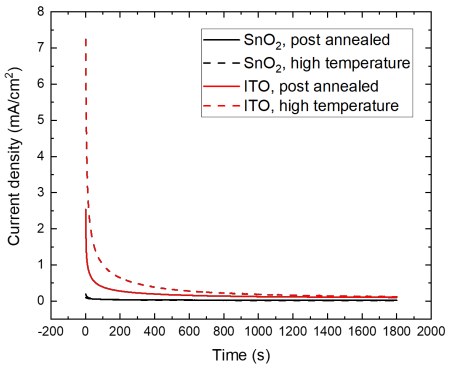

(c) Second chronoamperometry at 3 V vs RHE, 30 min

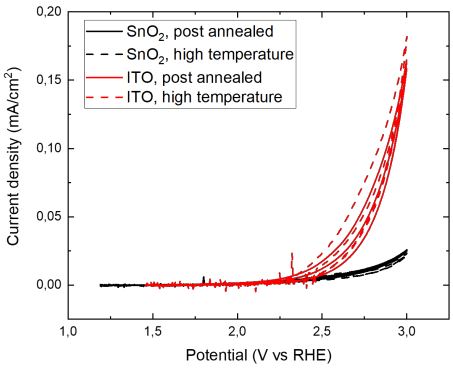

(d) Second CV from 0 V vs OC to 3 V vs RHE

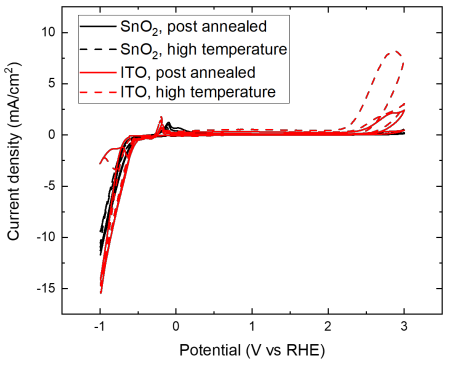

(e) Third CV from -2 V vs RHE to 3 V vs RHE

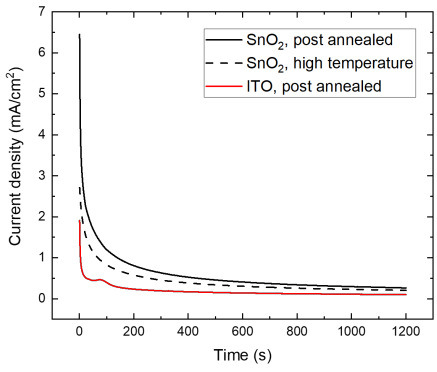

(f) Third chronoamperometry at 4 V vs RHE, 20 min

Figure F.1: Electrochemical tests performed in the electrolysis cell with as anode SnO_2 and ITO sputtered at high temperature (500 and 350 °C respectively) and at room temperature with post annealing at 500 and 400 °C respectively. Tests were done in the order presented in 0.5 M $KHCO_3$ pumped through the system at a flow-rate of 37 mL/min.

F.2. THICKNESS STUDY

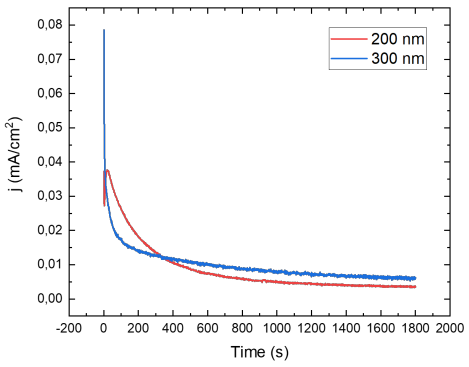

(a) Chronoamperometry at 2 V vs RHE, 30 min

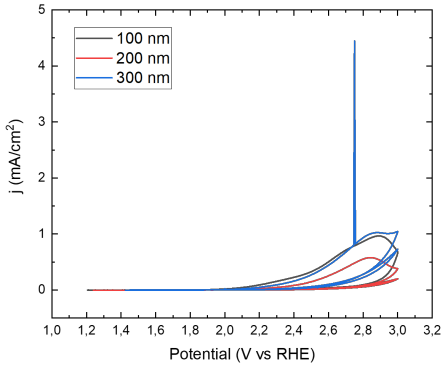

(b) CV from 0 V vs OC to 3 V vs RHE

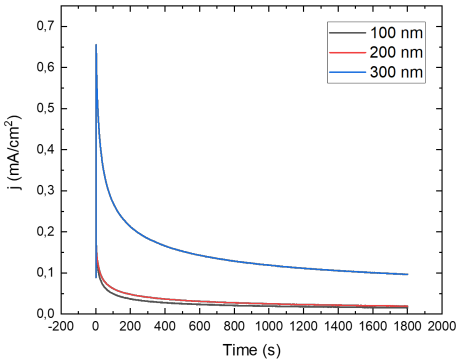

(c) Second chronoamperometry at 3 V vs RHE, 30 min

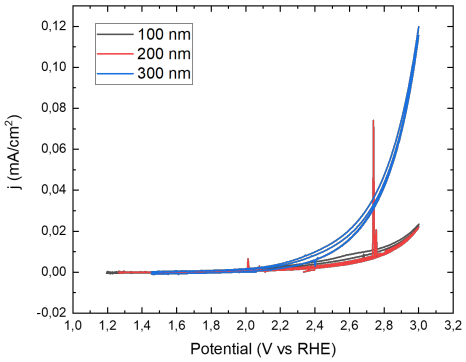

(d) Second CV from 0 V vs OC to 3 V vs RHE

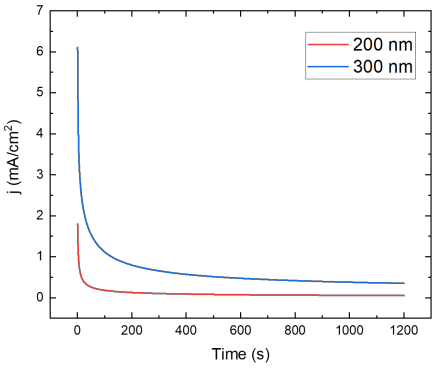

(e) Third chronoamperometry at 4 V vs RHE, 20 min

Figure F.2: Electrochemical tests performed in the electrolysis cell with as anode SnO_2 sputtered at high temperature as thin layer of 100, 200 or 300 nm. Tests were done in 0.5 M $KHCO_3$ pumped through the system at a flow-rate of 37 mL/min.

F.3. MORPHOLOGY STUDY

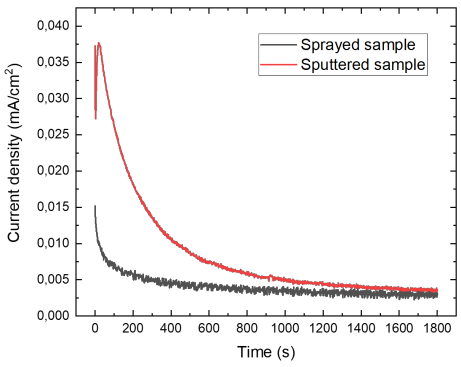

(a) Chronoamperometry at 2 V vs RHE, 30 min

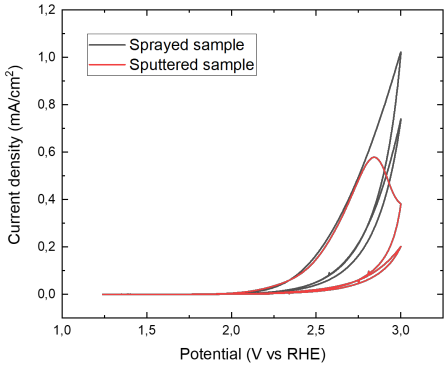

(b) CV from 0 V vs OC to 3 V vs RHE

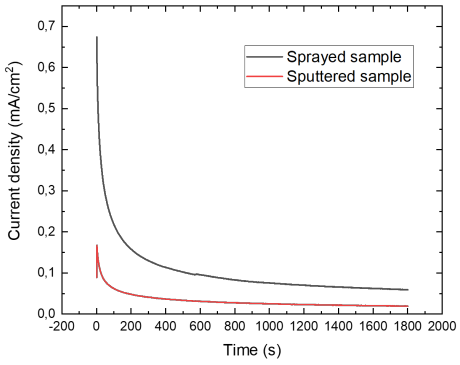

(c) Second chronoamperometry at 3 V vs RHE, 30 min

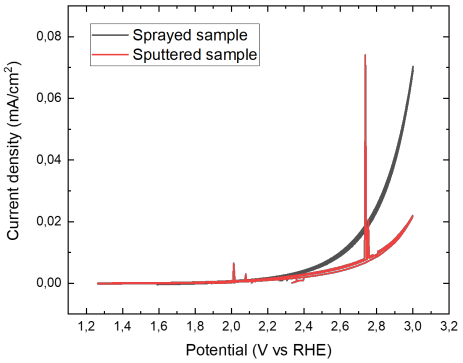

(d) Second CV from 0 V vs OC to 3 V vs RHE

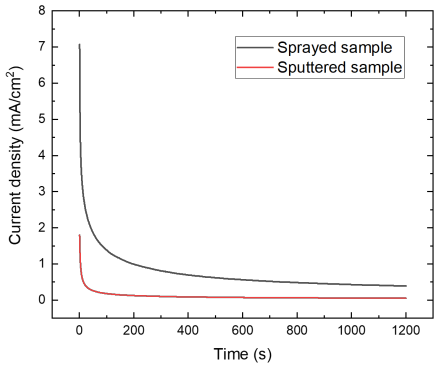

(e) Third chronoamperometry at 4 V vs RHE, 20 min

Figure F.3: Electrochemical tests performed in the electrolysis cell with SnO_2 anodes deposited via DC magnetron sputtering at high temperature and deposited via 10 cycles of spray pyrolysis. Tests were done in 0.5 M $KHCO_3$ pumped through the system at a flow-rate of 37 mL/min.

F.4. COMPOSITION STUDY

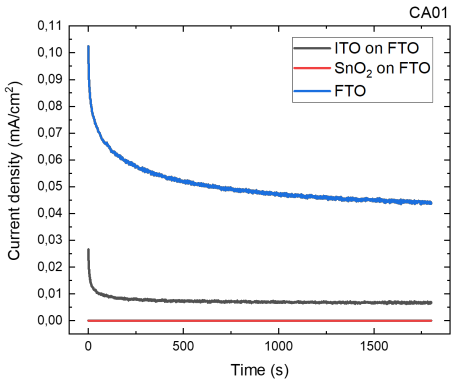

(a) Chronoamperometry at 2 V vs RHE, 30 min

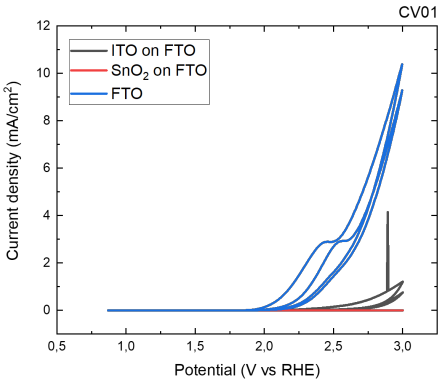

(b) CV from 0 V vs OC to 3 V vs RHE

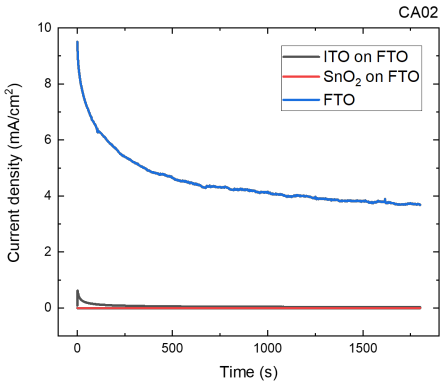

(c) Second chronoamperometry at 3 V vs RHE, 30 min

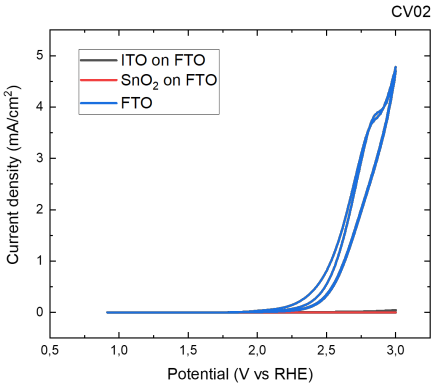

(d) Second CV from 0 V vs OC to 3 V vs RHE

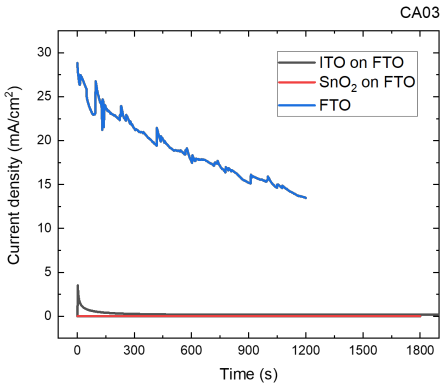

(e) Third chronoamperometry at 4 V vs RHE, 20 min

Figure F.4: Electrochemical tests performed in the electrolysis cell with SnO_2 and ITO anodes deposited via DC magnetron sputtering at room temperature onto FTO substrates and post annealed at 500 and 400 °C respectively. Tests were done in 0.5 M $KHCO_3$ pumped through the system at a flow-rate of 37 mL/min.

F.5. SUBSTRATE EFFECT

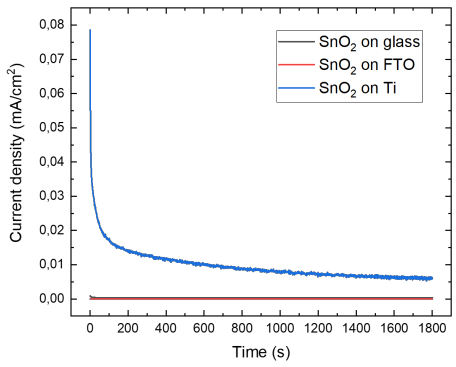

(a) Chronoamperometry at 2 V vs RHE, 30 min

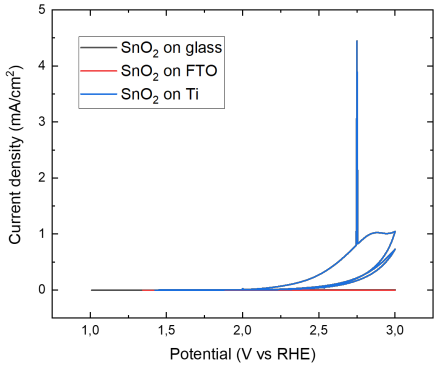

(b) CV from 0 V vs OC to 3 V vs RHE

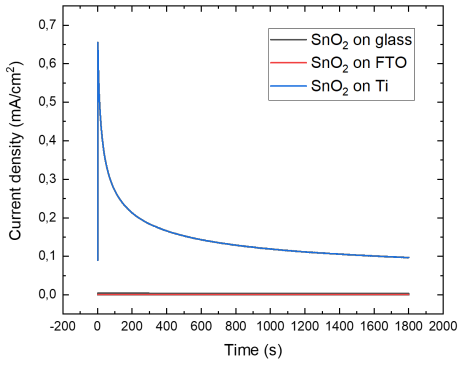

(c) Second chronoamperometry at 3 V vs RHE, 30 min

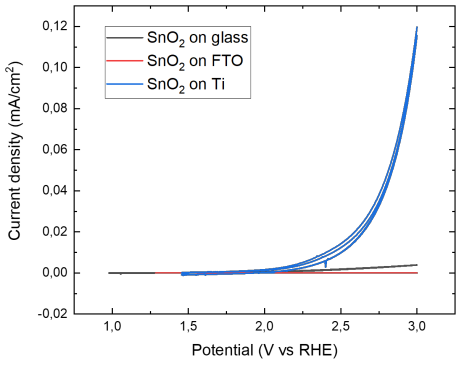

(d) Second CV from 0 V vs OC to 3 V vs RHE

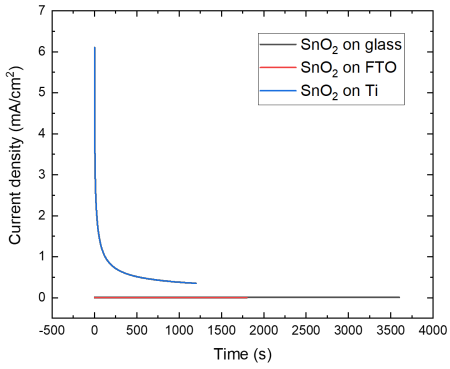

(e) Third chronoamperometry at 4 V vs RHE, 20 min

Figure F.5: Electrochemical tests performed in the electrolysis cell with SnO_2 anodes deposited onto glass and FTO via DC magnetron sputtering at room temperature with post annealing treatment (500 °C) as well as of SnO_2 deposited on Ti at high temperature (500 °C). Tests were done in 0.5 M $KHCO_3$ pumped through the system at a flow-rate of 37 mL/min.

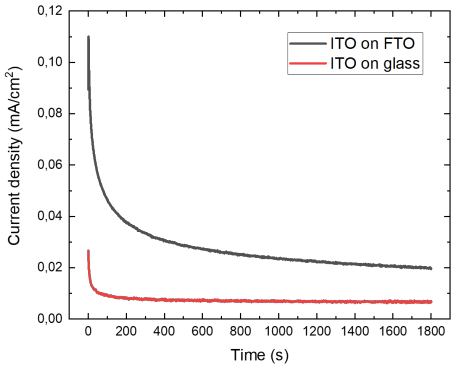

(a) Chronoamperometry at 2 V vs RHE, 30 min

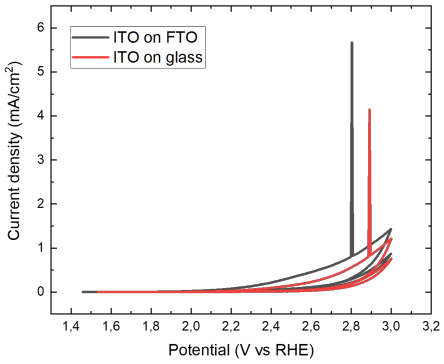

(b) CV from 0 V vs OC to 3 V vs RHE

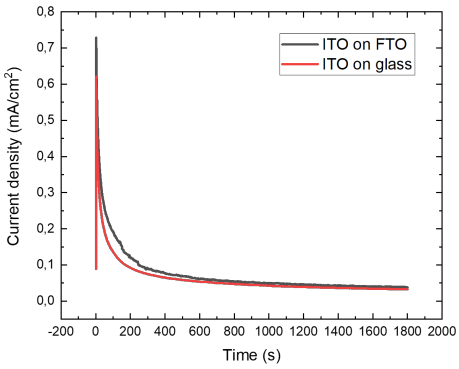

(c) Second chronoamperometry at 3 V vs RHE, 30 min

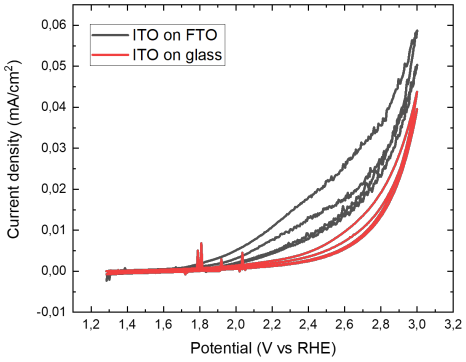

(d) Second CV from 0 V vs OC to 3 V vs RHE

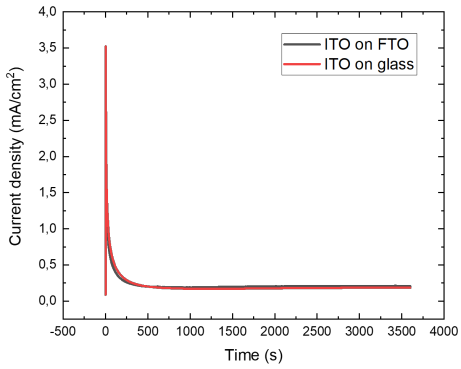

(e) Third chronoamperometry at 4 V vs RHE, 20 min

Figure F.6: Electrochemical tests performed in the electrolysis cell with ITO anodes deposited onto glass and FTO via DC magnetron sputtering at room temperature with post annealing treatment (400 °C). Tests were done in 0.5 M $KHCO_3$ pumped through the system at a flow-rate of 37 mL/min.

F.6. Sn_3O_4

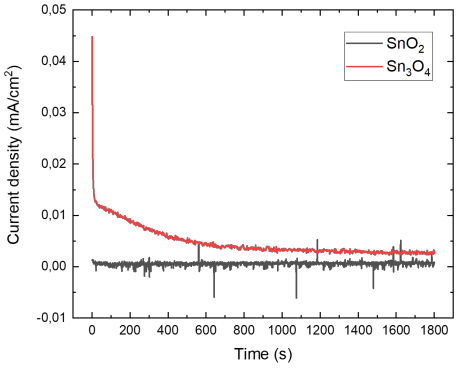

(a) Chronoamperometry at 2 V vs RHE, 30 min

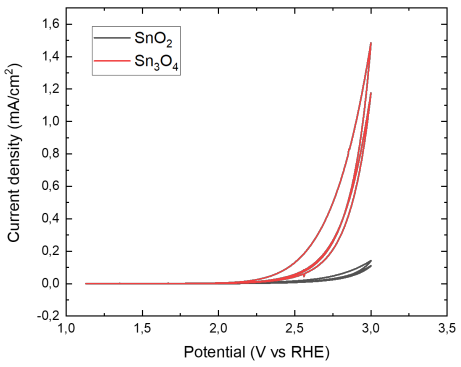

(b) CV from 0 V vs OC to 3 V vs RHE

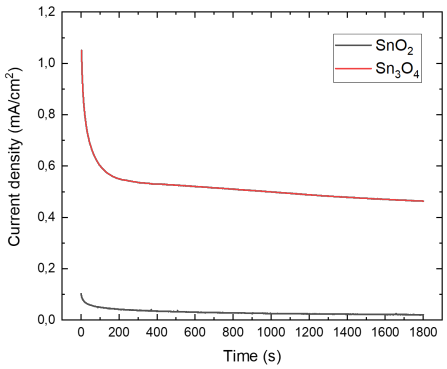

(c) Second chronoamperometry at 3 V vs RHE, 30 min

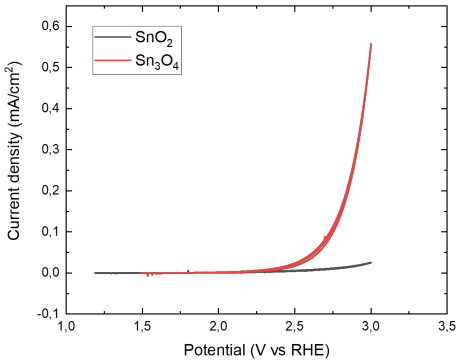

(d) Second CV from 0 V vs OC to 3 V vs RHE

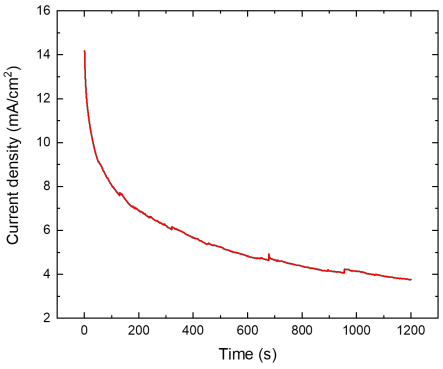

(e) Third chronoamperometry at 4 V vs RHE, 20 min

Figure F.7: Electrochemical tests performed in the electrolysis cell with a Sn_3O_4 electrode deposited via DC magnetron sputtering for 7 min 14 s at room temperature under 15 sccm Ar and 5 sccm O_2 at 15 W and post annealed at 500 °C. Tests were done in 0.5 M $KHCO_3$ pumped through the system at a flow-rate of 37 mL/min.